LBNL-40442
UC-410

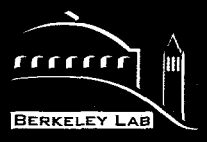

ERNEST ORLANDO LAWRENCE
BERKELEY NATIONAL LABORATORY

The Interfacial and Surface Properties of Thin Fe and Gd Films Grown on W(110) as Studied by Scanning Tunneling Microscopy, Site-Resolved Photoelectron Diffraction, and Spin Polarized Photoelectron Diffraction

Eric D. Tober
Materials Sciences Division

June 1997
Ph.D. Thesis

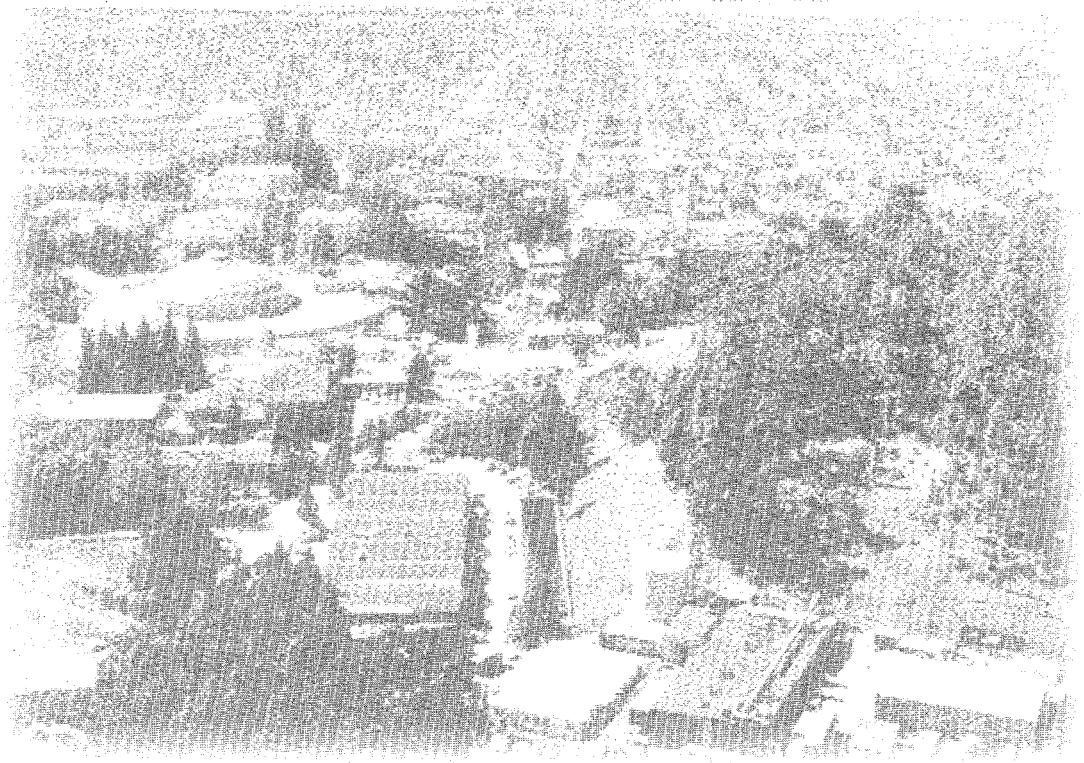

LBNL-40442

The Interfacial and Surface Properties of Thin Fe and Gd Films Grown on W(110) as Studied by Scanning Tunneling Microscopy, Site-Resolved Photoelectron Diffraction, and Spin Polarized Photoelectron Diffraction

by

Eric Dean Tober

B. S. (California Polytechnic State University, San Luis Obispo) 1988

M. S. (San Jose State University, San Jose) 1990

DISSERTATION

Doctor of Philosophy

in

Physics

in the

OFFICE OF GRADUATE STUDIES

of the

UNIVERSITY OF CALIFORNIA

DAVIS

1997

Acknowledgements

I would like to thank Professor Charles S. Fadley of the University of California, Davis for the many years of advice, assistance, and patience in the face of the occasional (very rare) experimental mishap which made this work possible. I would also like to thank Dr. Ajith Kaduwela for the many helpful discussions with respect to his multiple scattering code, Dr. Ian Tidswell for assistance with aligning and polishing W(110) crystals, and Dr. Dieter Weller for advice concerning the deposition of rare-earth films and the loan of his deposition cell. Furthermore, I would like to express my gratitude to Drs. S. Thevuthasan, K. Higashiyama, C. Westphal, and F. J. Palomares for their assistance with various measurements that were performed for this work. Finally, I would like to thank all of my fellow graduate students in Professor Fadley's research group for all of their help regarding this work.

Support for these studies was provided by the Director, Office of Energy Research, Materials Sciences Div., of the U.S. Dept. of Energy, under Contract No. DE-AC03-76SF00098, the Office of Naval Research under contract (N00014-94-0162), and the National Energy Research Supercomputing Cntr. at LBNL.

Abstract

Combined scanning tunneling microscopy (STM) and low energy electron diffraction (LEED) measurements from Gd films grown on W(110) prepared with and without annealing have been used to provide a detailed picture of the growth of such films, permitting a quantitative structural explanation for previously-measured magnetic properties and the identification of a new two-dimensional structure for the first monolayer. The analysis of the film roughness of room-temperature-grown films as a function of coverage and lateral length scale reveals that the growing Gd surface follows scaling laws for a self-affine surface. Annealing these as-deposited films at elevated temperatures is found to drastically alter the morphology of the films, as seen by both STM and LEED. Nanometer-scale islands of relatively well-defined size and shape are observed under certain conditions. Finally, the first monolayer of Gd is observed to form a (7x14) superstructure with pseudo-(7x7) symmetry that is consistent with a minimally-distorted hexagonal two-dimensional Gd(0001) film. Furthermore, a new beamline and photoelectron spectrometer/diffractometer at the Advanced Light Source have been used to obtain full-solid-angle and site-specific photoelectron diffraction (PD) data from interface W atoms just beneath (1x1) Fe and (7x14) Gd monolayers on W(110) by utilizing the core level shift in the W $4f_{7/2}$ spectrum. A comparison of experiment with multiple scattering calculations permits determining the Fe adsorption site and the relative interlayer spacing to the first and second W layers. These Fe results are also compared to those from the very different Gd overlayer and from the clean W(110) surface. Such interface PD measurements show considerable promise for future studies. Finally, the rare-earth ferromagnetic system of Gd(0001) has been examined through the use of spin polarized photoelectron diffraction from the Gd 4s and 5s photoelectron multiplets, both of which exhibit highly spin polarized ^7S and ^9S photoelectron peaks. The relative spin

asymmetries in the ^7S to ^9S peak intensity ratio as a function of temperature have revealed distinct features near both the bulk and the previously reported surface Curie temperatures, indicating that short range magnetic order does indeed persist above the bulk ordering temperature. We measure a separation of 60-80 K between the surface and bulk transition temperatures. Furthermore, our results suggest that the energy splitting between the ^7S and ^9S peaks exhibits a systematic variation with temperature that has not been seen in previous experiments involving core-level photoemission from Gd; this effect may be due to a spin and temperature dependent core-hole screening process or variations in the exchange arising from the valence electrons.

TABLE OF CONTENTS

Chapter 1.

General Introduction

Understanding the interplay between structure, morphology and magnetism for thin solid films, solid surfaces, and solid-solid interfaces is an area of rapidly growing interest as technology more demands and experimental technique now allows the creation of well ordered nanometer-scale and atomic-scale systems. This is especially important in technologies such as magnetic recording where, as dimensions continue to shrink, surface and interface effects become increasingly more significant. In this dissertation, several powerful surface and interface probes have been utilized to study the magnetic and structural properties of epitaxial films and surfaces consisting of the simple ferromagnets Fe and Gd. Some of the specific physical questions addressed are: "How do thin films of Fe and Gd grow on the non-magnetic substrate W(110)?", "What consequences does such growth have on the magnetic properties of these films?", "What is the structure at the Fe/W and Gd/W interface?", and "Does the Gd(0001) surface exhibit magnetic order above the bulk ordering temperature of 292.5 K?" These questions and the applications of various techniques to answering them will be discussed in further detail at the end of this chapter. The specific experimental methods employed in this dissertation are: photoelectron spectroscopy and diffraction (PS and PD), scanning tunneling microscopy (STM), low energy electron diffraction (LEED), Auger electron spectroscopy (AES), and the magnetooptic Kerr effect (MOKE). Figure 1.1 shows a schematic illustration of the first three structural probes PD, LEED, and STM, together with the complementary information they provide. AES, like PS, is a useful tool for quantifying the elemental composition of surfaces. A schematic of the MOKE technique, which explores the magnetic character of a thin film or surface, is contained in Fig. 1.2. To more fully understand the capabilities of the aforementioned techniques, a brief description will be given of each.

Photoelectron Spectroscopy and Diffraction

The basis of photoelectron spectroscopy lies in the photoelectric effect first proposed by Einstein in 1905 [1]. In this effect, a photon of energy hν impinges on a surface and, if it has sufficient energy, ejects an electron with kinetic energy E_k. The equation describing energy conservation for the photoelectron is then:

$$E_k = h\nu - E_b^v(i) \qquad [1]$$

where $E_b^v(i)$ is then the binding energy of the ejected electron for a given orbital "i" as referenced to the vacuum level. In photoelectron spectroscopy [2], one typically illuminates a surface with monochromatic soft x-rays or ultra-violet light and then measures the kinetic energy and intensity of the emitted photoelectrons. For emission from core orbitals, $E_b^v(i)$ is characteristic of a given orbital for a specific atomic species, and thus measuring the photoelectron energy spectrum at the simplest level gives information on the type of emitting atoms present. Furthermore, information on the chemical environment of the emitter can also be derived from core-level binding energy shifts induced by changes in the bonding environment and valence-electron charge distribution. Finally, the valence-band structure of a material can also be studied by focusing on binding energies in the zero to ~20 eV range. An example of a photoelectron spectrum is shown in Fig 1.3 for a Gd(0001) surface taken with Al Kα excitation (hν = 1486.6 eV); the origins of the various peaks are labeled.

Beyond the ability to perform spectroscopy with photoelectrons, one may also perform diffraction experiments. Typically in such measurements a specific core-level is chosen and its intensity is measured as a function of emission angle. Fig. 1.4 displays the

experimental geometry used for such measurements in this work, including the important angular variables: the angle α between the incident light direction (parallel to the light wave vector $k_{h\nu}$) and the photoelectron analyzer direction (parallel to the photoelectron wave vector **k**), the polar emission angle θ as measured from the sample surface, and the azimuthal angle ϕ measured about the sample normal $\bar{n}$ and with respect to a fixed direction lying in the sample surface. The angle of photon incidence $\theta_{h\nu}$ will not be important here, although it has in other experiments been used to vary the surface sensitivity of the measurement [2]. If a measurement is made of the angular dependence of the photoelectron intensity in an ordered solid, characteristic and very strong angular dependent variations in intensity $I(\theta,\phi)$ are observed. These variations are due to the fact that the emitted photoelectrons will scatter from neighboring atoms as they leave the crystal, giving rise to interference between the direct (or unscattered) Φ^o and scattered Φ j photoelectron waves [3(a)]. In the simplified case of single scattering, the relationship between the intensity and the interference of these outgoing waves is:

$$I(\theta,\phi) \propto \left|\Phi^\circ + \sum_j \Phi_j\right|^2 \qquad [4]$$

where the sum is over all scatterers j. For the simple case of emission from an s orbital, the primary and scattered waves can be written more explicitly by:

$$\Phi^\circ = \hat{\varepsilon}\cdot\hat{k}\exp(-L/2\Lambda_e) \qquad [5]$$

and :

$$\Phi_j = \frac{\hat{\varepsilon}\cdot\hat{r}_j}{r_j}\left|f_j(\theta_j,r_j)\right| W_j(\theta_j)\exp(-L/2\Lambda_e)\exp\left\{i\left[kr_j(1-\cos(\theta_j))+\psi_j(\theta_j)\right]\right\} \qquad [6]$$

where $\hat{\varepsilon}$ is the polarization direction of the incident radiation, $\hat{r}_j$ is a unit vector pointing from the emitter to the scatterer j, r_j is the distance from the emitter to the jth scatterer, L and L_j are the path lengths for inelastic scattering of Φ^o and Φ_j respectively, Λ_e is the inelastic attenuation length, θ_j is the scattering angle for the jth atom, $f_j(\theta_j,r_j)$ is the spherical wave scattering factor including the scattering phase shift of $\Psi_j(\theta_j,r_j)$, $W_j(\theta_j)$ is the Debye-Waller factor for the jth scatterer and k is the magnitude of the photoelectron wave vector. Fig. 1.5 schematically shows the PD process, with various quantities defined. Typical attenuation lengths Λ_e are on the order of 5 to 20 Å for the E_k used in PD; this is illustrated in a compilation of experimental results for different solid elements shown in Fig. 1.6 [4]. Beyond the parameters mentioned above, the photoelectron diffraction process will also depend on the inner potential V_o (cf. Fig. 1.5), which acts as a barrier for electron escape from the surface, and can significantly change the direction of low-energy electron propagation due to a refraction effect [3(b)]. Values for V_o are typically in the range of 10-20 eV. Also, the solid angle of acceptance of the photoelectron spectrometer Ω_o inherently involves an integration over diffraction features that must be allowed for in theoretical modeling. For the spectrometer used in most of this thesis, this solid angle corresponded to a cone of half angle 5°.

For emission from orbitals with initial angular momentum $\ell_{initial} > 0$, the above expressions in Eqns. 5 and 6 become more complicated, involving sums over initial and final magnetic quantum numbers as well as interferences between the two dipole-selection-rule allowed final state channels ($\ell_{final} = \ell_{initial} \pm 1$). Such sums and interferences are automatically taken into account in the computer programs that I have used to model my data [5,6].

Photoelectron diffraction contains some important aspects which make it particularly well suited for studying surfaces and thin films. First, as previously mentioned, the inelastic attenuation lengths in the energy range used are very small. This typically restricts the significant portion of the measured PD to the top 10 or less layers of the sample under scrutiny, as the signal from deeper into the bulk is strongly attenuated. Therefore, this technique is most sensitive to the surface and near-surface regime. Secondly, as the direct wave is proportional to 1/r (cf. Fig. 1.5), the scattering/interference effects are strongest from atoms closest to the emitter; inelastic scattering further acts to focus on the near-neighbor atoms. This makes PD predominantly a probe of the short range structural order surrounding the emitter. Another important aspect of core-level photoemission, also mentioned above, is its sensitivity to the local chemical and structural surroundings of the emitter. This sensitivity can give the experimentalist the ability to distinguish between two or more otherwise identical emitters existing in structurally and/or chemically different sites, and this aspect will be utilized in Chapter 3. Finally, core-level emission from a magnetic atom can exhibit splittings (multiplet splittings) with the different peaks in the spectrum being strongly spin polarized with respect to the emitting atom's magnetic moment. In magnetically ordered systems, this can enable the use of PD as not only a structural probe, but also as a probe of short range magnetic order. A first application of such spin-polarized photoelectron diffraction (SPPD) to a ferromagnet will be discussed in further detail in Chapter 4.

In order to interpret the measured PD data obtained in this work, fully-converged multiple scattering calculations of photoelectron diffraction patterns were performed utilizing codes developed by Kaduwela et al [6] and based on the Rehr-Albers formalism [7] of separable Green's functions to describe the scattering process in a convenient and time-saving way. These calculations typically require cluster sizes of a 100-120 atoms for

convergence and incorporate all of the previously discussed physical variables. Also included in this code are the previously-mentioned effects of: instrumental angular broadening Ω_O, refraction at the sample surface due to the inner potential V_O, and the angular momenta and interferences between the two possible final state channels (λ+1 and λ-1). The exact parameters used for each calculation are discussed in the appropriate chapters.

Scanning Tunneling Microscopy

The STM technique was first developed to the degree of directly imaging atoms by Binnig and Rohrer in 1982 [8]. From this inception only 14 years ago, STM has already become one of the pre-eminent surface science techniques in use today. Its usefulness lies in its ability to directly image surface morphology from a very large scale up to microns (10^{-6} m), down to a very small atomic structure on a scale of 10^{-10}-10^{-11} m, and surface electronic structure on the same fine scale. Strictly speaking, STM images surface electronic structure via tunneling from electronic wave functions which protrude from the surface, so care is needed to be able to assert that one is really imaging an atom. Nonetheless, it is clear that many atomically resolved images of surface structures have by now been obtained. A couple of excellent reviews on this topic appear in the references for this chapter [9,10].

A brief description of the STM technique is as follows: An atomically sharp tip is brought close to the sample surface (cf. middle panel of Fig. 1.1) with a bias voltage $V_{Bias} \equiv V_b$ applied between the two; this bias is typically on the order of ±10 mV to ±10 V. The resulting energy-level diagram between tip and sample is shown in Fig. 1.7, in which F indicates the location of the Fermi level in both, and ϕ_{tip} and ϕ_{sample} are the

respective work functions. When the tip is brought close enough to the surface, a significant number of electrons are then capable of tunneling from the tip to the surface (or vice versa, depending on the sign of V_b) giving rise to a tunneling current I. The bias dependence of the tunneling current at low voltages can be approximated by [9]:

$$I \propto \exp(-2s\kappa) \qquad [7]$$

where s is the distance between the tip and surface and κ is the reciprocal decay length of the electron wave function as described by:

$$\kappa = \sqrt{\frac{2m\varphi}{\hbar^2}} \qquad [8]$$

where φ is the average barrier height (not to be confused with the azimuthal angle ϕ in the previous section), and m is the electron mass. The effective barrier height will thus depend on which filled states are tunneling into which empty states. For the configuration shown in Fig. 1.7 of electrons tunneling into states of energy E above the Fermi level and therefore a negative V_b (as measured by the tip voltage with respect to the sample), the barrier height can be approximated by: $\varphi = (\phi_{tip} + \phi_{sample})/2 + V_b/2 - E$, where ϕ_{tip} and ϕ_{sample} are the work function values of the tip and sample, respectively. For a typical φ of 4 eV, the decay length $\kappa^{-1} \cong 0.1$ nm, making the tunneling current highly sensitive to changes in s on this order. This sensitivity to small changes in the tip-to- sample separation is the basis for the high resolution obtainable by STM.

A more detailed expression for the tunneling current that could in principle be used to calculate it from first principles via first order perturbation theory is [10]:

$$I = \frac{2\pi e}{\eta} \sum_{\mu\nu} f(E_\mu)[1 - f(E_\nu + eV_b)] \left| M_{\mu\nu} \right|^2 \delta(E_\mu - E_\nu) \qquad [9a]$$

where $M_{\mu\nu}$ is the tunneling matrix element, f(E) is the Fermi function, E_μ is the energy of state μ, with μ and ν running over all the states of the tip and surface, respectively. The tunneling matrix element may then be expressed in terms of the wavefunctions of the two electrodes as being [10]:

$$M_{\mu\nu} = \int d\mathbf{S} \cdot (\Psi_\mu^* \nabla \Psi_\nu - \Psi_\nu \nabla \Psi_\mu^*) \qquad [9b]$$

where Ψ_ν is the wavefuncion and the integral is over a given plane in the barrier region.

There exist two basic modes of operation for the standard scanning tunneling microscope: the constant current mode and the constant height mode. The constant current mode involves a feedback loop between the measured tunneling current and a voltage applied to a piezo-electric driver for the tip; this driver regulates the tip-sample separation. As the tip is scanned back and forth over the sample, the STM attempts to maintain a constant current between the tip and the sample surface. The feedback loop then monitors this current and adjusts the piezo voltage accordingly so as to achieve the height s necessary to meet this requirement. Hence, the experimentalist selects the set-point tunneling current I_o, the sample-tip bias V_b, and the scanning speed of the tip in order to acquire the desired image in terms of piezo voltage vs. tip position. The piezo voltage can then be calibrated against a known vertical tip height displacement such as a monatomic step on a surface to finally render the image in terms of tip height vs. tip position. The second constant height mode involves scanning the tip at a nearly constant height above the sample surface, and simultaneously observing the changes in tunneling

current which result. The STM thus finally monitors the fluctuation in tunneling current as a function of tip position, giving rise to the constant height image. Each method has its advantages and limitations. Constant current gives information in three dimensions on the sample surface, yet requires slower acquisition times and is more sensitive to spurious noise due to the feedback loop continuously adjusting the piezo height. Constant height mode often gives higher lateral resolution and always permits faster scan times, but lacks the quantitative information of the third dimension that one sometimes needs to fully characterize surface features. Regardless of these differences, each method measures the outermost surface topography through the surface density of states (cf. Eq. 9a,b), thus providing real space information on the short and long range order present at the surface.

Low Energy Electron Diffraction:

LEED was first pioneered by Davisson and Germer in 1927 as the first experimental demonstration of the deBroglie wave character of a particle [11] and it is by now probably the most commonly used method for determining surface atomic order and surface atomic structure [12]. Typically, this technique involves illuminating a sample with a monoenergetic, focused beam of electrons of energy E_0 from 20 - 300 eV and imaging the elastically scattered and diffracted beams, as schematically illustrated in the right panel of Fig. 1.1. To do this, one requires a phosphor screen held at a fixed potential and constant radial distance from the point at which the beam hits the surface. LEED is sensitive to only the first few layers of the sample due to the low attenuation length of electrons in this energy range; thus, it is surface sensitive for the same fundamental reason as PS and PD. For LEED, the ordered arrays of atoms which make up a sample surface act as diffraction gratings for the incident electrons. The coherence length required for this effect is on the order of 10 nm, making LEED an effective probe of the long range two-dimensional

atomic order present in the top few atomic layers. In diffraction, the two-dimensional Bragg condition can be written as [12]:

$$\mathbf{k}_{\parallel}^{'} = \mathbf{k}_{\parallel} + \mathbf{g}_{\mathbf{hk}} \qquad [10]$$

where $\mathbf{k}_{\parallel}^{'}$ and $\mathbf{k}_{\parallel}$ are the wavevectors of the diffracted and incident electrons parallel to the surface, $\mathbf{g}_{hk} = h\mathbf{a}^* + k\mathbf{b}^*$ is a two-dimensional reciprocal lattice vector, and $\mathbf{a}^*$ and $\mathbf{b}^*$ are the primitive translation vectors of the two dimensional surface reciprocal lattice. The vectors $\mathbf{a}^*$ and $\mathbf{b}^*$ are in turn calculated from:

$$\mathbf{a}^* = 2\pi\frac{\mathbf{b}\times\mathbf{n}}{A}, \quad \mathbf{b}^* = 2\pi\frac{\mathbf{n}\times\mathbf{a}}{A}, \; A = \mathbf{a}\cdot\mathbf{b}\times\mathbf{n} \qquad [11]$$

where **a** and **b** are the primitive translation vectors of the real surface lattice(s) and **n** is a unit vector along the surface normal. Each spot in the pattern viewed by LEED is then associated with one of the reciprocal lattice vectors, and is thus indicated by (hk). In this manner, the LEED pattern is then simply a reflection of the periodicities in the surface reciprocal lattice.

LEED can also give additional quantitative and qualitative information about the order present at the surface beyond the simple two dimensional periodicities associated with long-range order. Sharp, distinct spots are indicative of a surface with good long range periodic order of at least the scale of the instrument's coherence length. However, if spots are blurry or appear overly large, this could mean that at longer distances the surface ordering is poor. A more detailed analysis of the spot intensity with varying beam energy (often referred to as LEED I-V curves), including comparison with multiple scattering calculations, can yield structural information for the top surface layers in three dimensions.

Hence, LEED can be used to give information on both the long range order and the shorter range structural environment in surfaces and overlayers, although our own use of it here will stop short of any sort of comparison with theoretical calculations.

Auger Electron Spectroscopy:

The same experimental systems used to perform LEED measurements can quite often be used for Auger electron spectroscopy as well. This makes such systems ideal for combined analysis of surface order and surface composition. The Auger process is schematically illustrated in Fig. 1.8. In this process [13], a core-hole is produced in some level A by either an incident x-ray or electron of sufficient energy. This core-hole is then filled by an electron from a shallower level B with the accompanying release of energy equal to the difference in energy between the shallow level and the deeper core hole. The released energy can take one of two forms: the emission of an x-ray with energy $\approx E_A - E_B$ or the emission of an Auger electron at some kinetic energy from another shallow level C. Auger emission is then the channel which results in the emission of an electron. Energy conservation requires that the emitted electron has a kinetic energy E_k of:

$$E_k \approx E_A - E_B - E_C \qquad [12]$$

where E_A is the initial energy level of the deepest core-hole, E_B is the initial energy level of the electron which fills the core-hole, and E_C is the initial energy level of the emitted electron, as shown in Fig. 1.8. For every emitted electron in this process, there is then a characteristic combination of atomic energy levels which result in a fixed E_k value. This is quite different from the case of photoemission, where E_k varies with the photon energy for emission from a given orbital. This makes AES a particularly useful tool for

determining surface composition, as each element gives rise to a specific set of Auger excitations with particular E_k's for each transition.

Magnetooptic Kerr Effect:

The use of MOKE to study thin film and surface magnetism was first introduced in 1985 by Moog and Bader [14], and in this form it is often referred to as the surface magnetooptic Kerr effect or SMOKE. The MOKE technique is based on the original magneto-optic studies performed in the mid to late 1800's by Faraday & Kerr [15] which examined the effects of magnetized media on the polarization of transmitted and reflected light. MOKE is a particularly powerful technique for the study of magnetism due to its high degree of sensitivity (with measurable signals being obtained from as little as ~1 monolayer (ML) of material), its ability to directly probe sample magnetization and hysteresis, and its compatibility with ultra high vacuum (UHV) systems. A few reviews on the theory and instrumentation of this technique have appeared [16]. In this type of measurement, one typically illuminates the sample to be studied with linear polarized light from an intensity-stabilized He-Ne laser. The polarized light then acquires a Kerr rotation and ellipticity in the light polarization upon reflection from a sample with non-zero magnetization (Fig. 1.2). The effect can be described in terms of the off-diagonal elements of the dielectric tensor ε in the case where the incident light and magnetization direction of the sample are both along the surface normal [16(a),(b)]:

$$\varepsilon = N^2 \begin{vmatrix} 1 & iQ & 0 \\ -iQ & 1 & 0 \\ 0 & 0 & 1 \end{vmatrix} \qquad [13]$$

where N is the refractive index and Q is the magneto-optic constant of the sample. As the light enters the sample, it can be considered to be decomposed into two beams of left and right circularly polarized modes. Each of these modes experiences a different index of refraction n in a medium of magnetization $\vec{M}$ according to the relation:

$$n = N\left[1 \pm (\hat{k}_{h\nu} \cdot \hat{M})Q\right] \qquad [14]$$

where $\hat{k}_{h\nu}$ is the propagation direction of the light and + (-) is for the left (right) helicity. As the light re-emerges from the sample surface into vacuum, the two modes again propagate identically. However, as the two modes traveled with different velocity and attenuated unequally in the medium, the light has obtained a rotation in its polarization axis and an additional ellipticity (i.e., a component out of phase by $\pi/2$ with the initial incident beam). There exist three typical orientations possible for the standard MOKE apparatus: polar, longitudinal, and transverse, as illustrated in Fig. 1.2 (a)-(c). In the polar mode, the sample magnetization is set along the sample normal. For the longitudinal (transverse) mode, the magnetization is induced in the sample plane and the plane of incidence is parallel (perpendicular) to the magnetization direction. The most commonly used modes are the polar and longitudinal and we shall restrict further discussion to these two cases. The "thin-film" limit for a magnetic film on a non-magnetic substrate arises when $2\pi|N|d/\lambda << 1$, where d is the film thickness in Å and λ is the wavelength of the incident light. In this limit, the polar and longitudinal Kerr effects can be expressed in terms of their respective polarization rotations ϕ_{pol} and ϕ_{lon} as:

$$\phi_{pol} = -\left(\frac{4\pi}{\lambda}\right)\left(\frac{N^2}{1-N_{sub}^2}\right)Qd$$

and

$$\phi_{lon} = \left(\frac{4\pi}{\lambda}\right)\left(\frac{N_{sub}}{1-N_{sub}^2}\right)(\pi/2-\theta_{h\nu})Qd \qquad [15]$$

where $\theta_{h\nu}$ is the angle of incidence measured from the surface (cf. Fig. 1.4) and N_{sub} is the index of refraction of the non-magnetic substrate. It is interesting to note that the longitudinal effect is independent of N, yet can be enhanced by moving to directions of incidence that are further from the surface normal (unlike the polar Kerr). An example of the capabilities of MOKE is demonstrated in Fig 1.9(a) (from Ref. 16(a)) in which the hysteresis in the magnetization is measured from nearly a single monolayer of Fe deposited on a Pd(100) crystal. The ability to characterize the magnetic behavior of such thin layers makes MOKE an extremely valuable probe when studying magnetic thin films and surfaces.

Instrumentation Development

As part of this dissertation, several significant instrumentation development projects were involved. The end results of this work are described in more detail in Chapt. 5, but a brief overview is as follows:

A fully functioning MOKE apparatus was constructed and added to a previously constructed UHV surface and thin film analysis system consisting of PS/PD, LEED, and STM experimental elements with interchangeable samples and two-axis sample manipulation capabilities [16(d)]. The specifics of the MOKE developed for this system will be discussed further in the instrumental section of Chapt. 5. This unit was brought into a fully operating condition as part of this thesis.

Also completed as part of this work was the inclusion of a reverse-view LEED/AES system in a stand-alone UHV STM chamber to enable studies of long range order and surface composition. This LEED/AES unit was used in conjunction with the short range/long range probe of STM. This system was used for the work described in Chapt. 2.

Finally, an additional major endeavor was working as part of a team to construct an advanced photoelectron spectrometer/diffractometer for use on beamline 9.3.2 at the Advanced Light Source. This system was used for a significant fraction of the experimental work in this thesis, as described in Chapters 3 and 4.

Application to Magnetic Thin Films and Overlayers:

The ability to determine the magnetic and structural characteristics of magnetic thin films grown epitaxially on non-magnetic metallic substrates is becoming increasingly more important as technology moves more and more toward such systems for applications in magnetic recording. For example, thin films are to be found in the next generation of giant magneto-resistance (GMR) based devices currently in development. Furthermore, understanding the physics of such basic properties as surface and thin-film magnetism and its relation to structure is significant from a purely scientific viewpoint. The ability to bring the above array of complementary techniques to bear on these systems thus offers the experimentalist a unique capability to study such systems under a variety of conditions.

This dissertation can be divided into three main parts, all involved with structure and magnetism at surfaces and interfaces. First, the growth and structure of magnetic thin

films of Gd deposited on a non-magnetic substrate W(110) was studied, exploring the consequences of the resulting morphology on the magnetic characteristics of these films. As part of this work, a new (7x14) superstructure was proposed for the first "wetting" monolayer of Gd on W(110). Second, the structure of the interfaces between such films of both Gd and Fe and the W(110) substrate was determined utilizing high-resolution PD. And finally, spin polarized photoelectron diffraction measurements were made to examine changes in the short range magnetic order as a function of temperature for thick Gd films. The principal system studied in this work are thus Gd and Fe films deposited on W(110) single crystal substrates.

A number of recent studies of the magnetic properties of thin films of Gd grown epitaxially on W(110) single crystal substrates have been performed [17-28]. This system of a 4f ferromagnetic metal deposited on a non-magnetic transition metal has provided much interesting data, including indications of an elevated surface Curie temperature [17,18]. Although particular growth modes and film morphologies for this system have been inferred indirectly from techniques such as Auger electron spectroscopy (AES) and low energy electron diffraction (LEED) [17,29], as well as ac susceptibility [19-23], no direct observations of surface morphology using scanning tunneling microscopy (STM) have been made until a recent preliminary account that has been published as part of the initial work of this thesis [30].

Some important prior observations for Gd/W(110) are as follows. Based upon AES measurements, Weller et al. [17] first proposed that Gd films deposited on W(110) substrates held at between 723K and 773 K grow via the Stranski-Krastanov (SK) mode (3D island growth on top of one or more epitaxial, possibly pseudomorphic, monolayers). In this same work spin polarized LEED and MOKE were used to determine that the surface Curie temperature (T_{cs}) was higher than that of the bulk (T_{cb}) by ~22 K. A later

study by Tang et al. [18] employed spin polarized secondary electron emission spectroscopy and spin polarized photoelectron spectroscopy, and concluded that T_{cs} was ~60K higher than T_{cb}, that there was a ferromagnetic alignment of the in-plane component of the surface and bulk moments, and that the surface magnetization appeared to be canted with respect to the surface, involving both an in-plane and out-of-plane component. Gd is thus one of only two ferromagnetic materials for which T_{cs} has been observed to be greater than T_{cb}, with the other being Tb(0001), as studied by Rau et al. using electron capture by deuterons [31]. Kolaczkiewicz et al. [29] further investigated the growth modes and surface structures of Gd/W(110) utilizing LEED and AES. From breaks in AES intensities as a function of coverage Θ, they inferred that, for lower coverages $\Theta < 3$ ML and when deposited at room temperature, Gd grows in the Frank-Van der Merwe (FM) mode (smooth, layer-by-layer growth) to form Gd(0001). From this same data, it was suggested that the first Gd monolayer is a hexagonal (0001) plane compressed by 4.4% from the bulk spacing, with the Gd $[11\bar{2}0]$ direction (which points along the in-plane nearest-neighbor direction) being parallel to the W [001] direction. Farle et al. also performed a detailed study of the effects of annealing temperature and coverage on the ac magnetic susceptibility χ_{ac} [19,20] and MOKE [21] of this system. They found that, for films deposited at 300 K in the thickness range of 5-11 ML, annealing at 530 K after deposition sharpened and intensified the peak in χ_{ac} at T_c considerably. However, as the annealing temperature was increased to temperatures in the range of 550 K to 710 K, the peak broadened, moved to a higher T_c, and decreased markedly in intensity. The explanation put forth for these results was that the smooth films achieved after 530 K annealing broke up into large, 3D islands with increased annealing temperature. One of the aspects of this dissertation will be to directly observe for the first time the growth and morphology of Gd films on W(110) with STM for a variety of different annealing conditions and coverages in an attempt to more fully explore the connection of morphology and magnetism.

The exact structure of the interfaces between magnetic metals and a non-magnetic substrate can also have strong implications on the magnetism for a given system. A variety of techniques has been used in an attempt to identify the local structures at solid-solid interfaces. X-ray diffraction [32-34], electron microscopy [34], and low energy electron diffraction (LEED) [35] have all achieved some success in this area. Yet all of these measurements lack the ability to directly probe the structure of atoms that are specifically at the interface. Electron microscopy has the ability to image the interface, but only as columns of atoms. Photoelectron diffraction (PD) [3,36,37], on the other hand, can be specifically sensitive to interface atoms, provided that they exhibit a resolvable binding energy difference (chemical shift) from the other atoms present. Higher energy x-ray PD (XPD) from chemically shifted core-levels has been used to study the local structure at semiconductor/insulator [38], semiconductor/metal [39], and semiconductor/semiconductor [40,41] interfaces. The chemical shifts in these cases were quite large (>1 eV), enabling the use of standard laboratory X-ray sources and photoelectron spectrometers of modest resolution. However, when attempting to study the important class of systems represented by metal-metal interfaces, one typically encounters core-level shifts nearly an order of magnitude smaller (~100 meV), making standard XPD measurements on these systems prohibitive. Thus, studying a narrow core line (as e.g., 3d in the 4d transition metals or 4f in the 5d transition metals) and using high-resolution synchrotron radiation for excitation is necessary for being able to observe such effects. For example, for the clean W(110) surface, two peaks in the W $4f_{7/2}$ spectrum are observed, one arising from bulk W atoms and a second shifted to 320 meV lower binding energy (E_b) that is due to the under-coordinated W atoms at the surface [42] (we will term this a -320 meV shift). But if a metal overlayer is now placed on this surface, the former surface W atoms are now interface atoms, and they still can exhibit a shift relative to the bulk. Shinn et al. [43] have found such small interface core-level shifts (ICLS's) in

the W $4f_{7/2}$ photoelectron spectra from W(110) surfaces covered with one monolayer of Ni, Pt, or Fe in a pseudomorphic (1x1) structure (i.e., a structure in which the lateral registry of the overlayer follows perfectly the registry of the substrate surface atoms). Specifically, the ICLS's for Ni and Pt overlayers were measured as being -200 meV and +70 meV, respectively, again relative to the bulk binding energy. In the case of (1x1) Fe, the situation is thought to be even more complex, with the W $4f_{7/2}$ spectrum consisting of three components: one from the interfacial W layer shifted by -225 meV, another from what is thought to be the second W layer shifted by -80 meV, and the bulk W peak (which is found to remain at the same distance from the Fermi level as for the clean surface) [43]. We have in this dissertation utilized such ICLS's to perform for the first time interface-specific PD on two metal-metal systems, and we have used these data to determine the detailed atomic structure of one of them. Specifically, we have examined both the pseudomorphic (1x1) Fe monolayer on W(110) [43] and the non-pseudomorphic (7x14) Gd monolayer on W(110) [30] in order to determine the structure present at the interface.

As previously mentioned, Gd has an interesting characteristic - it is thought to display an elevated Curie temperature for the surface as compared to the bulk. To more fully investigate this aspect for Gd, we have performed SPPD experiments [44] on thick Gd(0001) films grown on W(110). The SPPD technique has been used in prior studies to examine the temperature dependence of the short range magnetic order in the ionic anti-ferromagnets MnO and $KMnF_3$ [44]. SPPD exploits the spin polarized nature of core photoemission multiplets. For a system which exhibits a magnetic transition, the observed diffraction from spin polarized peaks should vary between the disordered and ordered states of the system due to the presence (or absence) of the exchange interaction in the scattering potentials for a photoelectron that is either spin up or spin down with respect to a given scatterer. This will be discussed in greater detail in Chapt. 4. For this work, we

apply the SPPD technique for the first time to a ferromagnetic system in order to probe the ferromagnetic-to-paramagnetic transition for both the bulk and surface of Gd(0001).

References:

[1] A. Einstein, Ann. Physik 17, 132 (1905).

[2] C. S. Fadley, "Basic Concepts of X-ray Photoelectron Spectroscopy," appearing in Electron Spectroscopy, Theory, Techniques and Applications Vol. 2, eds. C. R. Brundle and A. D. Baker, (Pergamon Press, 1978).

[3] (a) C. S. Fadley, "The Study of Structures by Photoelectron Diffraction and Auger Electron Diffraction," appearing in Synchrotron Radiation Research: Advances in Surface and Interface Science, Vol. 1, ed. by R. Z. Bachrach, (Plenum Press, NY 1992), p. 421 and (b) Z. Hussain, S. Kono, L. Petersson, C. S. Fadley, and L. F. Wagner, Phys. Rev. B 23, 724 (1981).

[4] M. P. Seah and W. A. Dench, Surf. & Interf. Anal. 1, 2 (1979).

[5] a. C. H. Li and S. Y. Tong, Phys. Rev. Lett. 42, 901 (1979).
b. A. P. Kaduwela, D. J. Friedman, and C. S. Fadley, J. Elec. Spec. & Rel. Phen. 51, 689 (1990).

[6] A. P. Kaduwela, D. J. Friedman, and C. S. Fadley, J. Elec. Spec. & Rel. Phen. 57, 223 (1991).

[7] J. J. Rehr and R. C. Albers, Phys. Rev. B 41, 8139 (1990).

[8] G. Binnig, H. Rohrer, C. Gerber, and E. Weibel, Phys. Rev. Lett. 49, 57 (1982).

[9] M. B. Salmeron, "Scanning Tunneling Microscopy," appearing in Emerging Techniques for Catalyst Characterization, ed. by J. Horsley, (Catalytica, Inc., Mountain View, CA 1989).

[10] P. K. Hansma and J. Tersoff, J. Appl. Phys. 61, R1 (1987).

[11] C. J. Davidson and L. H. Germer, Phys. Rev. 30, 705 (1927).

[12] a) J. B. Pendry, Low Energy Electron Diffraction, (Academic Press, NY 1974)
b) H. Weinbergand and C. M. Chen, Low Energy Electron Diffraction, (Springer-Verlag, Heidelberg 1986).

[13] D. P. Woodruff and T. A. Delchar, Modern Techniques of Surface Science, (Cambridge Univ. Press, Cambridge 1986), p. 126.

[14] a) E. R. Moog and S. D. Bader, Superlatt. Microstruc. 1, 543 (1985).
b) S. D. Bader, E. R. Moog, and P. Grunberg, J. Mag. & Mag. Mat. 53, L295 (1986).
c) S. D. Bader and E. R. Moog, J. Appl. Phys. 61, 3729 (1987).

[15] a) M. Faraday, Trans. Roy. Soc. (London) 5, 592 (1846).
b) J. Kerr, Phil. Mag. 3, 339 (1877) & Phil. Mag. 5, 161 (1878).

[16] a) S. D. Bader, J. Mag. & Mag. Mat. 100, 440 (1991).
b) J. Zak, E. R. Moog, C. Lin, and S. Bader, Phys. Rev. B 43, 6423 (1991).
c) J. P. Qian and G. C. Wang, J. Vac. Sci. and Tech. A 8, 4117 (1990).
d) Y. J. Kim, doctoral dissertation, Univ. of Hawaii (1995)

[17] D. Weller, S. F. Alvarado, W. Gudat, K. Schroder, and M. Campagna, Phys. Rev. Lett. 54, 1555 (1985).

[18] H. Tang, D. Weller, T. G. Walker, J. Scott, C. Chappert, H. Hopster, A. W. Pang, D. S. Dessau, and D. P. Pappas, Phys. Rev. Lett. 71, 444 (1993).

[19] M. Farle, W. A. Lewis, K. Baberschke, Appl. Phys. Lett. 62, 2728 (1993).

[20] M. Farle, K. Baberschke, and U. Stetter, Phys. Rev. B 47, 11571 (1993).

[21] M. Farle, W. A. Lewis, J. Appl. Phys. 75, 5604 (1994).

[22] U. Stetter, M. Farle, and K. Baberschke, Phys. Rev. B 45, 503 (1992).

[23] A. Aspelmeier, F. Gerhardter, and K. Baberschke, J. Mag. Mag. Mat. 132 N1-3, 22 (1994).

[24] A. Berger, A. W. Pang, H. Hopster, J. Mag. Mag. Mat. 137, L1-L5 (1994).

[25] D. Li, C. W. Hutchings, P. A. Dowben, R. Wu, C. Hwang, M. Onellion, A. B. Andrews, J. L. Erskine, J. Appl. Phys. 70, 6565 (1991).

[26] D. Li, J. Zhang, P. A. Dowben, M. Onellion, Phys. Rev. B 45, 7272 (1992).

[27] A. W. Pang, A. Berger, H. Hopster, Phys. Rev. B 50, 6457 (1994).

[28] B. Kim, A. B. Andrews, J. L. Erskine, K. Kim, B. N. Harmon, Phys. Rev. Lett. 68, 1931 (1992).

[29] J. Kolaczkiewicz and E. Bauer, Surf. Sci. 175, 487 (1986).

[30] E. D. Tober, R. X. Ynzunza, C. Westphal, and C. S. Fadley, Phys. Rev. B 53, 5444 (1996).

[31] C. Rau, C. Jin, M. Robert, Phys. Lett. A 138, 334 (1989).

[32] R. Feidenhans'l, Surf. Sci. Rep. 10, 105 (1989).

[33] M. Takahasi, S. Nakatani, T. Takahashi, X. Zhang, M. Ando, S. Fukatsu, and Y. Shiraki, Jpn. J. Appl. Phys. 34, 2278 (1995)

[34] A. Bourret, P. Fuoss, and S. Tatarenko, Phys. Rev. Lett. 70, 311 (1993)

[35] J. B. Pendry, Surf. Sci. Rep. 19, 87 (1993)

[36] C. S. Fadley, S. Thevuthasan, A. P. Kaduwela, C. Westphal, Y. J. Kim, R. Ynzunza, P. Len, E. D. Tober, F. Zhang, Z. Wang, S. Ruebush, A. Budge, and M. A. Van Hove, J. Elec. Spec. & Relat. Phen. 68, 19 (1994).

[37]. C.S. Fadley, M.A. Van Hove, Z. Hussain, and A.P. Kaduwela, J. Electron Spectrosc. 75, 273 (1995).

[38] J. Denlinger, E. Rotenberg, U. Hessinger, M. Leskovar, and M. Olmstead, Appl. Phys. Lett. 62, 2057 (1993).

[39] S. A. Chambers and V. A. Loebs, Appl. Phys. Lett. 60, 38 (1992).

[40] E. Maillard-Schaller, O. M. Kuettel, and L. Schlapbach, Phys. Stat. Sol. A 153, 415 (1996).

[41] O. M. Kuettel, E. Schaller, J. Osterwalder, and L. Schlapbach, Diam. & Rel. Mat. 4, 612 (1995).

[42] T. M. Duc, Phys. Rev. Lett. 43, 789 (1979).

[43] N. D. Shinn, B. Kim, A. B. Andrews, J. L. Erskine, K. J. Kim, and T.-H. Kang, Mat. Res. Soc. Symp. Proc. 307, 167 (1993).

[44] a) B. Sinkovic and C. S. Fadley, Phys. Rev. B 31, 4665 (1985).

b) B. Sinkovic, B. Hermsmeier, and C. S. Fadley, Phys. Rev. Lett. 55, 1227 (1985).

c) B. Hermsmeier, J. Osterwalder, D. J. Friedman, and C. S. Fadley, Phys. Rev. Lett. 62, 478 (1989).

d) B. Hermsmeier, J. Osterwalder, D. J. Friedman, T. Tran, and C. S. Fadley, Phys. Rev. B 42, 11895 (1990).

e) B. Sinkovic, D. J. Friedman, and C. S. Fadley, J Mag. and Mag. Mat. 92, 301 (1991).

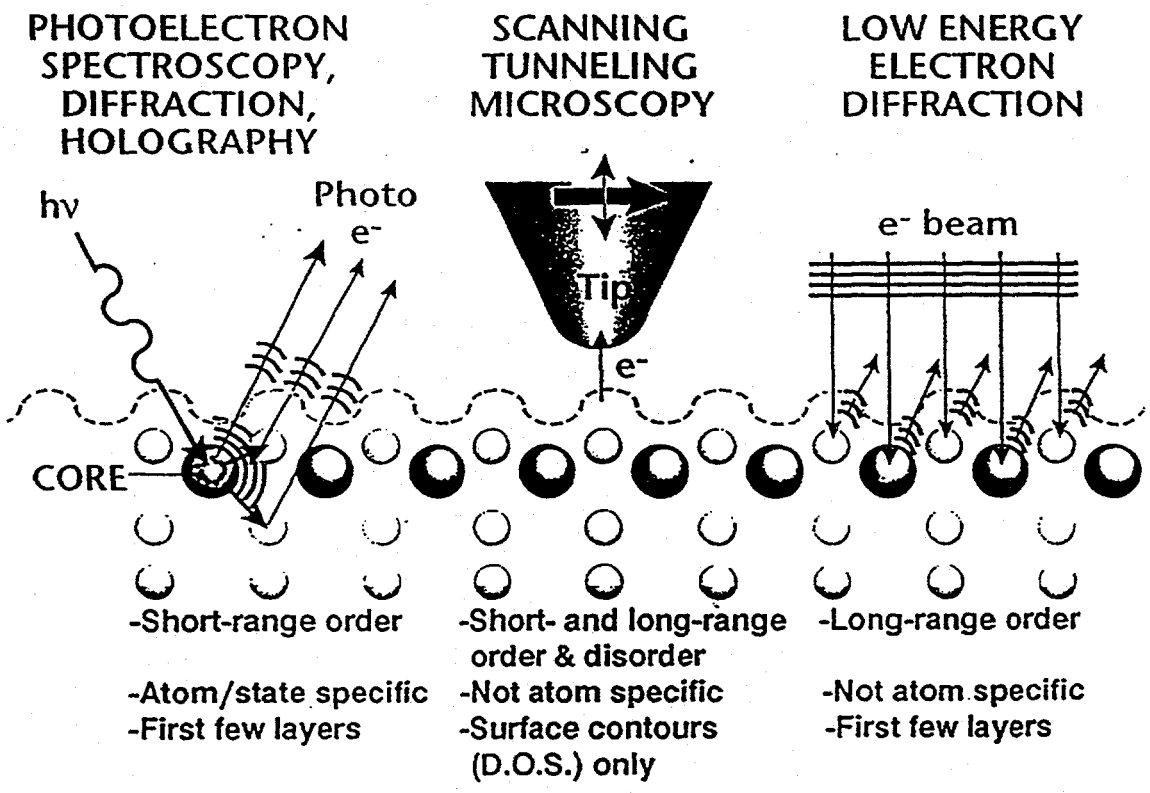

Fig. 1.1 A schematic indication of the measurements involved in photoelectron spectroscopy and diffraction (PS/PD), scanning tunneling microscopy (STM), and low energy electron diffraction (LEED), including the complementary information provided by each technique.

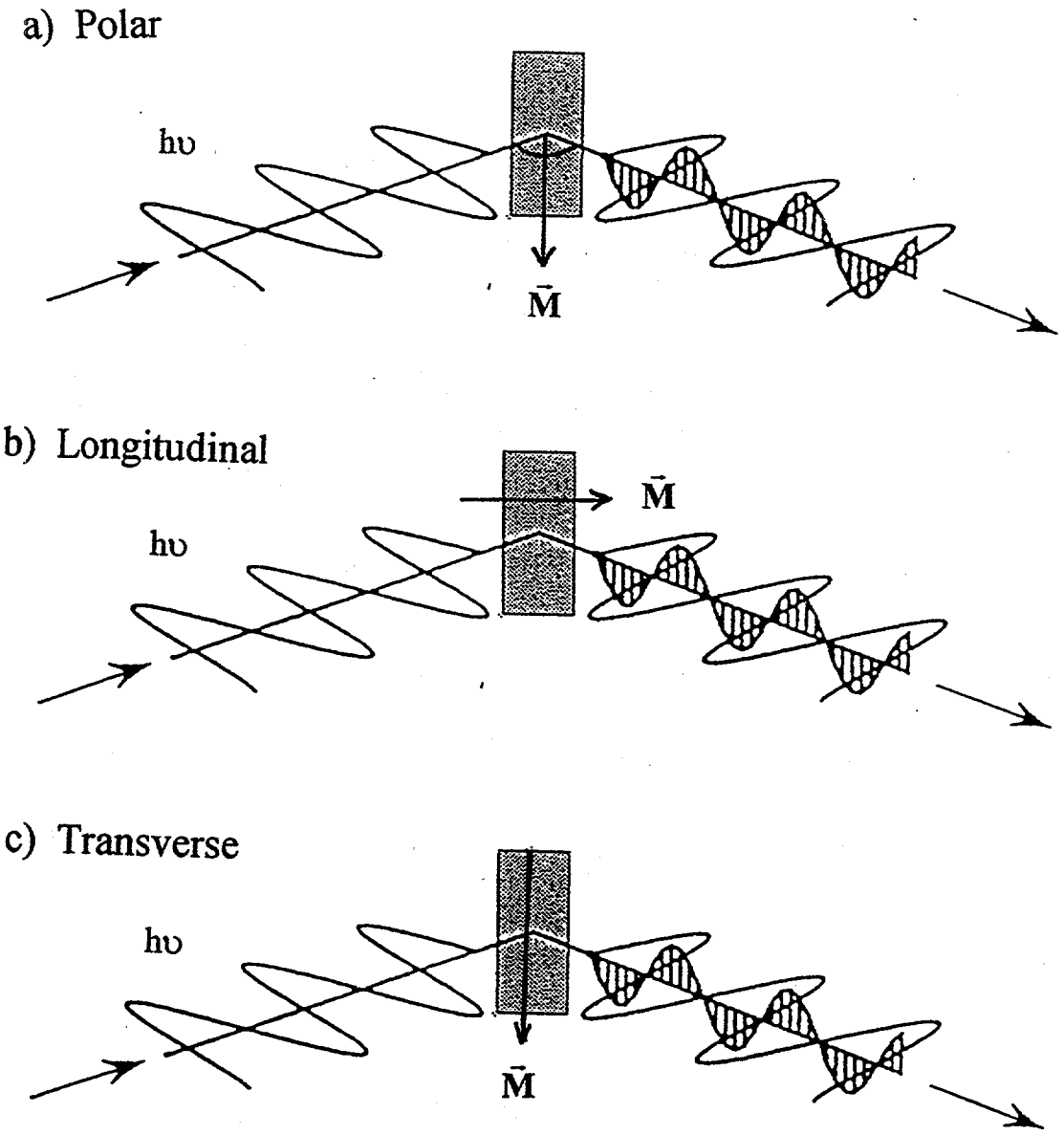

Fig. 1.2 A schematic illustration of the magneto-optic Kerr effect (MOKE) from Ref. 15(a) in which polarized light gains a rotation upon reflection from a magnetized medium in the (a) polar, (b) longitudinal, and (c) transverse modes.

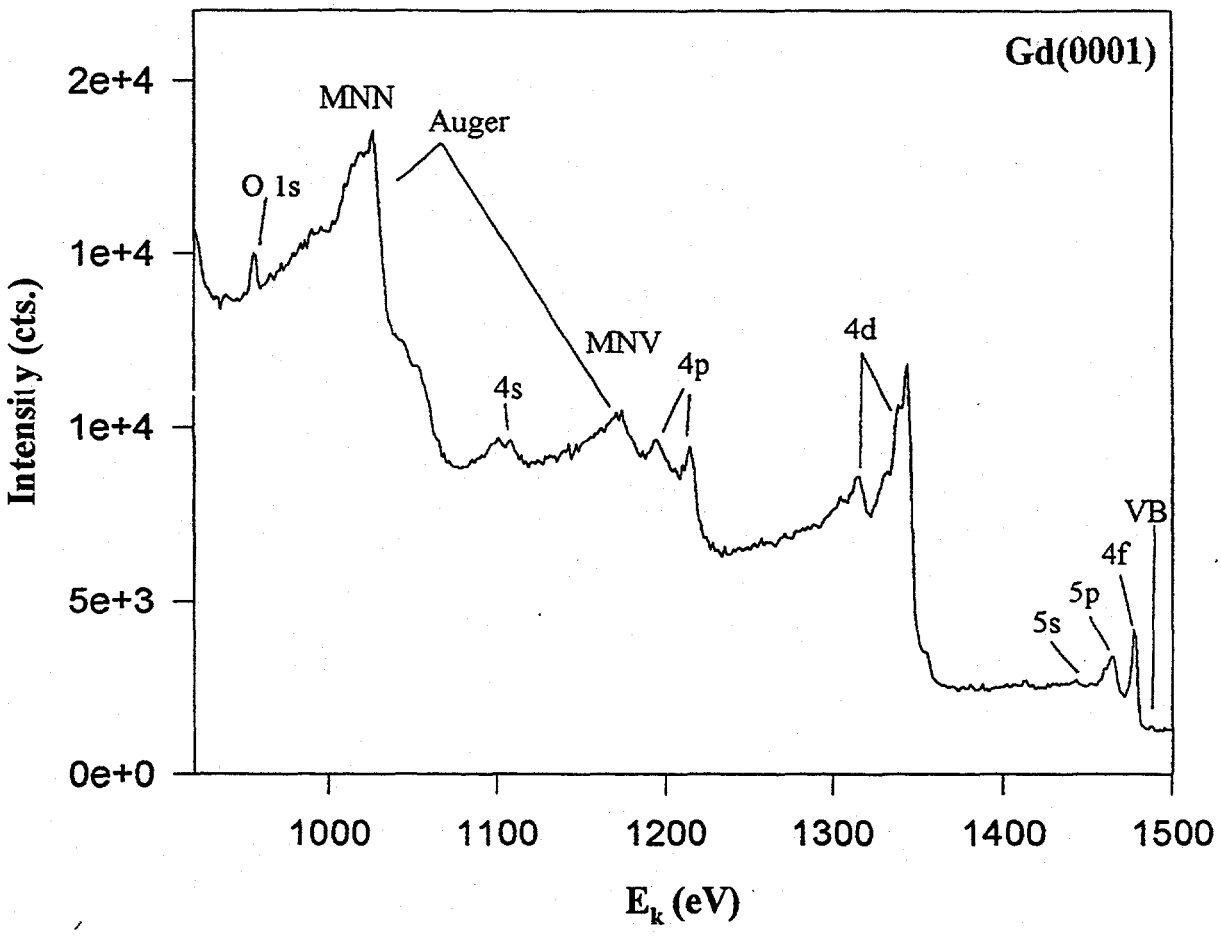

Fig. 1.3 A sample photoelectron spectrum taken from a clean Gd(0001) surface with Al Kα excitation. Peaks from various core-levels are labeled accordingly.

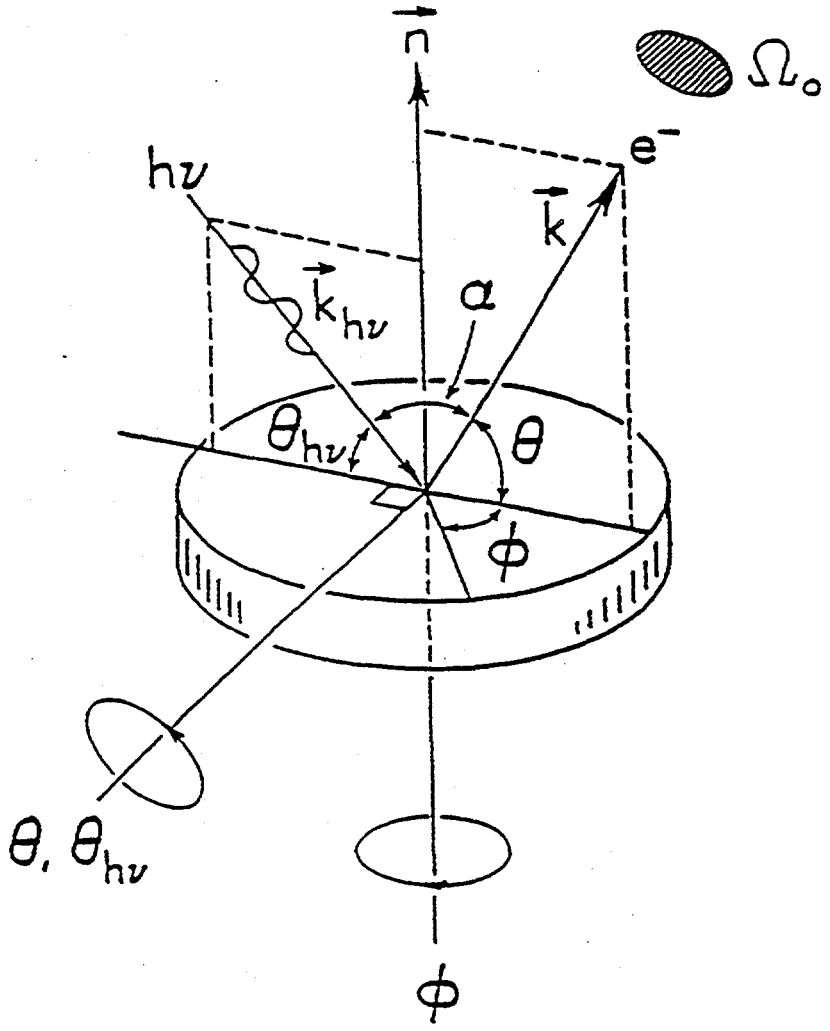

Fig. 1.4 Illustration of the basic experimental geometry used in PD. The polar angle θ of electron emission is measured from the surface, α is the angle between the incident photons and the outgoing wave vector, and ϕ is the azimuthal rotation angle about the surface normal measured with respect to some fixed crystallographic direction. In our later work on Gd on W(110), ϕ will be measured with respect to the [001] axis lying in the W(110) surface and the $[10\bar{1}0]$ axis lying in the Gd(0001) surface.

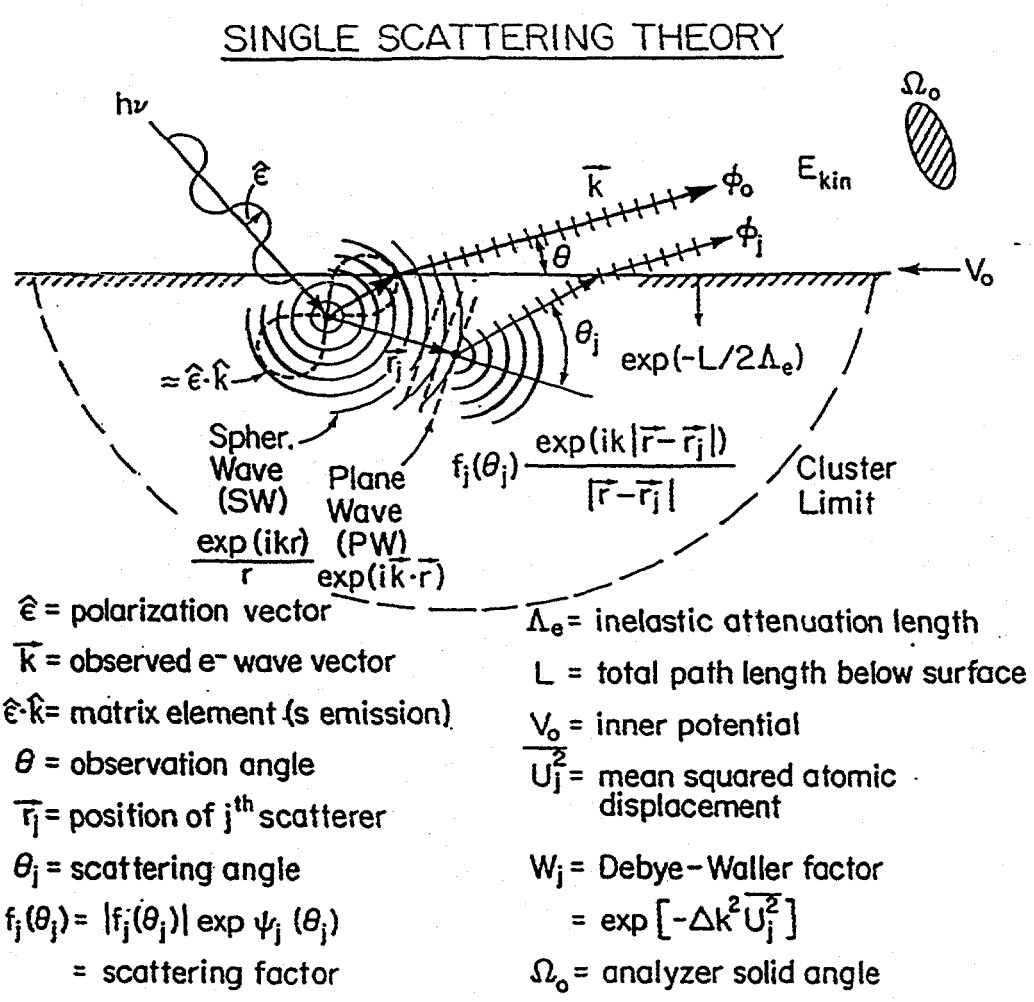

Fig. 1.5 A schematic representation of the PD process with important physical variables indicated. Only the case of single scattering is shown for simplicity.

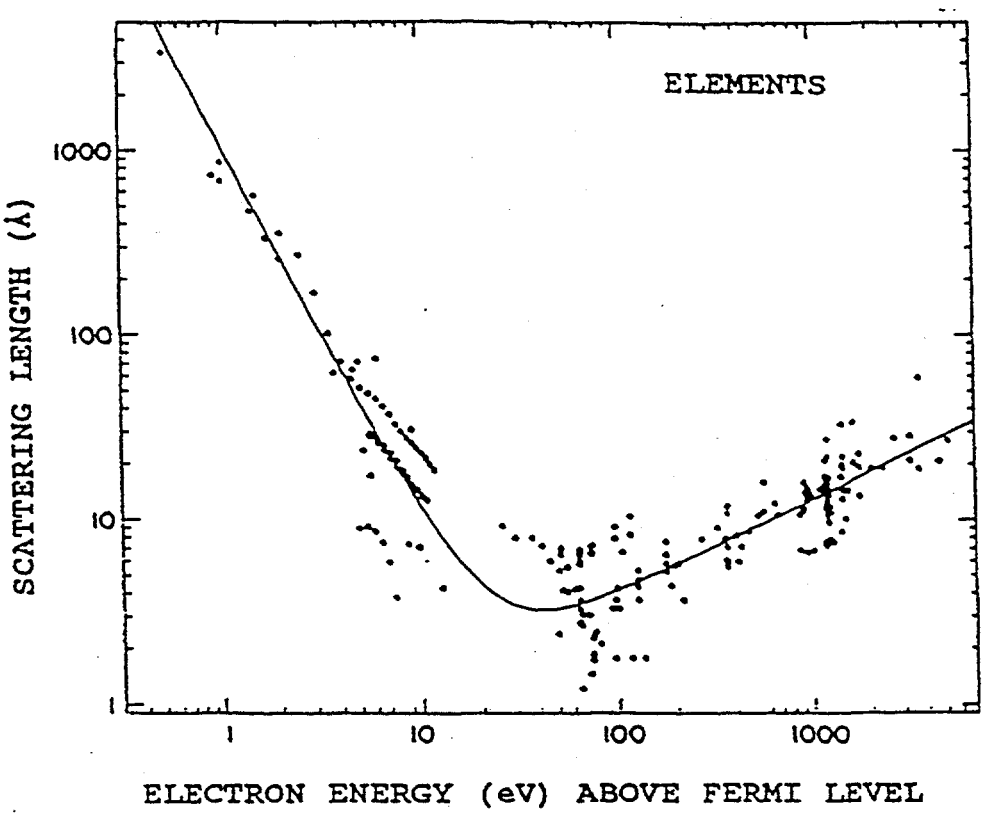

Fig. 1.6 A compilation of inelastic attenuation lengths Λ_e for various solid elements versus electron kinetic energy [from Ref. 4]. The solid line is a so-called "universal" curve describing this data in an average sense.

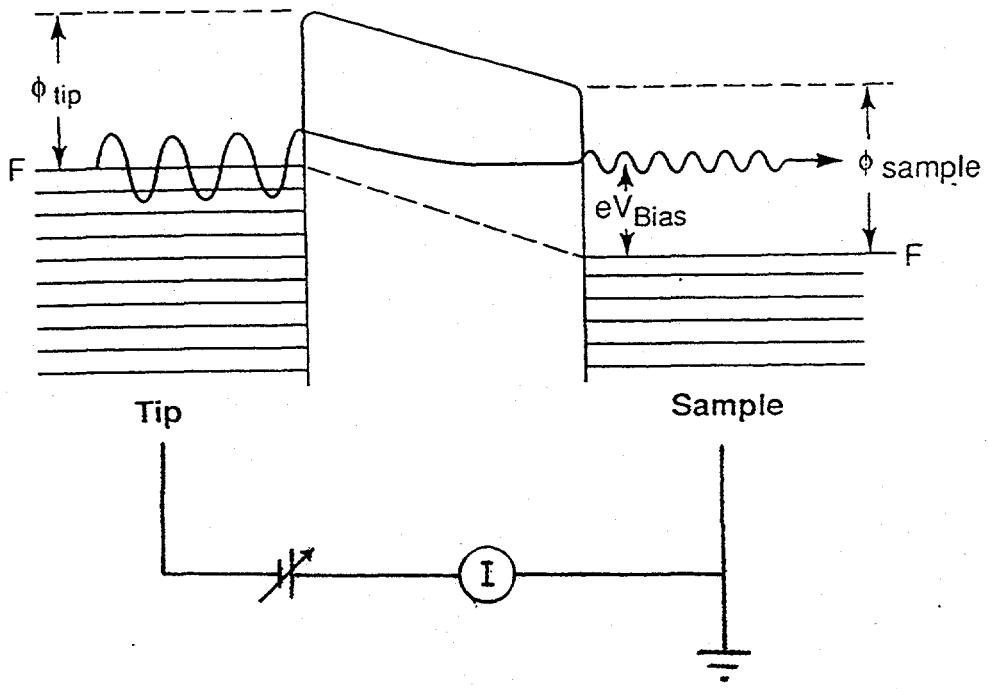

Fig. 1.7 A diagram of the energy-distance relationship in the tunneling process for STM [from Ref. 9]. The amplitude of the electron wavefunction from the tip decays in vacuum and is then coupled in to the energy levels above the sample Fermi level.

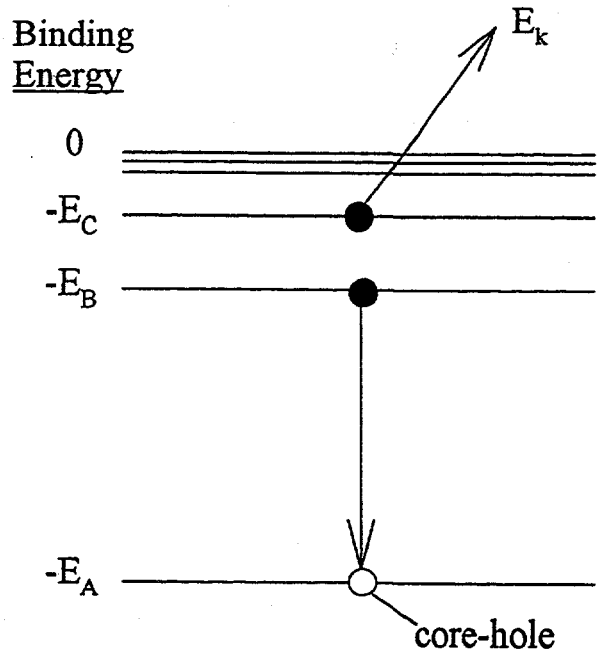

Fig. 1.8 An energy diagram for the Auger process. An electron from level B filling a core-hole in level A stimulates the emission of a electron from a more shallow level C. The levels are labeled with their one-electron binding energies.

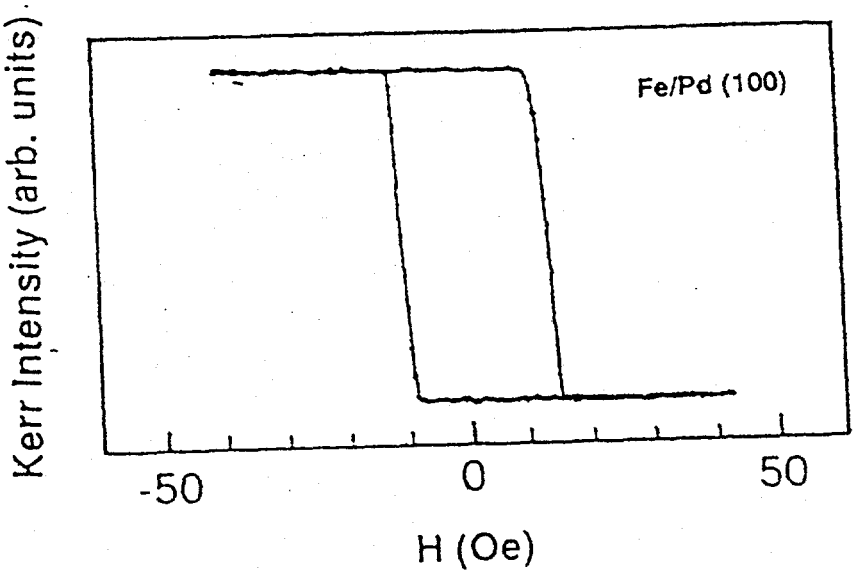

Fig. 1.9 A polar Kerr hysteresis loop taken from 1.2 ML of Fe on a Pd(100) substrate , demonstrating the high level of sensitivity obtainable with this technique [from Ref. 16(a)]. Here the rotation angle ϕ_{pol} is plotted vs. applied field.

Chapter 2.

A Scanning Tunneling Microscopy and Low Energy Electron Diffraction Study of Gadolinium Thin Film Growth on Tungsten (110)

2.I. Introduction

Over the last ten years, a number of studies of the magnetic properties of thin films of Gd grown epitaxially on W(110) single-crystal substrates have been performed [1-12]. This system of a 4f ferromagnetic metal deposited on a non-magnetic transition metal has provided much interesting data, including indications of an elevated surface Curie temperature [1,2]. Although particular growth modes and film morphologies for this system have been inferred indirectly from techniques such as Auger electron spectroscopy (AES) and low energy electron diffraction (LEED) [1,13], as well as ac susceptibility [3-7], no direct observations of surface morphology using scanning tunneling microscopy (STM) have been made until a recent preliminary account that we have published [14]. In the present study, the effects of coverage and annealing temperature on the morphology of such Gd films will be examined in detail for the first time with STM, with LEED providing complementary information on the type of long-range atomic order present. These results yield a more quantitative understanding of the structure-magnetism relationships for this prototypical epitaxial ferromagnet, and also reveal a new superstructure for the first monolayer. Furthermore, an analysis of the room temperature growth of the Gd films on W(110) reveals that the growing film exhibits scaling behavior in accordance with a self-affine surface.

Some important prior observations for Gd/W(110) are as follows. Weller et al. [1] first proposed based upon AES measurements that Gd films deposited on W(110) substrates held at between 723K and 773 K grow via the Stranski-Krastanov (SK) mode

(3D island growth on top of one or more epitaxial, possibly pseudomorphic, monolayers). This same work used spin polarized LEED and the magneto-optic Kerr effect (MOKE) to determine that the surface Curie temperature (T_{cs}) was higher than that of the bulk (T_{cb}) by 22 K. A later study by Tang et al. [2] employed spin polarized secondary electron emission spectroscopy and spin polarized photoelectron spectroscopy, and concluded that T_{cs} was 60K higher than T_{cb}, that there was a ferromagnetic alignment of the in-plane component of the surface and bulk moments, and that the surface magnetization appeared to be canted or to consist of mixed domains of in-plane and out-of-plane magnetization. Gd is thus one of only two ferromagnetic materials for which T_{cs} has been observed to be greater than T_{cb}, with the other being Tb(0001), as studied by Rau et al. using electron capture by deuterons [15]. Kolaczkiewicz et al. [13] further investigated the growth modes and surface structures of Gd/W(110) utilizing LEED and AES. From breaks in the slopes of AES intensities as a function of coverage Θ, they inferred that, for lower coverages ($\theta < 3$ monolayers (ML)) and when deposited at room temperature, Gd grows in the Frank-Van der Merwe (FM) mode (smooth, layer-by-layer growth) to form Gd(0001). From this same data, it was suggested that the first Gd monolayer is a hexagonal (0001) plane compressed by 4.4% from the bulk spacing, with the Gd $[11\bar{2}0]$ direction (which points along the in-plane nearest-neighbor direction) parallel to the W [001] direction. Farle et al. also performed a detailed study of the effects of annealing temperature and coverage on the ac magnetic susceptibility χ_{ac} [3,4] and MOKE [5] of this system. They found that, for films deposited at 300 K in the thickness range of 5-11 ML, annealing at 530 K after deposition sharpened and intensified the peak in χ_{ac} at T_c considerably. However, as the annealing temperature was increased to temperatures in the range of 550 K to 710 K, the peak broadened, moved to a higher T_c, and decreased markedly in intensity. The explanation put forth for these results was that the smooth films achieved after 530 K annealing broke up into large, 3D islands with increased annealing temperature.

We have here thus studied the surface morphology of Gd/W(110) with STM and LEED for a range of coverages from 1 to 20 ML (with special attention to 11 ML), examining the films as deposited at ambient temperature, and with final annealing at 530 K and 710 K, and attempting to relate the morphology to the observations made in prior studies, as well as to general models for epitaxial growth.

2.II. Experimental

All measurements were carried out in an ultrahigh vacuum system combining LEED, AES, and STM that is described elsewhere [16 and Chapt. 5]. The Gd films were grown at a rate of 0.11-0.15 ML/min. (as determined by both a quartz crystal thickness monitor and quantitative AES measurements) at pressures of 4-5 x 10^{-11} Torr. Subsequent measurements with LEED, AES, and STM were performed at pressures of 2-3 x 10^{-11} Torr. The substrate was a tungsten single crystal, mechanically and electrochemically polished to within 0.5° of (110) as measured by x-ray diffraction. The crystal was cleaned by flashing to 2200 K, prolonged annealing at 1500-1550 K in O_2 at 5.0 x 10^{-7} Torr, and finally flashing off the resulting oxide layer at 1825 K for 50 seconds. The resulting substrate and deposited Gd films were determined to be clean by AES (<0.05 ML of combined C and O contamination) and they accumulated < 0.10 ML in combined C and O after the approximately eight hours required to finish each series of LEED and STM measurements. STM images of the clean W surface showed flat terraces between monatomic steps with average widths of approximately 36.0 nm. However, portions of the crystal surface were found to have areas with much smaller (~ 7 nm) to much larger (~200 nm) terrace widths as well. The annealing temperatures of the Gd films were measured with an infrared pyrometer calibrated with a Pt-Rh thermocouple for T < 1273

K and a W-Re thermocouple for higher temperatures. All of the AES, LEED, and STM measurements were performed at room temperature.

2.III. Gd Film Growth on W(110): Post-Deposition Annealing & Coverage

In the LEED/AES study of Kolakzkiewicz et al. [13], it was observed that when depositing Gd on W(110) at room temperature, sharp breaks occurred in the slope of the Gd 138 eV Auger signal as the coverage increased. This was taken as an indication that, as deposited, the Gd grew in the FM layer by layer mode on top of W(110). Using STM, we examined the room temperature growth of Gd on W(110) as a function of coverage θ. Fig. 2.1 contains STM images obtained from Gd thin films deposited on W(110) at room temperature in the coverage range of 0.3 to 6.0 ML. At the low coverage of 0.3 ML (Fig. 2.1(a)), the Gd appears to form small, 1 ML high elliptical islands of roughly the same size (approximately 1.73 x 2.54 nm) with the long axis aligned along the W[$\bar{1}$10] direction. The island height as seen by the STM tip is 0.29 nm. For θ = 0.6 ML (Fig. 2.1(b)), the islands have been replaced with long vertical stripes, again with the long axis aligned along the W[$\bar{1}$10] direction. These stripes tend to have a separation of approximately 1.03 nm and exhibit a 0.07 nm corrugation in height perpendicular to their common axes. Figure 2.2 contains a close-up image from Fig. 2.1(b) with a corresponding tip height scan showing the stripe spacing and height corrugation along W[001]. In the LEED study of Kolaczkiewicz et al. [13], it was seen that for films with θ < 1 ML annealed to 1200 K, a series of reconstructions occurred that could be explained by different bonding geometries of the Gd on top of the W(110) surface. Specifically, in the coverage range of 0.47 - 0.60 ML, a 6x2 reconstruction was formed with respect to the W(110), a representation of which is shown in Fig. 2.3. For this proposed structure, the Gd atoms would rest in parallel rows along W[$\bar{1}$10] with alternating adsorption sites between rows, one a bridge site and the other an atop site. Assuming a hard sphere approximation and using the

atomic radii for W and Gd, one arrives at a height difference of 0.04 nm between the two adsorption sites and a separation between rows of the same type of site equal to 0.95 nm. This is close to the separation between rows and the tip height corrugation measured here by STM with a room temperature deposition. The ideal coverage of the 6x2 overlayer would be 0.55 ML, which is also very close to our average coverage of 0.6 ML. The LEED pattern we observed for this un-annealed film was, however, fuzzy and indistinct due to the lack of long range order. This being the case, a positive 6x2 identification for this surface is difficult, but our STM results suggest that it is indeed beginning to form in small domains. For all the films deposited with $\theta < 1$ ML, no second layer growth was observed until the first monolayer of Gd was completely filled, suggesting the need for completely "wetting" the W(110) surface before additional layers start to form. When depositing films with $\theta > 1$ ML (Figs. 2.1(c) & (d)) it can be seen that the Gd does not grow in a layer-by-layer mode. Instead, it grows in a rough, multi-tiered structure in which more than a single layer of Gd is left incomplete at a given time. This contradicts the assertions made in the AES study of Ref. [13] in which it was proposed that Gd grows in the FM mode at room temperature. Perhaps this difference has to do with a different step density and/or different surfactant impurity levels between the two studies, but for the conditions of our experiments, the STM results are unambiguous.

When analyzing the growth mechanism of a given system, there are two characteristic values that can be used as characterize film growth and topology: the surface roughness δ and the lateral surface correlation length L_C [17-20]. The surface roughness is equivalent to the rms standard deviation of the surface height from its average: $\delta \equiv [\langle z^2(\mathbf{r})\rangle - \langle z(\mathbf{r})\rangle^2]^{1/2}$, where $z(\mathbf{r})$ is the surface height at position $\mathbf{r} = (x,y)$ along the surface and the critical surface correlation length L_C denotes the measurement length beyond which variations in the surface roughness saturate with increased scale. Scaling theory then allows us to use these characteristic values to better understand the type of growth

occurring. For one special case of a self-affine surface, $kz(k'\mathbf{r}) = z(\mathbf{r})$ for some factors k and k' and over some limited length scale. Then the local standard deviation of the surface height ξ over a given length scale L and for a given coverage θ can be described as [19,20]:

$$\xi(L,\theta) = L^{\alpha} f(\theta / L^{\alpha/\beta}) \qquad [1]$$

Here, the deposition rate can be assumed to be constant such that, in the absence of evaporation, θ is proportional to time, and f(x) can be shown to behave as x^{β} for $x << 1$ and as a constant for $x >> 1$. The parameters α and β are the spatial and dynamic scaling exponents, respectively, for the growing surface. At a given coverage θ, the interface roughness $\xi(L,\theta)$ is found to saturate above a critical length L_c beyond which $\xi(L,\theta) = \delta(\theta)$. Below L_c, $\xi(L,\theta)$ should be governed by the exponent α and follow $\xi(L,\theta) \propto L^{\alpha}$. To test the applicability of this kind of scaling to Gd growth on W, Fig. 2.4 displays the power law dependence of $\xi(L,\theta)$ derived from our STM images as a function of L for three Gd films grown at room temperature with $\theta > 1$ ML. There is good power law behavior for all three films, with the lowest two coverages of 2.2 ML and 6.0 ML showing essentially the same value for α of 0.593-0.595, and the highest coverage of 11.0 ML deviating somewhat from this at 0.445. The average value of α measured for these three films is 0.54 . To determine the dynamic scaling exponent β, one must now examine the dependence of the surface roughness δ as a function of coverage. Below the saturation coverage θ_c where $\theta/L^{\alpha/\beta} << 1$, δ should follow the power law: $\delta(\theta) \propto \theta^{\beta}$. However, in defining the coverage here, the first layer of Gd should not be included in the analysis for coverages greater than 1 ML. This is because a fundamentally new growth mechanism is taking over after the establishment of the first monolayer (whose properties we will consider in more detail below). So, for our films with $\theta > 1$ ML, the above function must be adjusted as follows:

$$\delta(\theta) \propto (\theta - 1\ (ML))^{\beta} \qquad [2]$$

Fig. 2.5(a) displays the height distributions of various Gd films grown at room temperature, and Fig. 2.5(b) shows the coverage dependence of the surface roughness δ derived from this data. The curves in Fig. 2.5(a) immediately show that δ increases from 0.6 ML to 6.0 ML, and then seems to saturate. We now fit Eq. 2 to the data in Fig 2.5(b) for $1 \leq \theta \leq 6$ ML, not considering coverages beyond 6 ML for which δ saturates, and obtain the value of 0.475 for the dynamic scaling parameter β. For pure stochastic roughening, one would expect $\beta = 0.5$ [18,19], which is in excellent agreement with our measured value. However, pure stochastic roughening would require also that $\alpha = 0$ [19]. The α determined here of 0.54 for Gd is much closer to that predicted by Lai and Das Sarma of 0.66 [19,21] for films undergoing surface diffusion coupled with step-flow and/or island nucleation during growth. Some evidence of step flow growth can in fact be seen in the STM image of the 2.2 ML film displayed in Fig. 2.1(c). So, it is quite plausible that our value of α reflects the involvement of step induced growth processes in these Gd films.

With annealing, Gd films deposited at room temperature are observed to change their morphology drastically. Fig. 2.6 displays the effect of a 10 min. post-deposition anneal at 530 K for Gd films in the coverage range of 1.9-6.8 ML. These results thus span roughly the same coverage range as those of the room-temperature morphologies shown in Figs. 2.1(c) and (d). At $\theta = 1.9$ ML (Fig. 2.6(a)), one can observe small islands of roughly 4 atomic layers in height with an average area and radius of 301 nm^2 and 9.79 nm, respectively. Roughly 28% of the surface exists in islands which is equivalent to 0.93 ML of Gd in total. Therefore, we conclude that the islands must be resting on a base "wetting" monolayer of Gd on top of the W(110) substrate, resulting in an SK growth

mode. This same conclusion is reached for every coverage deposited up until 6.8 ML, at which time the Gd islands coalesce to form a nearly smooth, monatomically stepped film (Fig. 2.6(d)) (The gray-scale for height in Fig. 2.6(d) is greatly magnified as compared to 2.6(a)-(c), making this surface look rougher in comparison.) Just prior to reaching the critical coverage for a smooth film, it can be seen that the Gd islands begin to coalesce with one another (Fig. 2.6(c), θ = 5.1 ML) in contrast to the distinct, separate islands present for lower θ. In this regime, the average inter-island separation and island radius have approached the critical point at which the onset of coalescence occurs. Upon annealing to even higher temperatures (such as 710 K), the relative size of the islands produced is observed to increase slightly; however the critical coverage at which island coalescence to a smooth film occurs increases dramatically. This probably reflects the increased mobility of Gd atoms at elevated annealing temperatures for overcoming the Schwöbel barrier and jumping up step edges to form taller islands, even for significantly higher coverages. Fig. 2.7 contains a series of STM images from films of varying coverage between 1.9 ML and 20.0 ML that have been annealed at 710K. The critical coverage for a smooth film when annealing at 710 K is now roughly 20 ML (Fig. 2.7(d)). The island morphologies for films of various coverages annealed at 530 K and 710 K are shown in Fig. 2.8, where average island height and average island area are plotted as a function of coverage in Figs. 2.8(a) and (b), respectively. The first monolayer of Gd has again been subtracted from the coverage values, allowing us to consider only the Gd residing in the islands (the first monolayer will be dealt with separately in Sec. 2.V). It is interesting to note that the average island height appears to vary linearly with the amount of Gd deposited and that the islands produced with both 530 K (solid circles) and 710 K anneals (solid squares) seem to follow the same dependence on θ. A similar behavior is also observed for the average island area. In this case, however, the area appears to follow a power law dependence $A \propto (\theta - 1)^x$ where $x = 2.2$ is the best fit to the data in Fig. 2.8(b). This indicates that the average island radius would also vary nearly linearly

with coverage as well. If one assumes a linear relation between the average island height and the average island radius with respect to (θ-1), then one can arrive at a constant height to radius aspect ratio of 1:9 for these islands using the best fit from Figs. 2.8 (a) and (b). Fig 2.8 can thus be used, in principle, to synthesize Gd islands over a range of well-defined sizes and shapes, permitting a systematic study of the magnetism in such nano-particles.

When distinct islands are formed on the W(110) substrate, both their shape and alignment are driven by the epitaxy of the Gd base monolayer with respect to the substrate. A close-up STM view of a Gd island formed by annealing a 4.4 ML film at 530 K is displayed in Fig. 2.9. It can be seen quite clearly in Figs. 2.7(b), (c), and 2.9 that the Gd islands facet into quasi-hexagonal shapes, with one set of two shorter parallel sides lying along the [001] axis of the W substrate (which is in turn parallel to the Gd $[11\bar{2}0]$ direction as seen by LEED in Refs. 13 & 14). The measured angles between the facets of these islands are 120±2°, consistent with the hexagonal structure of the Gd lattice perpendicular to its [0001] direction. For reference, a similar sort of island growth has been observed for Pt films deposited on W(110) and W(111) and annealed to T > 880 K [22] and for Ag thin films deposited on Si(100) [23]. Also evident in Fig. 2.9 are monatomic steps underneath the island running very nearly perpendicular to the W(001) direction and with a mean spacing of ~7 nm. Note also that these steps appear to persist in their directional orientation up to the edge of the island, regardless of the angle between the step and the island. This latter observation suggests that the local surface structure (in particular the first monolayer to be discussed below) is not perturbed as the island grows.

The LEED patterns for these islanded films are quite complex, involving a combination of W and Gd 1x1 spots together with a large number of higher order spots. A series of LEED patterns for clean W(110), a 710 K-annealed 1.3 ML Gd/W(110) film, and for a very thick film of Gd (0001) are shown in Figs. 2.10(a),(b), and (c), respectively. By

comparing the patterns in Figs. 2.10(a) and (c) with that for the film containing islands (Fig. 2.10(b)), the overlap of the W(110) 1x1 and the Gd(0001) 1x1 spots can be seen quite clearly. The higher order spots are quite interesting and are found to have a 7x7 periodicity with respect to the W(110) substrate. This 7x7 periodicity arises due to the lattice mismatch between the first Gd(0001) monolayer and the W(110) substrate and will be discussed in further detail in Sec. 2.V. All films containing islands display a LEED pattern similar to that shown in Fig. 2.10(b), giving additional support for SK growth on an underlying monolayer for these films.

2.IV. Morphology & Magnetic Behavior of Gd/W(110)

Farle et al. studied the effect of post-deposition annealing on the ac susceptibility χ_{ac} of Gd films with a total coverage of 11 ML. They observed a broad peak in χ_{ac} for these films as deposited at 300 K, which they took to be indicative of local strain and film inhomogeneity that in turn lead to a broadening in the distribution of T_c. They then annealed these 11 ML films to 530 K, which greatly sharpened and intensified the peak in χ_{ac}; this peak appeared at a T_c value of 247 K that is only about 50 K below T_{cb} for bulk Gd. These results are summarized in Fig. 2.11(d). This sharpening was thought to be due to some sort of relaxation of local strain and the formation of a more uniform and flat film. Finally, after 710 K annealing, the intensity of the peak in χ_{ac} dropped to only 4% of its original value, and its position shifted to a T_c value of 283 K that is much closer to the bulk value of 297 K (again see Fig. 2.11(d)). Farle et al. explained the decrease in peak intensity as arising from the formation of large three-dimensional islands with considerable open space between them, with the island shape then leading to an increase of the in-plane demagnetization factor N. This island formation they predicted to have the effect of lowering the measured χ_{ac} signal according to the relation:

$$\chi_{ext} = \frac{\chi_{int}}{[1 + N\chi_{int}]} \qquad (3)$$

where χ_{ext} is the predicted ac susceptibility and χ_{int} is the intrinsic ac susceptibility of the material [6]. From the observed increase in T_c, they estimated the average thickness of the islands that formed to be 20-25 ML. Aspelmeier et al. [7] then successfully modeled these results for an 11 ML-thick film annealed at 710 K by assuming circular 3D Gd islands of uniform size (7.6 nm or about 22 ML in thickness and 500 nm in diameter).

We first consider the effects of annealing on 11 ML films as seen by STM, and then attempt to directly correlate surface morphology with prior susceptibility measurements. STM images of an un-annealed 11 ML thick Gd film and 11 ML films annealed to 530 K and 710 K for 10 min. are shown in Figs. 2.11(a)-(c), respectively, with corresponding single-line STM height profiles shown in Figs. 2.12(a)-(c) and LEED patterns displayed in Figs. 2.13(a)-(c). Before annealing (Figs. 2.11(a), 2.12(a)), the film is rough, consisting of multi-tiered structures and crevices. The LEED pattern for this surface (Fig. 2.13(a)) shows a diffuse, hexagonal (1x1) pattern, indicating a Gd(0001) film with poor long-range order parallel to the surface that is fully consistent with the STM image. After annealing to 530 K (Figs. 2.11(b), 2.12(b)), the film covers the surface smoothly within a typical 1500 nm x 1500 nm STM scan; there are only a few single-atom steps of ~0.3- 0.4 nm in height between adjacent smooth layers, and a few small mounds on the topmost layer. For reference, a single monatomic step on Gd(0001) should be 0.29 nm in height. LEED for this case (Fig. 2.13(b)) shows a sharp hexagonal (1x1) pattern that one would expect for a well-ordered Gd(0001) film. This type of temperature induced smoothening has also been seen previously for the homoepitaxial growth of Fe thin films on Fe(001) [24]. If a film prepared as in 2.11(a) or (b) is annealed to 710 K, it is found to break up into large 3D islands which in turn sit on top of a full-coverage base monolayer of Gd (Figs. 2.11(c),

2.12(c)) with a LEED pattern as shown in Fig. 2.13(c); the properties of this base monolayer (including the explanation of the LEED pattern) will be described in greater detail in Section V. As in the case of the islands produced by 530 K annealing for $\Theta < 7.0$ ML, the Gd islands in 2.11(c) are also found to facet into quasi-hexagonal shapes, with one set of two shorter parallel sides lying along the [001] axis of the W substrate (which is in turn parallel to the Gd [$11\bar{2}0$] direction). These islands are also of a fairly narrow size distribution, with an average area of ~8.40±1.40 x 10^4 nm^2 and a thickness range of 11.3 ±4.7 nm (equivalent to a range of 23-55 ML). Roughly 32% of the film surface is covered by islands with an island density of approximately 4.1 x 10^{-6} per nm^2. The measured angles between the facets of these islands are, as in the case of islands produced by 530 K annealing for lower coverages, found to be 120±2°, consistent with the hexagonal structure of the Gd lattice perpendicular to its [0001] direction.

In order to relate these structures to magnetic properties, we first approximate these islands as thin circular disks of average thickness t = 11.3 nm and average diameter d = 2 x $[(8.40 \times 10^4\ nm^2)/\pi]^{1/2} = 3.27 \times 10^2$ nm. This yields a ratio $g \equiv t/d = 3.46 \times 10^{-2}$, from which the in-plane demagnetization factor can be calculated [4]:

$$N = \frac{\pi g}{4} - g^2 \qquad (4)$$

The quantitative analysis of our STM images thus leads to a value for N of 2.6±0.7 x 10^{-2} that is close to , but over twice as large as, the value of 1.0 x 10^{-2} estimated recently by Aspelmeier et al. with assumed size parameters for the islands [6]. We further note that χ_{ac} as measured after the 530 K anneal is approximately equal to χ_{int} since the film is atomically smooth and N for this case is estimated to be only about 5 x 10^{-7} [4]. At the peak in Fig. 2.11(d), the χ_{ac} signal for the 530K annealed surface is roughly 1200 SI

units. Using this value, together with the value for N determined from our STM measurements, we can use Eq. 4 to predict that the peak in χ_{ac} should drop by 97% after 710 K annealing, in excellent agreement with the 96% drop observed by Farle et al. [4]. Furthermore, one can estimate from the previously-measured thickness dependence of T_c for Gd films prepared so as to be smooth [4] that the T_c for such large flat islands of 11.3 nm thickness will be approximately 286 K, again in excellent agreement with the χ_{ac} results for the 11 ML film, which show a T_c of ~282 K [4].

2.V. The first Gd monolayer

Finally, we turn to another intriguing feature of the growth of Gd on W(110) that has been characterized for the first time in this work, and for which a preliminary account appears elsewhere [14]. The first monolayer of Gd forms a lateral two-dimensional superstructure of large-scale periodicity with respect to the substrate, as illustrated in Figs. 2.14 and 2.15. This Gd superstructure is evident in real-space constant-height STM images of a 1 ML Gd film annealed to 710 K (Fig. 2.14(a)) and of the regions between the large islands of an 11 ML Gd film annealed to 710 K (Fig. 2.15(a)). It is also obvious in the reciprocal-space LEED pattern of Fig. 2.14(b) for the surface in Fig. 2.14(a), which shows finely-spaced satellite spots around the Gd and W (1x1) spots. Here, the Gd(1x1) pattern coincides with the six most intense spots, as indicated by "+" in the figure, and the closest lying W(1x1) spots to these are indicated by "-" (a similar LEED pattern was observed for 1 ML coverage in ref. [13], but with no quantitative comments as to origin). This same structure is visible in STM between the Gd islands for all coverages in the range of $1 < \theta < 20$ ML for films annealed at 710 K and in the range of $1 < \theta < 7$ ML for films annealed at 530 K. (Greater coverages gave smooth multilayer films when annealed to 530 K, as we have noted above.). We find that the superstructure has rectangular periodicities along the [001] and the [$\bar{1}$10] directions of the W substrate of 23.5±1.7 Å and 15.9±1.8

Å, respectively, from STM measurements, and 23.7±2.1 Å and 16.4±0.7 Å from LEED patterns (assuming that the W(1x1) spots represent bulk distances). These periodicities are thus very close to (7x7) with respect to W(110), which would yield 22.1 Å and 15.6 Å along the [001] and the [$\bar{1}$10] directions. The height corrugation measured by STM is approximately 0.5 Å.

Our suggested model for this superstructure simply overlays a slightly distorted hexagonal Gd(0001) monolayer on top of the W(110) surface with the Gd [11$\bar{2}$0] direction parallel to W [001]. This is similar to the Nishiyama-Wasserman orientation as previously observed by Li et al. for the heavy rare-earths grown on W(110) surfaces [25]. As shown in Fig. 2.15(b), the overlayer thus forms a Moiré pattern with the substrate that has an overall (7x$\underline{14}$) periodicity as judged with respect to W(110). Relative to bulk Gd, the Gd monolayer is expanded by 1.2% along the W [001] direction and compressed by 0.6% along the [$\bar{1}$10] direction. This gives a Gd:W coincidence-lattice match of 6:7 and 5:7 along the W [001] and [$\bar{1}$10] directions, respectively. The corrugation is then probably due to variations in interlayer spacing between the Gd overlayer and the W substrate over the many different Gd absorption sites involved, and/or more complex changes in the surface density of states over the unit cell as sensed directly by STM. Fig. 2.15(b) also indicates that this model has pseudo-(7x7) periodicity: two pseudo-(7x7) cells of 22.1 Å and 15.6 Å along the W [001] and [$\bar{1}$10] directions are contained in a true (7x14) cell, with the (7x7) periodicity being in excellent agreement with our STM and LEED results, as noted above. No other combinations of compression and expansion of the Gd lattice of such small extents were found to produce a superstructure with the correct periodicity. Hence, these findings are in disagreement with the 4.4% compression determined for the first Gd monolayer by a previous AES study based on a quantitative determination of coverage [13]. We note that somewhat similar Moiré superstructures have been observed for 1 ML of FeO grown epitaxially on Pt(111) [26,27] and for 4 ML

of Cu grown epitaxially on Ru(0001) [28]; these structures have been attributed to the lattice mismatch between the substrate and a weakly interacting overlayer, giving rise to a periodic rippling of the surface that is qualitatively the same as that seen here.

VI. Conclusions

In conclusion, our STM measurements of the morphology of Gd films on W(110) prepared with and without annealing have provided a much more detailed picture of the growth modes involved and some of their scaling properties, permitted a quantitative structural explanation for previously-measured magnetic properties, and revealed a new two-dimensional structure for the first monolayer. As deposited at room temperature, Gd does not grow layer-by-layer, but rather in a multilayer mode. Analysis of the film roughness as a function of coverage and lateral length scale suggests that the growing Gd surface follows scaling laws for a self-affine surface. Furthermore, the determination of the scaling exponents α and β indicates that growth may be mediated by surface diffusion in conjunction with step flow and/or island nucleation. Annealing as-deposited films at elevated temperatures is found to drastically alter the morphology of these films, as seen by both STM and LEED. Annealing films thicker than 7 ML at 530 K produces smooth, monatomically stepped surfaces. For coverages in the range of $1 \leq \theta \leq 7$ ML, 530 K annealing produces films containing large 3D islands with quasi-hexagonal symmetry and relatively uniform size resting on a base monolayer; this is thus an example of Stranski-Krastanov growth. The uniformity of the island sizes thus produced suggests this as a method for synthesizing arrays of nanometer-scale ferromagnetic particles for further study. Annealing to 710 K is observed to create even larger islands with a critical coverage for smooth films increasing to ~20 ML. Careful measurement of the island dimensions for an 11 ML film enables the prediction of a 97% reduction in peak intensity

for ac magnetic susceptibility (compared to 96% from prior experiments [4]), and of a Curie temperature of approximately 284 K (again in agreement with prior experiments [4]). Finally, the first monolayer of Gd is observed to form a (7x14) superstructure with pseudo-(7x7) symmetry as well that is consistent with a minimally-distorted hexagonal two-dimensional Gd(0001) film. The superstructure arises due to the incommensurate epitaxial first monolayer of Gd resting on top of the W(110) surface with a coincidence lattice match for Gd:W of 6:7 and 5:7 along W [001] and [$\bar{1}$ 10], respectively.

Acknowledgments: The authors would like to thank D. Weller for the loan of a Gd deposition source and for many helpful comments, A. P. Kaduwela for aid in superstructure modeling, and I. Tidswell for assisting with W single-crystal alignment. Support for these studies was provided by the Director, Office of Energy Research, Materials Sciences Div., of the U.S. Dept. of Energy, under Contract No. DE-AC03-76SF00098, and the Office of Naval Research under contract (N00014-94-0162).

References:

[1] D. Weller, S. F. Alvarado, W. Gudat, K. Schroder, and M. Campagna, Phys. Rev. Lett. 54, 1555 (1985).

[2] H. Tang, D. Weller, T. G. Walker, J. Scott, C. Chappert, H. Hopster, A. W. Pang, D. S. Dessau, and D. P. Pappas, Phys. Rev. Lett. 71, 444 (1993).

[3] M. Farle, W. A. Lewis, K. Baberschke, Appl. Phys. Lett. 62, 2728 (1993).

[4] M. Farle, K. Baberschke, and U. Stetter, Phys. Rev. B 47, 11571 (1993).

[5] M. Farle, W. A. Lewis, J. Appl. Phys. 75, 5604 (1994).

[6] U. Stetter, M. Farle, and K. Baberschke, Phys. Rev. B 45, 503 (1992).

[7] A. Aspelmeier, F. Gerhardter, and K. Baberschke, J. Mag. Mag. Mat. 132 N1-3, 22 (1994).

[8] A. Berger, A. W. Pang, H. Hopster, J. Mag. Mag. Mat. 137, L1-L5 (1994).

[9] D. Li, C. W. Hutchings, P. A. Dowben, R. Wu, C. Hwang, M. Onellion, A. B. Andrews, J. L. Erskine, J. Appl. Phys. 70, 6565 (1991).

[10] D. Li, J. Zhang, P. A. Dowben, M. Onellion, Phys. Rev. B 45, 7272 (1992).

[11] A. W. Pang, A. Berger, H. Hopster, Phys. Rev. B 50, 6457 (1994).

[12] B. Kim, A. B. Andrews, J. L. Erskine, K. Kim, B. N. Harmon, Phys. Rev. Lett. 68, 1931 (1992).

[13] J. Kolaczkiewicz and E. Bauer, Surf. Sci. 175, 487 (1986).

[14] E. D. Tober, R. X. Ynzunza, C. Westphal, and C. S. Fadley, Phys. Rev. B 53, 5444 (1996).

[15] C. Rau, C. Jin, M. Robert, Phys. Lett. A 138, 334 (1989).

[16] K. Higashiyama, S. K. Lewis, R. X. Ynzunza, E. D. Tober, Y. J. Kim, and C. S. Fadley, Surf. Sci. 291, 47 (1993).

[17] G. Meyer and K. H. Rieder, Appl. Phys. Lett. 64, 27 (1994).

[18] A. Zangwill, "Theory of Growth Induced Roughness," appearing in Microstructural Evolution of Thin Films, edited by H. A. Atwater and C. V. Thompson, (Academic Press, NY, 1995).

[19] W. M. Tong and R. Stanley-Williams, "Kinetics of Surface Growth - Phenomonology, Scaling, and Mechanisms of Smoothening and Roughening," Annual Reviews of Phys. Chem. 45, 401 (1994).

[20] F. Family and T. Vicsek, J. Phys. A 18, L75 (1985).

[21] Z.-W. Lai and S. Das Sarma, Phys. Rev. Lett. 66, (1991).

[22] T. E. Madey, K. J. Song, C. Z. Dong, Surf. Sci. 247, 175 (1991).

[23] A. Samsavar, E. S. Hirschorn, F. M. Leibsle, and T. C. Chiang, Phys. Rev. Lett. 63, 2830 (1989).

[24] J. A. Stroscio, D. T. Pierce, and R. A. Dragoset, Phys. Rev. Lett. 70, 3615 (1993).

[25] H. Li, D. Tian, J. Quinn, Y. S. Li, S. C. Wu, and F. Jona, Phys. Rev. B 45, 3853 (1992).

[26] H. C. Galloway, J. J. Benitez, and M. Salmeron, Surf. Sci. 298 N1, 127 (1993).

[27] Y. J. Kim et al., Ph.D. thesis, University of Hawaii, 1995.

[28] C. Günther, J. Vrijmoeth, R. Q. Hwang, and R. J. Behm, Phys. Rev. Lett. 74, 754 (1995).

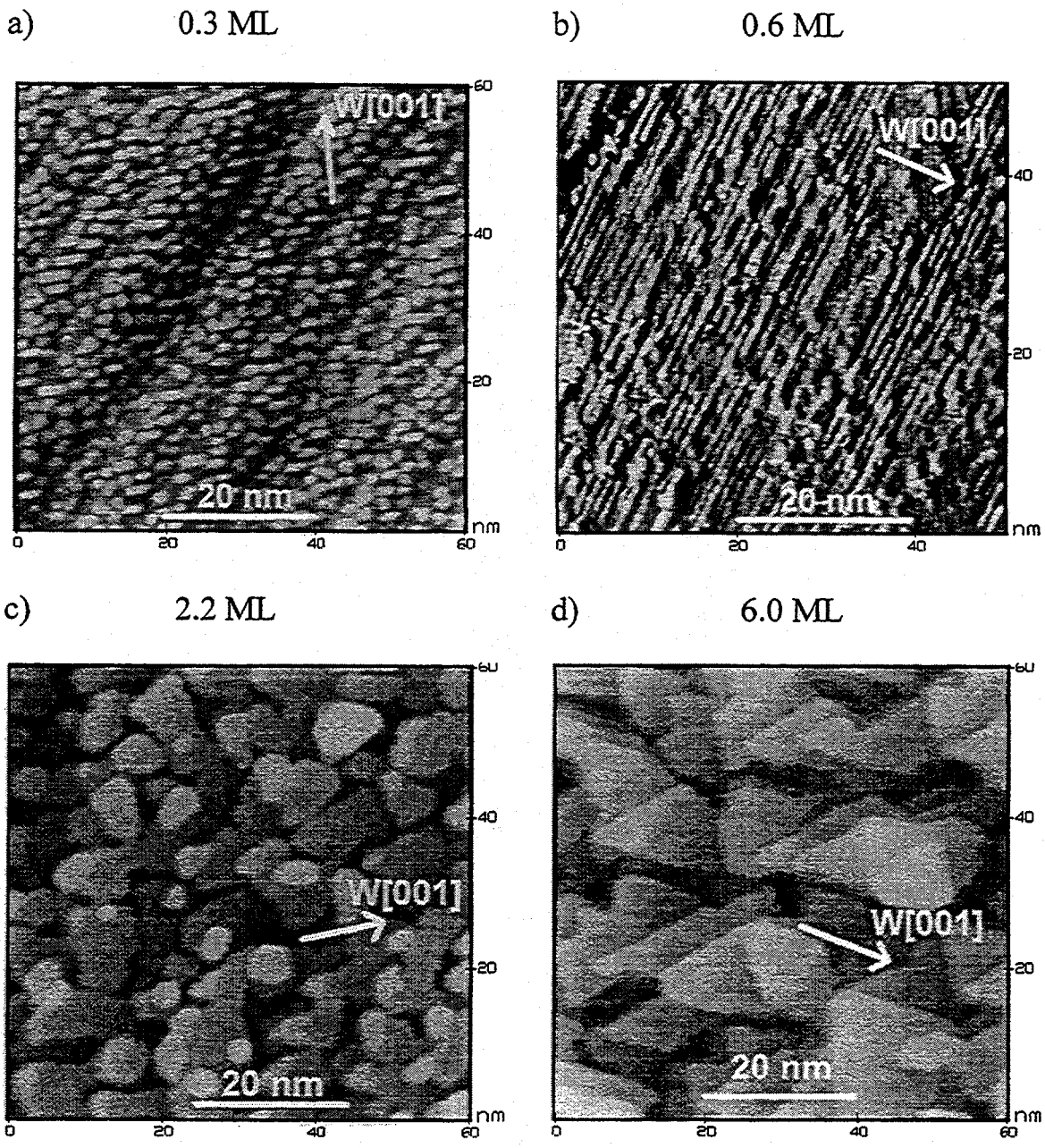

Figure 2.1: STM images of Gd thin films deposited on W(110) at room temperature for select coverages θ: (a) θ = 0.3 ML, (b) θ = 0.6 ML, (c) θ = 2.2 ML, and (d) θ = 6.0 ML. (a), (c), and (d) are constant current images and (b) is a constant height image. Bias voltage V_b = +800 mV, and set-point current I_o = 2.0 nA.)

a)

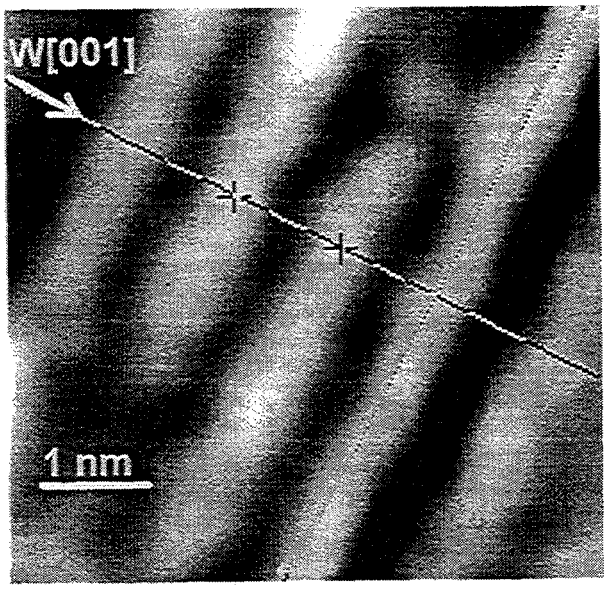

b)

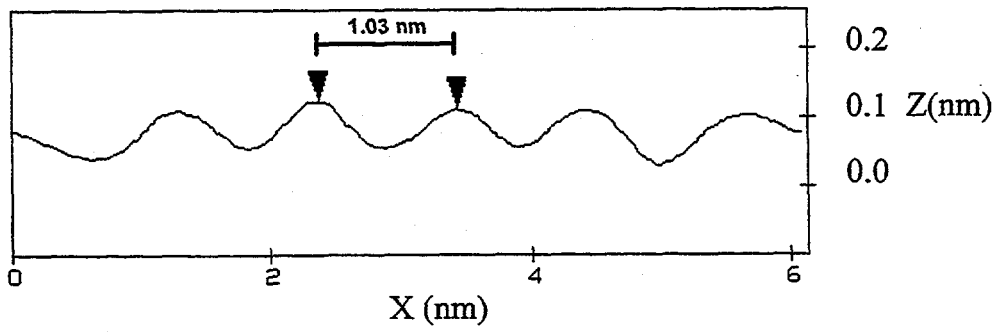

Figure 2.2: (a) Constant-current STM image close-up of a striped region found for 0.6 ML coverage and room temperature deposition, as shown also in Fig. 1(b). (V_b = +800 mV, I_o = 2.0 nA) (b) Single line STM scan of relative tip height (Z) vs. horizontal tip position (X) taken from (a) and perpendicular to the periodic array of bright rows, i. e. along the W[001]. The vertical corrugation has an average height change of 0.07 nm.

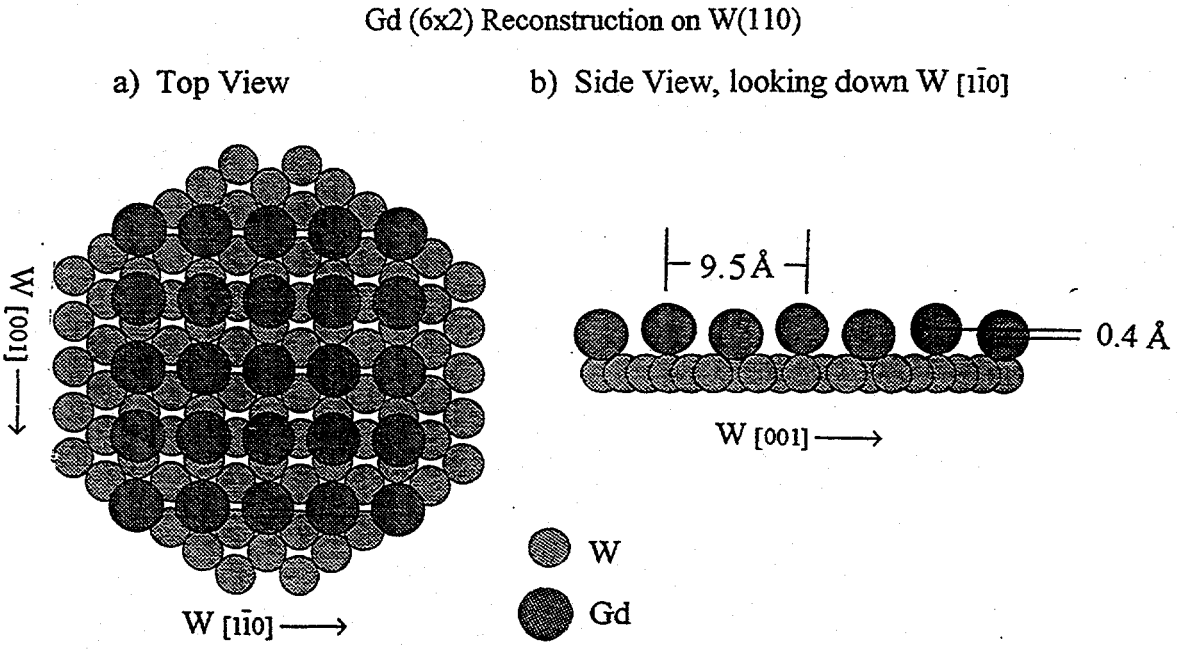

Figure 2.3: Atomic structure model proposed in Ref. 13 for the 6x2 reconstruction of Gd on W[110]. Note the high and low rows of Gd atoms with spacing very close to that seen in Fig. 2.

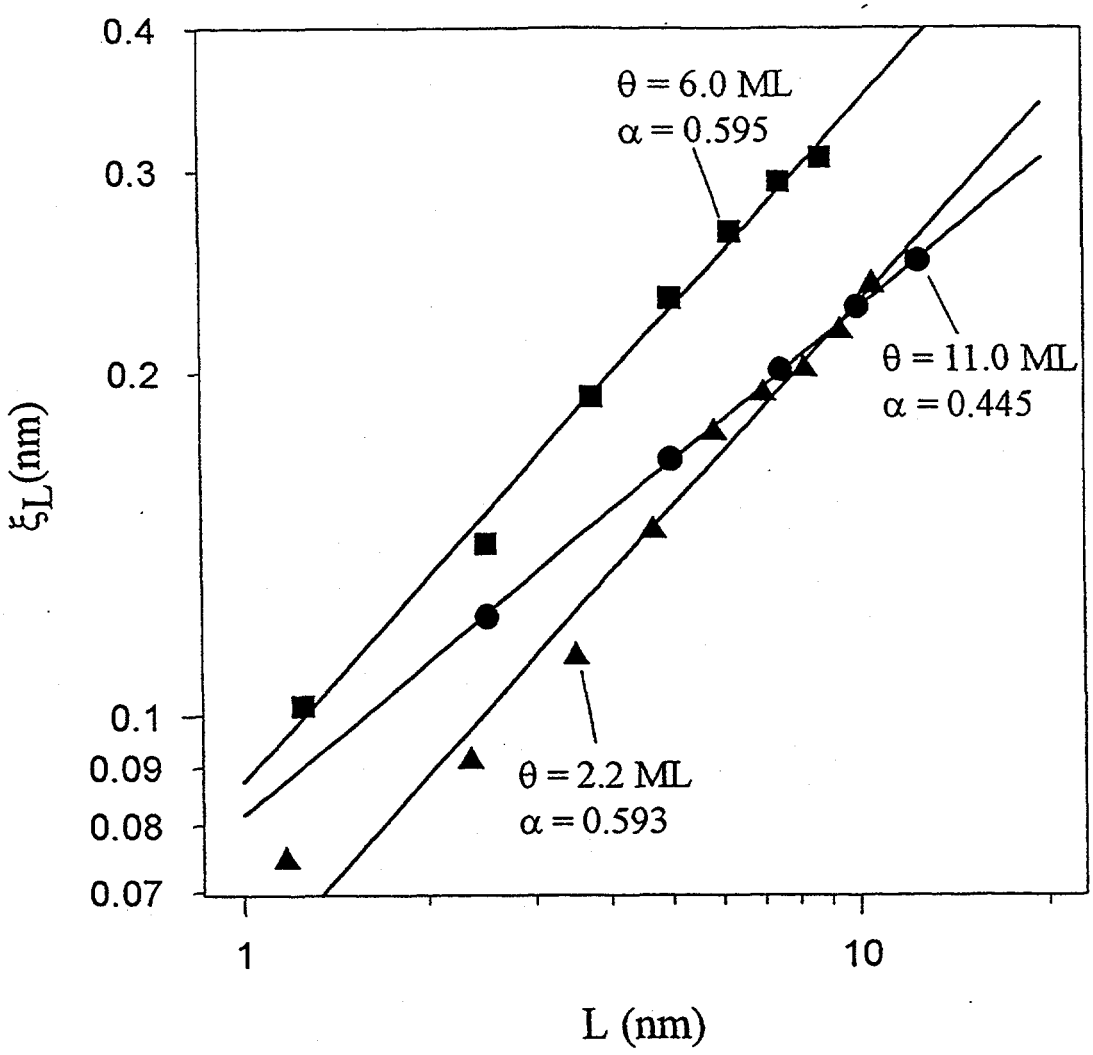

Figure 2.4: STM rms tip height $\xi(L)$ (surface roughness) as a function of the lateral sampling length scale L for various coverages θ of Gd. The data have been fitted to the scaling relation: $\xi(L) \propto L^{\alpha}$.

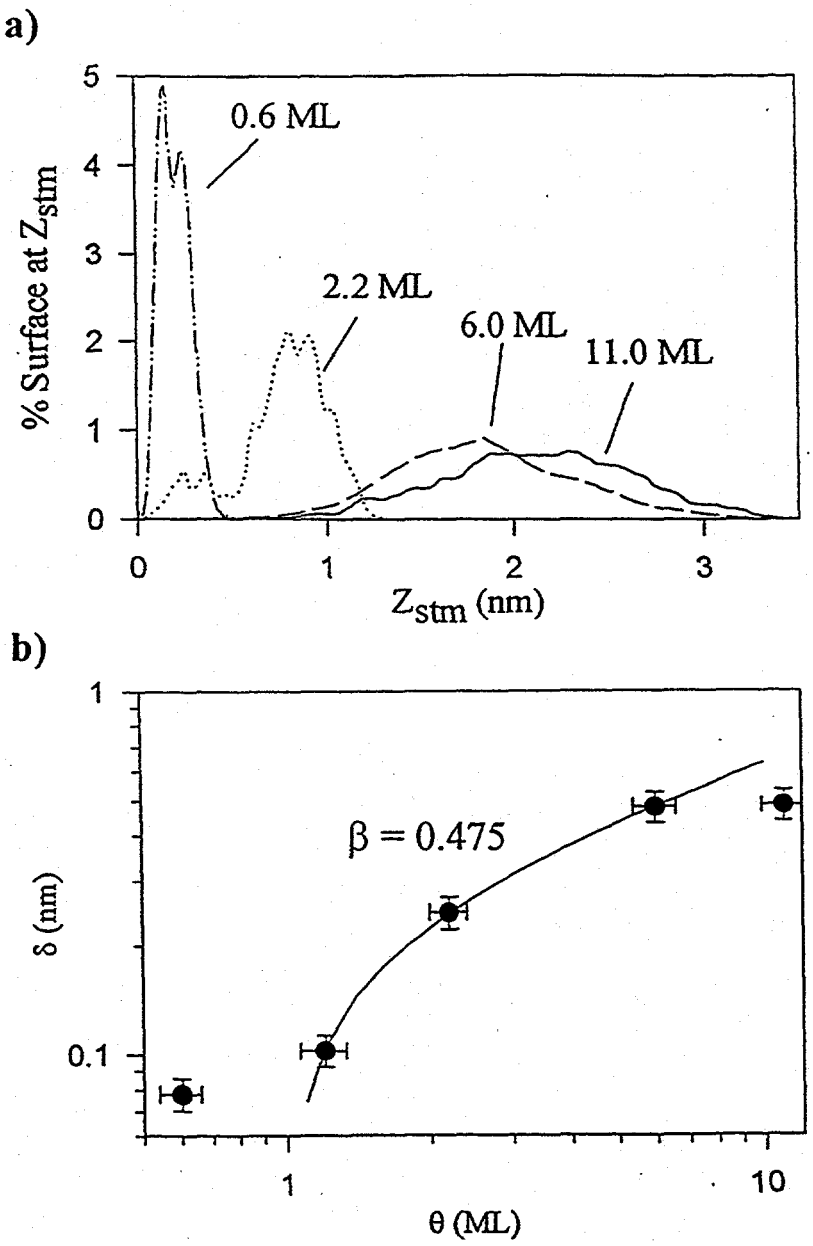

Figure 2.5: (a) STM tip height distribution histograms of % surface at height Z_{stm} for various coverages of Gd (b) Overall STM rms tip height δ (total surface roughness) as a function of Gd coverage θ. Data are fitted to the scaling relation: $\delta \propto (\theta - 1)^{\beta}$ within the non-critical coverage region of $1 \leq \theta \leq 6$ ML.

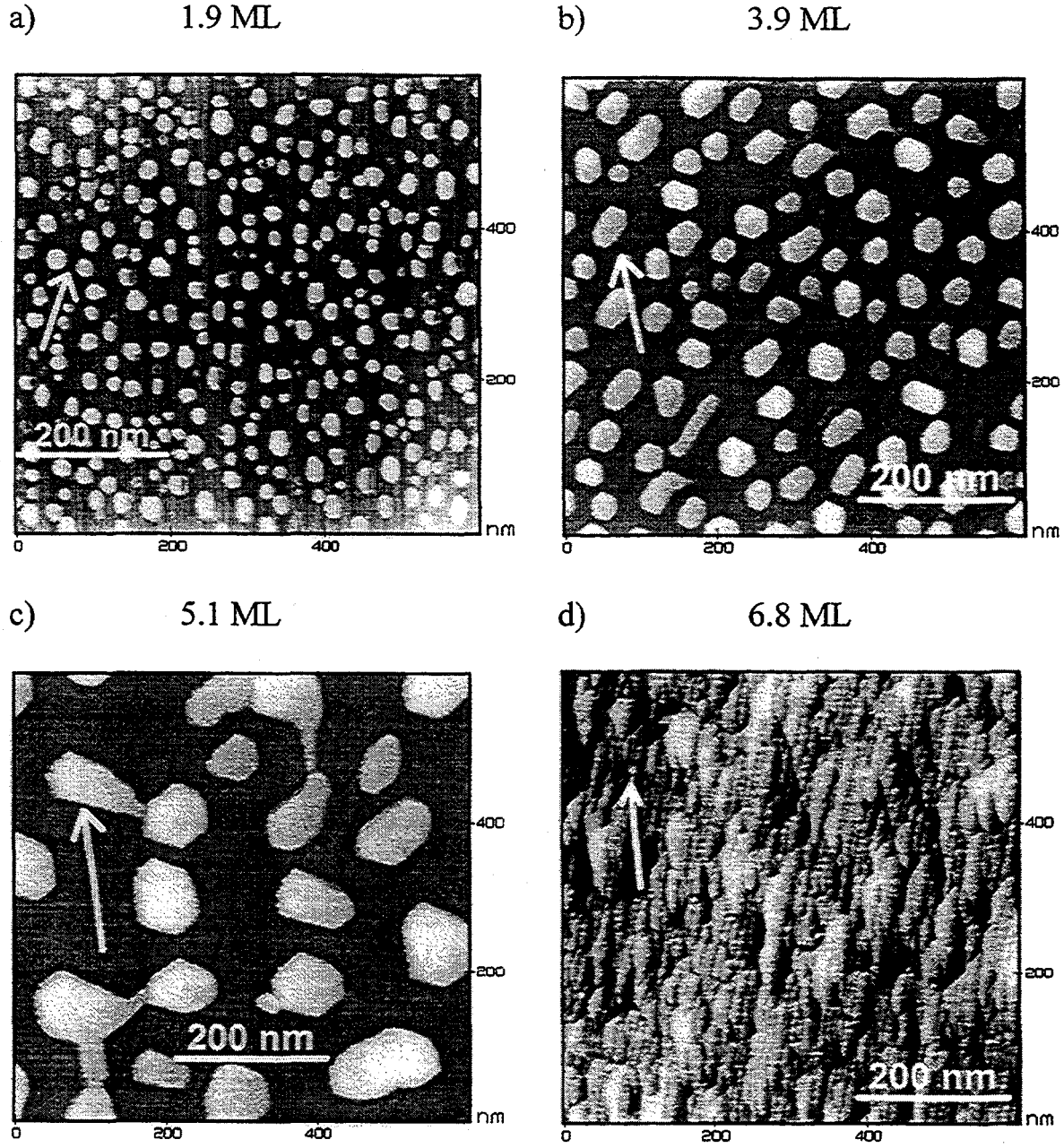

Figure 2.6: Constant current STM images (V_b = +800 mV, I_o = 2.0 nA) over 600 nm x 600 nm of Gd films deposited on W(110) at room temperature and then annealed to 530 K for a range of coverages: (a) 1.9 ML, (b) 3.9 ML, (c) 5.1 ML and (d) 6.8 ML. The height scale in (d) is much amplified, with the apparent roughness being only at the level of monatomic steps. White arrows indicate W[001] direction.

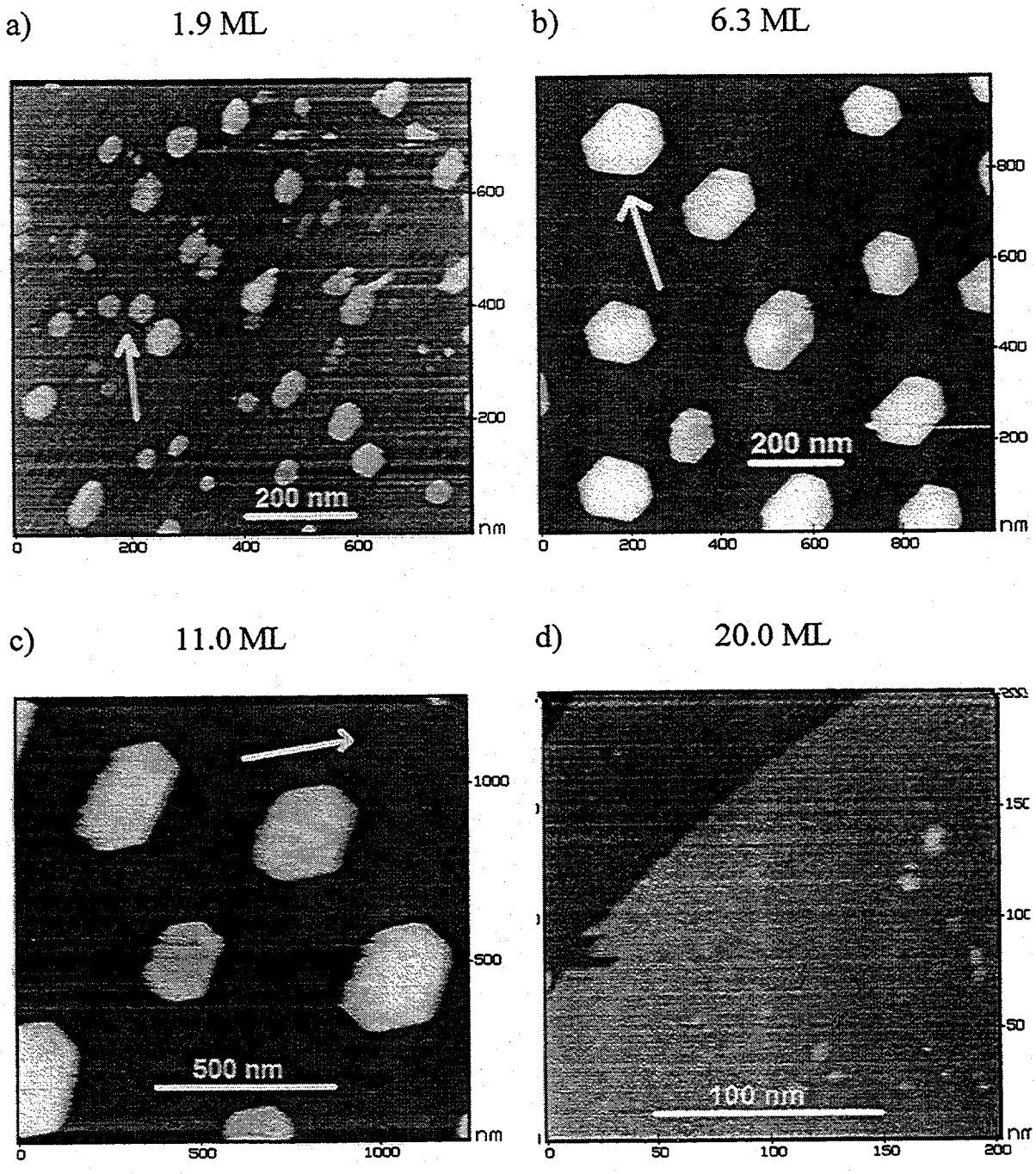

Figure 2.7: Constant current STM images of Gd films deposited on W(110) at room temperature and annealed at 710K for a range of different coverages (V_b = +800 mV, I_o = 2.0 nA): (a) 1.9 ML, 800 nm x 800 nm, , (b) 6.3 ML, 1000 nm x 1000 nm, (c) 11.0 ML, 1200 nm x 1200 nm,, and (d) 20 ML, 200 nm x 200 nm. White arrows indicate W[001] direction.

a)

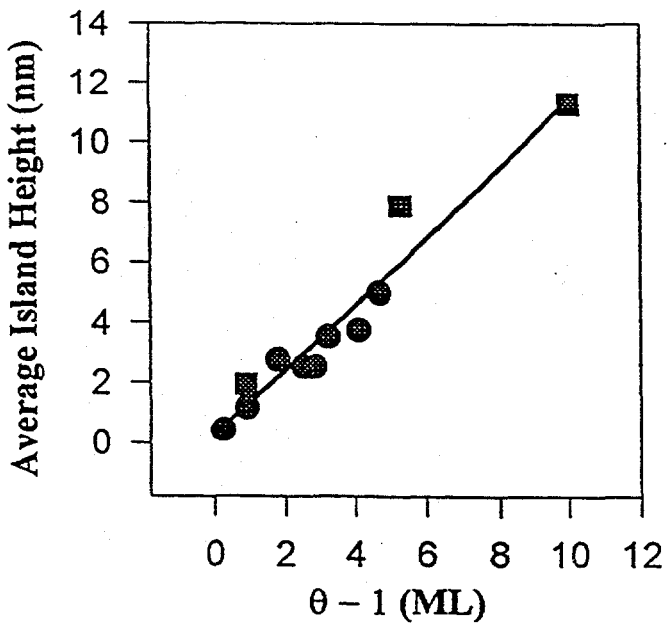

b)

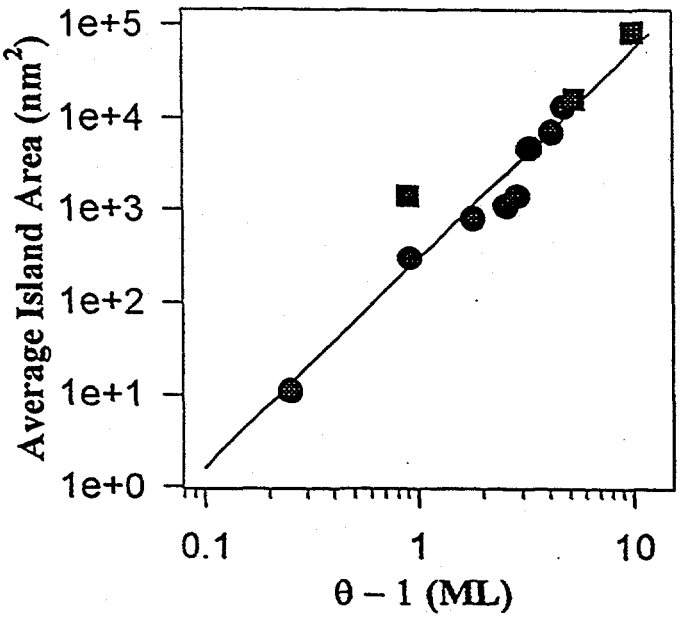

Figure 2.8: (a) Average island height $\bar{t}$ vs. Gd coverage θ and (b) average island area $\bar{A}$ vs. Gd coverage θ for Gd films on W(110) deposited at room temperature and annealed to 530 K (●) and 710 K (■).

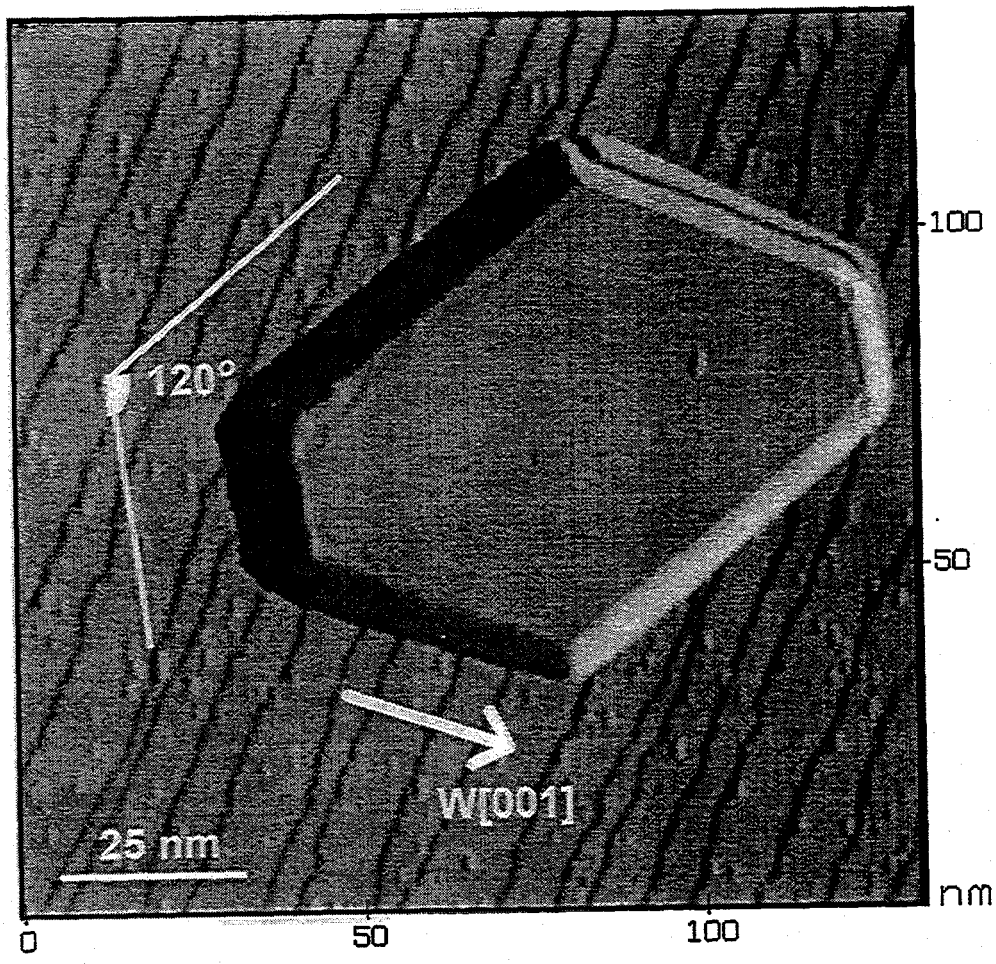

Figure 2.9: Close-up constant-current STM image of a Gd island from a 4.4 ML Gd deposition on W(110) with 530 K annealing (V_b = 800 mV, I = 2.00 nA). Note the monatomic steps in the basal layer underneath the island, which is concluded to be covered by a 7x14 Gd monolayer. The average height of this island above the basal layer was 3.50 nm or ~100 ML.

Figure 2.10: A series of LEED patterns at slightly different beam energies E_o from (a) clean W(110), beam energy E_o = 139.4 eV, (b) 1.3 ML Gd/W(110) with 710 K anneal, E_o = 101.1 eV, and (c) 40 ML Gd(0001) with 800 K anneal, E_o = 94.6 eV.

a)

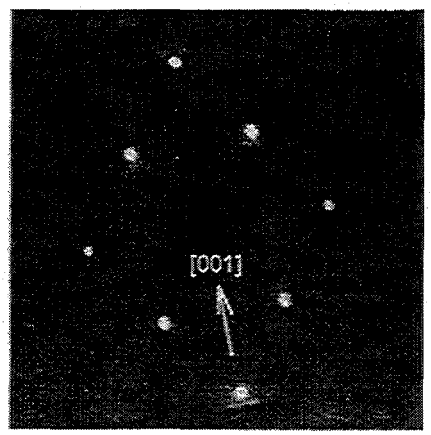

Clean W(110)

E_o = 139.4 eV

b)

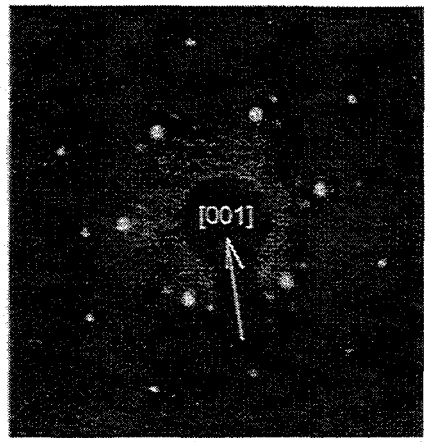

1.3 ML Gd/W(110)

E_o = 101.1 eV

c)

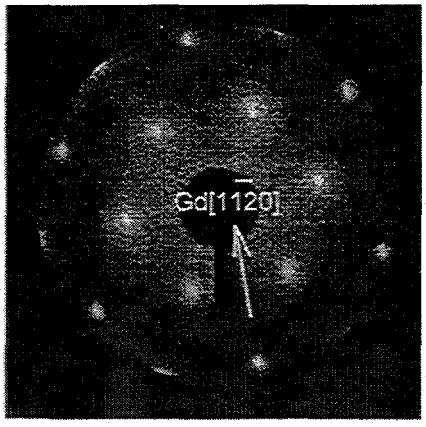

40 ML Gd/W(110)

E_o = 94.6 eV

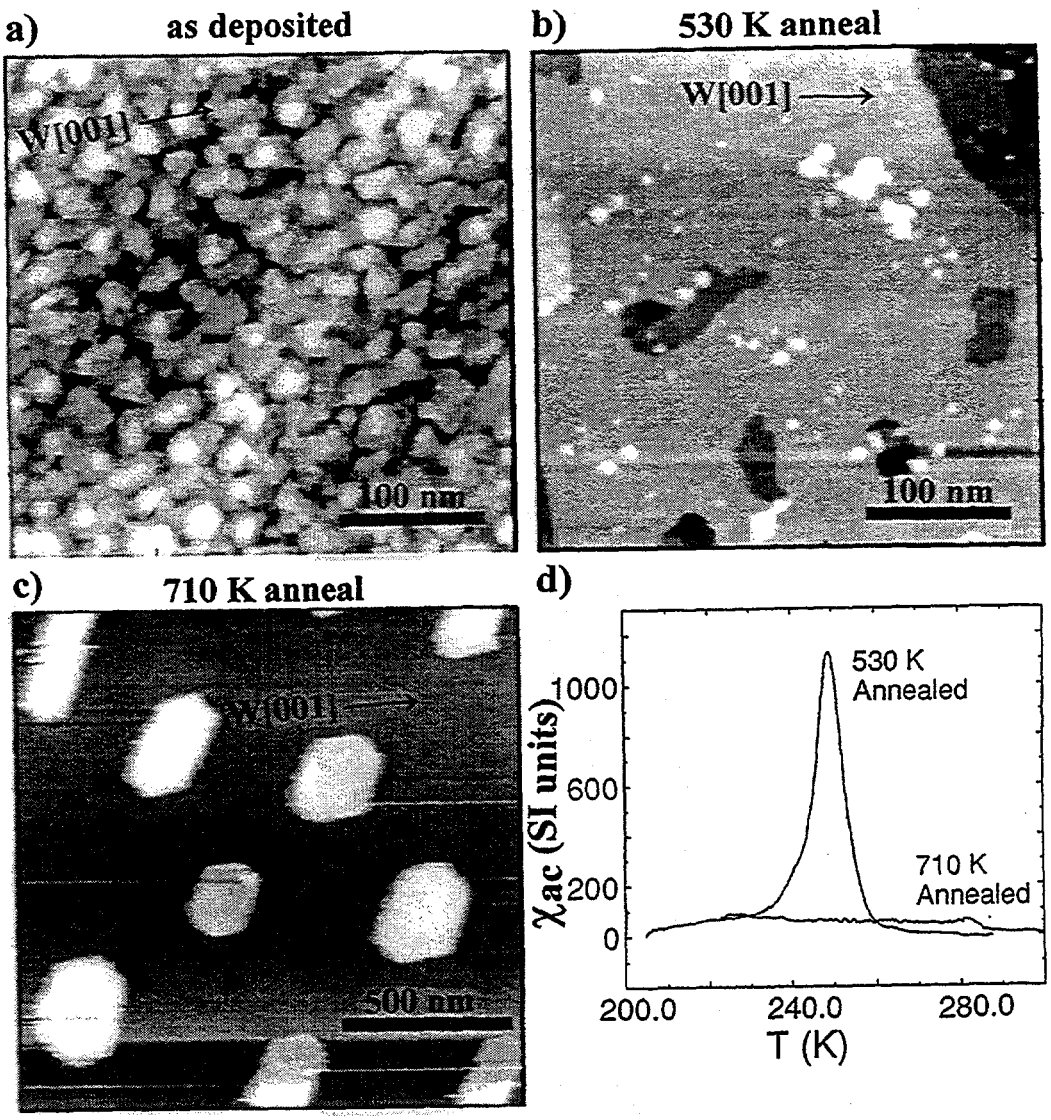

Figure 2.11: Constant-current STM images of 11 ML Gd films deposited on W(110) at 300 K, with post-deposition annealing temperature, overall image size, sample bias V_b, and tunneling current I indicated: (a) Film as deposited: 350 nm x 350 nm, V_b = 800 mV, I = 2.00 nA; (b) Film annealed at 530 K: 350 nm x 350 nm, V_b = 800 mV, I = 2.00 nA; (c) Film annealed at 710 K: 1500 nm x 1500 nm, V_b = 800 mV, I = 1.00 nA; (d) Previously-obtained ac magnetic susceptibility data from Ref. 4 for 11 ML Gd films at the same two annealing temperatures as (b) and (c).

Figure 2.12: Single line STM scans of relative tip height (Z) vs. horizontal tip position (X) taken from Figs. 1(a)-(c) for 11 ML Gd films deposited on W(110), with the scanning from left to right, parallel to the bottom of the image frames. (a) Film as deposited (from Fig. 11(a)). (b) Film annealed at 530 K (from Fig. 11(b)). The two step heights at right are roughly 0.29 nm high, and represent monatomic steps. (c) Film annealed at 710 K (from Fig. 11(c)). The two island heights shown are approximately 10.3 and 14.7 nm. Tip heights have been estimated by using the observed monatomic step heights on the Gd(0001) surface as the expected step height of 0.29 nm.for an approximate calibration.

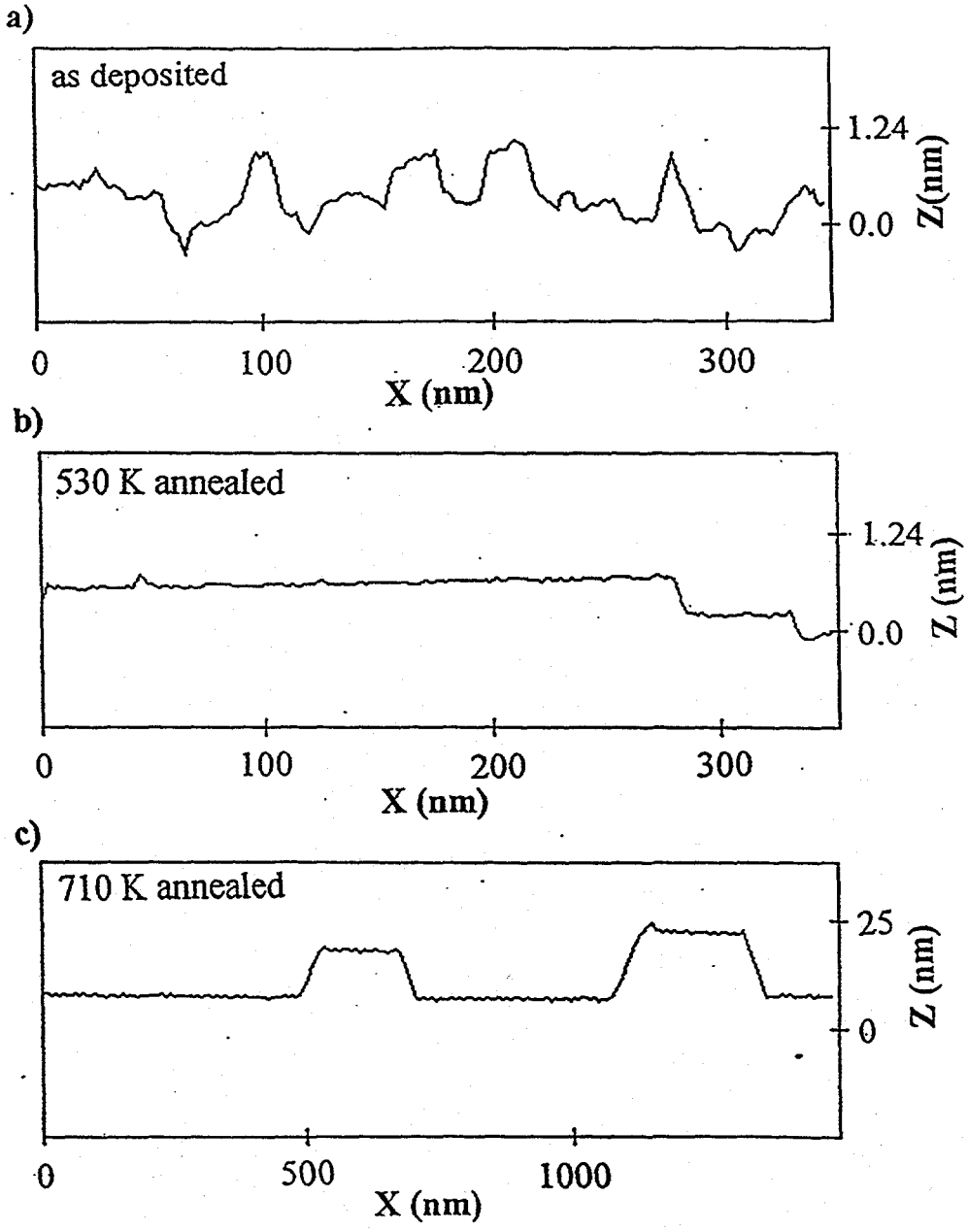
a)
as deposited
1.24
0.0
Z(nm)
0
100
200
300
X (nm)
b)
530 K annealed
1.24
0.0
Z (nm)
0
100
200
300
X (nm)
c)
710 K annealed
25
0
Z (nm)
0
500
1000
X (nm)

Figure 2.13: LEED patterns corresponding to the 11.0 ML Gd films shown in Figs. 11(a)-(c): (a) as-deposited at room temperature, E_o = 91.8 eV, (b) 530 K annealed, E_o = 99.6 eV, (c) 710 K annealed, E_o = 124.6 eV. Note the strong similarity between (c) and Fig. 10(b).

a)

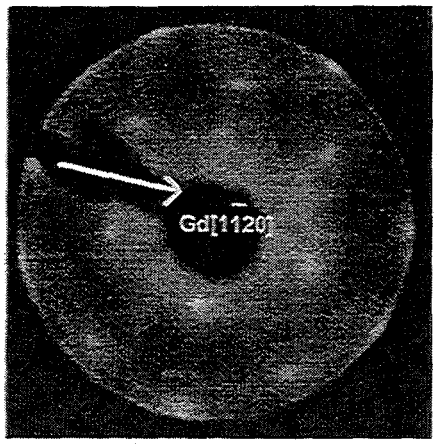

as-deposited
11 ML Gd/W(110)

$E_o = 91.8$ eV

b)

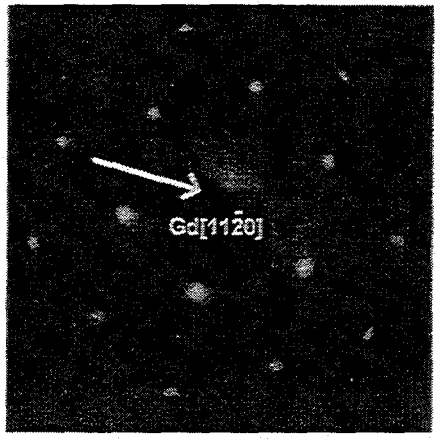

530 K annealed
11 ML Gd/W(110)

$E_o = 99.6$ eV

c)

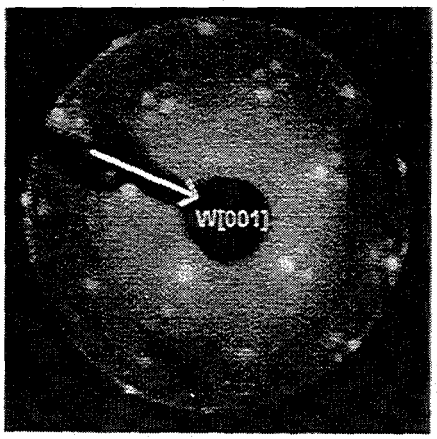

710 K annealed
11 ML Gd/W(110)

$E_o = 124.6$ eV

a)

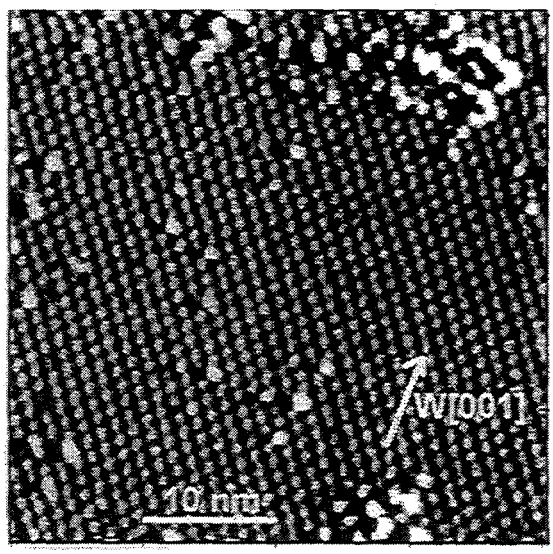

b)

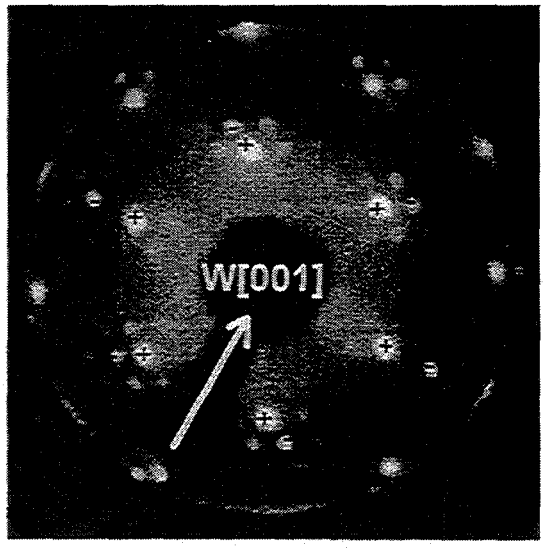

Figure 2.14: (a) Constant-height STM image of the superstructure present with 1 ML of Gd annealed to 710 K 40 nm x 40 nm, V_b = 800 mV, I = 2.00 nA. (b) LEED pattern produced by the structure in (a) at a beam energy of 102.1 eV; the closest in sets of Gd(1x1) spots are indicated by + , and of W(1x1) by - .

Figure 2.15: (a) Constant-current STM image of the superstructure visible between the Gd islands of an 11 ML thick film annealed to 710 K: 8 nm x 8 nm, V_b = 800 mV, I = 2.00 nA. (Thermal drift in the STM causes a slight canting of the image.) (b) Our proposed atomic model for the superstructure formed by 1 ML Gd on W(110), with the rectangular (7x14) unit cell indicated, and the pseudo-(7x7) periodicity also evident.

a)

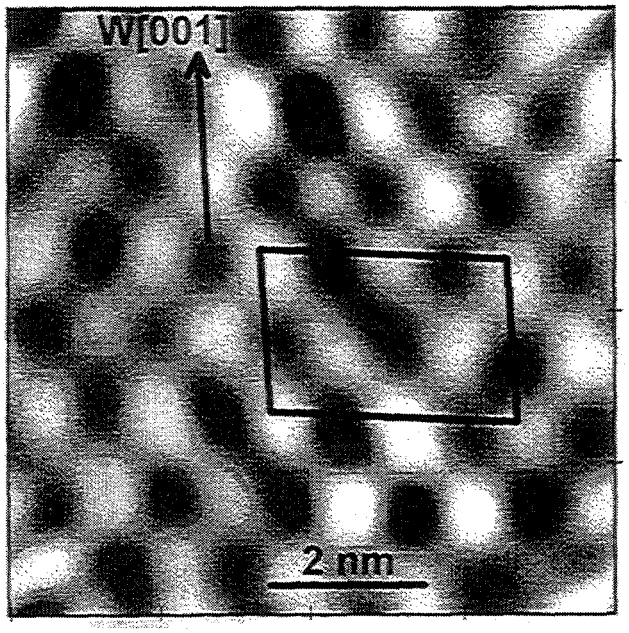

b)

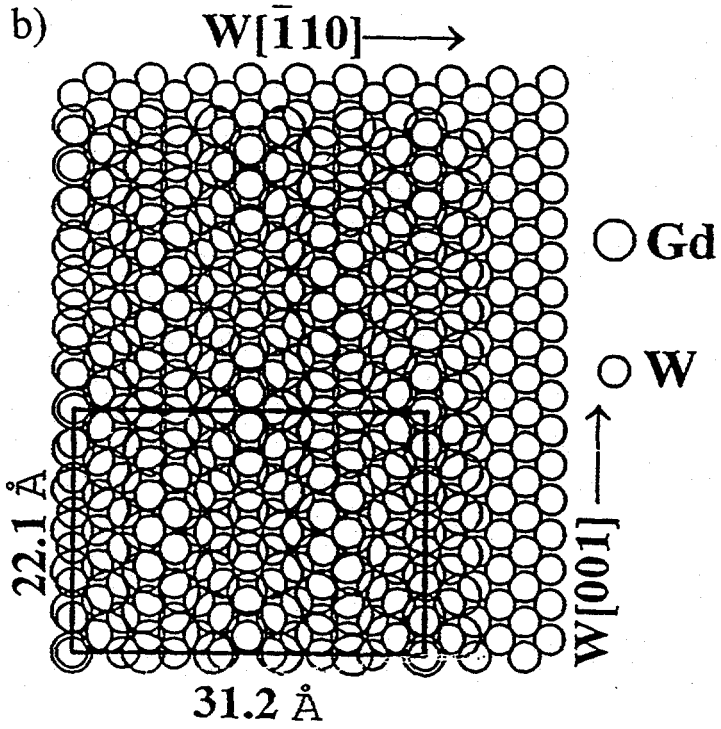

Chapter 3.

Interface Structures of Ordered Fe and Gd Overlayers on W(110) from Photoelectron Diffraction

3.I Introduction

In recent years, a variety of techniques has been used in an attempt to identify the local structures at solid-solid interfaces. X-ray diffraction [1-3], electron microscopy [3], and low energy electron diffraction (LEED) [4] have all achieved some success in this area. Yet all of these measurements lack the ability to directly probe the structure of atoms that are specifically at the interface. For example, electron microscopy has the ability to image the interface, but only as columns of atoms, and LEED is neither atom nor interface specific. Photoelectron diffraction (PD) [5-7], on the other hand, can be specifically sensitive to interface atoms, first through its core-level element specificity and second through a resolvable binding energy difference (chemical shift) from the other atoms present. X-ray PD (XPD) from chemically shifted core-levels has in fact been used to study the local structure at semiconductor/insulator [8], semiconductor/metal [9], and semiconductor/semiconductor [10,11] interfaces. The chemical shifts in these cases were quite large (>1 eV), enabling the use of standard laboratory X-ray sources and photoelectron spectrometers of modest resolution. However, when attempting to study the important class of systems represented by metal-metal interfaces, one typically encounters core-level shifts nearly an order of magnitude smaller (~100 meV), making standard XPD measurements on these systems prohibitive. Thus, studying a narrow core line (as e.g., 3d in the 4d transition metals or 4f in the 5d transition metals) and using high-resolution synchrotron radiation for excitation is necessary for the observation of such

effects. For example, for the clean W(110) surface, two peaks in the W $4f_{7/2}$ spectrum are observed, one arising from bulk W atoms and a second shifted to 320 meV lower binding energy (E_b) that is due to the under-coordinated W atoms at the surface [12]. We will term this a -320 meV shift. But if a metal overlayer is now placed on this surface, the former surface W atoms are now interface atoms, and they can still exhibit a shift relative to the bulk. Shinn et al. [13] have found such small interface core-level shifts (ICLS's) in the W $4f_{7/2}$ photoelectron spectra from W(110) surfaces covered with one monolayer (ML) of Ni, Pt, or Fe in a pseudomorphic (1x1) structure. Specifically, the ICLS's for Ni and Pt overlayers were measured as being -200 meV and +70 meV, respectively, again relative to the bulk binding energy. In the case of (1x1) Fe, the situation is thought to be even more complex, with the W $4f_{7/2}$ spectrum consisting of three components: one from the interfacial W layer shifted by -225 meV, another from what appears to be the second W layer shifted by -80 meV, and the bulk W peak (which is found to remain at the same distance from the Fermi level as for the clean surface) [13]. We have in this study utilized such ICLS's to perform for the first time interface-specific PD on two metal-metal systems, and we have used these data to determine the detailed atomic structure of one of them. Specifically, we have examined both the pseudomorphic (1x1) Fe monolayer on W(110) [13] and the non-pseudomorphic (7x14) Gd monolayer on W(110) [14]. These data have been compared to those obtained for the clean W(110) surface in a separate study by Ynzunza et al. [15] and to multiple scattering calculations to permit structural conclusions.

3.II Experimental

The PD measurements were performed with the advanced photoelectron spectrometer/diffractometer [7] situated on bend magnet beamline 9.3.2 of the Advanced Light Source (ALS) at the Lawrence Berkeley National Laboratory [16]. This system

couples a high-resolution/high-luminosity Scienta SES-200 analyzer to a high-resolution spherical grating monochromator, and it is thus possible to acquire individual photoelectron W $4f_{7/2}$ spectra with both excellent statistics (~40,000 peak counts) and resolution (≤80 meV) in the short data acquisition times (~40 s/spectrum) required for large-scale PD measurements. The overlayers were formed by evaporating either Fe or Gd from water-cooled electron bombardment Knudsen cells at a rate of ~0.2 ML/min and a pressure of 1-2 x 10^{-10} torr onto W(110) substrates at near 300 K. The substrate was cleaned by oxygen reduction at 1300° C in 5x10^{-7} Torr of O_2, followed by flashing at ~2000° C. Deposition rates were determined with a quartz crystal thickness monitor, while sample cleanliness and overlayer coverages were determined by quantitative photoelectron spectroscopy. A slight excess of metal of 1.2 ML was deposited to insure a maximum degree of order in the Fe and Gd overlayers. After deposition, the samples were annealed to 700-750 K for 5 minutes to form the ordered Fe or Gd overlayers which were then checked with LEED. The (1x1) Fe/W(110) surface showed a sharp (1x1) LEED pattern indicative of a single monolayer of ordered Fe and in good agreement with previous results (Fig. 3.1, [17]), while the (7x14) Gd/W(110) surface showed a sharp spot pattern characteristic of both the (1x1) W and Gd layers and the (7x14) Gd superstructure (Fig. 2.2 and [14]). For all of the PD measurements discussed here, the angle between the light beam and the photoelectron analyzer was held constant at 70°, and the photon energy was kept at 71 eV. The samples were then rotated with a two-axis goniometer [5,6] so as to vary the photoelectron takeoff angle θ (here measured with respect to the sample surface) and the azimuthal angle ϕ (measured with respect to the W **[$\bar{1}$10]** direction in the sample plane) in order to perform scanned-angle PD measurements. Intensities were measured over essentially the full solid angle above the surface, with constant steps in θ of 3° and the step in ϕ varying with θ according to the equation: $\Delta\phi = [\Delta\phi_i \sin(\theta/2)]/\sin(\theta_i/2)$, with $\Delta\phi_i = 3°$ at $\theta_i = 12°$, in order to maintain nearly constant steps in solid angle over the full θ range of 12° to 90°. Due to the symmetry of the

surface, ϕ was only scanned over 180^{o}, but our final data presentations have been enlarged to the full 360^{o} by symmetric mapping.

3.III Results

W $4f_{7/2}$ photoelectron spectra for the clean W(110) surface, the (1x1) Fe-covered surface, and the (7x14) Gd-covered surface are shown in Figs. 3.2(a), (b), and (c), respectively. All of these spectra were obtained with $\theta = 45°$ and with ϕ pointing along the W [001] direction in the sample plane (i.e., $\phi = 90^{o}$). The spectra were resolved into components by fitting them with asymmetric Voigt functions of fixed width and spacing riding on a Shirley background. The resulting binding energies for these spectra are referenced to the Fermi level, as directly measured for each system. For each of the three spectra, there exist two prominent peaks, one at higher E_b corresponding to emission from the bulk W atoms (or 2nd layer W atoms for the (1x1) Fe covered surface) and a second at lower E_b due to emission solely from the top layer of W atoms (which can be at the free surface or at the metal-metal interface). In the case of the Fe or Gd covered surface, the PD effects associated with this lower E_b feature thus allow us to probe directly the local environment of the W atoms at the interface. The clean W(110) surface shift is measured to be -320 meV, while the ICLS's for the (1x1) Fe covered surface are -235 meV and -90 meV for the interface and 2nd layer, in good agreement with previous measurements by Shinn et al. [13]. The W $4f_{7/2}$ ICLS for the Gd covered surface is -390 meV, a noteworthy result because this is the largest shift yet observed for surface or interface atoms on W(110), and it is significantly greater than the clean surface shift of -320 meV.

These very different ICLS's for Fe and Gd may be qualitatively understood by considering the very different structures of the overlayers. The (7x14) Gd overlayer is much different structurally from the pseudomorphic (1x1) overlayers of Fe, Pt, and Ni. In

the case of Gd [14], a prior STM and LEED study has shown that the overlayer has a hexagonal arrangement of atoms essentially following the bulk structure of Gd with the [0001] direction normal to the film. This hexagonal structure is expanded relative to bulk Gd by 1.2% along W [001] and contracted by 0.6% along W **[$\bar{1}$10]** in order to form a 7x14 Moiré pattern or coincidence lattice with the W(110) substrate. This arrangement forces the Gd atoms into 24 different adsorption sites, leaving the underlying W atoms still largely under-coordinated, with 32 inequivalent emitter sites. Thus, as averaged over the various W emitters of either interface or second-layer type, the Gd appears to be a "disordered", rather weakly bound, overlayer. This Gd overlayer should in turn afford greater core-hole screening for the first layer of W atoms at the interface, thus lowering the 4f binding energy relative to that of the W atoms at the clean surface, as seen in experiment. The (1x1) overlayers by contrast leave the W atoms at the interface fully coordinated. Thus one would expect qualitatively that the ICLS of the (1x1) overlayers would be much smaller (i.e. closer to the bulk) than that of the clean surface or Gd covered surface, as is also the case.

The above interface core-level shifts were then used to measure interface-specific PD effects. At the kinetic energies of the outgoing photoelectrons for these measurements ($E_k \cong 40$ eV) there should be a significant degree of back-scattering occurring as well as forward scattering [9]. Therefore, the PD patterns from the W interface atoms should contain information not only about the overlayer structure, but also about the structure of the second layer of W atoms beneath the interface. Fig. 3.3 shows such PD results over essentially the full 2π solid angle above the sample for the (1x1) Fe covered W(110) surface, with Fig. 3.3(a) being the diffraction pattern from the interface W $4f_{7/2}$ peak and Fig. 3.3(c) being that from the 2nd layer W $4f_{7/2}$ peak. The 2nd-layer data differ greatly from the interface results, as expected in view of the very different environments of the atoms involved. In fact, the 2nd-layer data are more similar to those from the bulk atoms

of clean W(110) [7,15], a result again consistent with these interface atoms being fully coordinated by nearest-neighbors that are all W atoms.

In order to quantitatively determine the structure for the Fe overlayer and the interlayer spacing between the overlayer and the first W layer (Z_{12}) and between the first and the second W layers (Z_{23}), we have performed full multiple scattering calculations for various geometries utilizing the Rehr-Albers formalism as implemented by Kaduwela et al. [18], and compared these results with the experimental data of Fig. 3.3(a) using R-factors developed specifically for PD [19]. Three high-symmetry adsorption sites for the Fe atoms in the overlayer on the W(110) surface are consistent with the two-fold symmetry observed in the PD data: a bridge site (A in Fig. 3.4), a two-fold degenerate hollow site (C), and an atop site (B). For example, oxygen has been found to adsorb at the hollow site C in a recent XPD study of (1x1) O/W(110) by Daimon et. al [20]. However, for Fe/W, the best fit to the data was achieved using the bridge site A, a site which also continues the in-plane bulk periodicity of the W(110) lattice. We performed the R-factor analysis for the bridge site by varying first Z_{12} and second Z_{23}. This is a reasonable procedure since we expect any expansion/contraction between the 1st and 2nd layer to be greater than that between the 2nd and 3rd. Via this procedure, we arrive at the best fit for $Z_{12} = 2.07 \pm .05$ Å and $Z_{23} = 2.28 \pm .05$ Å. These five R-factors have been normalized to the same minimum magnitude and summed to get the R_{av} values plotted in Fig. 3.5. The Fe layer is thus found to be slightly contracted from the hard sphere separation of 2.165 Å calculated for the bridge site on W(110) by 0.10 Å, while the first layer of W has expanded from the bulk interlayer W separation of 2.23 Å by 0.05 Å. The full 2π PD pattern generated from these best fit values is shown in Fig. 3.3(b). Although the latter expansion is at our estimated error limit, the sign of it is qualitatively consistent with a second layer whose strong bonding to Fe has moved its position and its binding energy away from that of the W atoms below.

PD from the non-pseudomorphic (7x14) Gd/W(110) interface differs significantly from that observed for the (1x1) Fe/W(110) interface. Shown in Figs. 3.6(a),(c) and (d) are single azimuthal PD scans from the W $4f_{7/2}$ surface or interface peak for the clean [15], Gd covered, and Fe covered W(110) surface taken at $\theta = 45°$, respectively. Figs. 3.6(f), (g), and (h) show analogous azimuthal scans from the bulk peak for clean and Gd-covered surfaces and the second-layer peak for an Fe-covered surface, respectively. Also included are Figs. 3.6(b) & (e) which contain matching azimuthal PD scans obtained from multiple scattering calculations for the clean surface [15] and the (1x1) Fe bridge site discussed previously. It is evident that the interface and bulk diffraction from the Gd/W interface changes very little from the PD of the clean surface. This is reasonable due to the large number of adsorption sites in which the Gd atoms sit on the W(110) surface. Hence, there are a large number of scattering geometries for interface or bulk W photoelectrons passing through the Gd overlayer. The (7x14) Gd acts then mostly as an attenuating (and hole screening, as noted before) layer, unlike the (1x1) Fe overlayer, which induces large changes in the interface and bulk diffraction as compared to the clean W(110) surface.

3.IV Conclusions

We have utilized W $4f_{7/2}$ core-level shifts to perform interface-specific PD on two very different metal-metal systems: W(110) surfaces covered by (1x1) Fe and (7x14) Gd monolayers. The full 2π PD data obtained for the (1x1) Fe/W(110) interface, coupled with full multiple scattering calculations, has allowed us to determine both the geometry at the interface (bridge site), as well as the interlayer spacings Z_{12} and Z_{23}. Because of the multiplicity of W-Gd bonding sites, the PD from the (7x14) Gd/W(110) interface was shown to be quite similar to that of the clean W(110) surface, and thus very different from the (1x1) Fe case. The large -390 meV ICLS for the Gd covered surface suggests greater

core-hole screening by this overlayer as compared to emission from the clean and Fe-covered surfaces. Although we have here studied only the simplest case of interfaces under a single monolayer, it should nonetheless be possible to use such interface-specific PD for studying more deeply buried metal-metal interfaces, with the only requirements being that the system studied has a narrow enough core level, that it exhibits a large enough ICLS to be resolved, and that the combination of interface depth, (tunable) photoelectron energy, and photon flux are such that a reasonable count rate is obtainable from an emitting species at the interface.

The author would like to thank Dr. A. P. Kaduwela, Calif. State Air Res. Board and Dr. Yufeng Cheng, LBNL and Penn. State Univ., for the use of their multiple scattering codes in our calculations, and Michel Van Hove for helpful suggestions concerning the theoretical analysis. Support for these studies was provided by the Director, Office of Energy Research, Materials Sciences Div., of the U.S. Dept. of Energy, under Contract No. DE-AC03-76SF00098, the Office of Naval Research under contract (N00014-94-0162), and the National Energy Research Supercomputing Cntr. at LBNL.

References:

1. R. Feidenhans'l, Surf. Sci. Rep. 10, 105 (1989).

2. M. Takahasi, S. Nakatani, T. Takahashi, X. Zhang, M. Ando, S. Fukatsu, and Y. Shiraki, Jpn. J. Appl. Phys. 34, 2278 (1995).

3. A. Bourret, P. Fuoss, and S. Tatarenko, Phys. Rev. Lett. 70, 311 (1993).

4. J. B. Pendry, Surf. Sci. Rep. 19, 87 (1993).

5. C. S. Fadley, in "Synchrotron Radiation Research: Advances in Surface and Interface Science", *Vol. 1: Techniques*, ed. by R. Z. Bachrach, (Plenum Press, New York, 1992), p. 421.

6. C. S. Fadley, S. Thevuthasan, A. P. Kaduwela, C. Westphal, Y. J. Kim, R. Ynzunza, P. Len, E. D. Tober, F. Zhang, Z. Wang, S. Ruebush, A. Budge, and M. A. Van Hove, J. Elec. Spec. & Relat. Phen. 68, 19 (1994).

7. C.S. Fadley, M.A. Van Hove, Z. Hussain, and A.P. Kaduwela, J. Electron Spectrosc. 75, 273 (1995).

8. J. Denlinger, E. Rotenberg, U. Hessinger, M. Leskovar, and M. Olmstead, Appl. Phys. Lett. 62, 2057 (1993).

9. S. A. Chambers and V. A. Loebs, Appl. Phys. Lett. 60, 38 (1992).

10. E. Maillard-Schaller, O. M. Kuettel, and L. Schlapbach, Phys. Stat. Sol. A 153, 415 (1996).

11. O. M. Kuettel, E. Schaller, J. Osterwalder, and L. Schlapbach, Diam. & Rel. Mat. 4, 612 (1995).

12. T. M. Duc, Phys. Rev. Lett. 43, 789 (1979).

13. N. D. Shinn, B. Kim, A. B. Andrews, J. L. Erskine, K. J. Kim, and T.-H. Kang, Mat. Res. Soc. Symp. Proc. 307, 167 (1993).

14. E. D. Tober, R. X. Ynzunza, C. Westphal, and C. S. Fadley, Phys. Rev. B 53, 5444 (1996) and to be published.

15. R. X. Ynzunza, E.D. Tober, F.J. Palomares, Z. Wang, H. Daimon, Z. Hussain, and C.S. Fadley, in preparation.

16. Z. Hussain, W. R. A. Huff, S. A. Keller, E. J. Moller, P. A. Heimann, W. McKinney, H. A. Padmore, C. S. Fadley, and D. A. Shirley, J. Elec. Spec. and Rel. Phen. 80, 401 (1996).

17. P. J. Berlowitz, J.- W. He, and D. W. Goodman, Surf. Sci. 231, 315 (1990).

18. J.J. Rehr and R.C. Albers, Phys. Rev. B41, 81139 (1990); A. P. Kaduwela, D. J. Friedman, and C. S. Fadley, J. Elec. Spec. & Rel. Phen. 57, 223 (1991).

19. R. S. Saiki, A. P. Kaduwela, M. Sagurton, J. Osterwalder, D. J. Friedman, C. S. Fadley, and C. R. Brundle, Surf. Sci. 282, 33 (1993).

20. H. Daimon, J. Palomares, R. X. Ynzunza, and C. S. Fadley, in preparation.

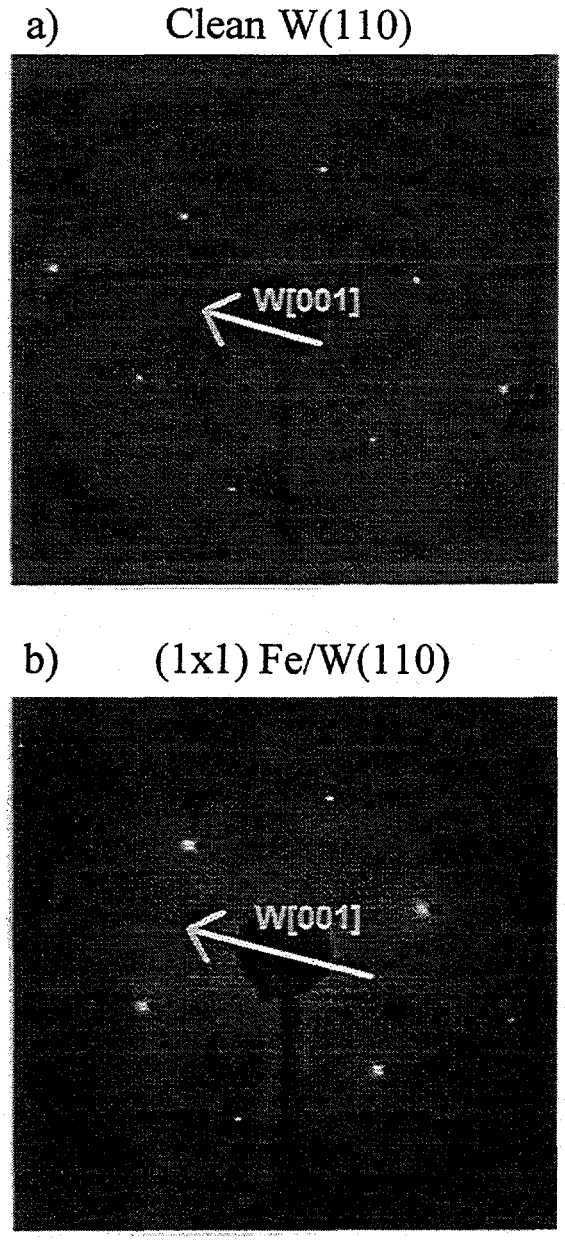

Figure 3.1. LEED patterns taken with a beam energy of 108 eV for (a) the clean W(110) surface and (b) the (1x1) Fe/W(110) surface.

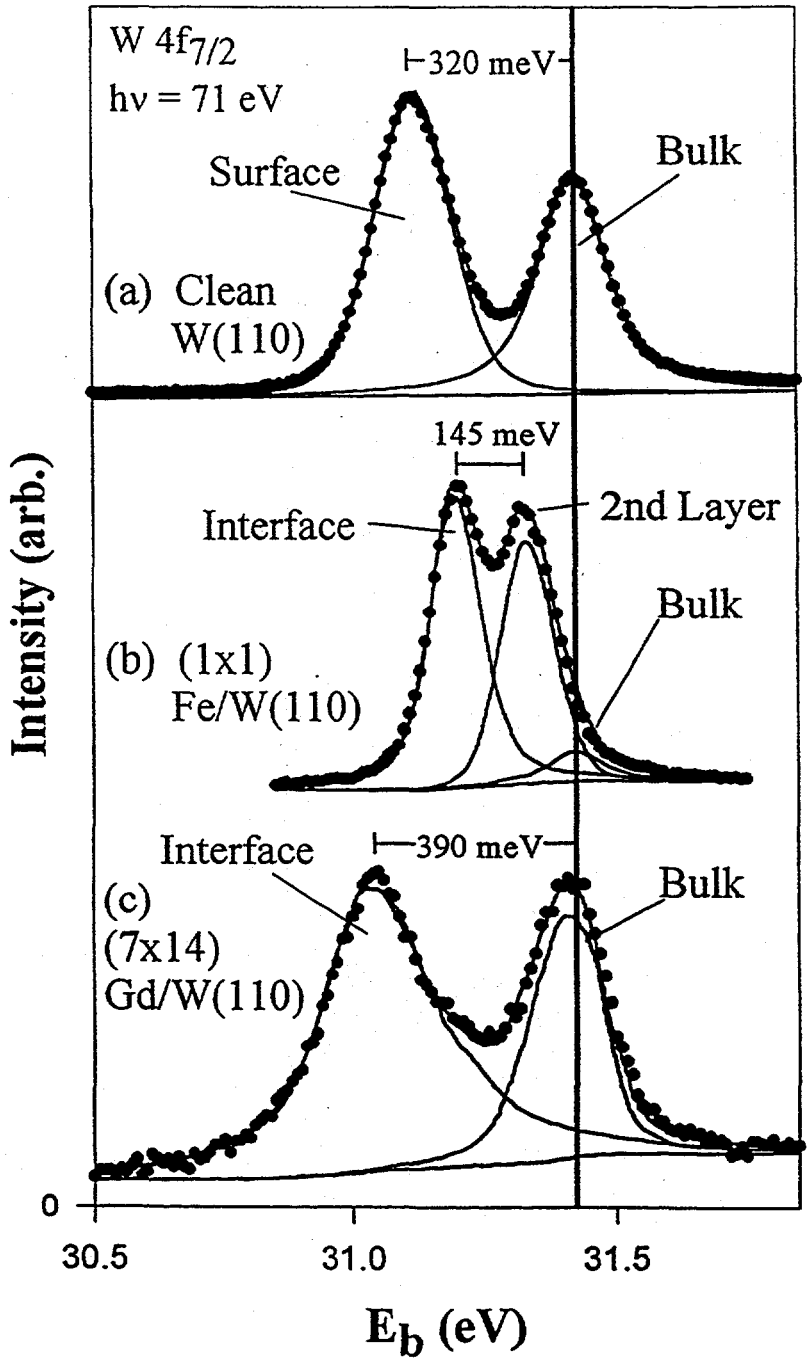

Figure 3.2. W $4f_{7/2}$ photoelectron spectra taken with $h\nu = 71$ eV, $\theta = 45°$, and ϕ along the W [001] azimuth from (a) the clean W(110) surface, (b) 1.2 ML of Fe in a(1x1) overlayer on W(110), and (c) 1.2 ML of Gd in a (7x14) Moiré structure on W(110).

Figure 3.3. Full-solid-angle W $4f_{7/2}$ photoelectron diffraction patterns for the (1x1) Fe/W(110) system taken from (a) the -235 meV shifted W interface peak, (b) theoretical multiple scattering calculations for the (1x1) Fe/W(110) interface with an optimized bridge adsorption site for the Fe, and (c) the -90 meV shifted W 2nd layer peak. The photoelectron kinetic energy outside the surface was $E_k = 40$ eV in all cases.

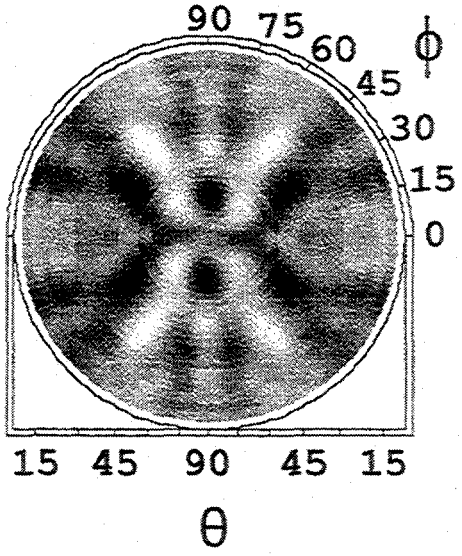

(a)

W $4f_{7/2}$ PD

(1x1) Fe/W(110)
Interface

(Experiment)

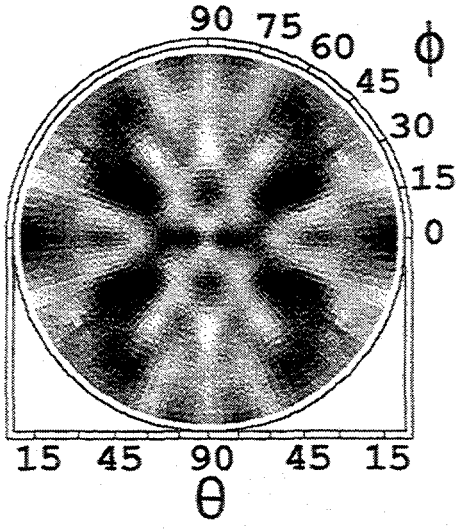

(b)

W $4f_{7/2}$ PD

(1x1) Fe/W(110)
Interface

(Theory)

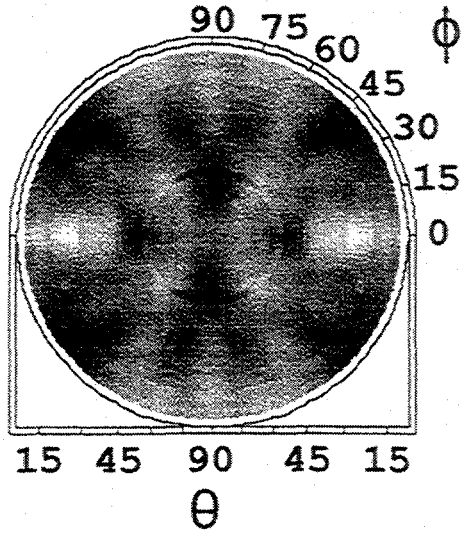

(c)

W $4f_{7/2}$ PD

(1x1) Fe/W(110)
2nd Layer

(Experiment)

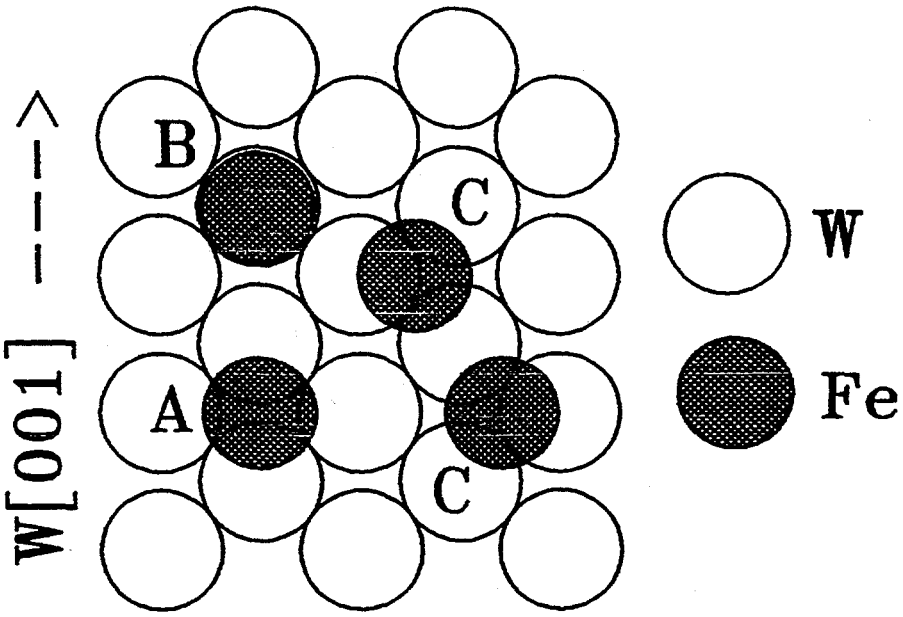

Figure 3.4. Three possible Fe adsorption sites for the (1x1) pseudomorphic overlayer, as used in the calculations: (A) bridge, (B) atop, and (C) two-fold degenerate hollow.

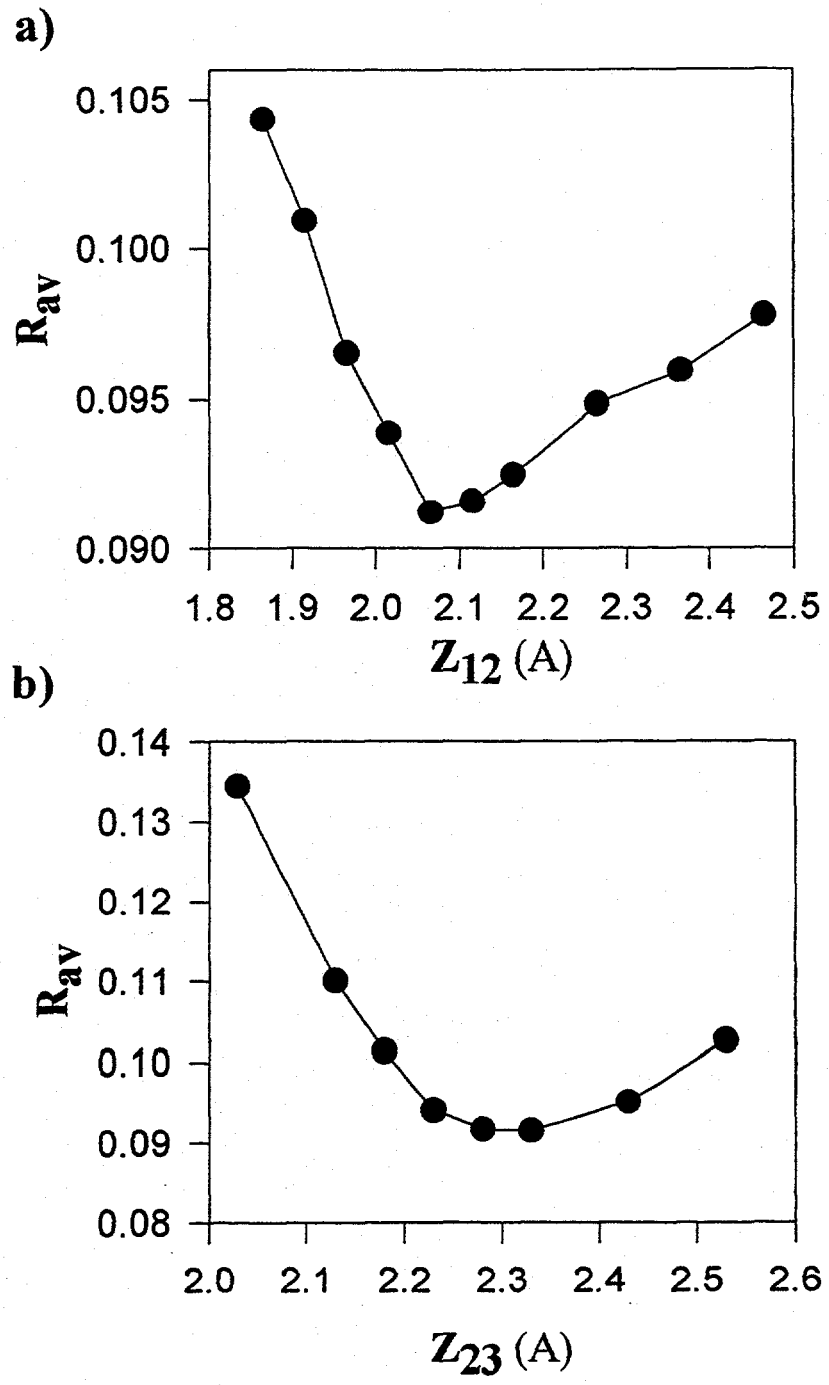

Figure 3.5. Averages over five R-factors from Ref. 19 as a function of (a) Fe and 1st layer W interlayer separation Z_{12} and (b) 1st and 2nd layer W interlayer separation Z_{23}.

Figure 3.6. Single W $4f_{7/2}$ azimuthal scans taken with $h\nu$ = 71 eV, and θ = 45° from (a) experiment for the -320 meV shifted clean-surface peak (Clean, E) , (b) theory for the clean surface peak in (a) (Clean, T, from ref. 15), (c) experiment for the -390 meV shifted interface peak of (7x14) Gd/W(110) (Gd, E), (d) experiment for the -225 meV shifted interface peak of (1x1) Fe/W(110) (Fe, E), (e) theory for the Fe/W case in (d), with Fe at the bridge site (Fe, T), (f) experiment for the clean W(110) bulk peak, (g) experiment for the bulk peak of (7x14) Gd/W(110) and (h) experiment for the 2nd layer peak of (1x1) Fe/W(110).

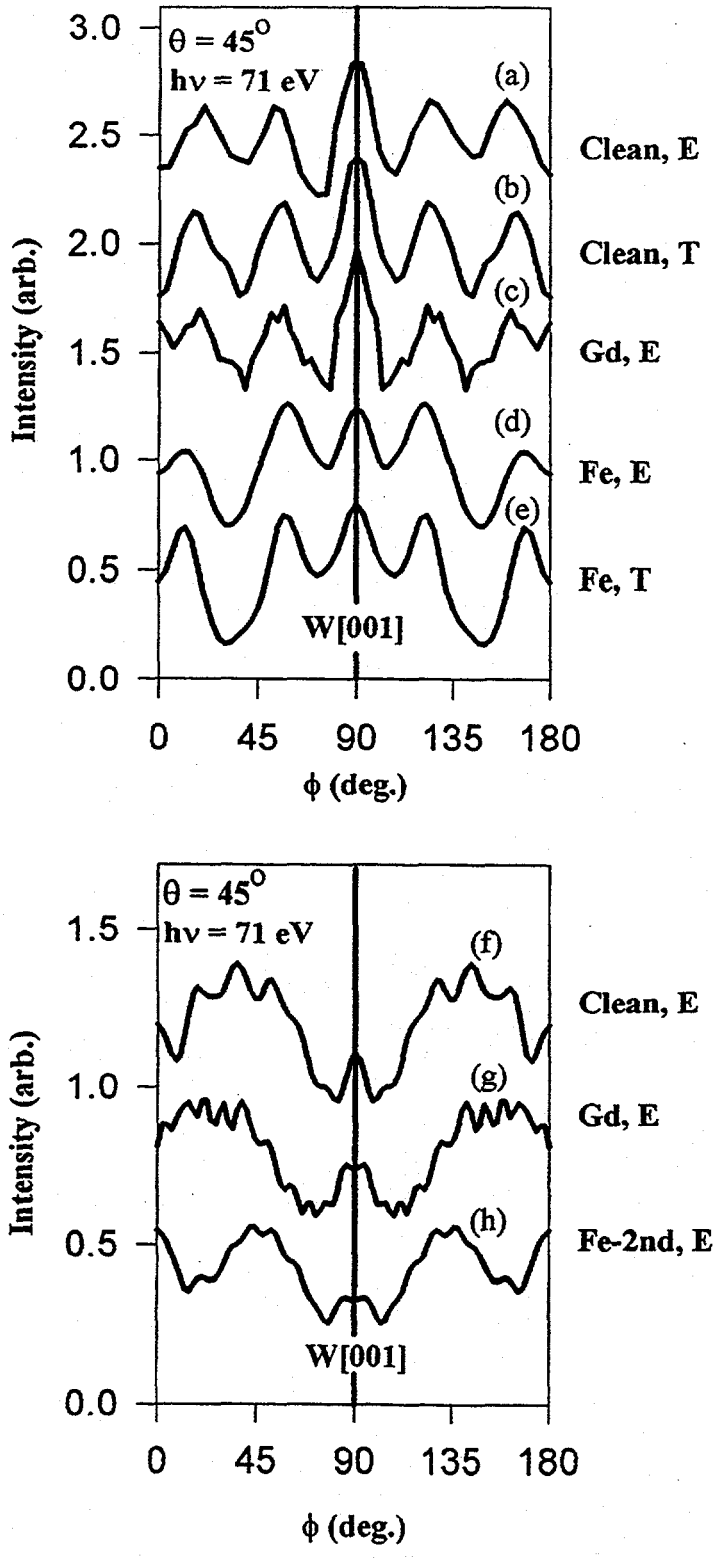
θ = 45°
hν = 71 eV
(a)
(b)
(c)
(d)
(e)
Clean, E
Clean, T
Gd, E
Fe, E
Fe, T
W[001]
Intensity (arb.)
3.0
2.5
2.0
1.5
1.0
0.5
0.0
0
45
90
135
180
ϕ (deg.)
θ = 45°
hν = 71 eV
(f)
(g)
(h)
Clean, E
Gd, E
Fe-2nd, E
W[001]
Intensity (arb.)
1.5
1.0
0.5
0.0
0
45
90
135
180
ϕ (deg.)

Chapter 4.

Bulk and Surface Ferromagnetic-to-Paramagnetic Transitions of Gd(0001) as Studied by Spin Polarized Photoelectron Diffraction

4.I Introduction

The rare-earth metal Gd has been found to display many unusual magnetic properties that are not commonly found in the other 'simple' ferromagnets such as Fe, Co and Ni. For bulk Gd, the easy axis of magnetization is found to lie along the [0001] direction (c axis) in the temperature range from 240 K to the bulk Curie temperature T_{cb} of 293 K [1]. As the temperature is decreased from 240 K down to 170 K, the easy axis tilts away from [0001], finally reaching a point at which the angle between the easy and c axes is 65°. Below 170 K, the easy axis once again moves towards the [0001] direction. More interesting effects also arise when one considers thin films of Gd for which surface phenomena become important. Typically, in order to obtain clean Gd films and surfaces for study, one evaporates Gd in ultrahigh vacuum (UHV) conditions onto a substrate such as a clean W(110) crystal, in which case the Gd grows with the [0001] or c axis normal to the surface and parallel to W [110] [2-5]. For films of thickness $t < 35$ nm, the easy axis is now found to lie in plane due to the demagnetizing field from the thin film overcoming the uniaxial anisotropy along the c axis [6-9]. Films with $t > 35$ nm, however, have been found to display either a canted magnetization or a mixture of in-plane and perpendicular magnetization [8-10], with an out-of-plane component arising from a temperature dependent reorientation transition occurring for these thicker films. Another interesting aspect of Gd is that it is thought to exhibit a surface Curie temperature T_{cs} that is higher than that of the bulk. Utilizing electron capture spectroscopy, Rau et al. first observed an increased T_{cs} in polycrystalline Gd [11] and later on saw a similar effect in a second rare-earth ferromagnet Tb(0001) [12], with the shifts relative to the bulk transition temperature

being roughly 15 K and 30 K, respectively. Later spin polarized low energy diffraction (SPLEED) and magnetooptical Kerr effect (MOKE) studies by Weller et al [13] and spin polarized secondary electron spectroscopy (SPSEES) and spin polarized photoelectron spectroscopy (SPPES) studies by Tang et al. [10] on well ordered 40 nm Gd(0001) films grown on W(110) have also observed the increased T_{cs} with shifts of up to 60 K in the surface transition temperature above that of the bulk being reported. Furthermore, surface contamination is found to completely eliminate the different T_{cs} [13], thus showing that this is indeed a surface effect. In this work we will apply the method of spin polarized photoelectron diffraction (SPPD) to this system in order to further elucidate the nature of the surface and bulk magnetic transitions that are present.

Normal photoelectron spectroscopy (PES) and SPPES, have been used previously to investigate the magnetic characteristics at and near the surface of Gd, but spin polarized photoelectron diffraction has not. For example, Mulhollan et al. [14] used SPPES to study the Gd 4f core level and valence bands and were able to unambiguously show the ferromagnetic alignment of the Gd surface with the bulk. However, the SPSEES work of Tang et al. [10] and subsequent SPPES studies by Li et al. on the Gd surface state and 4f excitation [15] also show that the ferromagnetic alignment between the bulk and surface is not perfect; that is, there exists a small out-of-plane component of the surface magnetization. The bulk 5d bands of Gd have shown some unusual properties as well. PES and SPPES on these bands [16,17] reveal a strong temperature dependence in the exchange splitting of the majority and minority spin states which goes to zero at the bulk transition temperature. Inverse photoemission (IPE) into the unoccupied 5d bands [18], however, exhibits an exchange splitting which persists 55 to 100 K beyond the bulk Curie temperature, indicating that the IPE spectra more strongly reflect the surface electronic structure and, consequently, the enhanced surface magnetic order. Finally, recent magnetic circular dichroism studies (MCD) on the rare earths [19] have shown a large

degree of dichroism in the Gd 4d and 4f core excitations, as well as a nearly parallel alignment for the bulk and surface magnetizations .

When attempting to measure the magnetic properties of various systems through the use of spin polarized electron diffraction and spectroscopy techniques such as SPPES, SPSEES, and SPLEED, one faces several significant experimental difficulties. Such measurements require either a spin polarization detector for the outgoing electrons (in SPPES or SPSEES) or a source of spin polarized electrons (in SPLEED), with all of the accompanying challenges and increases in data acquisition time that these entail. Also, all of these techniques necessitate having a homogeneously magnetized sample with a well defined magnetization direction, since the spin quantization axis is referred to the laboratory frame via the detector or the electron source. The technique of spin polarized photoelectron diffraction using atomic multiplets [20-24] which we have employed in this study, however, removes several of these complications. Basically, SPPD exploits the inherently spin-polarized nature of photoelectrons emitted from core-level multiplets. Because these multiplets result from the coupling of the core hole with the net magnetic moment on the valence electrons of a given emitter, the polarization is referenced to the emitter moment, rather than to any laboratory-based axis. Hence, this type of measurement does not even require a net magnetization of the sample, but only local magnetic domains of $\geq \sim 100$Å radius due to its short-range probing nature. And, via the core-level studied, SPPD is also chemically specific and state specific, and so can reveal the local magnetic environment surrounding a given type of emitting species A more detailed description of this method will be given in greater detail in Sec. 4.III.

4.II **Experimental**

The spin polarized photoelectron diffraction measurements were carried out on the high-resolution bend magnet beamline 9.3.2 [25] at the Advanced Light Source of the Lawrence Berkeley National Laboratory, utilizing an advanced photoelectron spectrometer/diffractometer including a Scienta ES200 photoelectron analyzer and a two-axis sample goniometer accurate to within ±0.2° and capable of regulating the sample temperature within the range of 200 - 2300 K More details concerning this spectrometer/diffractometer are discussed elsewhere [Chapter 5 or Ref. 26]. The Gd(0001) samples used in this study were approximately 100 monolayers (ML's) or ~30 nm in thickness and were prepared by evaporating Gd from an electron-bombardment-heated W crucible surrounded by a water-cooled stainless steel radiation jacket onto a clean W single crystal oriented to within 0.5° of (110). The substrate was held at room temperature in an ambient pressure of 1-2 x 10^{-10} Torr, with a Gd evaporation rate of 2.0 ML/min. The films were then annealed to 725-750 K for 5 min., resulting in a clean, well ordered film displaying a sharp hexagonal LEED pattern completely free of the superstructure spots which accompany films broken up by island formation. This recipe has been verified in a recent STM study by Tober et al. [4,5] to produce atomically flat Gd films. Photoelectron spectroscopy of the resulting surface using synchrotron radiation, as well as standard Al Kα and Mg Kα radiation, shows these films to be free of contamination from C, O, and N to within 0.03 ML and also to exhibit no detectable signal from the W substrate. Special attention was also paid to possible magnetic contaminants such as Fe, Co, and Ni, which were not present in amounts detectable within the limits of our measurements (≤0.02 ML). Valence band spectra taken with a photon energy of 38 eV and at normal emission also showed an intense, sharp peak near the Fermi edge arising from the Gd(0001) surface state [14,17,27,28] before and after each experimental cycle; examples of these as well as coverage determinations are contained in

Chapt. 5. The temperature was determined through the use of a chromel-alumel thermocouple placed at the junction between a liquid nitrogen cooled Cu braid and the sample; this thermocouple was calibrated initially by means of a second thermocouple placed directly on the sample surface. The overall accuracy of the measured temperature is estimated to be ±7 K, with the principal source of error being thermal drift during the acquisition time for a given spectrum (5 min.). For the SPPD measurements, the temperature was stepped sequentially from the minimum of 220 K to 512 K, in steps of 6 to 10 K with a Gd 5s or 4s spectrum being acquired at each step. Runs were also performed by stepping the temperature down from 512 to 220 K to ensure that there was no hysteresis present in the observed SPPD effects with temperature (as might arise from irreversible structural or surface compositional changes and not magnetic ordering). The low index directions of the Gd(0001) film were determined to within ±1° through azimuthal photoelectron diffraction (PD) measurements on the Mg Kα-excited Gd 4d peak taken at an emission angle of $\theta = 54°$ from the surface which passes through low-index directions of the $< 10\bar{1}2 >$ type.

4.III. **Theory of Spin Polarized Photoelectron Diffraction**

The technique of SPPD was first pioneered by Sinkovic et al. [20,21,24] as a means for examining short range magnetic order transitions, and such effects were first demonstrated in the ionic antiferromagnet $KMnF_3$. Later studies by Hermsmeier et al. [22,23] observed similar effects in MnO(001), another ionic antiferromagnet. The theory of SPPD, specifically as applied to $KMnF_3$, has also been discussed in detail elsewhere [24]. As previously noted, this form of SPPD exploits the spin-polarized nature of photoelectrons arising from multiplets, with the spin of the outgoing electron being measured with respect to the emitting atom or ion. Fig. 4.1 shows photoelectron spectra from two such multiplets (the 4s and the 5s) measured for our Gd(0001) sample at several temperatures

between 220 K and 400K. Each spectrum consists of a doublet containing the ^7S and ^9S final states possible when emitting a spin-up or spin-down s electron into a dipole allowed p photoelectron state. The emission is thus from a 5s or 4s core level within the $4f^7$ ^8S ground state of Gd. In this description of the Gd initial and final states, the three unpaired electrons in the $[5d6s6p]^3$ valence band states are ignored due to their highly delocalized nature and thus much reduced interaction strength with the 5s or 4s orbitals. This treatment in terms of 4f interaction only has also been shown to be correct in previous MCD photoemission studies performed on Gd 4d excitation [29] in which the analogous ^7D and ^9D character of the final states has been confirmed. For the present case, the overall 5s emission process is shown below, with the 4s following the same general form:

$$\Psi(^8S:\ 5s^2 4f^7) + h\nu \rightarrow \Psi(^8P:\ 5s^1 4f^7 + \text{photoelectron}, E_k\ p)\,, \qquad [1]$$

with the kinetic energy of the $\ell = 1 = p$ photoelectron being E_k, and the overall dipole transition being from an ^8S to an ^8P state, since the dipole operator cannot affect spin within an L-S coupling description. Due to the coupling between the outgoing photoelectron ($|E_k\ p:\ s = 1/2,\ \ell = 1\rangle$) and the core-hole final states ($|^7S:\ S = 3, L = 0\rangle$ and $|^9S:\ S = 4, L = 0\rangle$) needed to achieve the overall final states ($|^8P:\ S = 7/2, L = 1\rangle$), the photoelectrons associated with these doublets are highly spin polarized in nature. The exact degree of polarization can be determined by calculating the necessary Clebsch-Gordan coefficients for the two possible final state configurations [24]:

$$|^8P_1: S = 7/2, M_S = 7/2, L = 1, M_L = 0, \pm 1\rangle = \qquad [2]$$

$$(8/9)^{1/2}\ |^9S:\ S = 4, M_S = 4, L = 0, M_L = 0\rangle$$

$$\bullet\ |E_k\ p\downarrow:\ s = 1/2, m_s = -1/2, \ell = 1, m_\ell = 0, \pm 1\rangle$$

$$-\ (1/9)^{1/2}\ |^9S:\ S = 4, M_S = 3, L = 0, M_L = 0\rangle$$

$$\bullet\ |E_k\ p\uparrow:\ s = 1/2, m_s = +1/2, \ell = 1, m_\ell = 0, \pm 1\rangle$$

and

$$|^8P_2: S = 7/2, M_S = 7/2, L = 1, M_L = 0,\pm1> = \quad [3]$$

$$|^7S: S = 4, M_S = 3, L = 0, M_L = 0>$$

- $|E_k\, p\uparrow: s = 1/2, m_s = +1/2, \ell = 1, m_\ell = 0, \pm1>$

where the initial state spin is assumed for illustration to lie maximally along the z axis. The spin polarization of the photoelectrons is now defined in the usual way as: $P(\%) = 100[I_\uparrow - I_\downarrow]/[I_\uparrow + I_\downarrow]$. Hence, the polarization of the ^7S photoelectrons is +100%; i.e., the photoelectrons are all emitted with spin parallel to the net spin of the emitting atom, or anti-parallel to this atom's magnetic moment. The ^9S photoelectron spin polarization is given by [(probability of spin up) - (probability of spin down)] = 1/9 - 8/9 = -7/9 or -77.8%: i.e., the photoelectrons are primarily emitted with spin anti-parallel to the emitting atom's net spin, or parallel to its magnetic moment. In our subsequent analyses, we will assume that both of these peaks are totally spin polarized, so that our theoretical predictions may inherently overestimate the experimental SPPD effects, but not by more than ~10-20% of the total effect predicted.

We now have independent sources of spin-up and spin-down photoelectrons, as referenced with respect to the moment of the emitting atom. In a magnetically-ordered sample, such as our Gd(0001) films, the emitted photoelectrons will scatter from neighboring atoms as they leave the crystal, giving rise to the characteristic angular dependent variations in intensity $I(\theta,\phi)$ that are known in standard photoelectron diffraction [24,30]. These variations are in turn due to the interference between the direct (or unscattered) component Φ^0 and scattered components Φ_j of the outgoing

photoelectron waves. In the simplified case of single scattering, the relationship between the intensity and the outgoing wave components is:

$$I(\theta,\phi) \propto \left|\Phi^{0} + \sum_{j} \Phi_{j}\right|^{2} \qquad [4]$$

where θ is the polar angle of emission (measured from the sample surface) and ϕ is the azimuthal angle of emission (measured about the sample normal), and the sum is over all scatterers j. The primary and scattered waves can also be given for s emission and in a simple spherical-wave scattering model by:

$$\Phi^{0} = \hat{\varepsilon} \cdot \hat{k} \exp(-L/2\Lambda_{e}) \qquad [5]$$

and

$$\Phi_{j} = \frac{\hat{\varepsilon} \cdot \hat{r}_{j}}{r_{j}} \left| f_{j}(\theta_{j}, r_{j}) \right| W_{j}(\theta_{j}) \exp(-L/2\Lambda_{e}) \exp\left\{ i\left[kr_{j}(1-\cos(\theta_{j})) + \psi_{j}(\theta_{j}) \right] \right\} \qquad [6]$$

where $\hat{k}$ is the unit vector in the direction of photoelectron emission, $\hat{\varepsilon}$ is the polarization direction of the incident radiation, $\hat{r}_{j}$ is a unit vector pointing from the emitter to the scatterer j, L and L_{j} are the path lengths for inelastic scattering, Λ_{e} is the inelastic attenuation length, θ_{j} is the scattering angle for the jth atom, k is the magnitude of the photoelectron wave vector, r_{j} is the distance from the emitter to the jth scatterer, $f_{j}(\theta_{j},r_{j})$ is the spherical-wave scattering factor including the scattering phase shift of $\psi_{j}(\theta_{j},r_{j})$, and $W_{j}(\theta_{j})$ is the Debye-Waller factor for the jth scatterer.. The spherical wave scattering factor can be approximated by:

$$f(\theta_j, r_j) = \frac{1}{k} \sum_{\ell=1}^{\ell_{max}} (2\ell + 1) C_\ell(r_j) e^{i\delta_\ell} \sin(\delta_\ell) P_\ell(\cos\theta_j) \qquad [7]$$

where δ_ℓ is the ℓ^{th} partial-wave phase shift and $C_\ell(r_j)$ is the spherical wave correction factor to the ℓ^{th} element of the plane-wave scattering factor term, as derived by Rehr et al. [31]. The partial-wave phase shifts are, of course, determined by the coulomb and exchange potentials of the scattering atom in the solid. In a ferromagnetically ordered crystal, neighboring atoms will have moments aligned parallel to the emitting atom. If the emitted electrons are spin polarized with respect to the emitter's moment, a spin-up (spin-down) photoelectron will see a parallel (anti-parallel) aligned net spin on the scatterers. The emitted spin-up electron will then experience a different exchange interaction as compared to the spin-down electron and will scatter slightly differently. In particular, when the spin of the photoelectron is parallel to that of the scatterer, there will be an additional attractive 4f contribution to the exchange potential, and the scattering will be slightly stronger. In a paramagnetic solid, the magnetic order is absent and the spin-up and spin-down photoelectrons will experience the same average exchange interaction. Hence, the photoelectron intensity at a given set of angles θ and ϕ should vary according to the level of magnetic order present in the system. It is important to note that the photoelectron kinetic energy E_k must be kept relatively low ($\leq$100 eV) for these measurements, because at higher energies the variations due to exchange scattering become progressively less significant [22,23].

To model the SPPD effects, we have employed a local density approximation (LDA) to determine the coulomb and exchange portions of the muffin-tin potential for scattering in order to calculate the various δ_ℓ's via a standard methodology [21,24]. The variation in exchange scattering between the spin-up and spin-down electrons is dominated by the half

filled 4f shell in Gd (e.g., ~92% of the atom's 7.63 μ_B magnetic moment arises from the 4f electrons [32]). The 4f contribution to the total exchange potential is then included (absent) if the photoelectron is spin-up (spin-down) with respect the net spin of the spin-up scatterer. For our LDA calculations, this is handled by including the 4f charge density $\rho_{4f}(\mathbf{r})$ when determining the total exchange charge density $\rho(\mathbf{r})$ for a spin-up electron and excluding it for a spin-down. This gives rise to two different exchange potentials $\mathbf{V}_{\uparrow}^{ex}$ and $\mathbf{V}_{\downarrow}^{ex}$ in Gd for the parallel and anti-parallel aligned photoelectrons, respectively. In the case of a paramagnetic atom (i.e. no fixed alignment with respect to the emitter), roughly 1/2 of the $4f^7$ spins will be aligned in a given direction for scattering at any one time (assuming an Ising model for simplicity) , with the accompanying change in $\rho(\mathbf{r})$ giving an exchange potential of $\mathbf{V}_{\mathbf{para}}^{ex}$. We have employed the Slater [33] form for calculating the three LDA exchange potentials of relevance here:

$$\mathbf{V}^{ex}(\mathbf{r}) = -6\left[3\rho(\mathbf{r})/8\pi\right]^{1/3} \qquad [8]$$

Fig. 4.2 displays the three different exchange potentials calculated using Eq. 8 for muffin-tin potentials appropriate to bulk Gd, together with the location of the average radius of the 4f and 5d subshells in Gd. This figure makes the role of the 4f charge density clear, and also shows that we expect only about 20% changes in the exchange potential between the spin-up and spin-down electrons, a number which is comparable to that predicted before for spin-up and spin-down scattering from the Mn^{2+} $3d^5$ ion [20,23,24]. These potentials in turn, produce three different sets of partial phase shifts $\delta_\ell^{\uparrow}$, $\delta_\ell^{\downarrow}$, and δ_ℓ^{para}, three different scattering factors $f_{\uparrow}$, $f_{\downarrow}$, and f_{para}, and three different scattering phase shifts $\psi_{\uparrow}$, $\psi_{\downarrow}$, and ψ_{para} for each photoelectron peak. Fig. 4.3 contains the spherical wave scattering factors calculated using Eq. 7 for a Gd atom 3.58 Å from the emitter (the nearest-neighbor distance in bulk Gd along the $[10\bar{1}2]$ direction) as a function of scattering angle θ_S. Results are shown for the ^7S multiplets of Gd 5s (Fig. 4.3(a)) and Gd

4s (Fig. 4.3(b)) at the external kinetic energies used in our experiment (76.2 eV for the 5s ^{7}S, and 185.2 eV for the Gd 4s ^{7}S). Included in these calculations and our subsequent SPPD calculations is an inner potential value of 9.0 eV which was determined in a LEED study by Quinn et al. [34] on bulk Gd crystals. This inner potential is also quite close to the value one would expect from adding the valence band width of ~5.6 eV [35] to the work function of 3.3 eV [28,36] as determined for Gd(0001) films grown on W(110).) Figs. 4.4(a) and (b) show analogous results for the accompanying total scattering phase shifts ψ. The difference in each of the previously mentioned quantities relative to the paramagnetic case is plotted in Fig. 4.5 to more fully display the effect of the different exchange potentials.

Having successfully determined the partial phase shifts in each case, we can now calculate the expected photoelectron diffraction patterns of the spin polarized peaks in the 5s and 4s multiplets for both the ferromagnetically ordered and fully disordered or paramagnetic cases. This allows us to model the effects of the ferromagnetic-to-paramagnetic transition that we wish to observe through SPPD. To do this, we have employed a full multiple scattering cluster PD calculation utilizing the Rehr-Albers formalism [37]. The cluster consisted of 105 atoms, was cylindrically symmetric, and consisted of five atomic layers with the $[10\bar{1}0]$ "b" axis (as defined in Ref. 38) pointing along $\phi = 0°$ and the $[2\bar{1}\bar{1}0]$ "a" axis pointing along $\phi = 90°$. The overall thickness of the cluster perpendicular to the surface was thus 13.36 Å when including the height from the muffin tin radius extending beyond the atomic centers of the surface layer. Fig. 4.6 shows the basic geometry used in both the calculations and the experiments. The PD intensity in each case is calculated independently for the 4 top layers of the cluster and then summed to simulate the diffraction one would measure from the entire system. Inelastic mean free paths were calculated using methods derived by Tanuma et al. [39], and these yield values of ~4.9 Å for 5s emission and ~6.5 Å for 4s emission. Thus our cluster was roughly 2.1-

2.7 times the attenuation length in thickness, and it should thus represent most of the photoelectron intensity resulting from Gd(0001). Theoretical PD patterns of $I(\theta,\phi)$ for the Gd 5s and 4s ^7S paramagnetic cases are presented in Figs. 4.7(a) and (b), respectively. Assuming a 100% spin polarization for both the ^7S and ^9S peaks (as noted previously, this will lead to a slight overestimation of the SPPD effect as the ^9S is only 77.8% polarized), we have also calculated $I(\theta,\phi)$ for both 5s and 4s, treating separately the ^7S and ^9S ferromagnetically ordered cases (which will be designated $I^{\uparrow}_{7S}(\theta,\phi)$ and $I^{\downarrow}_{9S}(\theta,\phi)$, respectively) and the corresponding paramagnetically disordered cases (designated $I^{para}_{7S}(\theta,\phi)$ and $I^{para}_{9S}(\theta,\phi)$). We finally define the SPPD asymmetry $A(\theta,\phi)$ between the magnetically-ordered low temperature (LT) and the magnetically-disordered high temperature (HT) states in a way similar to that done previously [20,23,24] as:

$$A(\theta,\phi)=\frac{R_{LT}(\theta,\phi)-R_{HT}(\theta,\phi)}{R_{HT}(\theta,\phi)}\times 100\%, \qquad [9]$$

where it is assumed for theoretical modeling that $R_{LT}(\theta,\phi)=I^{\uparrow}_{7S}(\theta,\phi)/I^{\downarrow}_{9S}(\theta,\phi)$ and $R_{HT}(\theta,\phi)=I^{para}_{7S}(\theta,\phi)/I^{para}_{9S}(\theta,\phi)$. This gives a measure of the absolute percent change in the ratio of the ^7S to ^9S peak in going from the ferromagnetic to paramagnetic state, with full allowance for all photoelectron diffraction effects and the small difference in kinetic energy between the ^7S and ^9S peaks in each spectrum. The calculated asymmetries for the Gd 5s and 4s cases are shown in Figs. 4.8(a) and (b), respectively. For the 5s case, a region with a high degree of asymmetry is found near normal emission (A = +11.1 %, θ = 90°), with higher values also arising in the plane formed by the [0001] and [$10\bar{1}0$] directions (+4.3 %, θ = 54°, ϕ = 180°). A region of relatively low asymmetry can be found in the plane formed by the [0001] and [$2\bar{1}\bar{1}0$] directions (-1.7 %, θ = 54°, ϕ = 210° and equivalent to ϕ = 90° due to symmetry). This can be seen more clearly in the azimuthal and polar cuts of the asymmetries shown in Figs. 4.9 and 4.10. The

asymmetries calculated for Gd 4s emission (Fig. 4.8(b) and Fig. 4.10) of +1.5% at normal emission, and +5.0 % at $\theta = 54°$ and $\phi = 0°$ parallel to $[10\bar{1}0]$ are, overall, slightly weaker than those found in 5s emission. This is most likely due to the ~100 eV higher E_k used for the Gd 4s measurements, which leads to weaker exchange dependent scattering effects. It is also noteworthy that significant SPPD asymmetries were not observed in the calculations until at least three of the top atomic layers were ferromagnetically aligned. This indicates that SPPD effects in the Gd(0001) system arise mostly from inter-layer and/or forward scattering between ferromagnetically aligned layers as compared to intra-layer and/or back scattering. Therefore, any "surface" transitions observed by these measurements may be more indicative of transitions occurring in the top few layers and not in a single "magnetically-live" top layer.

4.IV **Experimental SPPD Results from Gd(0001)**

The SPPD asymmetries measured from Gd 5s and Gd 4s spectra in experiment were derived in a manner similar to that used for theory. We define the angle and temperature dependent ^7S to ^9S peak intensity ratio: $R(\theta,\phi,T) = I_{^7S}(\theta,\phi,T) / I_{^9S}(\theta,\phi,T)$, where the peak intensities $I_{^7S}(\theta,\phi,T)$ and $I_{^9S}(\theta,\phi,T)$ were determined by fitting the obtained spectra with two asymmetric Voigt functions of fixed and unequal widths riding on a Shirley inelastic background [40]. Examples of these fits are shown in Appendix A. Fig. 4.1 shows the effect of temperature on the relative intensities of the ^7S and ^9S peaks for both the Gd 5s and 4s multiplets; the ^9S peaks have here been normalized to be of equal height so that the small changes in relative intensity can be directly seen via the ^7S peaks. As the peaks are fairly well resolved from one another, the peak relative intensities and the SPPD asymmetries derived from them proved to be insensitive to the specifics of the fitting procedure utilized. We now define the experimental asymmetry as:

$$A(\theta,\phi,T) = \frac{R(\theta,\phi,T) - R(\theta,\phi,T_{max})}{R(\theta,\phi,T_{max})} \times 100\% \qquad [10]$$

where $R(\theta,\phi,T_{max})$ is the measured peak ratio at the high temperature limit of the experiment (T = 512 K), with θ and ϕ being the previously mention polar and azimuthal angles as used in both experiment and theory and defined in Fig. 4.6. In this manner, if T_{max} is assumed to be high enough for all short-range magnetic order to disappear, the theoretical asymmetries calculated previously should be comparable to the total percent change of those measured in experiment. $A(\theta,\phi,T)$ also obviously is defined so as to go to zero at the high end of the data range. Spin asymmetries were measured for emission along four directions, three for 5s and one for 4s, and the results are summarized in Fig. 4.11. The measured asymmetries for Gd 5s taken at normal emission ($\theta = 90°$, $\phi = 180°$, case 1), in the plane formed by the "$\bar{b}$" = $[\bar{1}010]$ and "c" = [0001] axes ($\theta = 54°$, $\phi =$ 180, case 2), and in the plane symmetry equivalent to that formed by the "a" = $[2\bar{1}\bar{1}0]$ and "c" = [0001] axes ($\theta = 54°$, $\phi = 90°$, case 3) are shown in Figs. 4.11(a), (b), and (c), respectively. The Gd 4s asymmetry taken at normal emission ($\theta = 90°$, $\phi = 180°$, case 4) is contained in Fig. 4.11(d). The 5s asymmetries in cases 1 and 2 display distinct and reproducible peaks over the temperature range 260 to 370 K, with a sharp upward slope near the bulk Curie temperature T_{cb} of 293 K and then a sharp downward slope upon approaching what has been measured previously [10] to be the surface Curie temperature T_{cs} of ~355 K. These 5s asymmetries do not level off until $T \cong 375$ K, and exhibit a maximum percent change from the peak to the right-hand "background" asymmetry at 375 K of ~+5.2 %. and ~+4.6 % for cases 1 and 2, respectively. This is in qualitative agreement with the large asymmetries calculated in the previous section of +11.1 % and +4.4 % for cases 1 and 2, with the theory exceeding the observed effect by factor of 2.2 for case 1, and being in excellent agreement with it for case 2. For case 3, by contrast, no statistically significant breaks in the asymmetry are observable within the estimated

accuracy of the measurement. Instead, one simply observes a gradual decrease in A as a function of temperature, with the curve more or less leveling off above about 425 K. Theory again agrees qualitatively with this result in predicting that the asymmetry should be much less (+1.5 %) along this direction as compared to the two previous cases. For the Gd 4s asymmetry (Fig. 4.11(d)), two pronounced features are present in the asymmetry near T_{cb} and T_{cs} as well: a 3.3% dip in A just below T_{cb} at ~260 K and a 2.6 % dip very near the previously observed T_{cs}. Alternatively, one finds a peak in A very close to T_{cb} and a peak about 20 K above what has previously been determined to be T_{cs}, near 375 K. The 4s asymmetry does not level off on going to higher temperature, an effect which could be due to the higher kinetic energy leading to more important Debye-Waller effects, and also to slightly different Debye-Waller effects for the two peaks involved, which are separated by ~8.2 eV in kinetic energy. The SPPD effects seen in 4s emission in case 4 are thus even more evident than those seen in the 5s measurements for cases 1 and 2. The peaks and dips, or absence thereof, seen in the four cases of Fig. 4.11 were also reproduced in at least three separate runs each, and for both ascending and, in select cases, also descending, temperatures, with good agreement between runs. Based upon this combined SPPD data set, we conclude that the experiment is sensitive to both the bulk and near-surface magnetic transitions, and that the near-surface Curie temperature is about 60-80 K above the bulk Curie temperature: $T_{cs} \approx$ 355-375 K.

Table 4.1 lists the measured and calculated maximum changes in asymmetry for the four sample orientations used in experiment. In this table, A_{max} is defined to be the overall change in A from below T_{cb} to above T_{cs}. As the Gd 4s measurement occurs at a higher E_k (~188 eV vs. ~78 eV for the 5s), one would expect the 4s measurement to be somewhat more sensitive to magnetic transitions in the Gd bulk due to the increased photoelectron attenuation length (6.5 Å for the 4s and 4.9 Å for the 5s as calculated according to Ref. 39). This and the shorter photoelectron de Broglie wavelength for 4s

involved may explain also why the 5s Cases 1 and 2 show only a single broad peak over both the bulk and surface transitions, while in the 4s Case 4, the effects of the two transitions are clearly resolved. Looking closely at Fig. 4.11(d), it can be seen that the dip in asymmetry near T_{cb} is larger than that near T_{cs} by about a factor of 1.3, and this is consistent with the greater sensitivity to the bulk transition expected at the 4s kinetic energy. The magnitude of the 4s asymmetry change is, however, nearly two times larger than predicted by theory, as shown in Table 4.1. This could be due to our not using a large enough cluster in the calculations, since the higher E_k also means more layers contributing to the observed intensities. Notice once again that, even for 4s Case 4 there are no significant variations in the asymmetry as the temperature is brought above 375 K (even though it still has a smooth upward trend). Overall, this indicates that short range magnetic order in the film's near-surface region ceases beyond this point (roughly 80 K above T_{cb} and 20 K above the highest previously reported T_{cs})

4.V. **Electron Correlation and Temperature Effects on Multiplet Intensity Ratios and Energy Separations**

In the course of performing our SPPD measurements on Gd(0001), some additional interesting effects were observed in the relative intensities and separations of the ^7S and ^9S components involved. Firstly, it is predicted from a simple model involving coupling of the photoelectron core hole to the unfilled valence subshell ($4f^7$ in our case) that the relative peak intensities within an L=0 or S multiplet will be equal to the ratio of the spin degeneracies of the final states [41,42]. For emission from the ^8S initial state into the ^7S and ^9S final states, the relative peak intensities would then be:

$$\frac{I(^7S)}{I(^9S)} = \frac{2S_f(^7S)+1}{2S_f(^9S)+1} = \frac{7}{9} = 0.778 \qquad [11]$$

where S_f is the final state spin of 3 for the ^7S and 4 for the ^9S. Looking back to Fig. 4.1, as well as to Table 4.2 which contains the average fitting results and ratios, it can be seen that the Gd 5s spectrum follows this rule very well, and much more closely than the 4s. The Gd 4s spectrum is seen to contain a ^7S component of much greater relative intensity than that of the ^9S, with our fit giving $I(^7S)/I(^9S) \cong 1.05$ as compared to the ratio of 0.79 observed for the 5s. Previous measurements by Kowalczyk on the Gd 4s spectrum from polycrystalline Gd with Al Kα excitation at a much higher photon energy (1486.6 eV) have also shown a similar ratio between the two peaks [43,44], but without comment as to its origin. The fact that this anomolous ratio is seen with both low and high photon energies rules out an explanation in terms of deviations from the high-energy sudden approximation limit that has been used successfully to explain core-level multiplet structures in both Mn [45] and Gd [29]. This violation of Eq. 11 for the Gd 4s spectrum is thus most likely due to enhanced correlation effects arising from the high degree of 4s-4f overlap. However, the apparent influence of these correlation effects in 4s emission from Gd is opposite in sign to that studied previously in the analogous 3s emission from ionic Mn^{2+}, for which the high-spin ^7S peak gains in relative intensity compared to the closest-lying low-spin ^5S peak [45]. Thus, the Gd 4s spectrum exhibits an anomalous intensity ratio that warrants further theoretical study. The 5s-4f overlap is much smaller, thus making correlation effects less significant in Gd 5s emission and leading to a closer agreement with the predictions of simple theory as to intensity ratio (cf. Table 4.2).

A similar reasoning in terms of correlation effects and configuration interaction has been used to explain the smaller ^7S to ^9S peak separations in the rare earth 4s levels as compared to those predicted by Van Vleck's theorem [41-43]. This theorem as applied to s-photoelectron multiplets [41] predicts the exchange splitting to be:

$$\Delta E_k(ns,n'l') = (2S + 1)K_{ns,n'l'} \qquad [12]$$

where S is the initial state spin (7/2 in our case) and $K_{ns,n'l'}$ is the exchange integral between the s orbital of the n shell (4s or 5s for Gd) and the l' orbital of the partially filled n' shell (4f for Gd). The splittings calculated using this equation are shown in Table 4.3 as $\Delta E_k(ns,4f)$ and can be compared to the experimental ΔE_k values given in Table 4.2. The experimental and theoretical Gd 5s splittings are found to agree excellently (3.91 eV versus 3.62 eV, respectively), whereas the same splittings for Gd 4s are very far apart (8.18 eV versus 13.92 eV), thus again showing that inter-shell correlations are much less significant than intra-shell correlations. In the case of the 4s, it was found that the theoretical splitting should be multiplied by a factor of 0.55 for the rare earth's [43]. It was proposed that this reduction in the 4s splitting arises from increased correlation effects from the significant 4s-4f overlap. Multiplying 13.92 eV by this factor gives us an expected splitting of 7.66 eV in better agreement with the measured value. So, both the multiplet peak intensity ratio and peak separation point toward the importance of correlation effects in the Gd 4s multiplet. Despite these effects in the 4s spectrum, however, we still expect on the basis of prior theory [45] that the two members of the doublet will be highly spin polarized, and thus that they can be used to derive the clear SPPD effects that are discernible in the 4s spin asymmetry, as shown in the previous section.

Finally, an additional temperature-dependent effect has been observed for the first time in the Gd 5s spectra. Specifically, we observe small, but reproducible and systematic, variations in the multiplet peak separations with temperature. Fig. 4.12 contains the 5s peak separations ΔE_k as a function of temperature for the first three cases in Fig. 4.11. The splittings for all three 5s cases shown go through a broad minimum near T_{cb} and then increase back to near their low temperature value as one exceeds T_{cs}. For the 4s case

(not shown here), on the other hand, ΔE_k displayed no statistically significant and reproducible variations with temperature. All three 5s curves in Fig. 4.12 also show signs of local minima centered at T_{cb} and T_{cs}. The magnitude of the effect is roughly 60 meV (1.6 % of the average separation) for the overall dips in the 5s curves. The observed variation in ΔE_k also was not found to be dependent on the choices of fitting parameters used to derive the multiplet intensity ratios and the peak separations. For example, we could fix the splitting at a constant average value over the entire temperature range and still obtain essentially identical results for the final ratios and asymmetries shown in Fig. 4.11. Thus, we do not believe that there is a converse correlation for which slight variations in the intensity ratio are responsible for the changes in ΔE_k seen in Fig. 4.12. It is also important to note that the changes in ΔE_k are independent of the observed SPPD effects on the asymmetry, as we measure nearly identical changes in the splitting for 5s even along a direction that shows no appreciable asymmetry changes (e.g. compare Figs. 4.11(c) with its counterpart 4.12(c)). Hence, we believe that this is a genuine effect for the 5s spectra and not an artifact of the fitting procedure.

To gain some further theoretical insight into the possible origin of these small temperature-dependent changes in the multiplet splitting, we again note that 0.63 μ_B of the Gd atom's 7.63 μ_B resides in the $(5d6s6p)^3$ valence electrons. Therefore, a small component of the overall exchange splitting in the 5s and 4s spectra should come from these valence electrons. Utilizing the tabulated Hartree-Fock calculations of Mann [46] as a source for the values of the additional exchange integrals $K_{ns,5d}$ and $K_{ns,6s}$, we can make an approximate estimate as to the amount of splitting arising from the 4s or 5s overlap with the valence electrons. Table 4.3 presents the values derived for the various exchange integrals of interest. From Eq. 12 and using only the dominant ns-4f exchange integral, we calculate the exchange splitting of the 5s (4s) multiplets as being $\Delta E_k(4f)$ =3.62 eV (13.92 eV) (cf. Table 4.3). Including the previously-derived empirical factor of

0.55 reduction due to correlation effects in the 4s multiplet [41], we have a calculated splitting of 7.66 eV for the 4s, as compared to the 8.2 eV that we measure here, a difference of only 7%. To estimate the additional splitting arising from the valence band, we can now use the fraction of the moment arising from these electrons and multiply this by the relevant exchange integrals:

$$\Delta E_k(VB) \equiv \Delta E_k[ns,(5d6s)^3] \cong [2S_{VB}+1][f(5d)K_{ns,5d}+f(6s)K_{ns,6s}] \qquad [13]$$

where S_{VB} is the spin associated with the valence band (~0.63/2), and f(5d) and f(6s) are the fractional occupations of the valence electrons in these shells. From the calculations of Wu et al. [35] we estimate the fractional occupations to be 25.3 % and 74.7 % for the 5d and 6s, respectively, neglecting the small 6p contribution. This gives as valence electron contributions to the multiplet splittings values of 0.121 eV for the 4s and 0.598 eV for the 5s, or 0.8% and 16.5% of the 4f splitting, respectively. Thus, small changes in these valence contributions induced by passage through a magnetic transition may be responsible for the observed decrease in the multiplet splitting near T_{cb} and T_{cs}, and the 5s spectra would be expected to be at least an order of magnitude more sensitive to such changes than the 4s spectra. The much smaller contribution for the 4s may explain why there was no distinct effect observed for this multiplet.

A possible explanation for the observed effect is then that, as the temperature is raised toward the transition region, the delocalized valence electrons begin to lose the fixed magnetization direction found in the ferromagnetic system before the highly localized 4f core electrons (which still maintain some degree of inter-atomic alignment). This would cause the valence component of the multiplet splitting to diminish when passing through T_{cb}. As all magnetic order is lost between atoms at higher temperatures (beyond T_{cs}), the valence and 4f core electrons once again become free to align locally with the same

magnetization direction, re-establishing the full multiplet splitting observed at low temperature. With the Gd 4s multiplet, the situation becomes more complicated due to the weaker valence electron coupling to begin with, as well as to the stronger correlation effects giving rise to a manifold of final states as compared to the relatively simple ^7S and ^9S states found in the 5s. Hence, variations with temperature among the different elements of the 4s configuration interaction (CI) manifold [41,45] due to spin polarization may produce changes in the multiplet peak splitting that cannot be explained simply by including valence effects.

An alternative, but closely related, explanation for the dips in splitting observed at both T_{cb} and T_{cs} for all three 5s cases is some sort of spin-dependent electron screening process that is slightly accentuated as the temperature passes through a point where there are large spin fluctuations in the adjacent valence electrons and 4f magnetic moments. For example, if on passing through the transition temperature, a spin-up 5s core hole on Gd (leading to a spin-down photoelectron and the ^7S final state) is screened slightly more effectively than a spin-down 5s hole (leading the ^9S final state), then the separation between the two peaks will be decreased. One way of viewing the interaction of the spin-polarized hole with its surroundings would be via an RKKY interaction [47] which could in turn via the oscillations in spin polarization induced around it be very sensitive to the nature of the magnetic order or magnetic fluctuations on the near-neighbor sites.

We are not aware of any prior discussion of such spin- and temperature- dependent multiplet and screening effects, but our experiments suggest that they occur, and further study of them would be of considerable interest. Another intriguing aspect of these results is that the measurement of ΔE_K could by itself constitute another way to detect magnetic phase transitions!

4.VI **Conclusions**

Spin polarized photoelectron diffraction measurements on the rare-earth ferromagnetic system Gd(0001) utilizing both the 4s and 5s photoelectron multiplets reveal the presence of ferromagnetic-to-paramagnetic transitions occurring at the bulk Curie temperature of 293 K and at a surface Curie temperature of ~350-375 K. Our value for the surface Curie temperature is thus in excellent agreement with the prior data of Tang et al. [10], although perhaps 10-20 K higher than their value. The maximum change in the 5s asymmetry is measured to be nearly 5% for both normal emission and emission at $\theta = 54°$ with ϕ parallel to the "$\bar{b}$" axis in plane ($\phi = 180°$). When ϕ is rotated by 90° from the last-mentioned position (i.e. $\theta = 54°$, $\phi = 90°$, lying in an axis symmetry equivalent to "a") no distinct breaks in the asymmetry are observed, illustrating the strong angular dependence of this effect. SPPD performed with more bulk sensitive conditions on the 4s level reveals a 2.6 to 3.3% effect at normal emission and a more pronounced change in the asymmetry occurring near T_{cb}. The 4s data also show distinct dips near both the bulk and surface Curie temperatures. Both the 5s and 4s SPPD asymmetries are observed to reach a constant value or a slow monotonic variation for temperatures T > 375 K, indicating that short range magnetic order ceases beyond this point. Full multiple scattering calculations based upon the Rehr-Albers approximation predict the SPPD effects qualitatively as a function of emission angle between the fully-ordered ferromagnetic and disordered paramagnetic states. At least three ferromagnetically aligned atomic layers are required in the calculations to produce significant SPPD asymmetries, suggesting that such transitions arise from the near surface layer and not a single "magnetically-live" layer. Furthermore, the ^7S to ^9S peak ratio of the 4s multiplet is observed to greatly exceed the ratio of 7/9 obtained from a simple atomic model, giving additional support for the importance of correlation effects in the case of 4s emission.

However, these effects appear to act on the 4s intensity ratio in the opposite direction to those discussed previously for the analogous 3s intensity ratio in Mn. Finally, the ^{7}S to ^{9}S peak-separation in the 5s spectra is observed to vary systematically with temperature, showing a broad minimum with a 60 meV decrease and two small dips as the temperature is increased through the bulk and surface Curie temperatures. Such effects on multiplet relative intensity and separation may be related to changes in the exchange splitting due to fluctuations in the valence electrons, to correlation-induced effects creating regions with different temperature dependence within a CI manifold, and/or to spin- and temperature-dependent screening effects. The temperature-dependent multiplet splitting might also be useful as a new probe of bulk and surface magnetic transitions.

Acknowledgments: The author would like to thank Dr. A. P. Kaduwela of the California State Air Resources Board for the use of his multiple scattering codes in our calculations, and Michel Van Hove of the Lawrence Berkeley National. Laboratory (LBNL) for helpful suggestions concerning the theoretical analysis. Support for these studies was provided by the Director, Office of Energy Research, Materials Sciences Division., of the U.S. Dept. of Energy, under Contract No. DE-AC03-76SF00098; the Office of Naval Research under contract (N00014-94-0162), and the National. Energy Research. Supercomputing Center. at LBNL.

References:

1) W. D. Corner and B. K. Tanner, J. Phys. C 9, 627 (1976).

2) J. Kolaczkiewicz and E. Bauer, Surf. Sci. 175, 487 (1986).

3) J. Giergiel, A. W. Pang, H. Hopster, X. Guo, S. Y. Tong, and D. Weller, Phys. Rev. B 51,10201 (1995).

4) E. D. Tober, R. X. Ynzunza, C. Westphal, and C. S. Fadley, Phys. Rev. B 53, 5444 (1996).

5) E. D. Tober, R. X. Ynzunza, C. Westphal, and C. S. Fadley, in preparation.

6) M. Farle, A. Berghaus, and K. Baberschke, Phys. Rev. B 39, 4838 (1989).

7) G. André, A. Aspelmeier, B. Schultz, M. Farle, and K. Baberschke, Surf. Sci. 326, 275 (1995).

8) A. Berger, A. W. Pang, and H. Hopster, J. Mag. and Mag. Mat. 137, L1 (1994).

9) A, W. Pang, A. Berger, and H. Hopster, Phys. Rev. B 50, 6457 (1994).

10) H. Tang, D. Weller, T. G. Walker, J. C. Scott, C. Chapert et al., Phys. Rev. Lett. 71, 444 (1993).

11) C. Rau and M. Robert, Phys. Rev. Lett. 58, 2714 (1987);C. Rau, J. Mag. and Mag. Mat. 31-34, 874 (1983);C. Rau and S. Eichner, Phys. Rev. B 34, 6347 (1986) & in "Nuclear Methods in Materials Research", eds. K. Bethge, H. Burman, H. Jex, and F. Rauch (Viewig, Braunschweig, 1980), p. 354.

12) C. Rau, C. Jin, M. Robert, Phys Lett. A 138, 334 (1989).

13) D. Weller, S. F. Alvarado, W. Gudat, K. Scröder, and M. Campagna, Phys. Rev. Lett. 54, 1555 (1985).

14) G. A. Mulhollan, K. Garrison,and J. L. Erskine, Phys. Rev. Lett. 69, 3240 (1992).

15) D. Li, J. Zhang, P. A. Dowben, and K. Garrison, J. Phys. Condens. Mat. 5, L73 (1993).

16) B. Kim, A. B. Andrews, J. L. Erskine, K. J. Kim, and B. N. Harmon, Phys. Rev. Lett. 68, 1931 (1992).

17) D. Li, J. Pearson, S. Bader, D. N. McIlroy, C. Waldfred, and P. A. Dowben, Phys. Rev. B 51, 13895 (1995).

18) A. V. Fedorov, K. Starke, and G. Kaindl, Phys. Rev. B 50, 2739 (1994).

19) E. Arenholz, E. Navas, K. Starke, L. Baumgarten, and G. Kaindl, Phys. Rev. B 51, 8211 (1995).

20) B. Sinkovic and C. S. Fadley, Phys. Rev. B 31, 4665 (1985).

21) B. Sinkovic, B. Hermsmeier, and C. S. Fadley, Phys. Rev. Lett. 55, 1227 (1985).

22) (a) B. Hermsmeier, J. Osterwalder, D. J. Friedman, and C. S. Fadley, Phys. Rev. Lett. 62, 478 (1989): (b) B. D. Hermsmeier, C. S. Fadley, M. O. Krause, J. Jiminez-Mier, P. Gerard, and S. T. Manson, Phys. Rev. Letters 61, 2592 (1988).

23) B. Hermsmeier, J. Osterwalder, D. J. Friedman, T. Tran, and C. S. Fadley, Phys. Rev. B 42, 11895 (1990).

24) B. Sinkovic, D. J. Friedman, and C. S. Fadley, J Mag. and Mag. Mat. 92, 301 (1991)

25) Z. Hussain, W. R. A. Huff, S. A. Keller, E. J. Moller, P. A. Heimann, W. McKinney, H. A. Padmore, C. S. Fadley, and D. A. Shirley, J. Elec. Spec. and Rel. Phen. 80, 401 (1996)

26) C.S. Fadley, M.A. Van Hove, Z. Hussain, and A.P. Kaduwela, J. Electron Spectrosc. 75, 273 (1995); and R. X. Ynzunza et al., to be submitted.

27) D. Li, C. W. Hutchings, P. A. Dowben, C. Hwang, R. T. Wu et al., J. Magnet. and Magnet. Mater. 99, 85 (1991).

28) D. Li, J. Zhang, P. A. Dowben, and M. Onellion, Phys. Rev. B 48, 5612 (1993).

29) G.. Van der Laan, E. Arenholz, E. Navas, A. Bauer, and G. Kaindl, Phys. Rev. B 53, R5998 (1996).

30) C. S. Fadley, "The Study of Surface Structures by Photoelectron Diffraction and Auger Electron Diffraction," appearing in Synchrotron Radiation Research: Advances in Surface and Interface Science, Vol. 1: Techniques, p. 421, ed. by R. Z. Bachrach (Plenum Press, NY, 1992), and C. S. Fadley, Surf. Sci. Rep. 19, 231 (1993).

31) J. J. Rehr, R. C. Albers, C. R. Natoli, and E. A. Stern, Phys. Rev. B 34, 4350 (1986); J. Mustre de Leon, J. J. Rehr, C. Natoli, and C. S. Fadley, Phys. Rev. B 39, 5632 (1989).

32) L. W. Roeland, G. J. Cock, F. A. Muller, A. C. Moleman, K. A. McEwen, R. G. Jordan, and D. W. Jones, J. Phys. F 5, L233 (1975).

33) J. C. Slater, Phys. Rev. 81, 385 (1951) and J. C. Slater, T. M. Wilson, and J. H. Wood, Phys. Rev 179, 28 (1969).

34) J. Quinn, Y. S. Li, F. Jona, and D. Fort, Phys. Rev. B 46, 9694 (1992).

35) R. Wu, C. Li, A. J. Freeman, and C. L. Fu, Phys Rev. B 44, 9400 (1991).

36) F. J. Himpsel, and B. Reihl, Phys. Rev. B 28, 574 (1983).

37) (a) A. P. Kaduwela, D. J. Friedman, and C. S. Fadley, J. Elec. Spec. & Rel. Phen. 57, 223 (1991); (b) J. J. Rehr and E. A. Albers, Phys. Rev. B 41, 8139 (1990).

38) N. Achiwa, R. R. Arons, H. Drulis, M. Drulis, and S. Kawano, "Magnetic Properties of Metals: Rare Earth Elements, Hydrides, & Mutual Alloys," eds. O. Madelung and H. P. J. Wijn, in Landolt Börnstein V19.d1, p. 42 (Springer-Verlag, Berlin, 1991).

39) S. Tanuma, C. J. Powell, and D. R. Penn, Surf. & Interf. Anal. 17, 911 (1991).

40) D. A. Shirley, Phys. Rev. B 5, 4709 (1972).

41) P. A. Cox and F. A. Orchard, Chem. Phys. Lett. 7, 273 (1970).

42) C. S. Fadley, "Basic Concepts of X-ray Photoelectron Spectroscopy," appearing in Electron Spectroscopy, Theory, Techniques, & Applications, V11, Chapt. 1, p. 102, eds. C. R. Brundle and A. D. Baker, (Pergamon Press, 1978).

43) F. R. Mcfeely, S. P. Kowalcyk, L. Ley, and D. A. Shirley, Phys. Lett. 49A, 301 (1974).

44) S. P. Kowalcyk, PhD. Thesis, Univ. of Calif., Berkeley (1976) - unpublished.

45) P.S. Bagus, A.J. Freeman, and F. Sasaki, Phys. Rev. Lett. 30, 850 (1973).

46) J. B. Mann, "Atomic Structure Calculations I.: Hartree-Fock Energy Results for the Elements Hydrogen to Lawrencium," Los Alamos Laboratory of the University of California, Springfield, Va., Distributed by Clearinghouse for Federal Scientific & Technical Information, U. S. Dept. of Commerce, (1967).

47) C. Kittel, Sol. Stat. Phys. 22, 1 (1968).

Tables:

Table 4.1. Maximum calculated and measured SPPD spin asymmetries for the Gd 5s and 4s for selected emission angles θ and ϕ.

Case No.	Core level	θ (deg.)	ϕ (deg.)	A (Theory)	A_{max} (Expt.)
1	Gd 5s	90°	180°	11.1 %	5.0 %
2	Gd 5s	54°	180°	4.3 %	4.6 %
3	Gd 5s	54°	90°	-1.7 %	< 1.8 %
4	Gd 4s	90°	180°	+ 1.5 %	3.3 %

Table 4.2. Experimental fitting results for the Gd 4s and 5s multiplets in the paramagnetic state. FWHM = full width half maximum of peak, R = ^{7}S:^{9}S peak ratio, ΔE_k = ^{7}S to ^{9}S peak splitting.

Core Level	FWHM (^{7}S)	FWHM (^{9}S)	R	ΔE_k(expt.)
Gd 4s	7.74 eV	6.82 eV	1.05	8.18 eV
Gd 5s	3.47 eV	2.56 eV	0.79	3.91 eV

Table 4.3. Exchange integral values calculated from Ref. 45 for orbital pairs of interest and resulting multiplet splittings from the 4f subshell ΔE_k (ns,4f) according to Eq. 12 and from the three valence band electrons ΔE_k (ns,VB) according to Eq. 13. The ΔE_k (4s,4f) of 7.66 eV in parentheses includes the 0.55 empirical multiplication factor of Ref 42. Also given in parentheses for ΔE_k (ns,VB) is its value as a percentage of ΔE_k (4s,4f).

ns	$K_{ns,4f}$(eV)	$K_{ns,5d}$(eV)	$K_{ns,6s}$(eV)	ΔE_k (ns,4f)	ΔE_k (ns,VB)
4s	1.740	0.089	0.063	13.92 eV	0.121 eV
				(7.66 eV)	(= 1.5%)
5s	0.452	0.834	0.209	3.62 eV	0.598 eV
					(=16.5%)

Fig. 4.1. Photoelectron spectra taken at normal emission ($\theta = 90°$, $\phi = 180°$) of (a) Gd 5s excited from Gd(0001) with $h\nu = 120$ eV and at three temperatures of interest: 220 K (solid line), 259 K (dashed line), and 400 K (dotted line). (b) Gd 4s excited with $h\nu = 565$ eV and at two temperatures: 220 K (solid line) and 253 K (dashed line). All spectra have had the inelastic background subtracted and are normalized to have equal ^9S intensity

a)

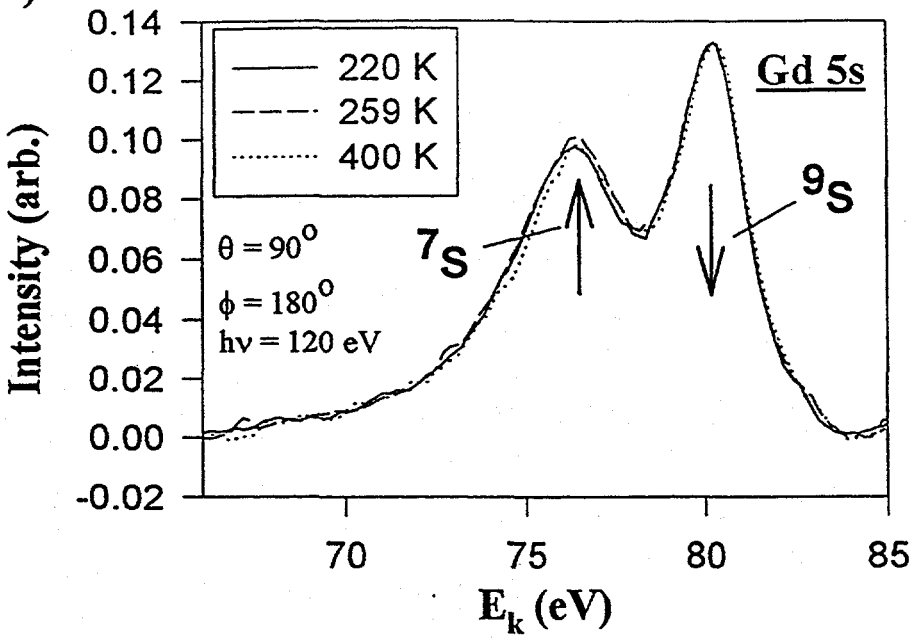
0.14
0.12
0.10
0.08
0.06
0.04
0.02
0.00
-0.02
Intensity (arb.)
220 K
259 K
400 K
θ = 90°
ϕ = 180°
hν = 120 eV
7S
9S
Gd 5s
70
75
80
85
Ek (eV)

b)

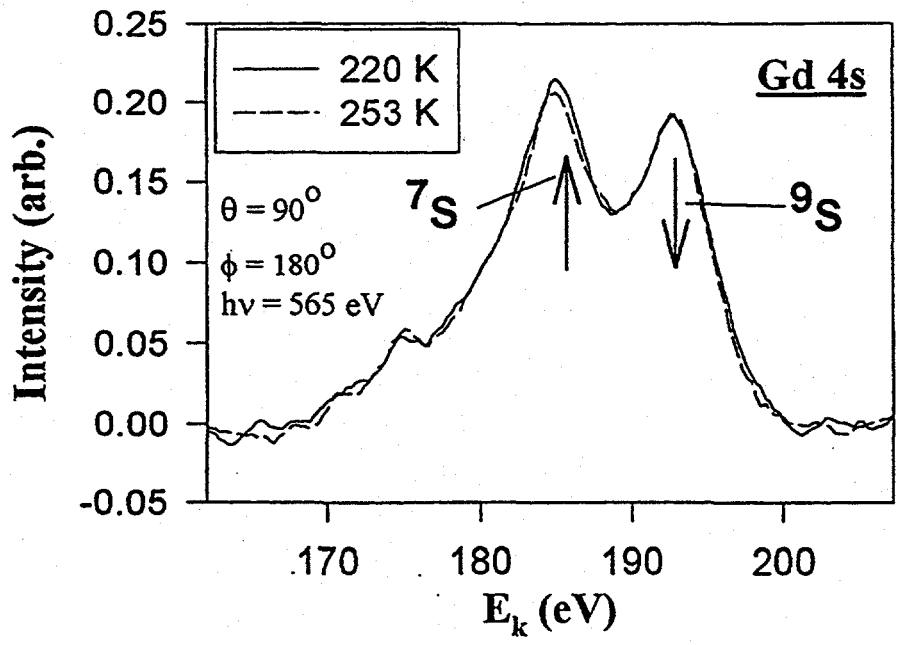
0.25
0.20
0.15
0.10
0.05
0.00
-0.05
Intensity (arb.)
220 K
253 K
θ = 90°
ϕ = 180°
hν = 565 eV
7S
9S
Gd 4s
170
180
190
200
Ek (eV)

Fig. 4.2. (a) Gd exchange potential V_{ex} for scattering with parallel (up - dashed line), anti-parallel (down - dotted line), and paramagnetic (solid line) alignment of photoelectron and scatterer spin calculated as a function of radius r inside the muffin tin. The average radius of the 4f and 5d subshells is also indicated. (b) Difference of parallel (anti-parallel) exchange potentials and the paramagnetic exchange potential, as a % of the paramagnetic potential.

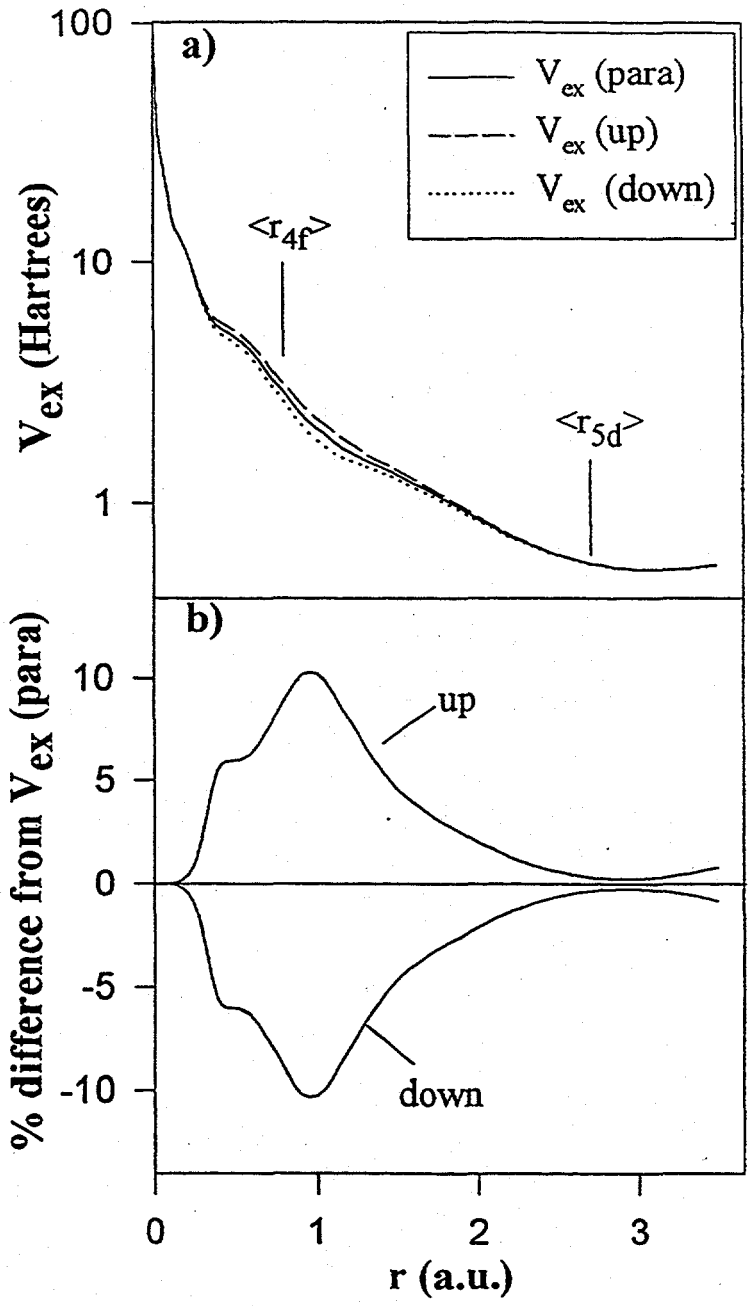
a)
b)
V_{ex} (para)
V_{ex} (up)
V_{ex} (down)
$<r_{4f}>$
$<r_{5d}>$
V_{ex} (Hartrees)
% difference from V_{ex} (para)
up
down
100
10
1
10
5
0
-5
-10
0
1
2
3
r (a.u.)

Fig. 4.3. Scattering factors magnitudes *f* for parallel (up - dashed line), anti-parallel (down - dotted line), and paramagnetic (solid line) alignment of photoelectron and scatterer spin calculated as a function of scattering angle θ_s for (a) Gd 5s ^{7}S with an experimental E_k of 85.2 eV and (b) Gd 4s ^{7}S with an experimental E_k of 194.2 eV. Included in each internal E_k is a 9.0 eV correction for the inner potential.

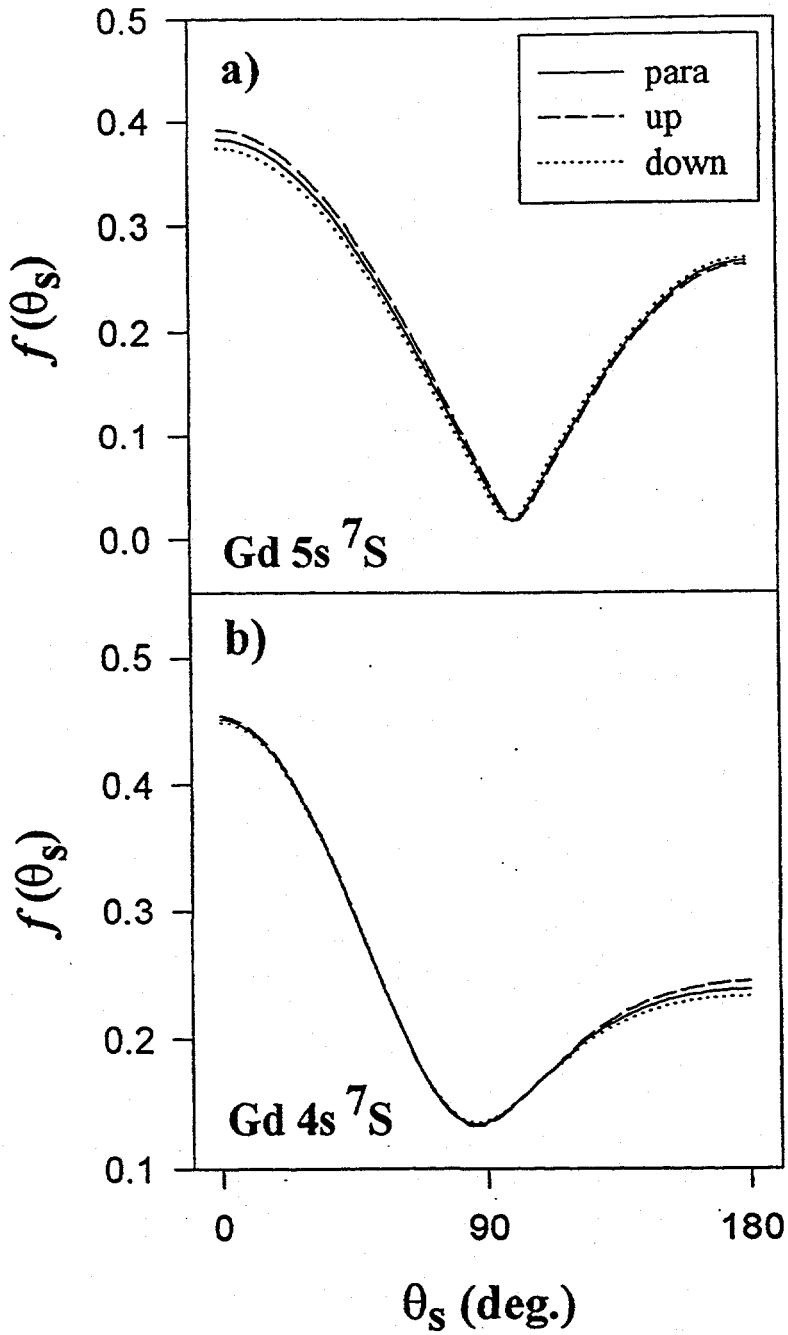
a)
para
up
down
Gd 5s ^{7}S
b)
Gd 4s ^{7}S
$f(\theta_S)$
θ_S (deg.)
0.5
0.4
0.3
0.2
0.1
0.0
0
90
180

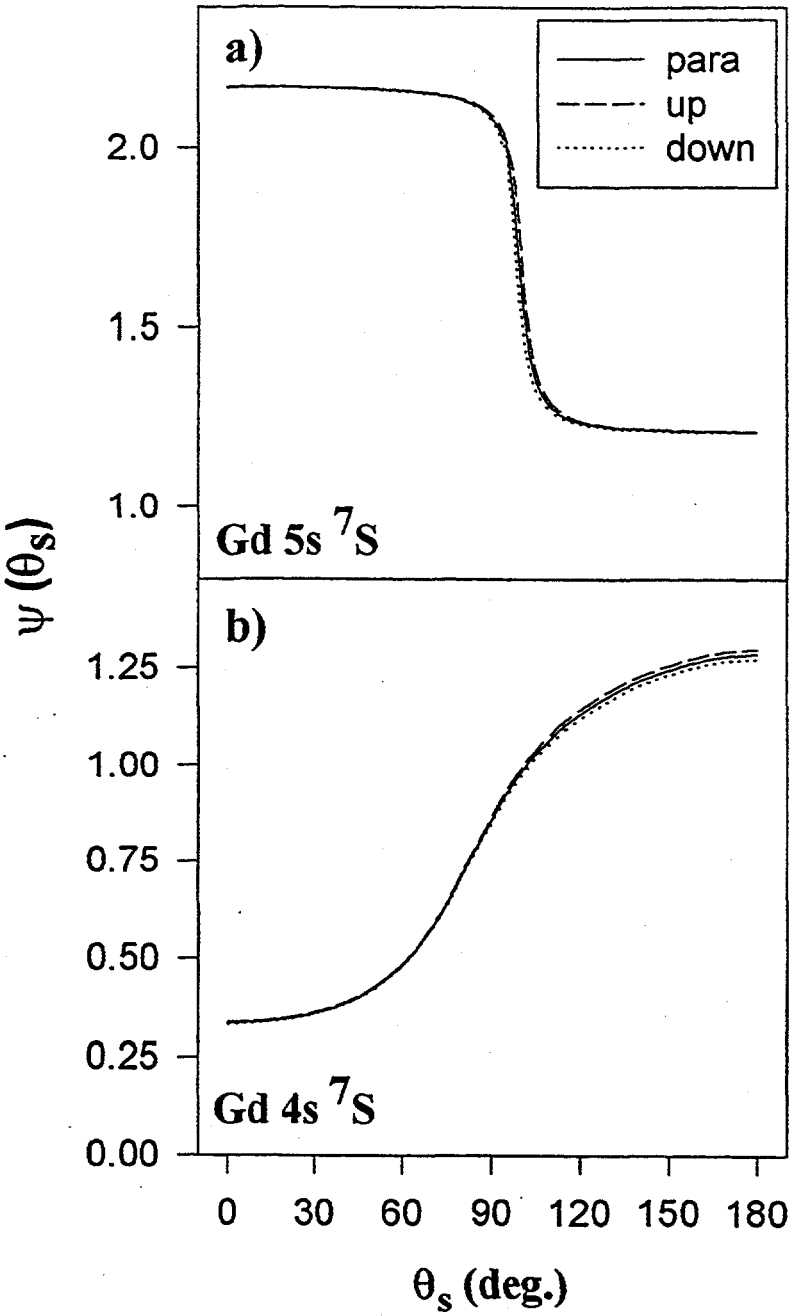

Fig. 4.4. Scattering phase shifts ψ for parallel (up - dashed line), anti-parallel (down - dotted line), and paramagnetic (solid line) alignment of photoelectron and scatterer spin calculated as a function of scattering angle θ_s for (a) Gd 5s ^{7}S with an experimental E_k of 85.2 eV and (b) Gd 4s ^{7}S with an experimental E_k of 194.2 eV. Included in each internal E_k is a 9.0 eV correction for the inner potential.

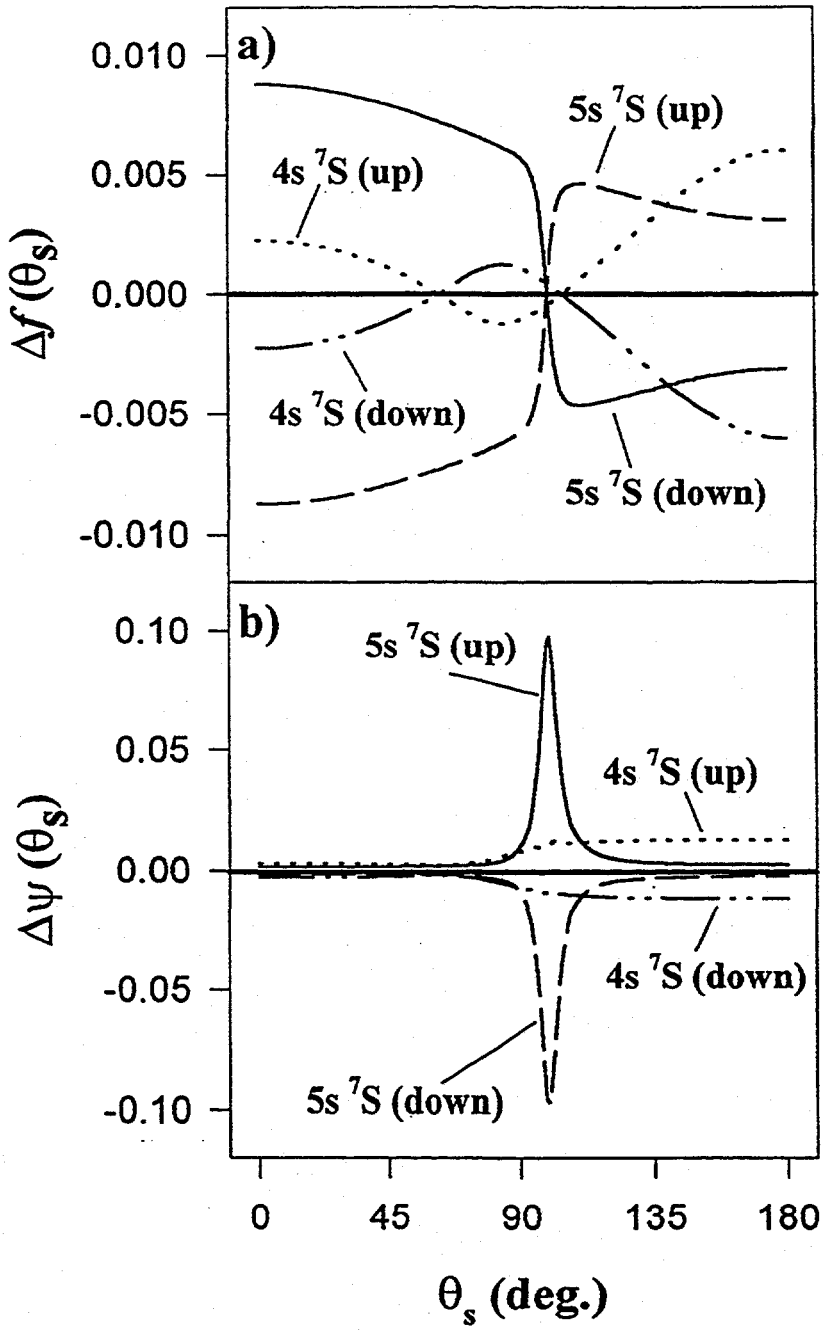

Fig. 4.5. Difference in (a) f and (b) ψ for parallel (up) and anti-parallel (down) alignments as measured relative to the paramagnetic cases. Curves are derived from Figs. 3 and 4 for the experimental E_k's of Gd 5s ^{7}S and 4s ^{7}S.

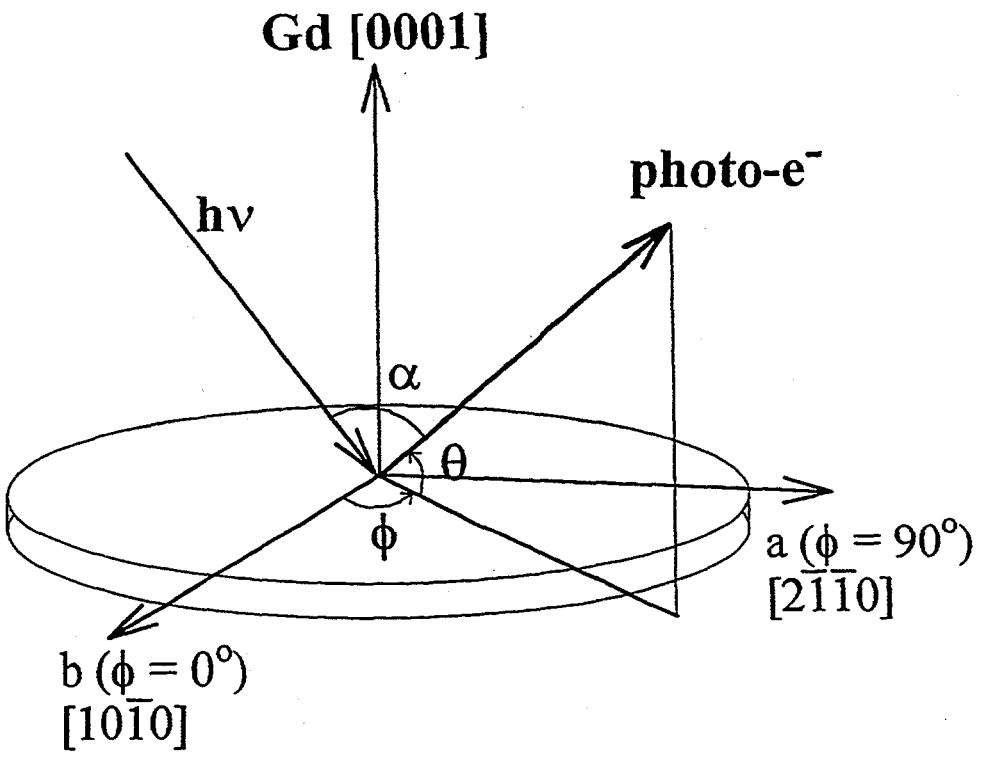

Fig. 4.6. Experimental geometry used for SPPD measurements and theoretical calculations. The polar angle θ is measured from the sample surface, and the azimuthal angle ϕ is measured about the sample normal and from the "b" = [10$\bar{1}$0] direction.

Fig. 4.7. Calculated multiple-scattering full-2π photoelectron diffraction patterns from the Gd(0001) surface for (a) Gd 5s emission (Ek = 85.2 eV) and (b) Gd 4s emission (E_k = 194.2 eV). Note that $\phi = 0°$ points along the "b" $[10\bar{1}0]$ axis.

a) Gd 5s PD (E_k = 76.2 eV)

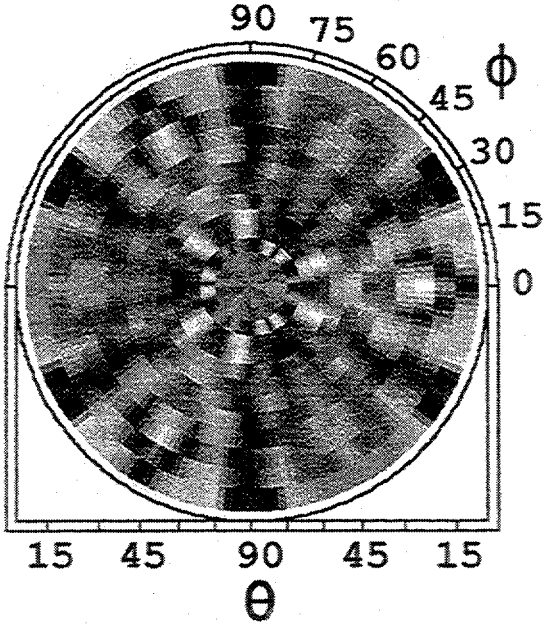

b) Gd 4s PD (E_k = 185.2 eV)

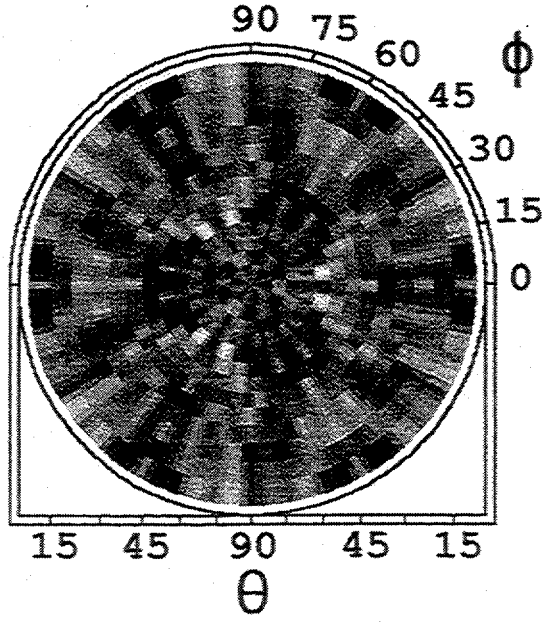

Fig. 4.8. Calculated SPPD spin asymmetry over the full 2π solid angle as derived from the results of Fig. 7 and Eq. 9 for (a) Gd 5s emission and (b) Gd 4s emission. Bright areas indicate positive asymmetry, dark indicate negative asymmetry. Note that $\phi = 0°$ points along the "b" $[10\bar{1}0]$ axis.

a) Gd 5s Asymmetry (E_k = 76.2 eV)

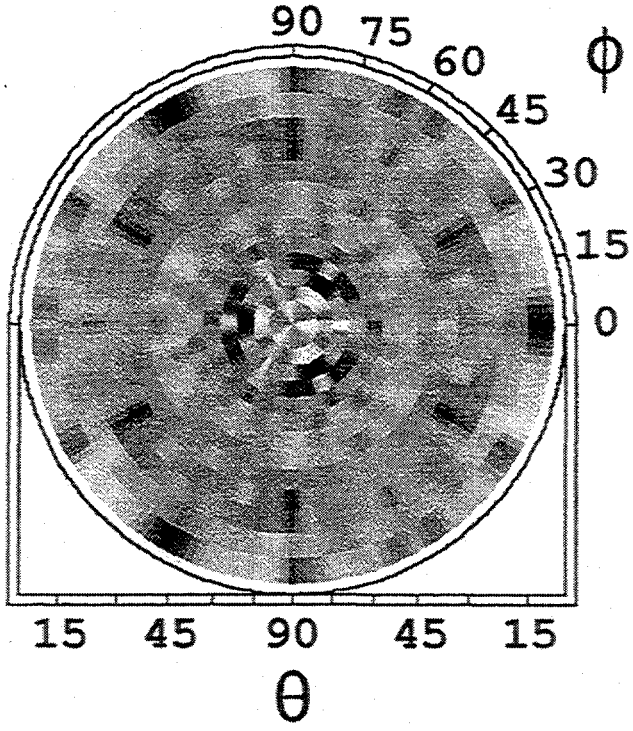

b) Gd 4s Asymmetry (E_k = 185.2 eV)

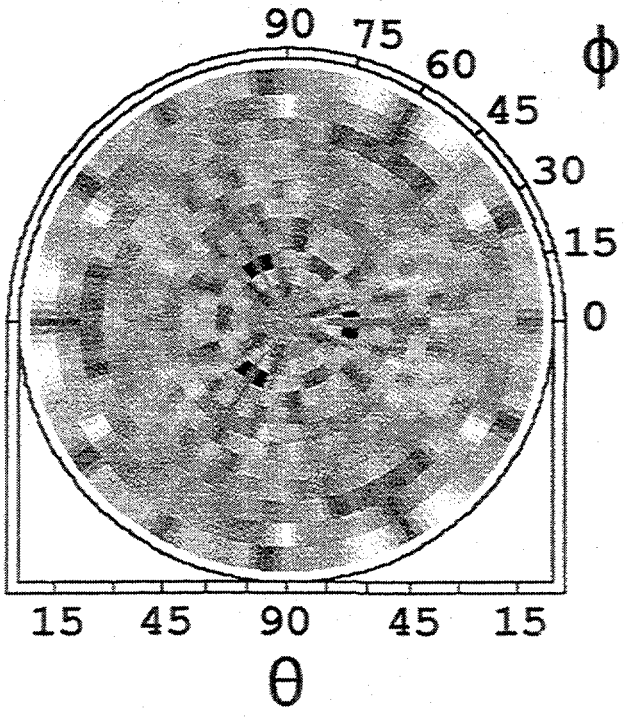

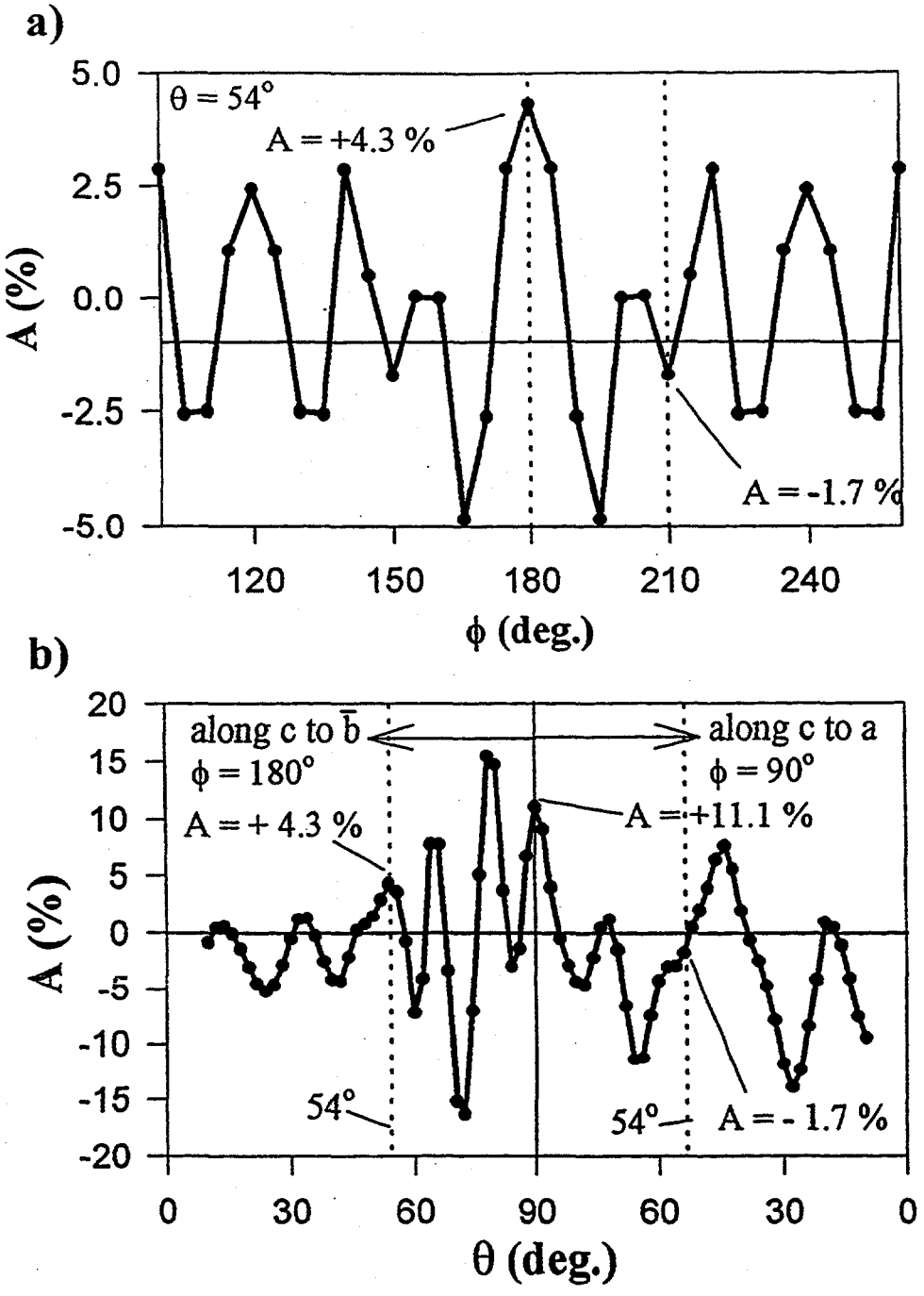

Fig. 4.9 Calculated SPPD asymmetry for Gd 5s emission (E_k = 85.2 eV) and for (a) varying azimuthal angle ϕ with θ fixed at 54° and (b) varying polar angle θ with ϕ fixed at 180° (left half) and 210° (right half).

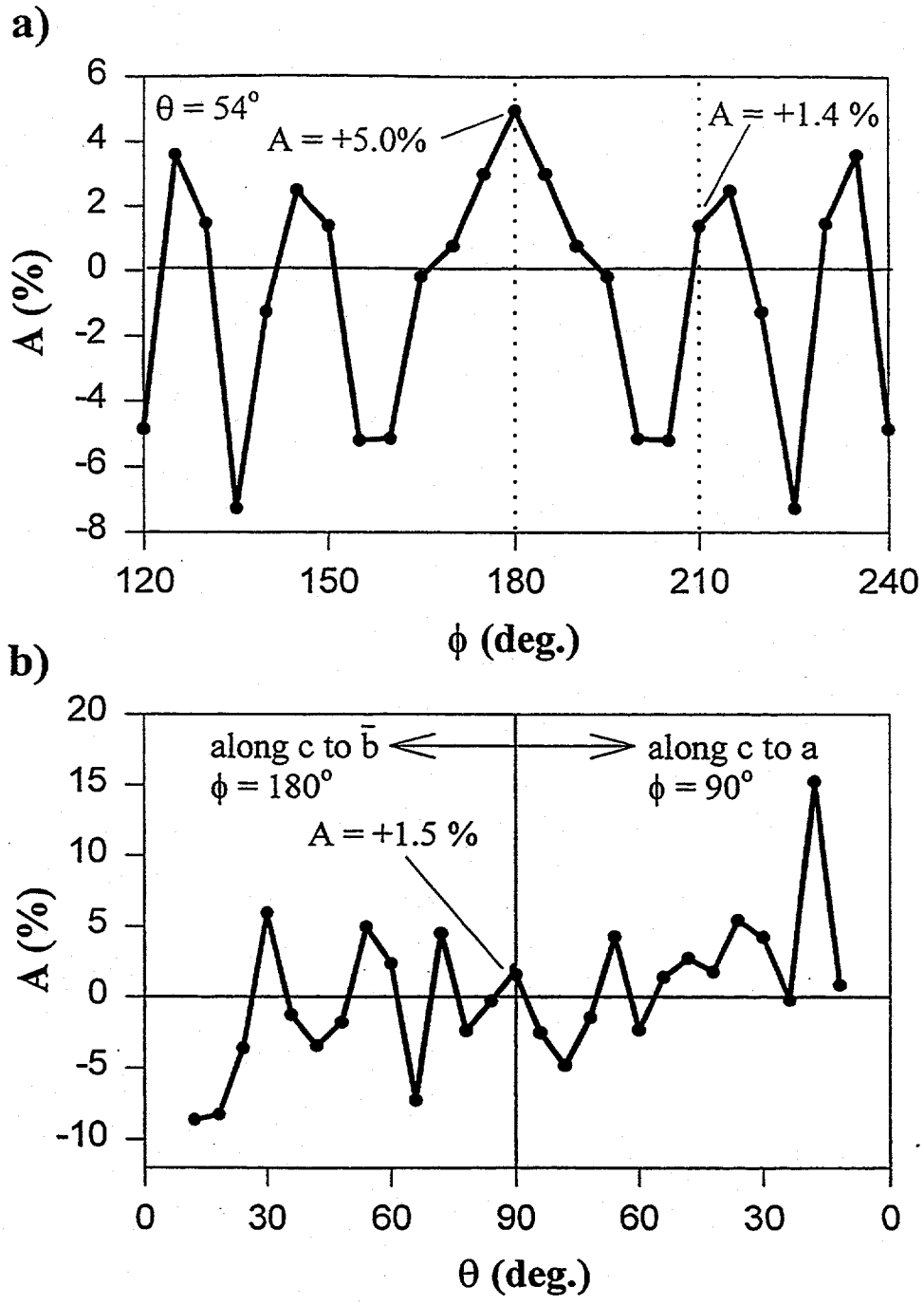

Fig. 4.10. Calculated SPPD asymmetry for Gd 4s emission (E_k = 194.2 eV) and for (a) varying azimuthal angle ϕ with θ fixed at 54° and (b) varying polar angle θ with ϕ fixed at 180° (left half) and 210°(right half).

Fig. 4.11. Experimental spin asymmetry $A(\theta,\phi,T)$ derived from ^{7}S and ^{9}S intensity ratios and Eq. 10 as a function of temperature T for (a) Case 1: Gd 5s emission along the normal ($\theta = 90°$, $\phi = 180^{o}$), (b) Case 2: Gd 5s emission ($\theta = 54°$, $\phi = 180°$, along "$\bar{b}$" axis), (c) Case 3: Gd 5s emission ($\theta = 54°$, $\phi = 90°$ equivalent to the "a" axis), and (d) Case 4: Gd 4s at normal emission ($\theta = 90$, $\phi = 180^{o}$).

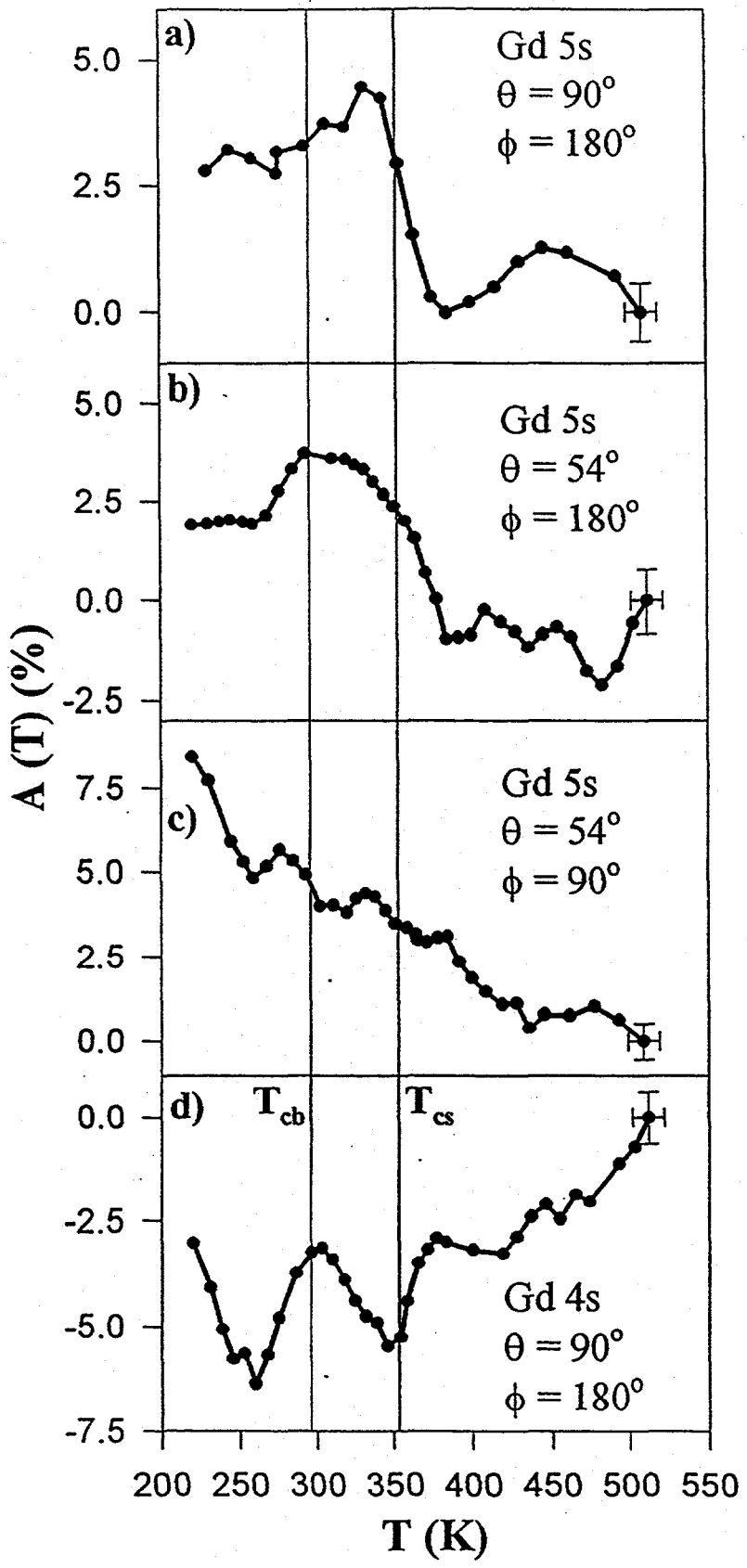
a)
Gd 5s
θ = 90°
ϕ = 180°
b)
Gd 5s
θ = 54°
ϕ = 180°
c)
Gd 5s
θ = 54°
ϕ = 90°
d)
T_cb
T_cs
Gd 4s
θ = 90°
ϕ = 180°
A (T) (%)
T (K)
5.0
2.5
0.0
-2.5
7.5
-5.0
-7.5
200 250 300 350 400 450 500 550

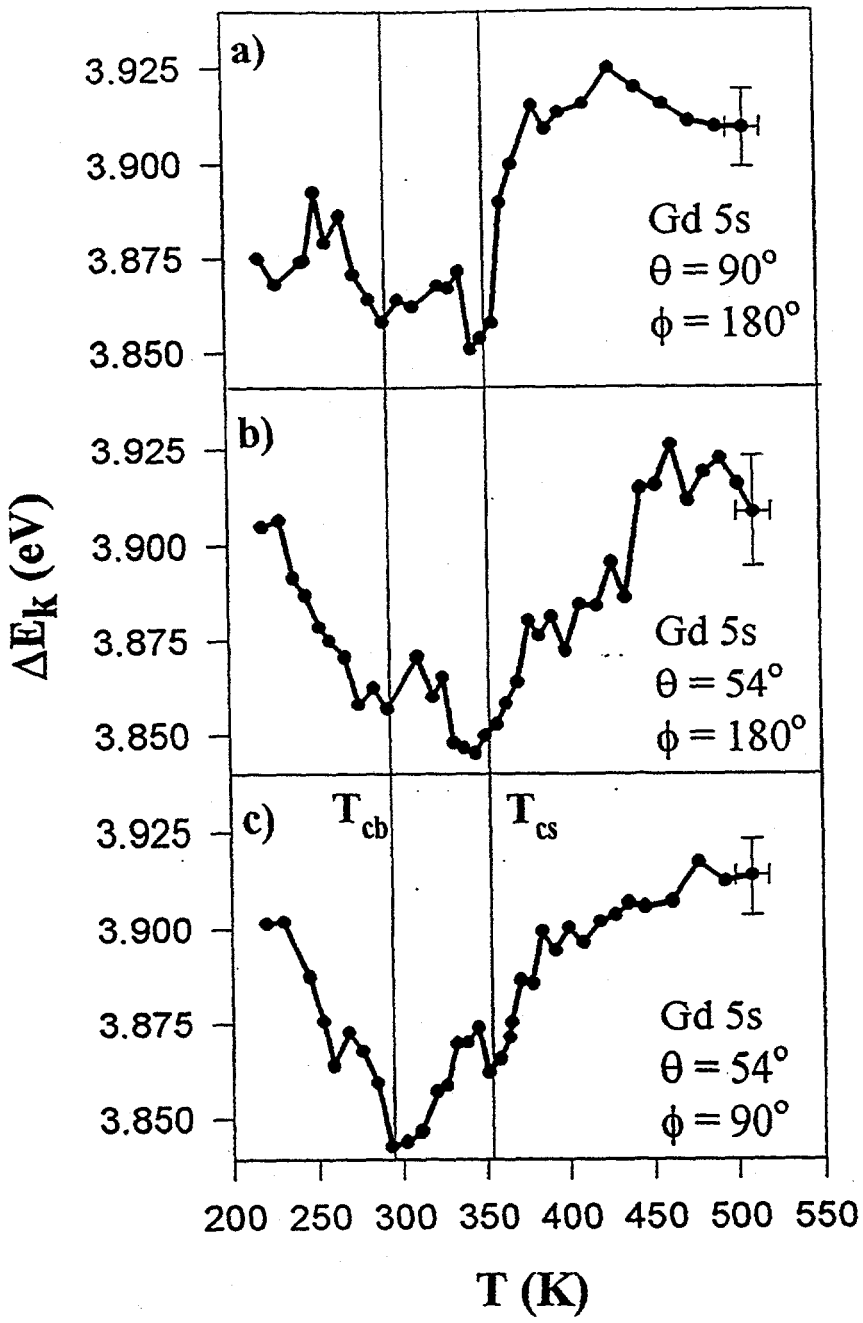

Fig. 4.12. Exchange-induced multiplet splitting ΔE_k between ^7S and ^9S as a function of temperature T for the three 5s cases in Fig. 11: (a) Case 1: Gd 5s (θ = 90°, ϕ = 180°, "$\bar{b}$" axis), (b) Case 2: Gd 5s (θ = 54°, ϕ = 180°, "$\bar{b}$" axis), and (c) Case 3: Gd 5s (θ = 54°, ϕ = 90°, equivalent to the "a" axis).

Chapter 5.

Experimental

5.I. Instrumentation

In Chapter 1, a number of techniques which have been employed in this dissertation were discussed, namely: PD, STM, LEED, AES, and MOKE. The experimental work carried out in the previous chapters involved the use of three separate instrumental systems which shall be designated systems 1,2, and 3. The STM studies of Gd on W(110) in Chapt. 2 were carried out on a stand-alone STM and LEED/AES apparatus (System 1), while the PD and SPPD work on Gd and Fe on W(110) in Chapts. 3 & 4 was performed of the Advanced Photoelectron Spectrometer/Diffractometer at beamline 9.3.2 in the Advanced Light Source (System 2). Finally, as part of this dissertation a MOKE instrument was designed and constructed for inclusion in a pre-existing apparatus incorporating XPD, LEED, and STM (System 3). Each of these instruments and some specific improvements made to them as part of this dissertation work will now be discussed in greater detail.

5.I.a. System 1: UHV STM and LEED/AES

As previously mentioned, the STM & LEED work in Chapt. 2 was performed on System 1 (Fig. 5.1). This system is equipped with a McAllister Associates UHV-STM with Digital Instruments Nanoscope II control electronics and software, an Omicron Spectaleed combined 4-grid LEED optics permitting AES measurements, a Princeton Applied Research model 5209 lock-in amplifier for detecting the AES signals, an Inficon model XTC quartz crystal thickness monitor, and an electron-bombardment-heated

molecular beam epitaxy (MBE) cell for depositing Gd. This Knudsen-type MBE cell with an external water-cooled shroud was initially borrowed from D. Weller of IBM Research, and then reproduced with a few minor improvements at LBNL for later use in all three of the experimental systems used in this thesis. System 1 includes the ability to heat samples from 300-2300 K through electron bombardment and a W-W/Re thermocouple mounted on a wobble stick which can be placed on the sample surface for direct temperature measurement. The base pressure of this system was 3×10^{-11} Torr, offering the excellent UHV conditions which were required for studying reactive surfaces such as various films of Gd on W(110). As part of this thesis work, the LEED/AES system was initially installed and brought into operation, and the Knudsen MBE cells were replicated for use in various projects.

5.I.b. System 2: Advanced Photoelectron Spectrometer/Diffractometer at the Advanced Light Source

The Advanced Photoelectron Spectrometer/Diffractometer (APSD or System 2, Fig. 5.2) at the Advanced Light Source (ALS) [1(a)], coupled with the high flux obtainable at this station from bend magnet beamline 9.3.2 [1(b)], enabled the accumulation of the high-resolution data required for the Fe/W(110) and Gd/W(110) interface PD in Chapt. 3. The high photoelectron intensities from this beamline and spectrometer/diffractometer also made possible the difficult Gd(0001) SPPD work presented in Chapt. 4, which required counting to 10^5-10^6 counts in Gd 4s and 5s spectra in order to clearly resolve the small ~1%-level changes in the multiplet peak intensity ratios. This system contains an SES-200 Scienta photoelectron spectrometer which is capable of extremely high resolution (< 3 meV with 2 eV pass energy and ~0.1% resolution over all pass energies), a four-grid LEED optics (Princeton Research, Model 118), two electron-bombardment MBE cells for

Fe and Gd (as described in connection with System 1 above), an Inficon model XTC quartz crystal thickness monitor, a dual anode Perkin Elmer (Model 04-548) Al and Mg K α x-ray source, and a two-axis sample goniometer with both electron bombardment sample heating and liquid N_2 sample cooling via a removable copper braid and cold finger (Fig. 5.3). It was thus possible to study samples over a total temperature range of 200-2300 K. The SES-200 analyzer has an angular acceptance of $\pm 5°$ in normal operation, but may be operated with a lower angular acceptance of $\pm 1°$ with the addition of a pinhole collimator which can be inserted *in situ*. The system consists of a sample preparation chamber on top of a main PS/PD measurement chamber; these two chambers are separable by a gate valve, and have base pressures of ~5-7 x 10^{-11} Torr and 7-9 x 10^{-11} Torr, respectively. An important aspect of the PS/PD analysis chamber is that the angle between the incident photons and the photoelectron spectrometer can be varied. This is achieved through rotating the entire analysis chamber and spectrometer about two differentially-pumped graphite-impregnated teflon seals (Balseal, as fabricated into the final seal assembly by APX Scientific). The chamber is connected to beamline 9.3.2 via a 13.75" diameter bellows section 19" long through which the incident light beam can pass to the sample. As previously mentioned, beamline 9.3.2 (Fig. 5.4) is a bend magnet beamline situated on sector 9 of the ALS. This beamline incorporates a spherical grating monochromator with three interchangeable gratings allowing access to a photon energy range of 30-1500 eV [1(b)]. Also included in this beamline are Au coated grids for monitoring the photon flux, a movable paddle with an aperture for calibrating and selecting circularly or linearly polarized light, adjustable entrance and exit slits for the monochromator, and a feedback mechanism correcting for beam movements by changing the pitch on the vertical focusing mirror (the second mirror in the beamline). The overall resolving power for photon energy obtainable with this beamline is $E/\Delta E \approx 10^4$. This is an excellent match with the SES-200 spectrometer, which has an energy resolving power of 10^4 with a typical 10:1 retardation of the electron energy before analysis in the

hemispherical electrostatic analyzer (which has a maximum resolving power of 10^3. The ability to achieve such high resolutions while simultaneously maintaining high photoelectron throughput was critical for studies such as the PD of the (1x1) Fe/W(110) interface (Chapt. 3) in which peaks separated by as little as 145 meV had to be clearly distinguished.

The APSD was constructed during the course of this thesis research, with the author being a member of the team that designed it and assembled it from various commercial and custom components. Special aspects in which the author was involved were the addition of the Princeton LEED optics and translation stage, the Fe and Gd MBE cells, the LN_2 sample cooling finger, the Fe core magnet for sample magnetization, the XTC quartz crystal microbalance, the software control for monitoring beam current, video CCD cameras for monitoring the polar and azimuthal angles as well as for capturing LEED images, and the debugging and installation of a fully operational software control system for the SES-200 analyzer.

5.I.c. System 3: VG ESCALAB5 with LEED, STM, & MOKE

As part of the work carried out for this dissertation, it was also necessary to design and construct a UHV MOKE apparatus to be incorporated into a pre-existing XPD, LEED, and STM system (System 3, Fig. 5.5). As can be seen in the figure, System 3 consists of two chambers separated by a gate valve. In the leftmost chamber is contained a Vacuum Generators ESCALAB5 photoelectron spectrometer equipped with a Surface Science Laboratories Model 3390 multi-channel detector, a long-travel two-axis sample goniometer which can span both chambers, and a VG dual anode Al and Mg Kα x-ray source. In the preparation chamber (right side in Fig 5.5) there is installed a a four-grid LEED optics (Princeton Research, Model 118), various electron bombardment and

evaporation MBE cells for deposition, an Inficon model XTC quartz crystal thickness monitor, a McAllister Associates UHV-STM with Digital Instruments Nanoscope II control electronics and software, and the new UHV MOKE apparatus. Also contained in the right side chamber is a sample exchange station which can contain up to 4 samples for use in the system; an MDC DG-275 wobble stick is used to effect this transfer. As the MOKE apparatus is a new instrument added for this dissertation, the design and operation of this system will be described in greater detail in the following two sections.

5.I.d. The UHV-MOKE--Design

When designing the MOKE apparatus to be installed in System 3, it was necessary to make the entire magnet assembly compact enough to fit inside the 10" diameter tube which makes up the right side chamber (Fig 5.6 shows schematics for 2 views of this chamber). It was also desirable that the experimentalist be given access to both the in-plane (longitudinal) and out of plane (polar) Kerr modes of measurement (as described also in Chapt. 1). For this to be possible, it was necessary to have a magnet assembly capable of rotating about the axis of the magnetic field direction centered between its poles. Also, it was required that the gap between the poles be >2x larger than the height of the sample on the manipulator to enable centering the sample between the poles in both modes. Figure 5.7 shows the dimensions of the magnet core constructed for this purpose. The magnet core consists of 99.95% pure Fe (purchased from Goodfellow Corp.) which gives both a low remnant magnetization (<0.5 Gauss) and a high saturation magnetization. The magnetic fields are applied to the core through two sets of windings wrapped about either end of the magnet core poles. There are a total of 10 layers of windings on each side with 32 winds per layer, thus giving a total of 320 windings per side. An additional layer of 30 windings was added to each side on a separate electrical circuit to enable

modulating the magnetic field at ~10% of its total value for ac susceptibility measurements. This layer can also be put in series with the base windings to increase the overall field output at the poles by ~10%. The windings are made up of 19 AWG UHV compatible kapton-coated wire purchased from MWS Wire Industries. The overall resistance of the coils is roughly 4 Ohms with a slight increase as the coil temperature rises. The coils are separated from the Fe core by four macor spacers, protecting the wires from damage during winding and from shorting to ground through the core. Figure 5.8 is a photograph of the assembled magnet core and windings. The performance of this magnet is quite good, putting out 1020 Gauss at 10 Amps current through the coils. The magnet can be run in three modes: 1) the main coils and modulation coils in series, 2) the main coils only, and 3) the modulation coils only. The field strength in the center between the poles as a function of coil current is displayed in Fig. 5.9 for all three modes. Below ~1000 Gauss, the variation of field with current is quite linear, giving conversion factors of current-to-field for the magnet of 102.3, 94.7, and 7.5 Gauss/Amp for modes 1, 2, and 3, respectively. Beyond 1000 Gauss, the magnetization of the Fe core begins to saturate and the variation of field with current is no longer linear. An additional concern when running such a magnet in UHV with kapton coated coils is that significant heating will occur at sustained high currents. To monitor this, a chromel-alumel thermocouple has been placed in the center of one set of coils to enable monitoring this temperature. The kapton coating is rated to 250° C in vacuum. However, it is advisable to keep the coil temperature below 200° C both to minimize outgassing during measurement and to avoid any long-term deterioration of the kapton. Hence, when setting the magnet current above 5 Amps, one should keep an eye on both the chamber pressure and coil temperature. Currents in excess of 5 A should be applied to the magnet for no more the 3-5 minutes at a time and the pressure in the chamber should not be allowed to increase by more than 5 x 10^{-10} Torr. If the temperature or pressure exceeds either of the two aforementioned conditions, the current supply should be turned of to let the magnet cool.

Placing the magnet properly inside the right chamber proved to be a difficult endeavor. It was decided to suspend the magnet through the top 2.75" port (Port 2 in Fig. 5.6) between two 8" glass viewports. This enabled the magnet to be rotated about the center of the poles by extending a solid stainless steel rod (clamped to the pole) up through a 4-way cross to an MDC Vacuum Products Corp. high-temperature rotary-motion feedthrough (Model HTBRM-275, as shown in Fig. 5.10). The coil and thermocouple leads could then be strung up through the 4-way cross to their respective current and thermocouple junction feedthroughs to connect to the outside. Figure 5.11 displays the three possible wiring arrangements on the 4-pin current feedthrough to achieve the three modes of magnet operation.

The method used to measure the Kerr rotation or ellipticity (both of which are proportional to the sample magnetization) involves the use of crossed polarizers, as discussed in Refs. 2 & 3. This method involves passing light from a high-stability linearly-polarized He-Ne laser (Spectra-Physics, Model 117 A) through a focusing lens and a prism polarizer to the sample at an incident angle $\theta_{h\upsilon}$, with the light polarization direction forming a 45° angle with respect to the plane of incidence. The light is then reflected from the sample surface and passed through a second polarizer set to within ~2° of the angle of extinction (the angle at which the second polarizer cancels the linearly polarized light reflected from the sample surface). Prior to reaching the second polarizer, the reflected light is also passed through a 1/4 or 1/2 λ retardation plate to correct for rotations arising from sources other than sample magnetization (such as viewport windows). As the ellipticity is out of phase with the Kerr rotation by 90°, using the 1/4 λ plate results in a measurement of the ellipticity while the 1/2 λ plate gives the Kerr rotation. Both the retardation plate and the second polarizer are mounted on high precision rotators since each must be adjusted in an iterative process of small rotations to achieve extinction.

From the second polarizer the beam is then passed through a final focusing lens and through a 632.8 nm bandpass filter finally sheltering a silicon photodiode (Ealing Electro-Optics, Model 28-8209) with an output of 13 V at saturation. Typical extinction voltages achievable with this arrangement are on the order of 50 mV. Tuning to 2° from extinction with the second polarizer gives base signal levels of approximately 2 to 4V for a strongly magnetic sample. The magnet field and data acquisition are handled by a 486 personal computer using an IEEE general purpose interface board (GPIB PCIIA, National Instruments, Inc.) card driven by a special program written in LabView (National Instruments, Inc.) for this purpose. (The operation of this program will be discussed in Sec. 5.I.d). The GPIB card is connected to a Hewlett Packard (model 6032A) programmable power supply as a source of coil current and a Keithley digital multimeter (DMM, model 196) to monitor the photodiode voltage. A schematic diagram of the entire MOKE apparatus is shown in Fig. 5.12. A complete list of all the elements used in this instrument is contained in Table 5.1.

5.I.d. The UHV-MOKE--Operation

The MOKE apparatus can be seen mounted to System 3 for acquiring longitudinal Kerr effect data in Fig. 5.13. The MOKE can also be mounted for measuring polar Kerr data by shifting the Spectra-Physics laser arm to a second viewport. A schematic figure depicting these two operation modes as seen from the end of the right chamber is contained in Fig. 5.14, with respective photographs of the instrument in these two conditions shown in Fig. 5.15.

To acquire MOKE data with this system,the following steps should be followed. All port numbers are shown in Figs. 5.6 & 5.14, and Fig. 5.12 serves as the reference for the assembly of electronics and optics:

1) Attach Si diode & polarizer arm to port 3.

2) Attach laser & polarizer arm to port 1 (port 5) for polar (longitudinal) MOKE mode.

3) Connect all electronics, placing output of Si diode signal into the DMM input jack of the Keithley 196. Connect GPIB lines between the PC and HP 6032 power supply, as well as between the PC and the Keithley 196 DMM (setting the DMM program mode to 31 for IEEE communication).

4) Power on the Spectra-Physics laser in intensity stabilized mode and direct the beam through one 10 mm prism polarizer to the center of the sample. Care should be taken to align the polarization direction of the beam and the polarizer at ~45° to the plane of incidence defined by the beam direction and the sample normal. The angle of incidence is also roughly 45° in this scheme. All electronics should be allowed to stabilize for at least 30 minutes prior to taking data.

5) Slowly bring the sample into position in the center between the magnet poles. Fig. 5.16 shows the proper positioning for performing longitudinal MOKE. For polar MOKE the sample should face with the sample normal upward, in the vertical direction, as shown in the bottom panel of Fig. 5.14.

6) Direct the reflected beam through the viewport of port 1 (port 5) for polar (longitudinal) MOKE mode by adjusting the tilt of the laser arm of the optics and

adjusting the horizontal and vertical position of the sample with the "x" and "y" micrometers at the rear of the manipulator arm. Be sure that the x-y locking mechanism on the leftmost port of the XPS/XPD chamber of System 3 is not engaged during this adjustment, and then lock the position after the horizontal and vertical positions are optimized. The sample normal should be at a right angle (parallel) to the magnetic field generated by the magnet poles. For a well-oriented single crystal, the longitudinal mode would be equivalent to setting θ equal to the angle required for centering the diffraction pattern in the LEED optics, with the polar mode being 90° from this. Care should be taken not to rotate θ from either of these angle settings, as a mixture of the longitudinal and polar modes would then result.

7) The reflected beam should then be passed through the center of the mica retardation plate, the second prism polarizer (both mounted on precision rotators), the second refocusing lens, and finally onto the Si photodiode shaded by the 632.8 nm filter. The filter stops background light from reaching the photodiode. The 1/4 (1/2) λ retardation plate should be used for Kerr ellipticity (rotation) detection. The signal intensity is stronger for ellipticity measurements and is therefore recommended for studies not requiring the quantitative measurement of the rotation, since both ellipticity and rotation are proportional to the sample magnetization.

8) Align all of the optics such that the beam passes normal to the surface of the optical elements (a requirement for good extinction characteristics). This can be achieved by rotating the elements to bring the weak reflected beam (from a given element) back onto the spot where the primary beam exits the viewport.

9) Rotate the retardation plate and the second prism polarizer incrementally to reduce the signal intensity from the Si photodiode. The signal intensity should be reduced down to

~50 mV. False minima may appear of a few 100's of mV in minimum intensity. This is not a true extinction and the user should try rotating one of these two elements by ~90° and attempt to achieve extinction again.

10) Having achieved extinction, note the angles of the 2nd prism polarizer and retardation and then rotate the 2nd prism polarizer an additional 2° in either direction. This will set the base point from which the rotation or ellipticity will be measured. In a strongly magnetic sample, the signal level will now be on the order of a few volts.

11) Connect one power lead from the current source to pin 1 on the power feedthrough (Fig. 5.11) and the second lead to ground. Attach a thick ground wire from ground to pin 4 and a jumper wire between pins 2 and 3. This should run the main and the modulation coils in series for the maximum field output as a function of current.

12) Start the SMOKE4.vi program in labview under the c:\SMOKE directory on the MOKE PC. Figure 5.17 shows the operation panel for this program. Enter in the desired maximum field H_{max}, the number of steps between H = 0 and H = H_{max}, the number of samples per step (the program averages over multiple samples), and the DMM filter level (reduces random noise). Select the coil mode to which the magnet is set.

14) To start the data acquisition, press the start arrow in the upper left hand corner of the Labview control window. As multiple sweeps have not yet been enabled in the software, a balance must be struck between the number of samples per step and total number of steps (total scan time increases with these values) and the thermal drift of the electronics to make the overall signal-to-noise acceptable. Scans lasting longer than 5 minutes may result in significant levels of thermal drift. Signal averaging can be performed by summing

up various single scans taken with identical parameters for the same conditions (tedious, but perhaps the best option for samples with small magnetizations).

15) The MOKE scan will start the magnet at H_{max} and step down to H = 0. At this point the program will pause and ask for the magnetic field direction to be switched. This must presently be done manually by interchanging the current and ground leads to the magnet power feedthrough. The need for this arises from the limitation of the HP supply which is not bipolar. Hitting the 'enter' key after switching the leads then allows the computer to sweep from H = 0 to H = $-H_{max}$ and then back up to H = 0 again. The program will then pause and ask for the leads to be changed once more, requiring the operator to repeat the previous exchange of the leads. Hitting 'enter' once again after this is accomplished will then allow the program to complete the scan with the magnetic field sweeping from H = 0 to H = H_{max}. After completing the scan, the program then asks the user to save the data in a text file with the filename entered by the user. (Just as this thesis was being completed, a simple switching circuit to enable the Labview program to control the effective current polarity delivered to the magnet was initiated with J. Severns of LBNL Engineering. Once this is completed and the Labview software modified slightly to accommodate it, a full sweep from 0 to H_{max} to $-H_{max}$ and back to H_{max} should be possible without operator intervention.)

There are a number of limitations which must be kept in mind while operating this particular instrument:

1) Never exceed 10.0 amps current in the magnet coils.

2) Never exceed 5.0 amps current for prolonged periods of time (i.e. longer than 5 min.) as the coils will heat excessively, and this could result in evaporating the kapton insulation

on the coil wire. As the coil resistance increases with temperature, heating of the coils also may result in a runaway feedback loop in which the HP power supply continually attempts to achieve a given current, yet lacks the power to do so due to the increase resistivity without increasing voltage. This could result in a runaway situation in which the coils overheat catastrophically.

3) Always monitor the coil current on the HP power supply. If the system is not behaving properly, turn off the power to this supply. This will prevent any catastrophic failures in the vacuum system (as described above).

4) If the pressure rises by more than 1.0×10^{-9} mbar (with a base pressure in the low 10^{-10}'s), the coils have become overly warm and should be allowed to cool.

There are a number of steps which could be taken in the future to improve the overall performance of this instrument and these are highly recommended:

1) Replace the HP 6032A power supply with a KEPCO BOP 50-8M 400 Watt supply. This will limit the system to a maximum field of 800 Gauss, but will have much faster sweep times with full bipolar performance negating the need for manual (or computer controlled) field switching.

2) Replace the 486-33 MHz PC with a Pentium 75 MHz or greater computer. The demands of Labview are a bit too great on the 486 PC, resulting in slower acquisition times.

3) Incorporate multiple sweeps for signal averaging in the MOKE software. This will improve the overall sensitivity of the system and help to reduce the effect of thermal drift.

5.I.e. The UHV-MOKE--Initial Tests

To test the performance of the MOKE instrument, Fe was deposited on two different non-magnetic substrates for measurement: W(110) and Si(111). Fig 5.18 displays the longitudinal Kerr ellipticity ε taken from a 13 Å (~6ML) Fe film grown on W(110). Notice the extremely sharp transition at the coercive fields H_c, which are found to be 20 Gauss. One advantage of the HP 6032A power supply is the ability to set the coil current to within 0.01 Amps. This enables determining H_c to within ± 1 Gauss. Shown in Fig. 5.19(a) is the longitudinal ε of a 25 Å (~13 ML) Fe film grown on Si(111) at room temperature. The signal is somewhat weaker (roughly 1/2) of that from the Fe/W(110) sample shown previously. This is probably due to Fe-Si alloying at the interface, which creates a non-magnetic or weakly-magnetic region between the magnetic Fe and the non-magnetic Si(111). The coercive field here is also much reduced to $H_c = 4 \pm 1$ Gauss. Annealing this film to 700 K for 5 minutes completely eliminates the Kerr ellipticity, as seen in Fig. 5.19(b), showing that all of the Fe is now part of a thick, non-magnetic iron silicide which has been formed on the Si(111) substrate. Fe films thinner than 10 Å on Si(111) also were found to display no measurable Kerr rotation or ellipticity due to alloying of the Fe and Si.

These test data thus fully demonstrate the capabilities of this MOKE system, and it should prove useful in future studies of various magnetic films by our group, particularly if some/all of the improvements described above are implemented.

5.II Quantitave Analysis by AES, STM, and PS

When studying thin films and surfaces, it is often critical to precisely determine the overlayer coverage, as well as the level of surface contamination from residual gases and

other sources of impurities. The three techniques of AES, STM, and PS are each capable of giving such information, although in different and complementary ways. In addition, the coverage for deposited films can be estimated by determining the deposition rate of the evaporation cell with a quartz crystal thickness monitor. The exact methods by which these techniques were employed in this dissertation for such determinations will be discussed below.

5.II.a. AES Analysis

In the STM and LEED study of Gd on W(110) discussed in Chapt. 2, AES was used to monitor the C and O contamination levels present on the W(110) substrate prior to film deposition and on the Gd film after deposition. Also, for films of coverage less than 3 ML, AES was used to monitor film thickness as well. The method used to perform quantitative analysis with AES is similar to that used in XPS, as laid out in Ref. 4 for thin non-attenuating overlayers of less than a few ML's thickness. The relevant equation is:

$$\frac{s'}{s} = \frac{N_l}{N_k} \cdot \frac{d\sigma_k / d\Omega}{d\sigma_\ell / d\Omega} \cdot \frac{\Lambda_e \sin\theta}{d} \qquad [5.1]$$

where s'/s is the fractional monolayer coverage of the overlayer, $d\sigma_k/d\Omega$ is the differential cross section for producing the kth Auger peak in the substrate, $d\sigma_\ell/d\Omega$ is the differential cross section for producing the ℓth Auger peak in the overlayer, N_k (N_ℓ) is the peak to peak intensity of the substrate (overlayer) Auger peak in the differentiated spectrum, Λ_e is the Auger electron attenuation length in the substrate at kinetic energy E_k, d is the interlayer spacing for the substrate along the surface normal, and θ is the polar Auger electron emission angle measured from the sample surface. The Auger cross sections $d\sigma_k/d\Omega$ and $d\sigma_\ell/d\Omega$ must in general include both a primary excitation factor and a

backscattering factor, and are difficult to calculate from first principles accurately. However, the ratio of these differential cross sections can be empirically estimated by measuring the bulk-like signal intensity for the substrate peaks that have been chosen for this analysis under identical conditions for both a very thick overlayer and the clean single-crystal substrate. The measured intensities should then be corrected by dividing by the respective Auger electron attenuation lengths. When this is not possible (i.e. when considering contaminants), the relative ratios can be estimated from the Auger sensitivities contained in Ref. 5. The Auger electron attenuation length in the substrate and overlayer can be calculated according the method developed by Tanuma et al. [6]. Table 5.2 contains the calculated values obtained for the pertinent Auger lines from W, Gd, C, and O. The Auger spectra are always collected at a mean value of normal emission with the Omicron LEED/AES system (actually averaging over the $\pm 51.5^{o}$ accepted by the 4-grid optics). So, using the values in Table 5.2 and inserting them into Eq. 5.1 gives:

O coverage on W using the O 503 eV and the W 350 eV lines,

$$\frac{s'}{s} = (0.11)\frac{N_{O(503eV)}}{N_{W(350eV)}} \qquad [5.2.a]$$

C coverage on W using the C 271 eV and W 350 eV lines,

$$\frac{s'}{s} = (0.32)\frac{N_{C(271eV)}}{N_{W(350eV)}} \qquad [5.2.b]$$

Gd coverage on W using the Gd 138 eV and W 179 eV lines,

$$\frac{s'}{s} = (0.74)\frac{N_{Gd(138eV)}}{N_{W(179eV)}} \qquad [5.2.c]$$

As examples of applying this type of analysis, Figure 5.20 contains Auger spectra taken from a W(110) sample before and after cleaning the sample through the oxidation and high temperature flashing cycle described in previous chapters and in more detail in the next section. Using Eqs. 5.2(a) and (b), the total contamination coverages arrived at before cleaning are 0.18 ML of C and 0.05 ML of O. After cleaning the sample, the coverages have been reduced to 0.03 ML of C and <0.01 ML of O. Figure 5.21 shows an AES spectrum taken from a W(110) substrate with approximately 0.83 ML of Gd deposited on it as determined by the quartz crystal thickness monitor (QCM). Determining the Gd coverage with Eq. 5.2(c) gives a total overlayer thickness of 0.79 ML, in close agreement with the prediction from the QCM.

5.II.b. STM Analysis

When attempting to determine the coverage for films thicker than 1 ML of Gd on W(110) for the morphology study in Chapt. 2, it was often useful to employ the STM for films containing islands. In order to perform such a calculation, it was necessary to determine the percentage of the film surface that existed in islands and the average island height. To do this, the Nanoscope II software has some very convenient analysis subroutines. One such routine is the 'bearing' menu in the data analysis portion of the program. Figure 5.22 shows the 'bearing' results for a nominally 2.5 ML (as determined by the QCM) Gd film on W(110) after a 530 K anneal. Using the break in the height distribution of the surface, one can distinguish between the percentage of the surface in islands (33.50% in the figure) from the percentage of the surface without islands. The average island height is then determined by examining single STM line scans of tip height when passing over these islands (Fig. 5.23). These operations must be performed over many different constant current images from various parts of the sample surface to be

statistically reliable and fully representative of the average surface. In the case of the previously shown film, the average percentage of surface existing in islands P is 35.4 ± 3.0% and the average island height t_{av} = 1.75 ± 0.29 nm. The total coverage existing in islands (in monolayers) is then equal to:

$$\theta_{isl} = \frac{Pt_{av}}{d} \qquad [5.3]$$

where d is the interlayer spacing of the Gd monolayers in the island (0.289 nm). This gives a coverage of 2.1 ML existing in the islands. As these films grow in the Stranski-Krastanov mode with one base monolayer of Gd forming with islands on top, this first monolayer must be added to determine the total coverage of Gd. This then gives a result of 3.1 ML as determined by STM as compared to the 2.5 ML predicted by the QCM: these two very different methods for estimating coverages are thus in good agreement. Table 5.3 contains the various coverages as determined by QCM and STM for some of the 530 K and 710 K annealed films used in Chapt. 2. All of the STM tip heights measured were calibrated with respect to W(110) monatomic step heights from the clean surface while the horizontal distances were calibrated using the known periodicities of highly ordered pyrolitic graphite. The agreement between the two sets of coverages is overall very good for all of the layers shown.

5.II.c. XPS Analysis

In the PD and SPPD studies contained in Chapts. 3 & 4, photoelectron spectroscopy was used to monitor sample cleanliness and overlayer coverages. The calculation for coverage is the same as that used previously for AES, except that the cross sections are now for photoelectron emission and much easier to calculate from first principles, and the

effect of retardation in the photoelectron hemispherical analyzer is also included via an energy-dependent transmission function [4]:

$$\frac{s'}{s} = \frac{N_l}{N_k} \cdot \left(\frac{d\sigma_k / d\Omega}{d\sigma_\ell / d\Omega} \right) \left(\frac{E_k^\ell}{E_k^k} \right)^x \left(\frac{\Lambda_e \sin\theta}{d} \right) \qquad [5.4]$$

where x is the exponent describing the effect of retardation (α = 0.15 for the Scienta SES200), and E_k^ℓ and E_k^k are the kinetic energies of the overlayer and substrate photoelectron peaks, respectively. The differential crossections are calculated in the standard manner [4]:

$$\frac{d\sigma}{d\Omega} = \frac{\sigma}{4\pi}\left[1 + \frac{\beta}{2}\left(\frac{3}{2}\sin^2\alpha - 1\right)\right] \text{ (for unpolarized light)} \qquad [5.5a]$$

$$\frac{d\sigma}{d\Omega} = \frac{\sigma}{4\pi}\left[1 + \beta\left(\frac{3}{2}\cos^2\gamma + \frac{1}{2}\right)\right] \quad \text{(for polarized light)} \qquad [5.5b]$$

where σ is the total cross-section of the photoelectron peak, β is the asymmetry parameter for the photoelectron peak, α is the angle between the incident light and the emitted photoelectron (α = 54.74°), and γ is the angle between the light polarization direction and the emission direction (γ = 30°). Convenient tabulations of σ and β appear in the literature [7]. Table 5.4 contains the calculated differential cross sections, total cross sections, and asymmetry parameters for the various photoelectron peaks and photon energies used. Electron attenuation lengths were calculated with the method of Tanuma et al. [6], the results of which are: 17.9 Å for 1454 eV electrons in W (W 4f excited by Al Kα) and 12.4 Å for 558 eV electrons in Gd (Gd 4d excited by 700 eV photons).

As an example of this kind of analysis, Figure 5.24 contains a typical photoelectron spectrum taken from a 700 K annealed, 1.5 ML (as determined by QCM) (1x1) Fe film deposited on W(110) eight hours after the original deposition. This spectrum was taken using Al Kα excitation with hν = 1486.6 eV at θ = 90°. The intensities for the relevant photoelectron peaks are: 8.03×10^2 cts for Fe 2p, 1.76×10^3 for W 4f, 1.50×10^1, for O 1s, and less than 5 cts for the C 1s. Using Eq. 5.4 and the values from Table 5.4, the various coverages are calculated to be: 1.44 ML of Fe, 0.15 ML of O, and < 0.15 ML of C (below the detection limit for the low statistics of this particular scan). The agreement between the Fe coverage predicted by the QCM and that measured by PS is quite good.

For the Gd SPPD studies, the oxygen contamination was monitored by measuring the 0 2p peak which occurs in the valence band (VB) at a binding energy of ~5 eV. The valence band was then measured before and after each SPPD run with a photon energy of 38 eV at normal emission. To enable using the valence band for quantitative measurement of the oxygen coverage, a photoelectron spectrum of a slightly contaminated Gd(0001) surface was taken at hυ = 700 eV with a valence band spectrum taken at hυ = 38 eV within five minutes of completing the higher energy scan (Fig. 5.25). Using Eq. 5.4 with the appropriate values from Table 5.4 for oxygen coverage on Gd(0001) at 700 eV photon energy, the total oxygen contamination is measured as being ~0.077 ML for this film. Matching the relative intensities of the O 1s to the Gd 4d at 700 eV photon energy with the O 2p to the Gd 4f in the valence band at 38 eV photon energy gives an equation for determining the O coverage from the valence band: $\theta_{oxy} = (0.0578\ ML)(N_{O2p}/N_{Gd4f})$. This relationship can also be semi-quantitatively checked by substituting the relevant cross sections, mean free path, and interlayer spacing into Eq. 5.4, which yields a prefactor of (0.260 ML) that is within a factor of four of the more accurate empirical number. However, in this low kinetic energy regime the calculation becomes less reliable due to the strong photoelectron attenuation and the fact that the O 2p excitation is from a delocalized

valence state which is highly influenced by the Gd surface as compared to a well defined core state (e.g. the O 1s) As the magnetic characteristics of the Gd (0001) surface are highly sensitive to contamination, it was important to monitor these levels closely. The results of such analyses showed that the oxygen contamination levels never exceeded 0.054 ML during any of the temperature-dependent SPPD data reported in Chapt. 4, and they were in the range of 0.02-0.04 ML during most of each scan.

5.III Experimental Procedures

5.III.a. W(110) single crystal preparation

The W(110) single crystals used in these experiments were cut from a 0.5" diameter rod and mechanically polished with diamond polishing pastes to within 0.5° of [110] as measured by Laue and X-ray diffraction. The samples were then electropolished in a 0.1 molar NaOH solution with a 6 V potential held between the crystal and a graphite electrode for 5 minutes. The resulting crystals had large amounts of residual carbon and oxygen on the surface as measured by XPS and AES. Flashing the crystals in UHV at 2000° C was found to remove all of the oxygen, yet left ~0.2 ML of carbon. Further flashing resulted in no reduction in the carbon levels, as this element evolves from the W bulk during high temperature flashes. In order to deplete the carbon in the near surface region of the W(110) crystals it was necessary to perform oxidation and flashing cycles. The crystal was first flashed to 2000° C for 5 sec. and then allowed to cool to 1300° C. At this point, O_2 was backfilled into the chamber at a pressure of 5×10^{-7} Torr. After 20 min. of oxidation, the sample was allowed to cool for 10 min. before evacuating the O_2 from the chamber. This resulted in a (1x1) oxide layer on the surface of the crystal with no detectable carbon. When UHV conditions were recovered, the sample was then

flashed for 5 sec. at 2000° C to remove the oxide layer. The resulting W(110) surface contained less than 0.05 ML of carbon and oxygen combined.

5.III.b Gd & Fe deposition

The Gd and Fe films used in these studies were prepared by molecular beam epitaxy (MBE) in UHV conditions. The deposition cells used in the film preparation utilize electron bombardment of W crucibles containing 99.95% pure Fe wire or 99.5% pure Gd strips. The entire filament/crucible assembly is surrounded by a water cooled radiation jacket to minimize outgassing, and its design is described elsewhere [8]. For the preparation of clean films, it was found necessary to have a base pressure of $<7 \times 10^{-11}$ Torr and a maximum pressure of $<2 \times 10^{-10}$ Torr during deposition. The deposition rates of these cells are quite stable for a given deposition power. Typically, a deposition power of 100 Watts (500 V with 20 mA emission current) resulted in a deposition rate of 0.20 - 0.40 ML/min for these materials.

5.III.c. Determining the W(110) substrate orientation

In all of the experiments carried out for this dissertation, it was of critical importance to determine with a high degree of precision the low index directions of the W(110) substrate. The two techniques best employed to this end are XPD and LEED. Fig. 5.26 contains a typical W 4f azimuthal XPD pattern obtained from a W(110) substrate at a polar angle θ of 45° and with Al Kα excitation. A 3.0^{o} tube array was used to improve angular resolution [9], which was $\sim\pm 2.0^{o}$ for this case. Clearly visible are two mirror planes, one of which lies along the [001] direction in the sample surface plane (as indicated in the figure). Though LEED lacks the precision of XPD, it is often a good starting point and consistency check. Fig. 5.27 shows a typical LEED pattern taken from a clean

W(110) surface, with the [001] direction again indicated. As the epitaxy of the overlayers is determined by the crystallographic directions of the substrate, proper identification of the substrate orientation also determined low index directions for the deposited overlayer. XPD and LEED measurements were also performed on thick overlayer films such as Gd(0001) to check the epitaxial registry.

References:

[1] (a) C.S. Fadley, M.A. Van Hove, Z. Hussain, and A.P. Kaduwela, J. Electron Spectrosc. 75, 273 (1995); (b) Z. Hussain, W. R. A. Huff, S. A. Keller, E. J. Moller, P. A. Heimann, W. McKinney, H. A. Padmore, C. S. Fadley, and D. A. Shirley, J. Elec. Spec. and Rel. Phen. **80**, 401 (1996).

[2] J.-P. Qian and G.-C. Wang, J. Vac. Sci. & Technol. **A 8**, 4117 (1990).

[3] Dr. Z. Q. Qiu, Professor of Physics, U. C. Berkeley, private communication.

[4] C. S. Fadley, "Basic Concepts of Photo-electron Spectroscopy," appearing in Electron Spectroscopy, Theory, Techniques and Applications Vol. 2, eds. C. R. Brundle and A. D. Baker, (Pergamon Press, 1978).

[5] R. Shimizu and S. Ichimura, Quantitative Analysis by Auger Electron Spectroscopy, Toyota Foundation Research Report I-006, No. 76-0175' 81.03.

[6] S. Tanuma, C. J. Powell, and D. R. Penn, Surf. & Interf. Anal. **17**, 911 (1991); C.J. Powell, private communication.

[7] S.M. Goldberg, C.S. Fadley, and S. Kono, J. Electron Spectrosc. **21**, 285 (1981); J.J Yeh and I. Lindau, Atomic Data and Nuclear Data Tables **32**, 1 (1985).

[8] D. Weller and D. Pappas, private communication.

[9] R.C. White, C. S. Fadley, and R. Trehan, J. Electron Spectrosc. **41**, 95 (1986).

Table 5.1. Elements required for MOKE instrument operation

Element	Quantity	Description
Gateway 486, 33MHz PC	1	Data acquisition and magnet control unit
Spectra-Physics, 117A Laser	1	He-Ne, linearly polarized (2.7W) laser w/ intensity stabilization
HP6032A power supply	1	GPIB programmable, 60V/50A supply
Kiethley 196 DMM	1	GPIB programmable, digital multi-meter
Ealing Electro-optics Si photodiode and supply (Model 28-8209 & 28-7581)	1ea	0-13V output Si photodiode
Oriel Corp.:		
Prism polarizer (#25202)	2	10mm prism polarizer
Retardation plate (#25450)	1	1/2 λ mica retardation plate
Retardation plate (#25420)	1	1/4 λ mica retardation plate
Focusing lens (#40340)	1	f = 50 mm lens
Focusing lens (#40400)	1	f = 350 mm lens
Precision rotater (#13011)	2	rotater for retardation plate and 2nd polarizer
Polarizer rotater (#25020)	1	rotater for 1st polarizer
X translator (#14781)	1	translation stage for horizontal Si diode alignment
Z translator (#16021)	1	translation stage for vertical Si diode alignment
Ealing Electro-optics 632.8 nm filter (Model 35-8630)	1	25.4 mm diameter, 632.8 nm filter
National Instruments IEEE 488.2 GPIB card (Model PCIIA)	1	communications card for driving GPIB instruments

Table 5.2. Values for Auger coverage calculation

Auger Peaks	Empirical $(d\sigma_k/d\Omega)/(d\sigma_\ell/d\Omega)$	Λ_e
Gd(138eV) on W(179 eV) (Gd on bulk W)	0.3460	4.8 Å
O (503 eV) on W(350 eV) (O contaminant on W)	0.0377	6.7 Å
C (271 eV) on W(350 eV) (C contaminant on W)	0.1075	6.7 Å

Table 5.3. QCM and STM coverage determinations for selected Gd films grown on W(110)

θ_{QCM}(ML)	T_{anneal}(K)	P (%)± 3.0	A_{av} (nm^2)	t_{av} (nm)	θ_{STM}(ML)
1.3	530	12.0	10.9	0.45	1.2
1.9	530	27.8	301	1.18	1.9
2.5	530	35.4	810	1.75	3.1
3.2	530	36.0	1.09×10^3	2.52	3.9
3.8	530	36.5	1.42×10^3	2.52	3.9
4.4	530	27.6	4.78×10^3	3.50	4.1
5.1	530	33.5	7.16×10^3	3.74	5.1
6.0	530	26.9	1.32×10^4	4.97	5.4
1.9	710	13.5	1.42×10^3	1.93	1.9
6.4	710	19.5	1.63×10^4	7.87	6.3
11.0	710	31.6	8.40×10^4	11.3	12.4

Table 5.4 Calculated differential crossections for relevant photoelectron peaks

Peak	hυ (eV)	E_k (eV)	σ	β	dσ/dΩ
W 4f	1486.6	1454.1	0.1449	1.045	1.35×10^{-2}
Gd 4d	1486.6	1344.3	0.1422	1.328	1.38×10^{-2}
O 1s	1486.6	956.6	0.0400	2.000	4.22×10^{-3}
C 1s	1486.6	1202.1	0.0130	2.000	1.37×10^{-3}
Fe 2p	1486.6	773.6	0.2216	1.453	2.18×10^{-2}
Gd 4d	700.0	557.7	0.5666	1.075	5.30×10^{-2}
O 1s	700.0	170.0	0.3082	2.000	3.25×10^{-2}
C 1s	700.0	415.5	0.1225	2.000	1.29×10^{-2}

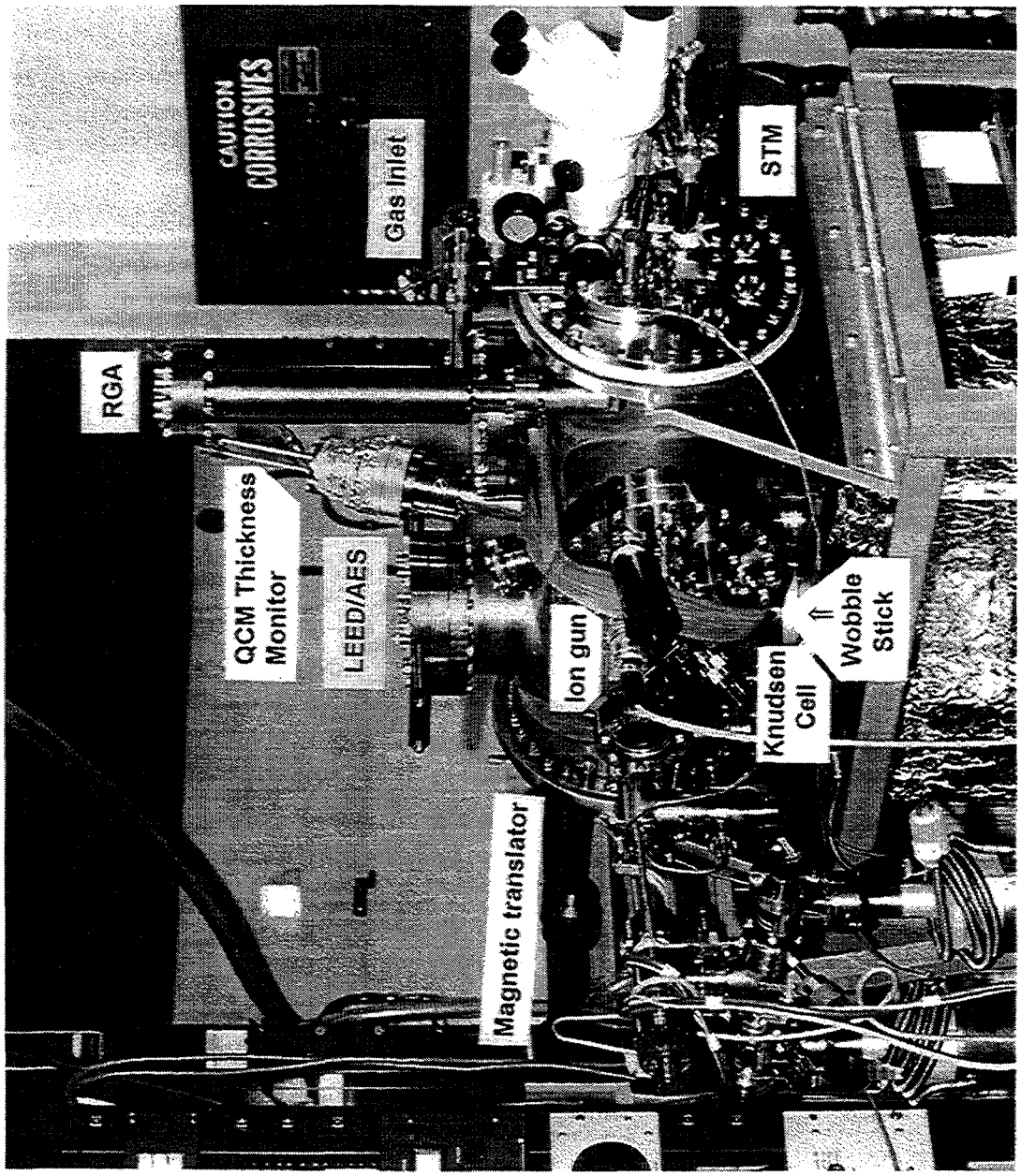

Fig. 5.1 Photograph of stand-alone STM - LEED/AES (System 1)

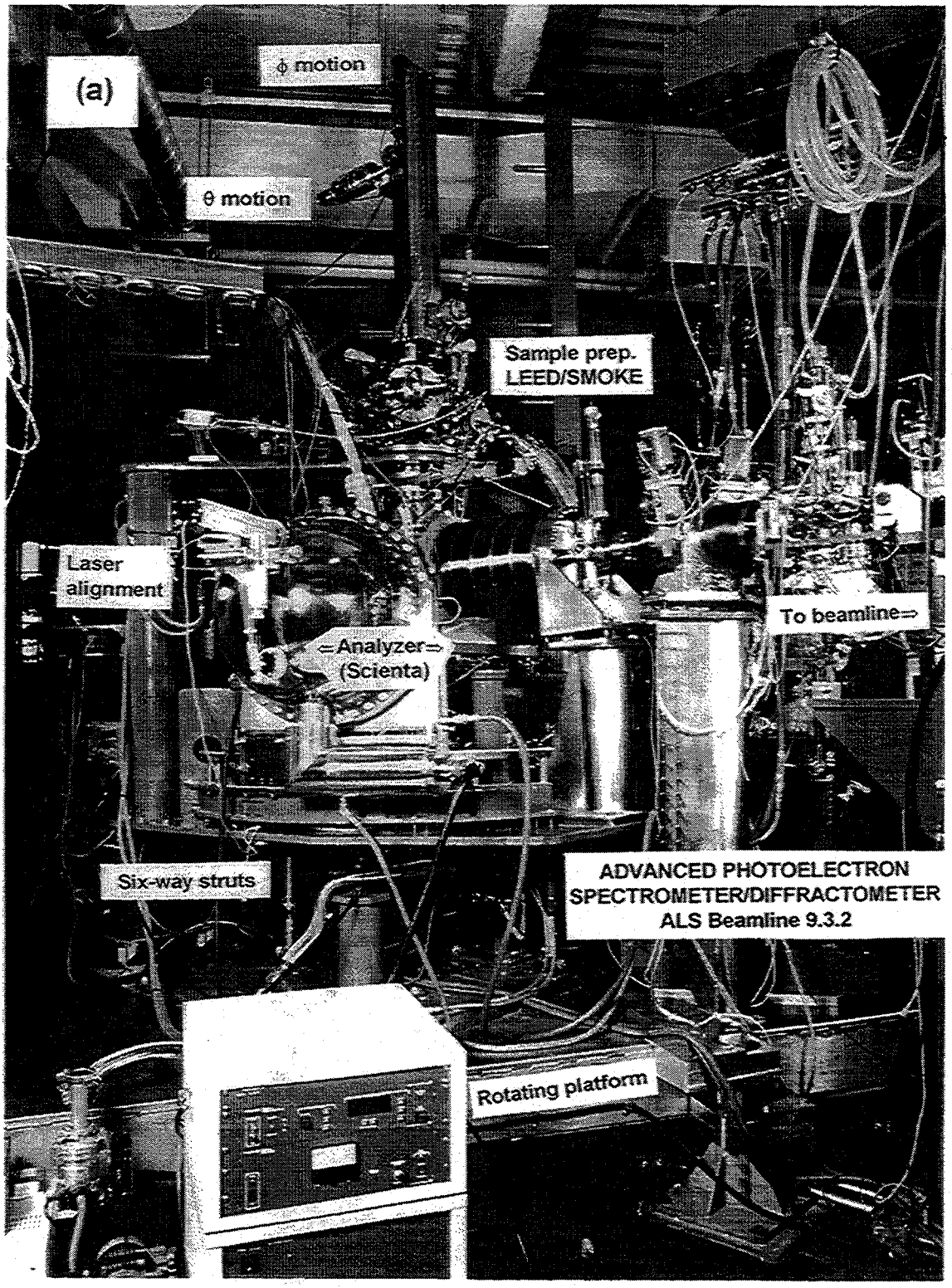

Fig. 5.2 Photographs of Advanced Photoelectron Spectrometer/Diffractometer (APSD or System 2)

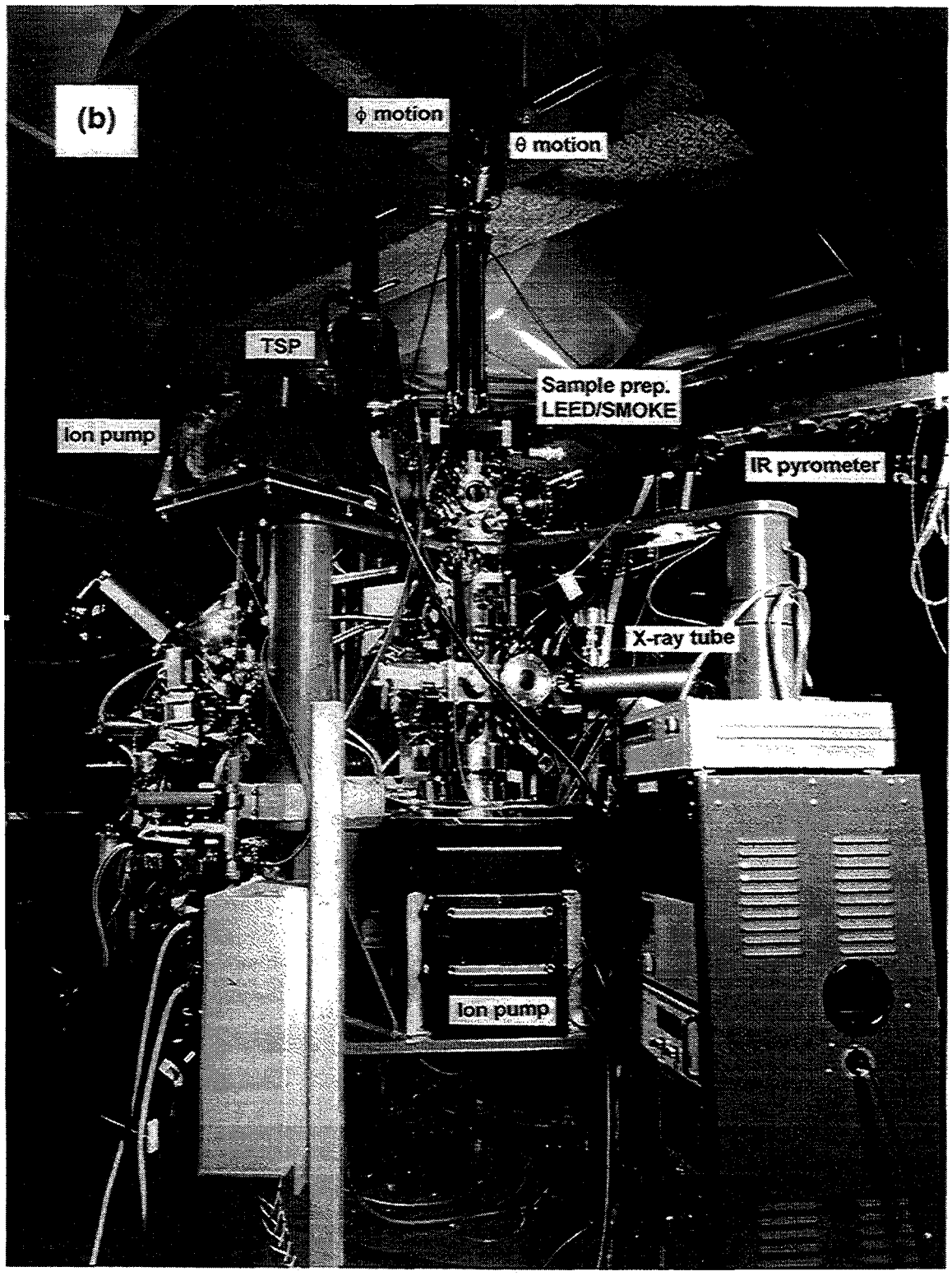
(b)
ϕ motion
θ motion
TSP
Sample prep.
LEED/SMOKE
Ion pump
IR pyrometer
X-ray tube
Ion pump

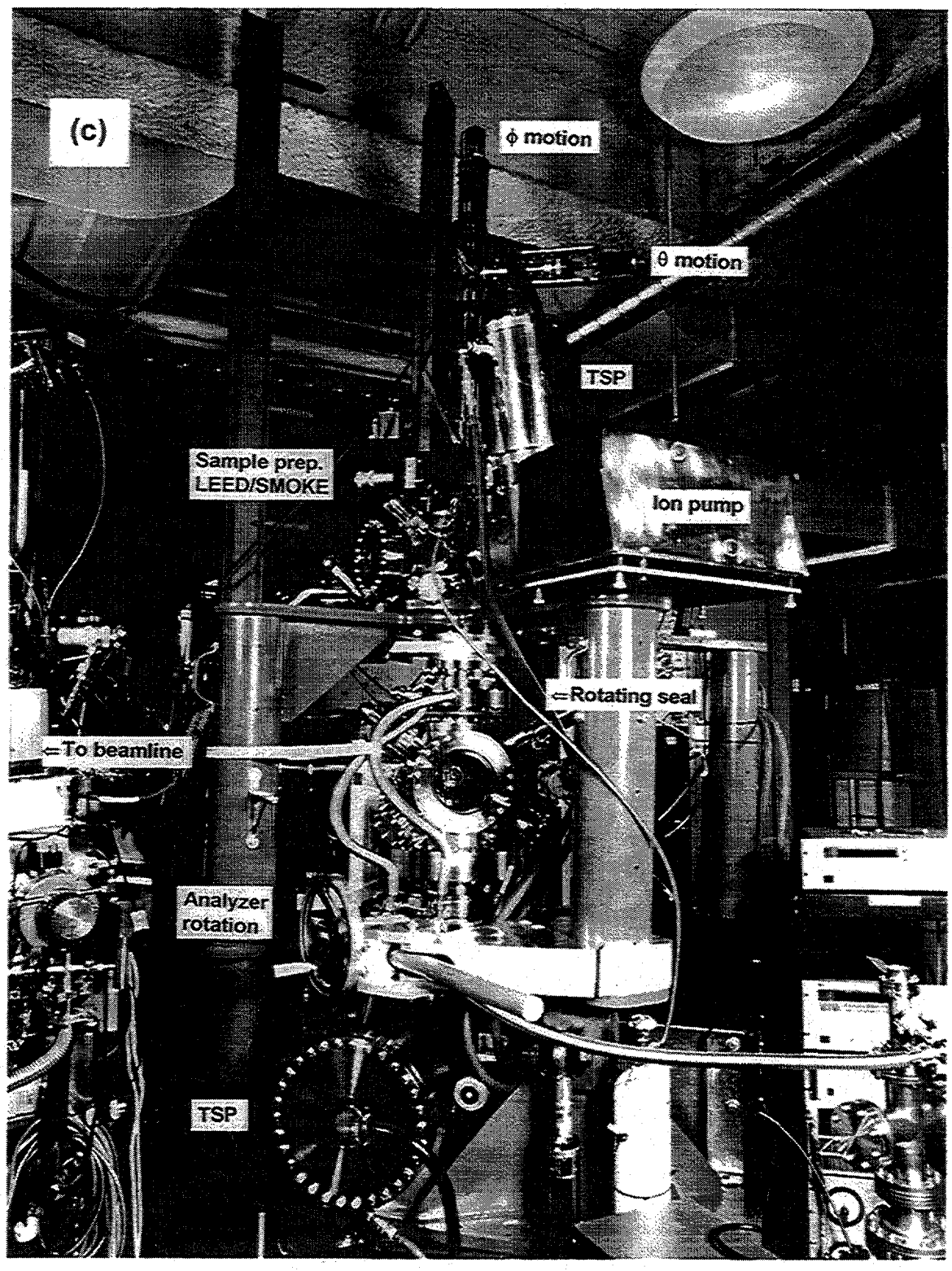
(c)
ϕ motion
θ motion
TSP
Sample prep.
LEED/SMOKE
Ion pump
⇐Rotating seal
⇐To beamline
Analyzer
rotation
TSP

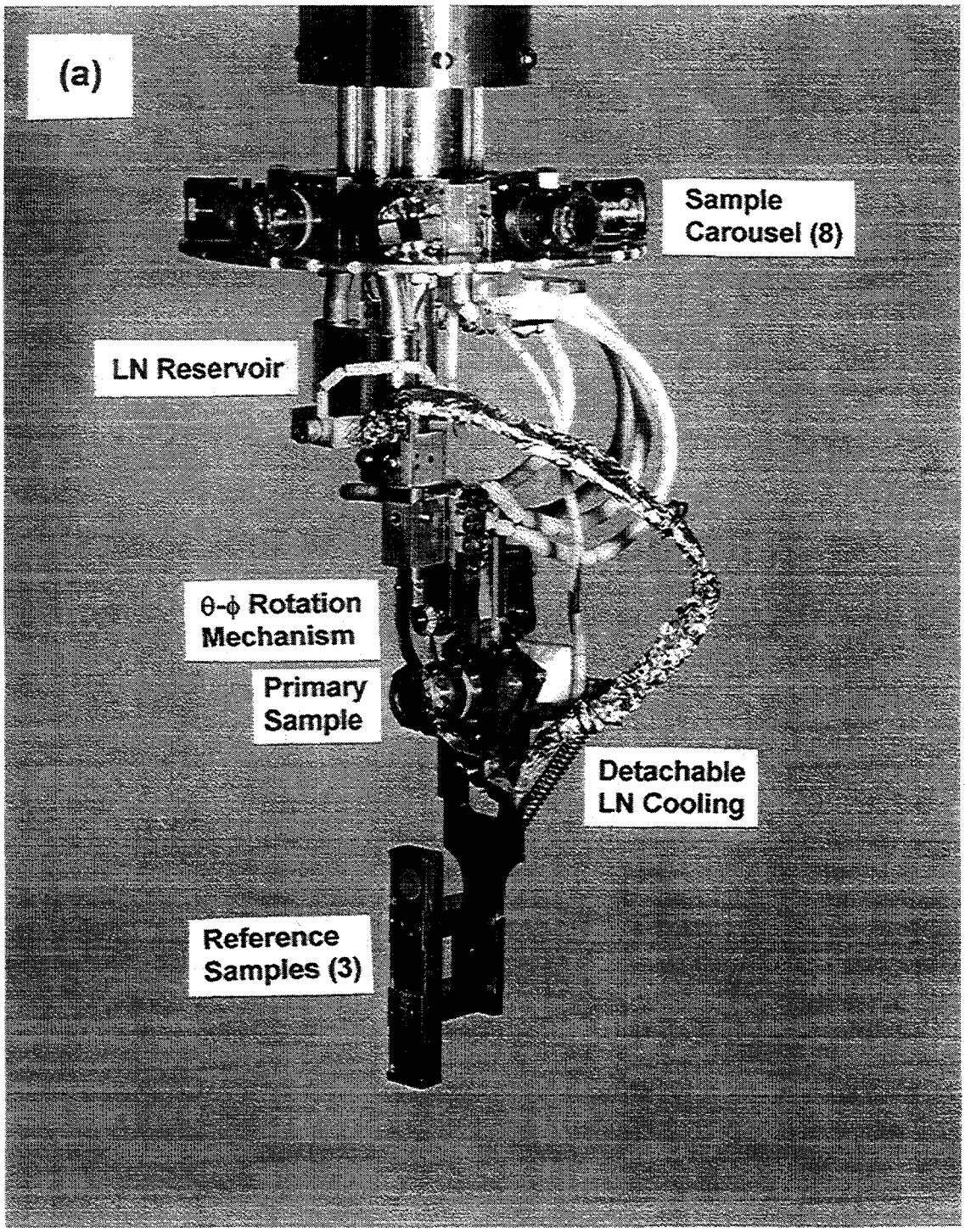

Fig. 5.3 Photographs of two axis sample goniometer with sample cooling mechanism, as installed on APSD.

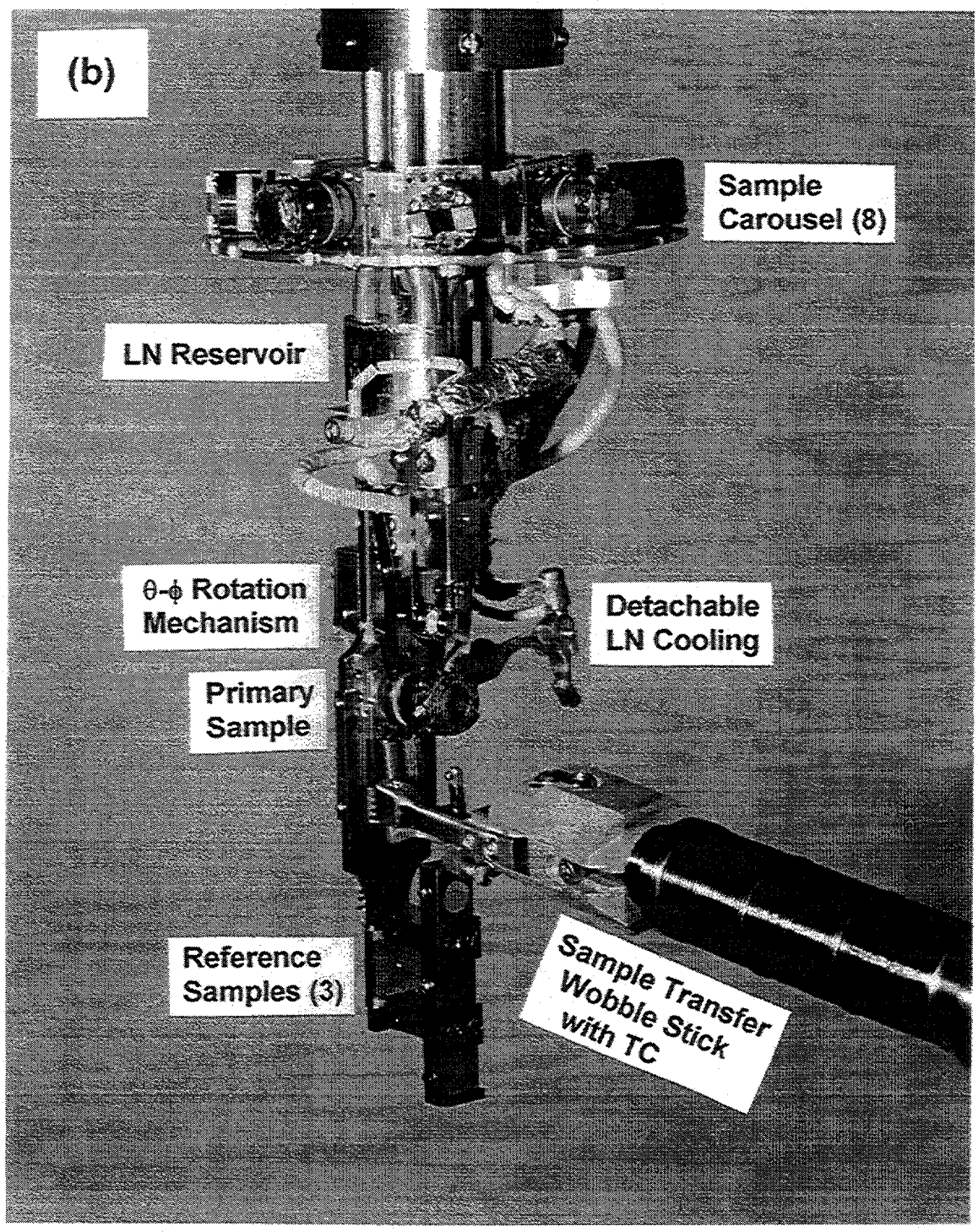
(b)
Sample Carousel (8)
LN Reservoir
θ-ϕ Rotation Mechanism
Detachable LN Cooling
Primary Sample
Reference Samples (3)
Sample Transfer Wobble Stick with TC

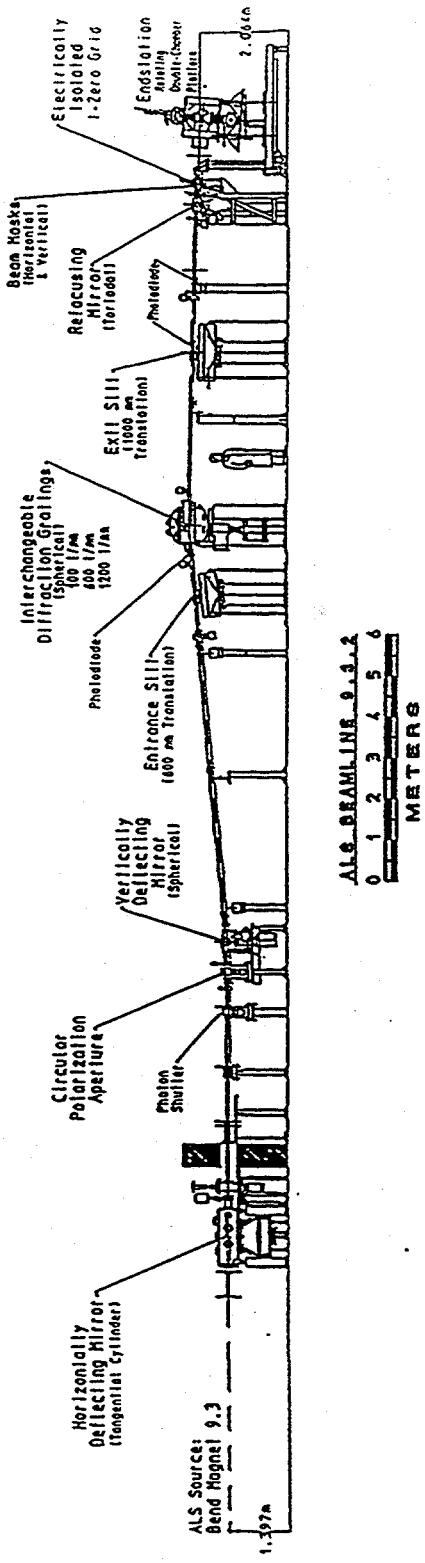

Fig. 5.4 Schematic of beamline 9.3.2 at the Advanced Light Source, LBNL, Berkeley, CA.

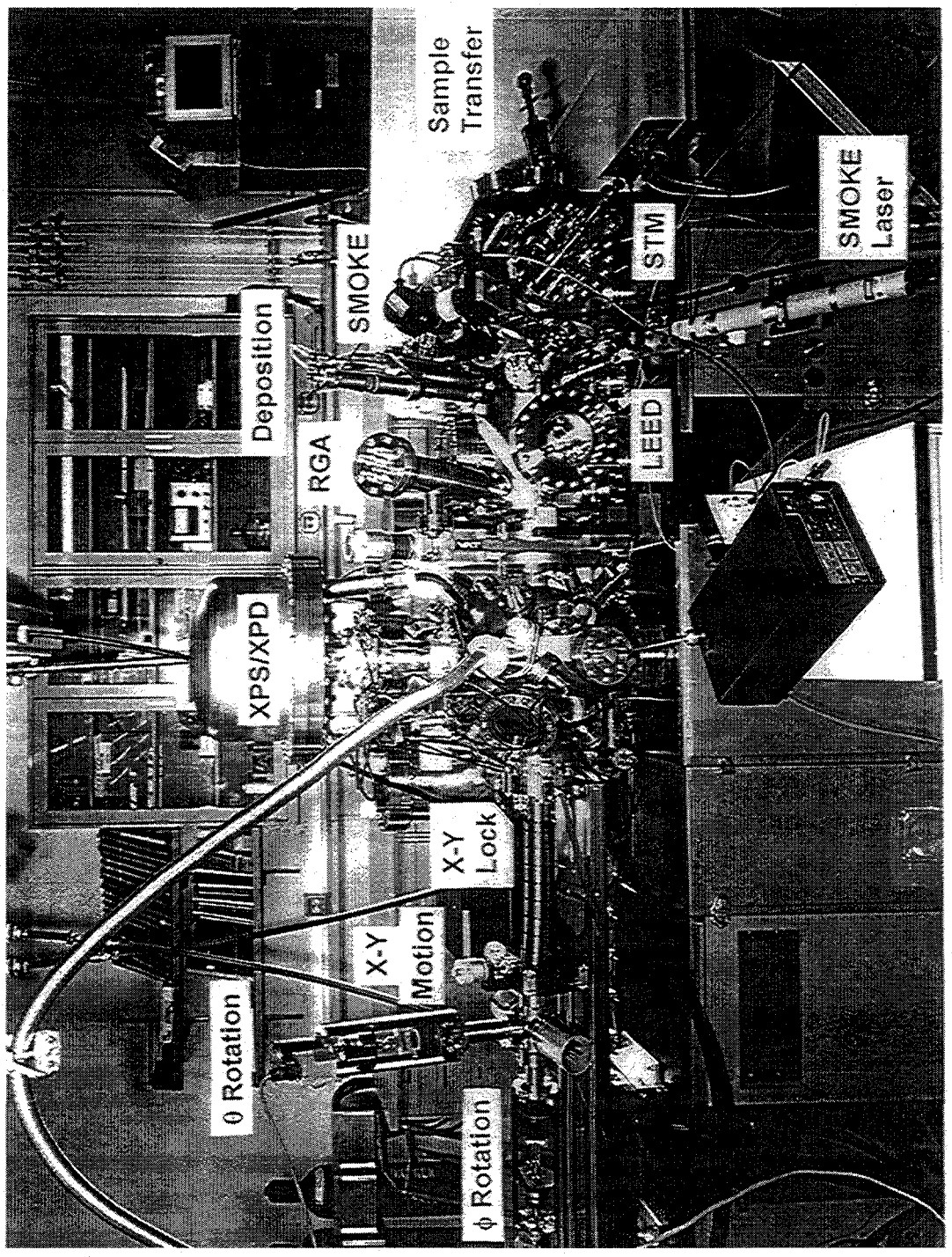

Fig 5.5 Photograph of a VG ESCALAB5 system with special modifications to combine XPS and XPD withSTM, LEED, and MOKE (System 3)

TOP VIEW

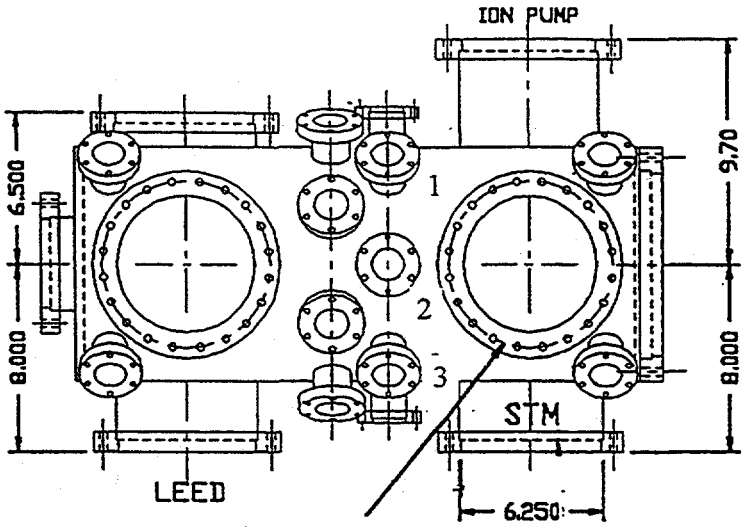

SIDE VIEW

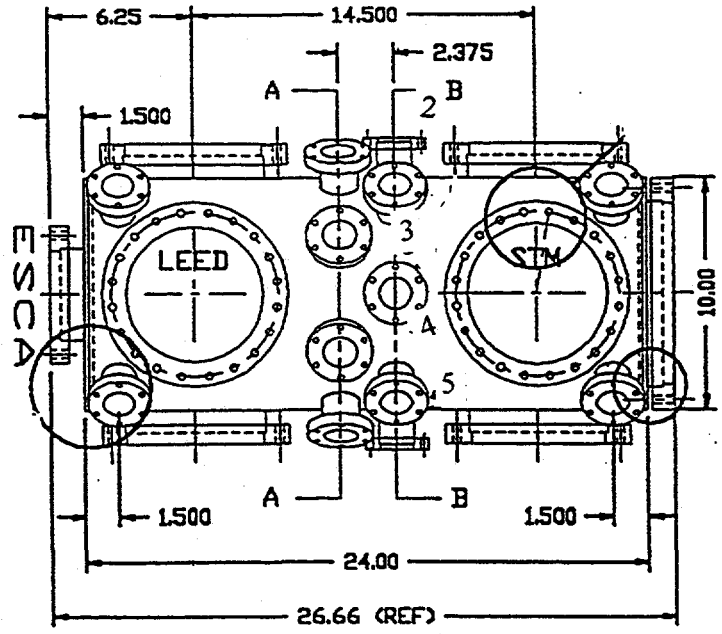

Fig. 5.6 Mechanical drawing of the preparation chamber on System 3 in which the MOKE was installed (a) top view, (b) side view. Certain ports pertinent to the MOKE installation are labelled.

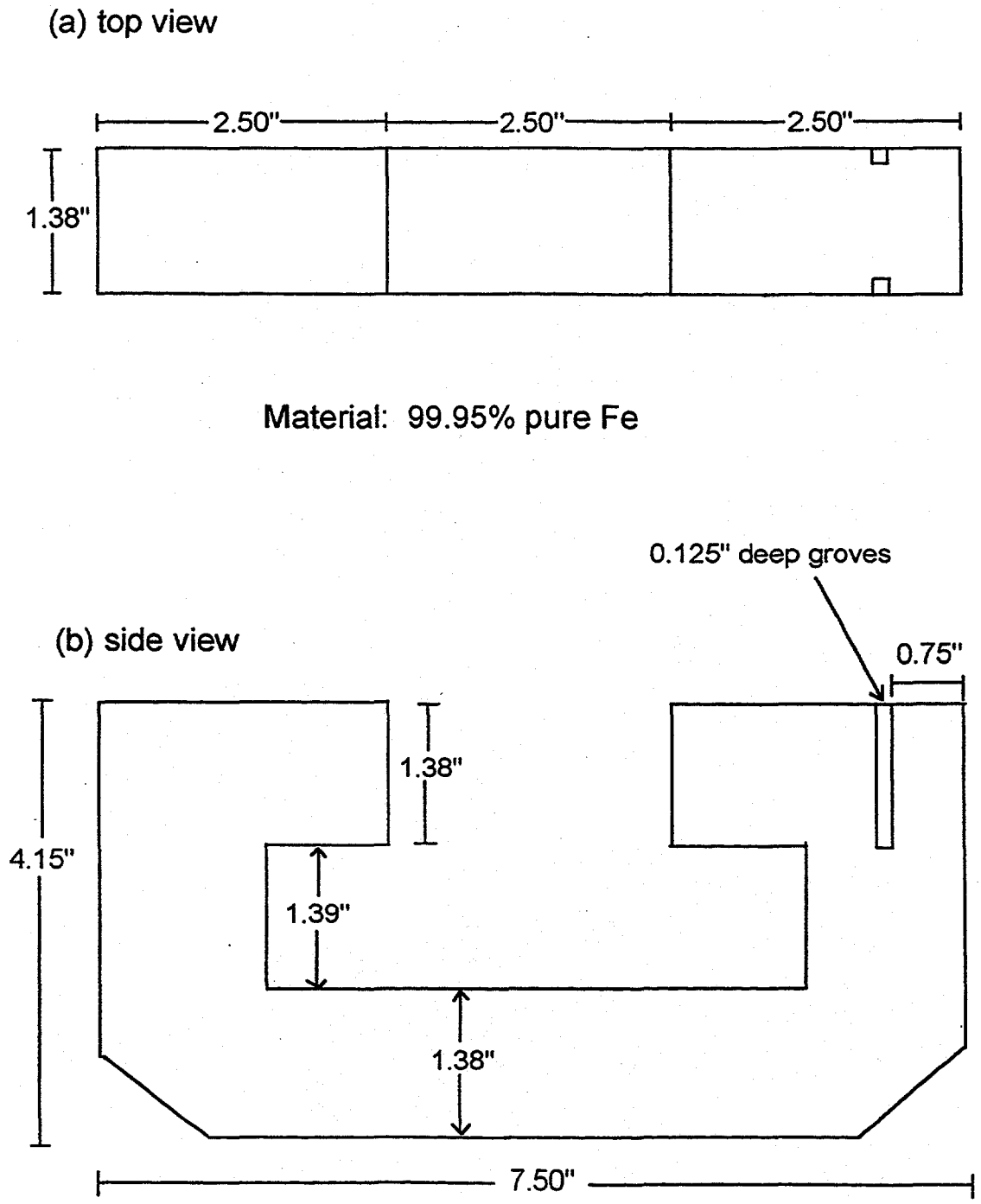

Fig. 5.7 Schematic diagram of the UHV MOKE magnet.

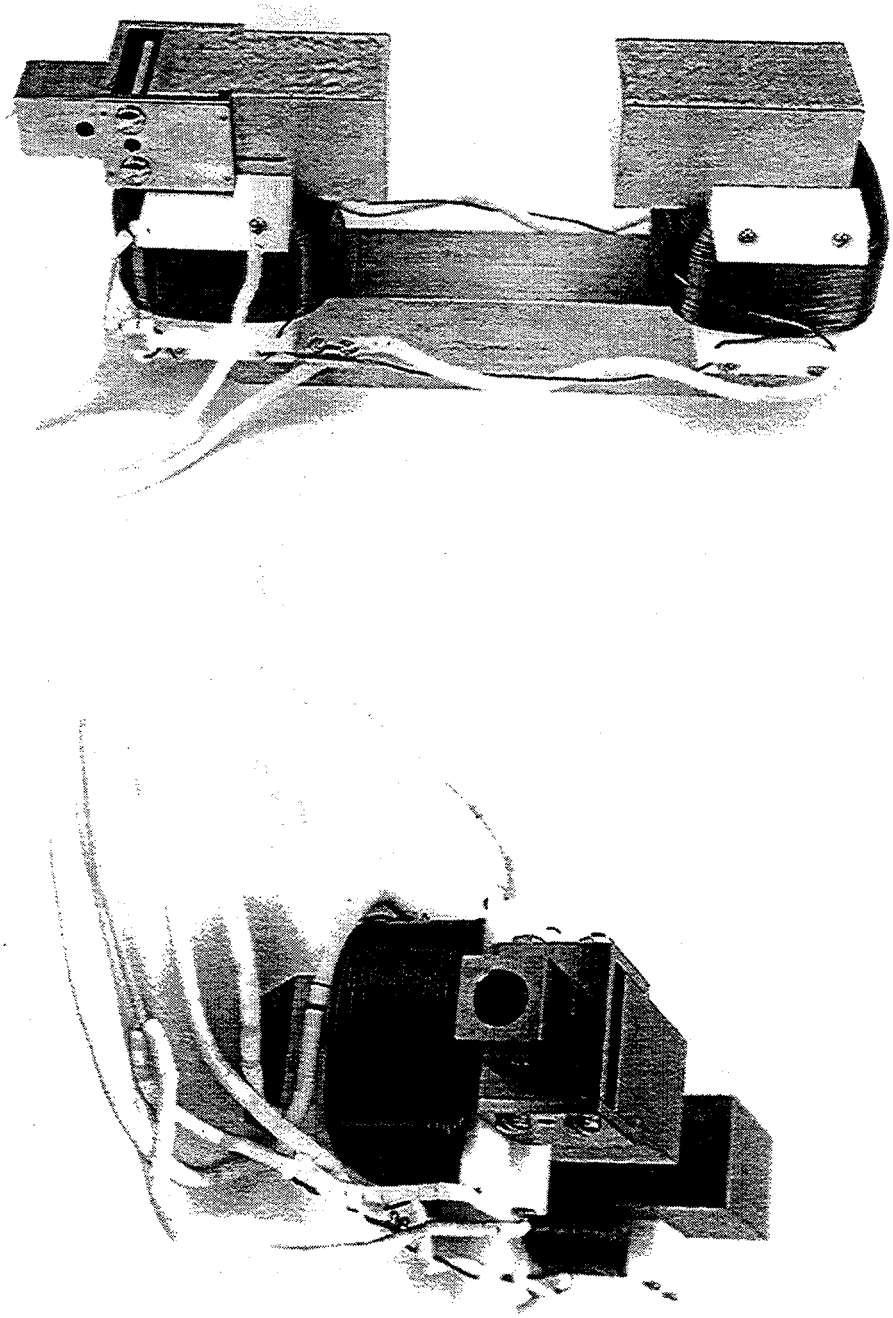

Fig. 5.8 Photograph of the assembled UHV MOKE magnet with kapton coated magnetization coils.

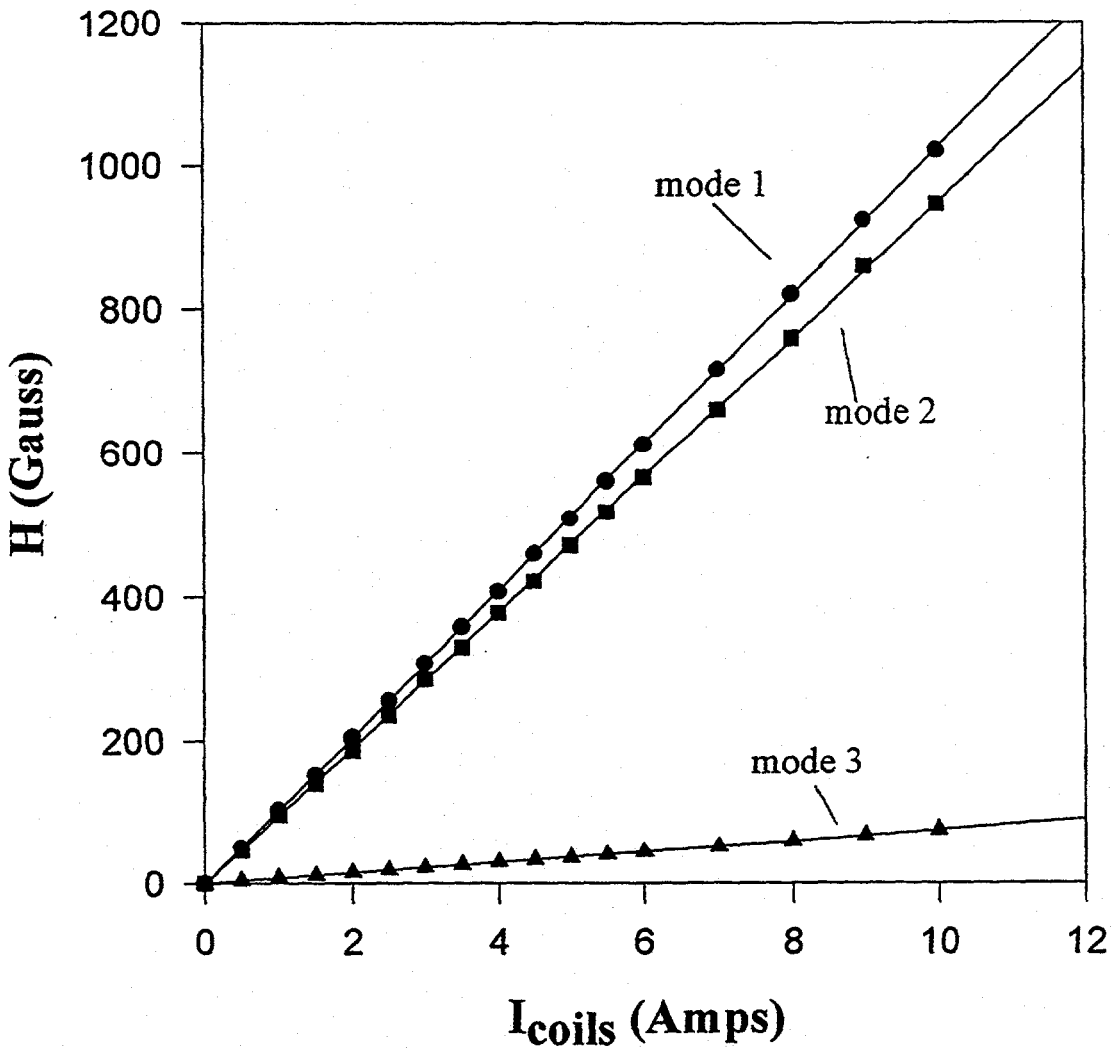

Fig. 5.9 Calibration curves of magnetic field H measured in the center of the poles vs. coil current for the three operation modes described in the text.

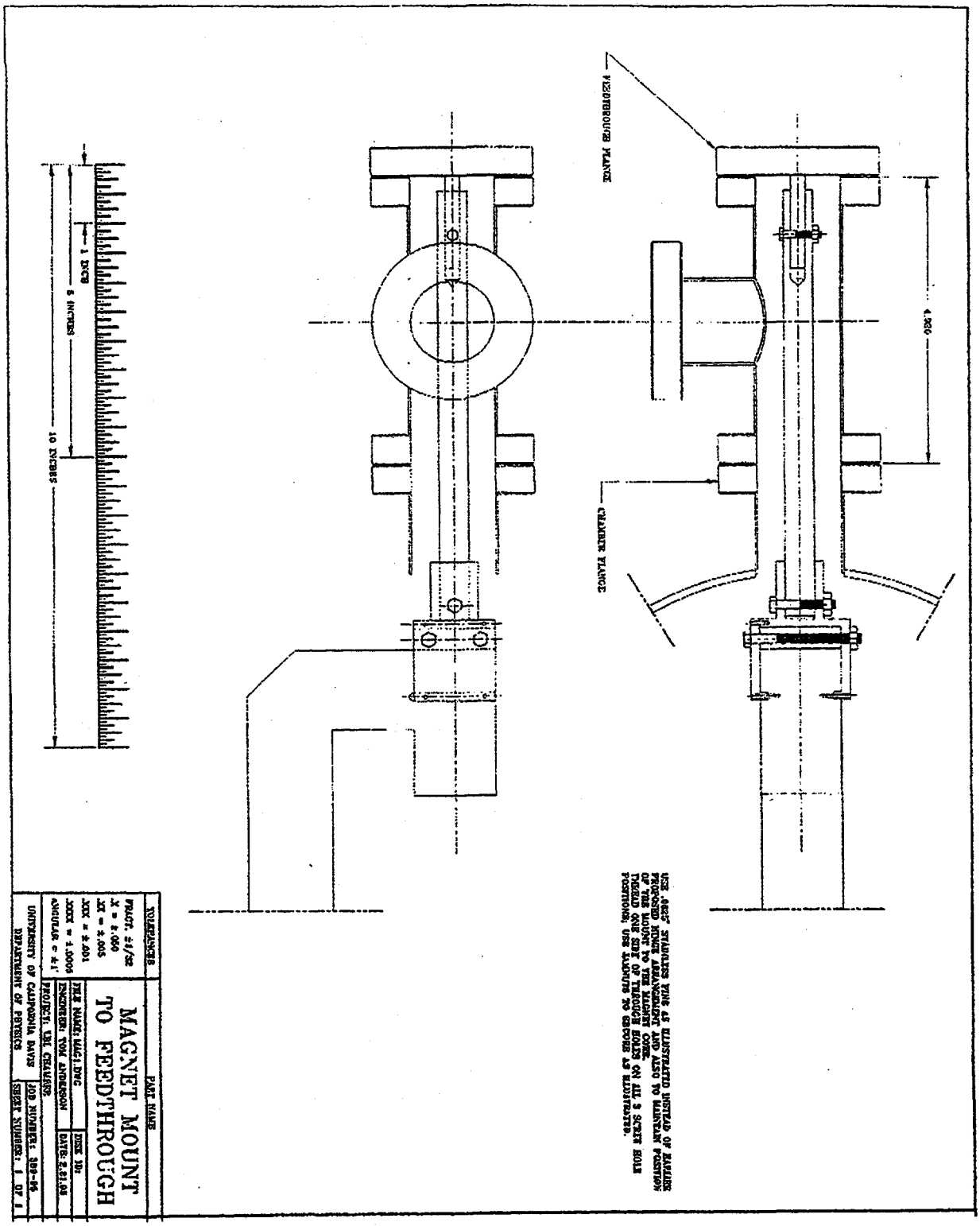

Fig. 5.10 Schematic diagram of the UHV MOKE magnet and rotation assembly. The MDC rotary feedthrough mounts on the flange labelled for this purpose.

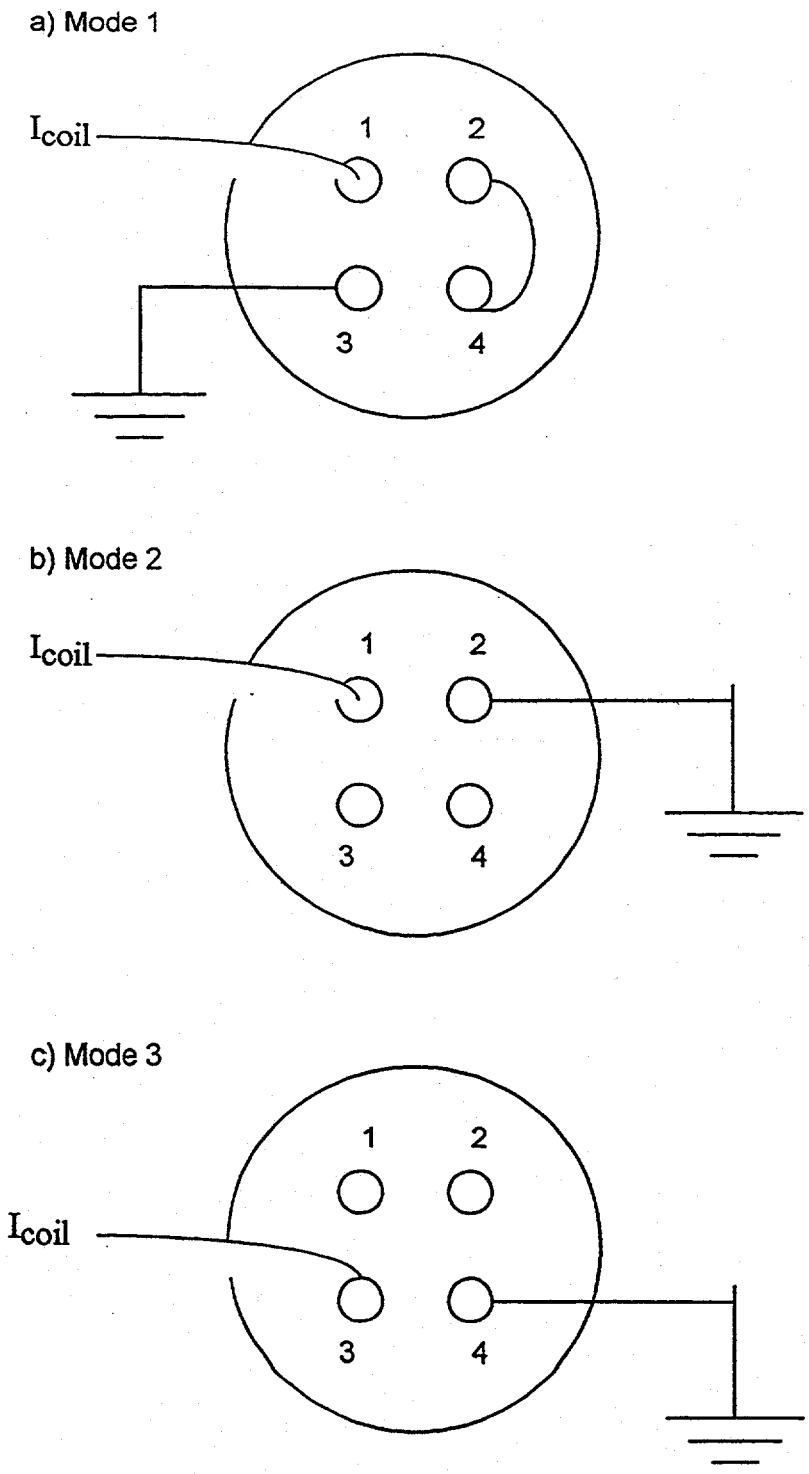

Fig. 5.11 Diagram of current feedthrough for magnetization coils as seen facing the feedthrough from the atmospheric pressure side outside vacuum side wired for (a) main and modulation coil serial operation, (b) main coil operation only, and (c) modulation coil operation only.

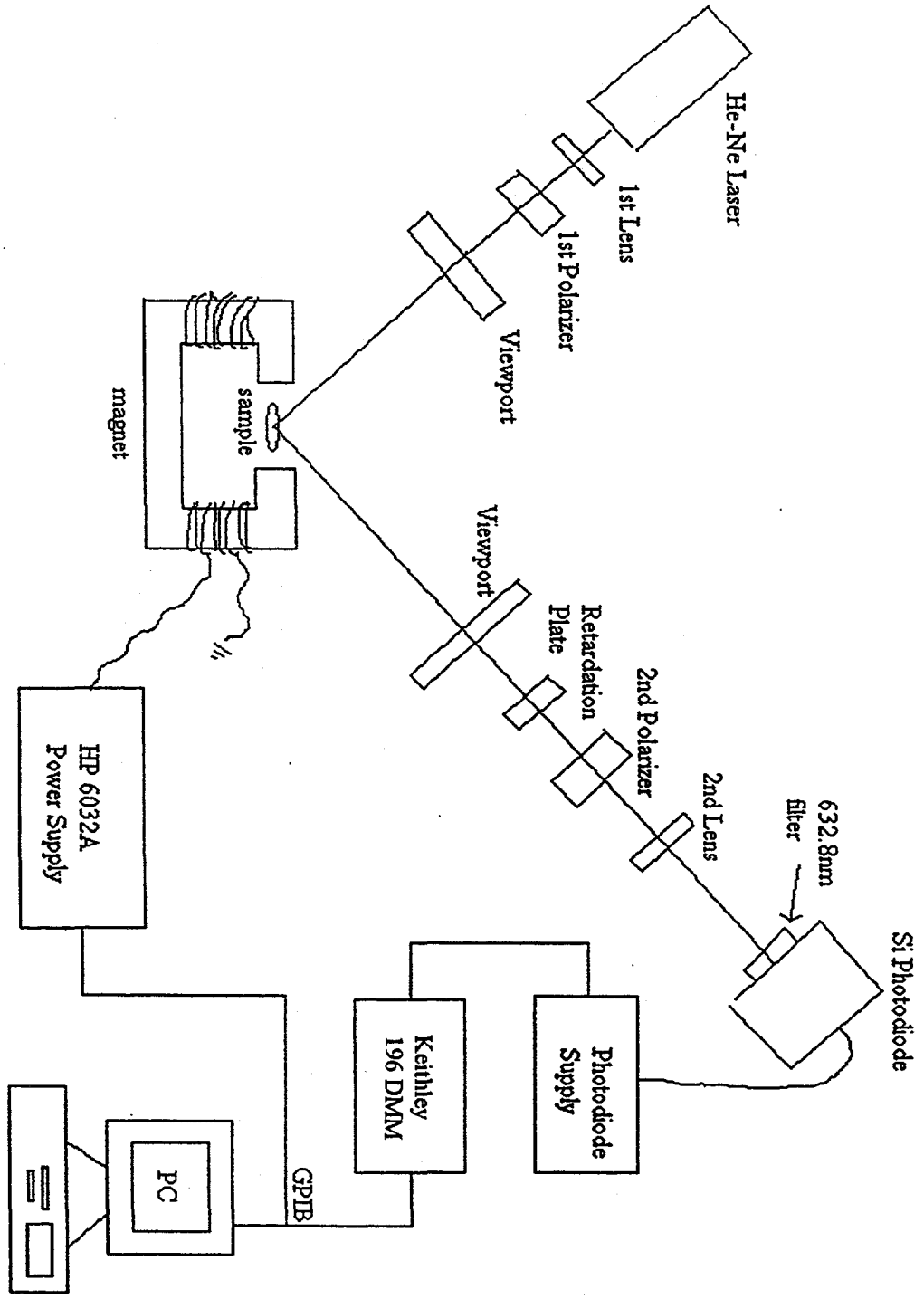

Fig. 5.12 Diagram of Kerr rotation detection scheme with appropriate optics arrangement.

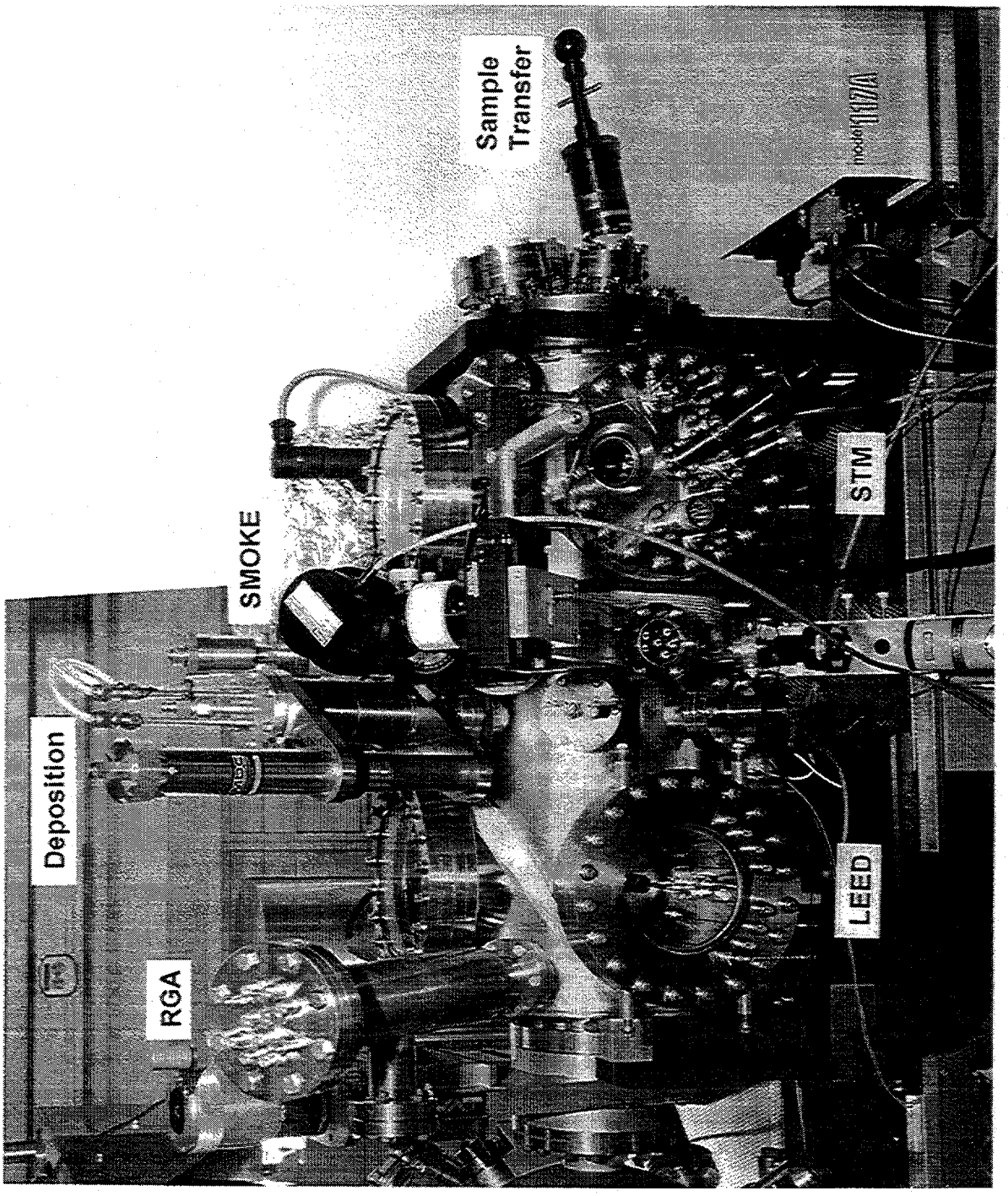

Fig. 5.13 Close up photograph of LEED/STM/MOKE chamber in System 3.

a) Longitudinal MOKE

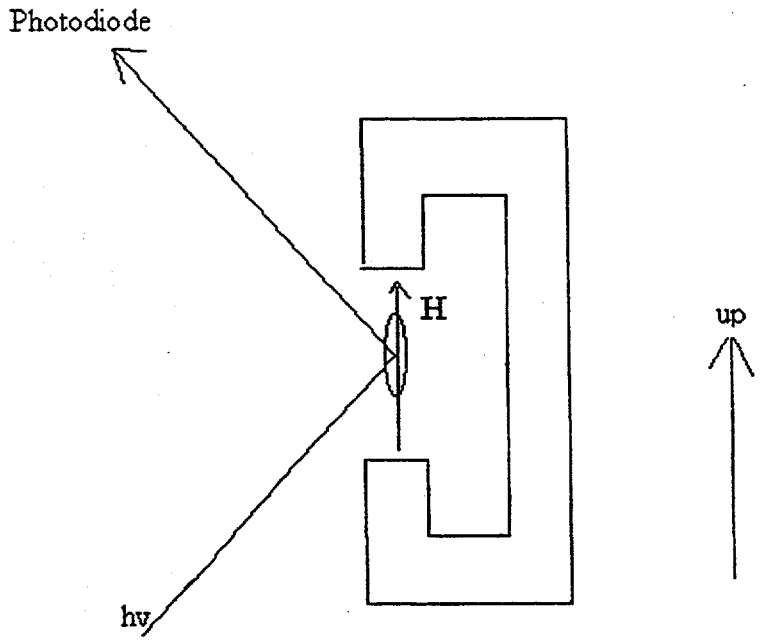

b) Polar MOKE

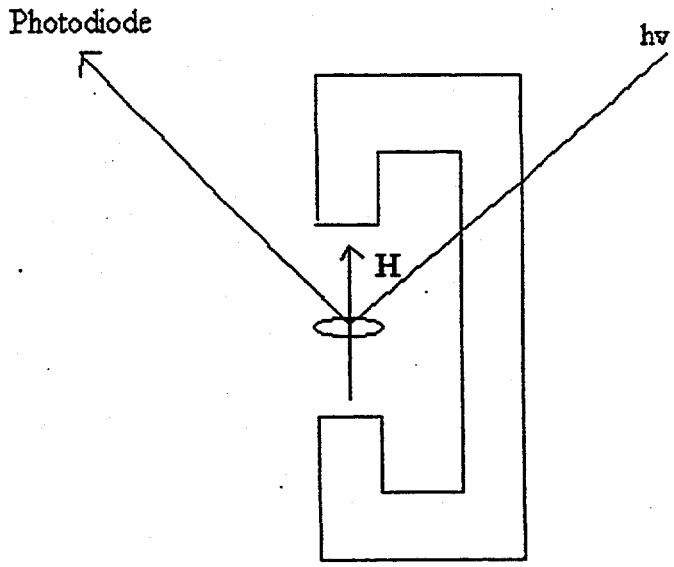

Fig. 5.14 Diagram of the two possible Kerr rotation detection modes: (a) longitudinal and (b) polar.

a)

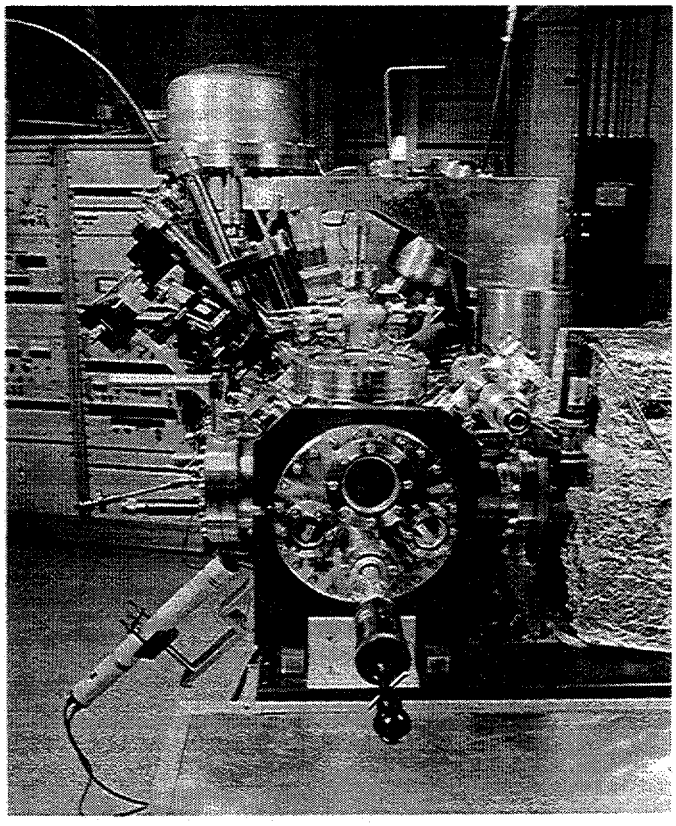

b)

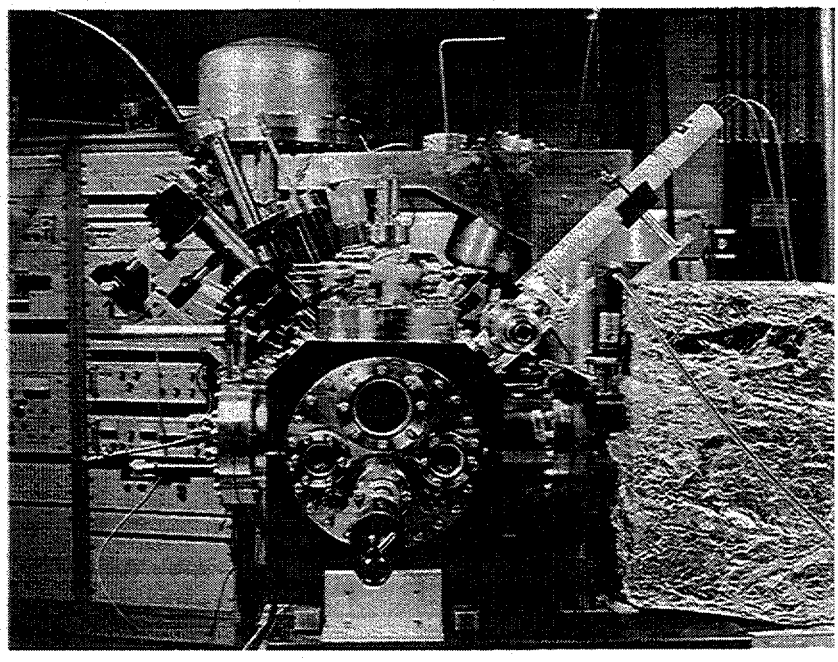

Fig. 5.15 Photograph of the MOKE instrument configured for (a) longitudinal and (b) polar Kerr rotation or ellipticity measurements.

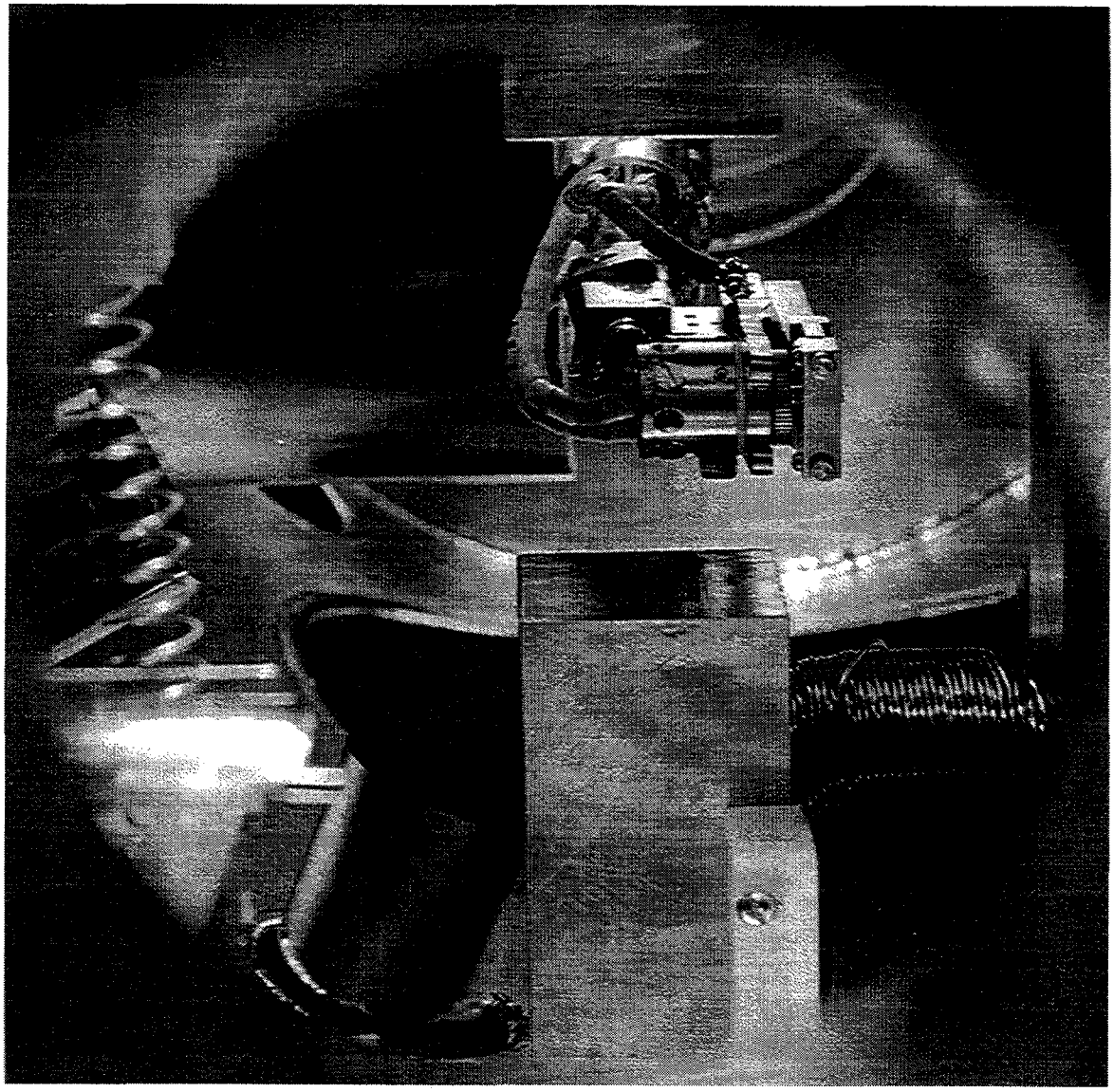

Fig. 5.16 Photograph of sample positioning between the magnet poles (shown for longitudinal measurement)

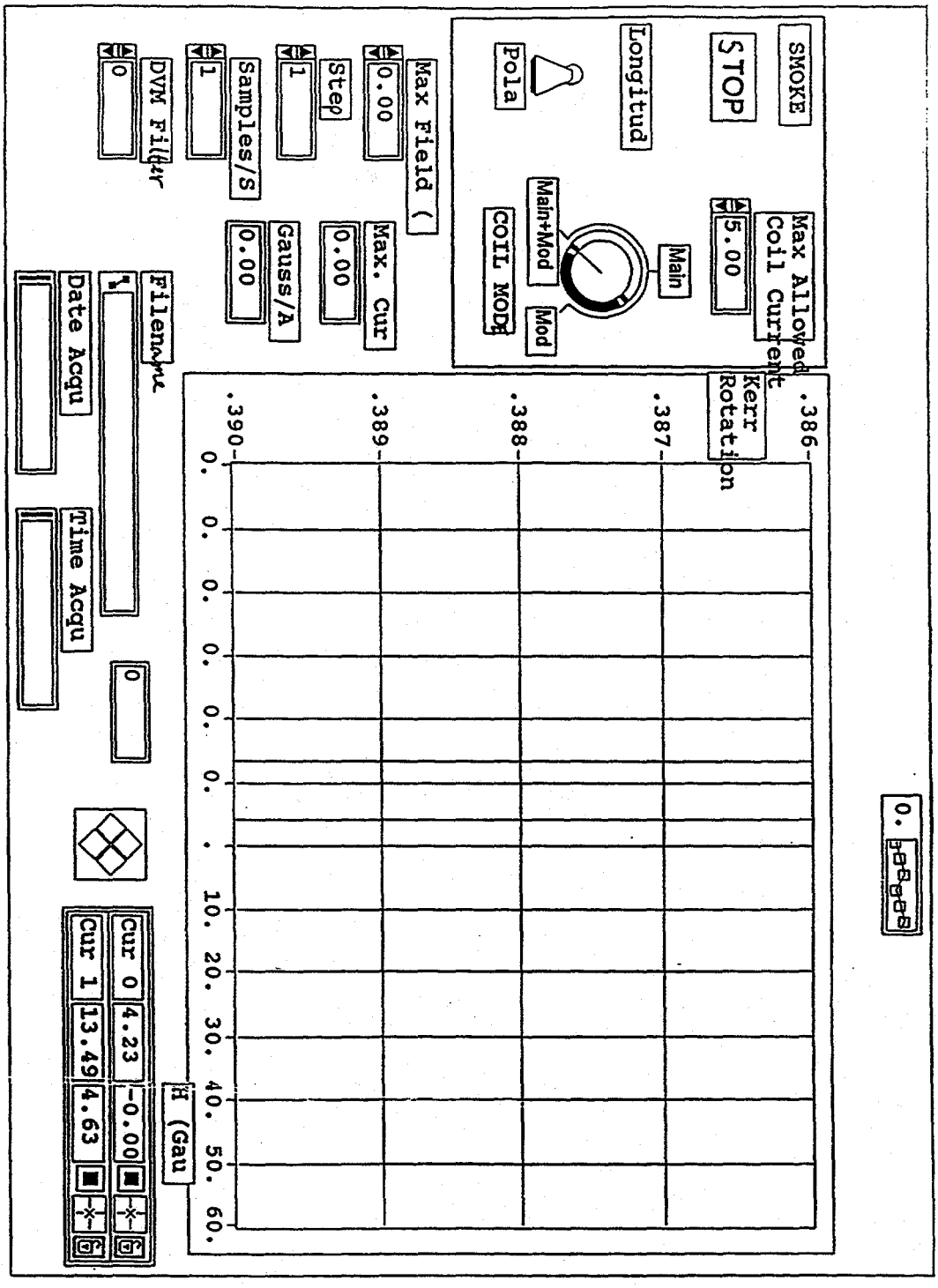

Fig. 5.17 Front panel of the SMOKE4.vi Labview program for operating the instrument.

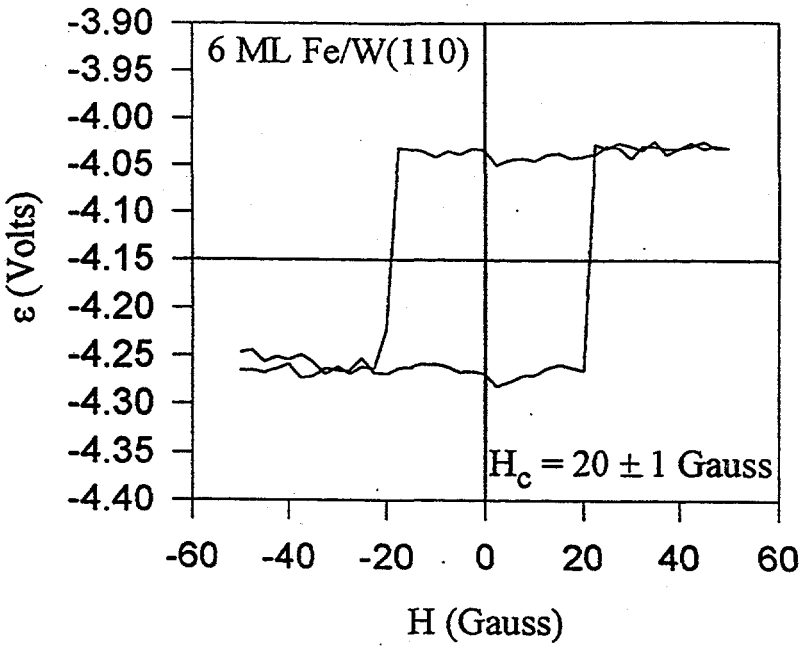

Fig. 5.18 Longitudinal Kerr ellipticity of an ~ 6 ML Fe film grown on W(110) at room temperature.

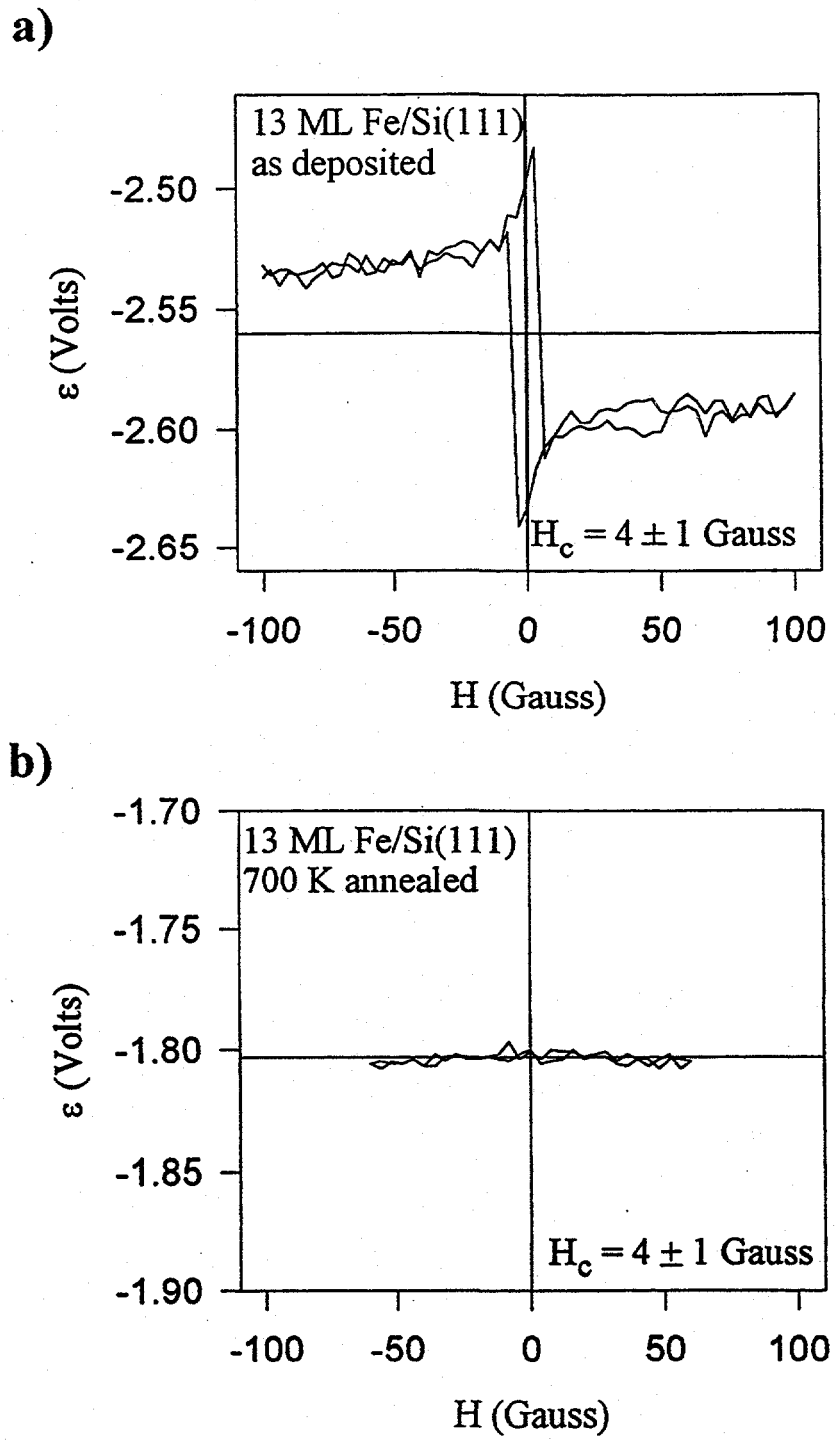

Fig. 5.19 Longitudinal Kerr ellipticity of an ~ 13 ML Fe film grown on Si(111) at room temperature (a) without post-deposition annealing, (b) with post-deposition annealing to 700 K for 5 min.

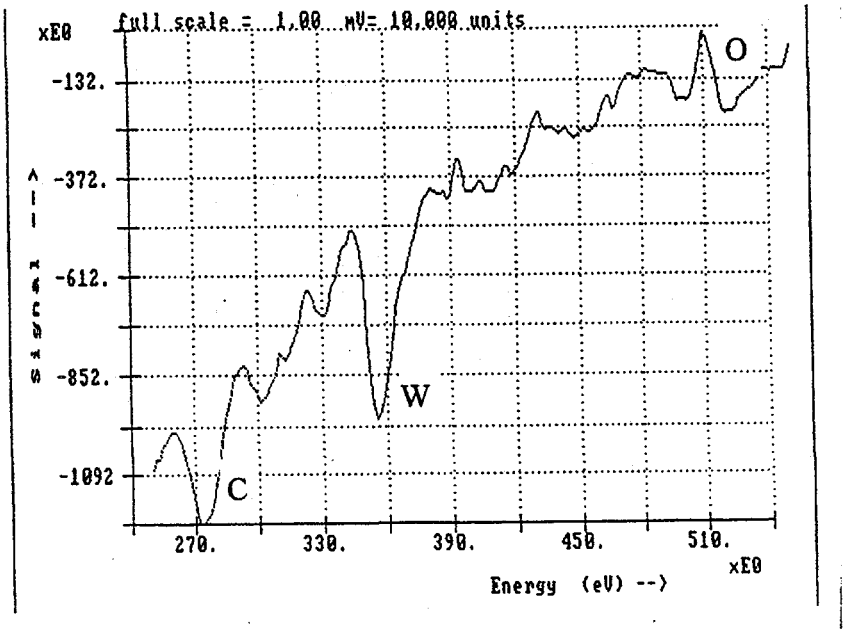

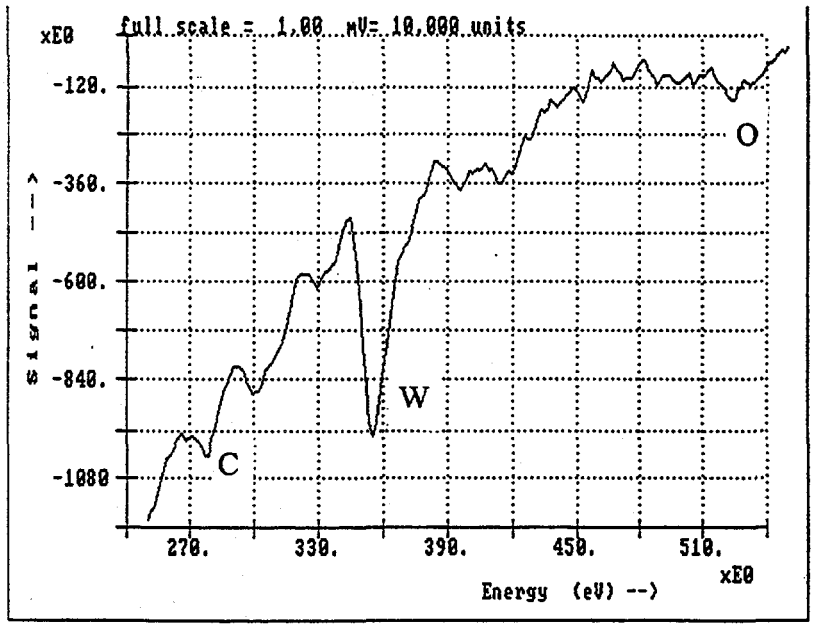

Fig. 5.20 Auger spectra of a W(110) surface taken with a 3 keV primary beam energy (a) before cleaning and (b) after cleaning by sample oxidation and a 2000° C flash.

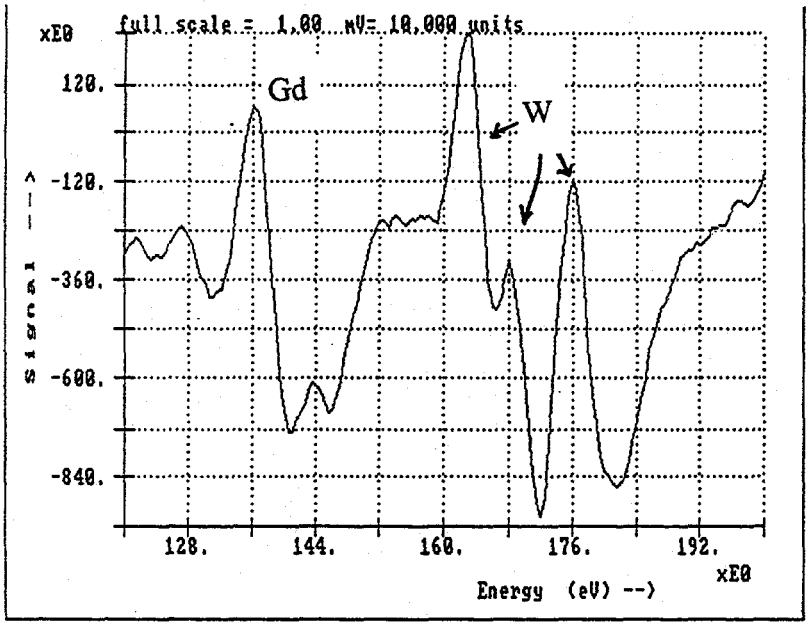

Fig. 5.21 Auger spectrum of 0.8 ML Gd film grown on W(110) with a 3 keV primary beam energy.

Fig. 5.22 Result of a "bearing" analysis to measure the fraction of the surface above a given height in a constant-current STM image from a 2.5 ML Gd film grown on W(110) and annealed to 530 K for 10 min (V_{bias} = 800 mV, I_{set} = 2.0 nA). The usual image is shown at left, and the bearing curve at right.

depth[nm] 6.50
percentage 33.50

Center Line Average = 6.89 nm

Scan Size[nm] = 200.00

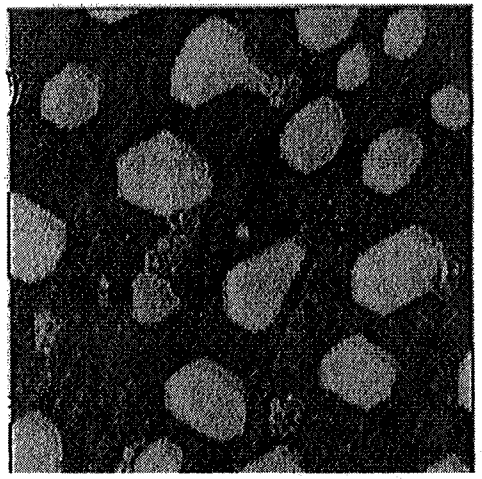

area
bearing

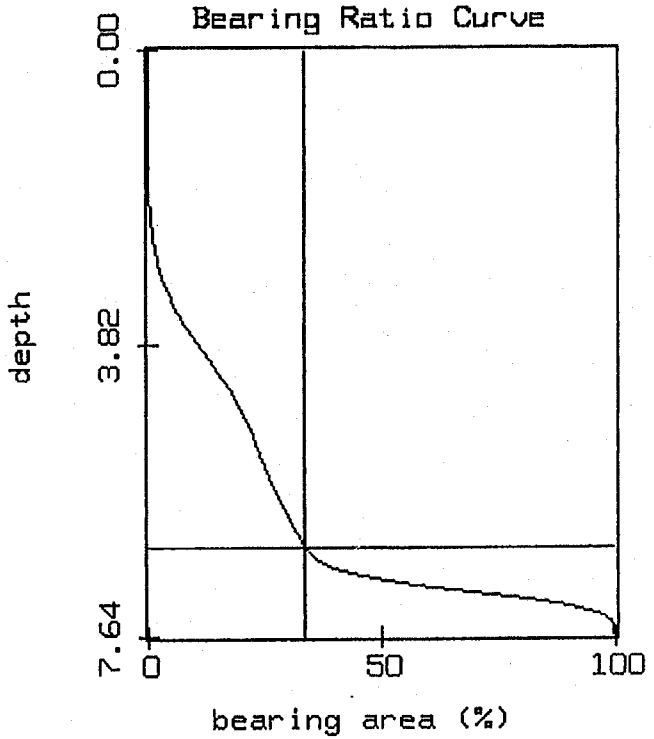

Data taken Sat Jan 29 22:42:04 1994
Buffer 3(GD013194.N04(F)), Rotated 0°, XY axes [nm], Z axis [nm]

Fig. 5.23 A single line scan of tip height vs horizontal displacement from a constant current STM image of a 2.5 ML Gd film grown on W(110) and annealed to 530 K for 10 min (V_{bias} = 800 mV, I_{set} = 2.0 nA). Also shown at lower right is a Fourier transform of this line scan.

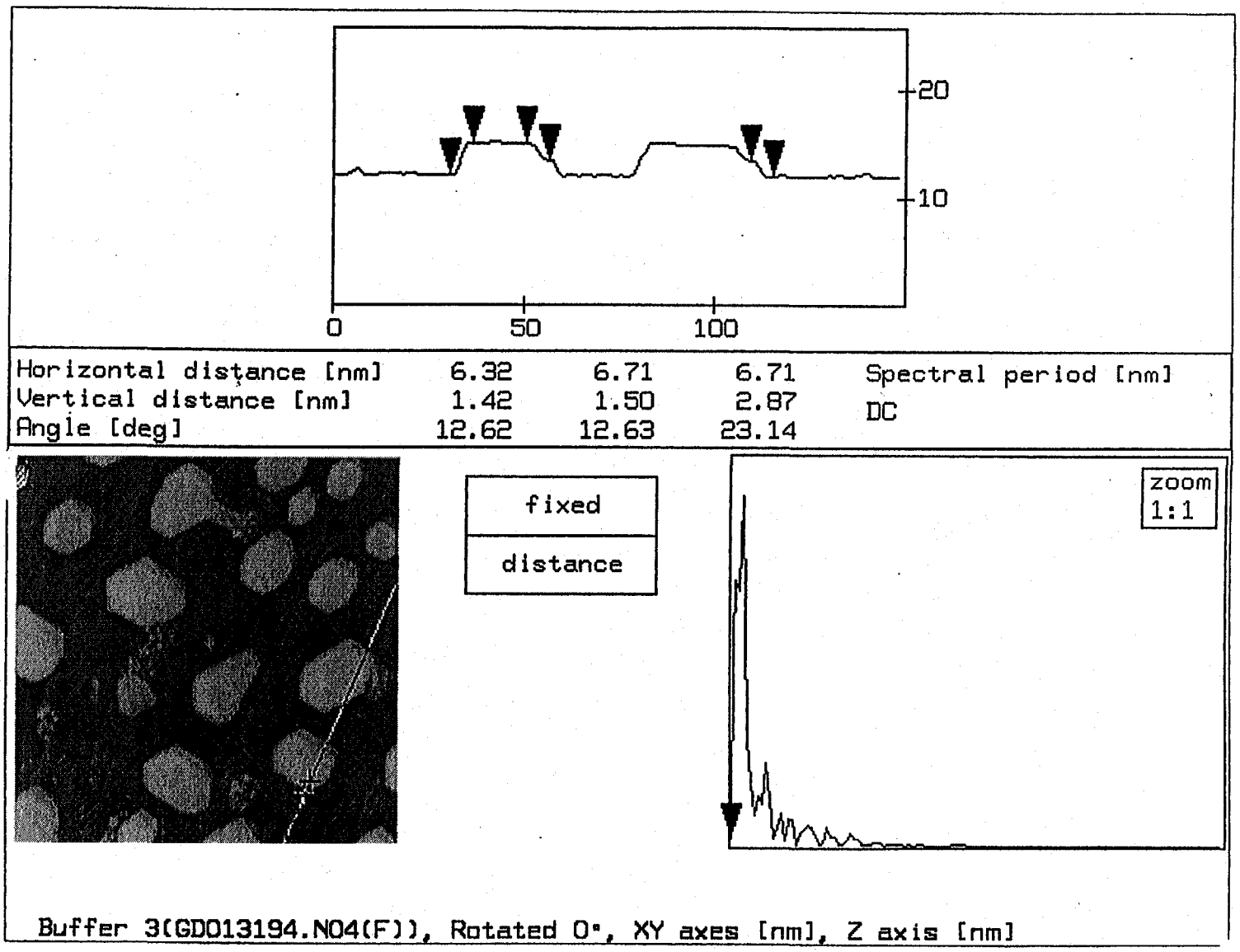
20
10
0
50
100
Horizontal distance [nm] 6.32 6.71 6.71 Spectral period [nm]
Vertical distance [nm] 1.42 1.50 2.87 DC
Angle [deg] 12.62 12.63 23.14
fixed
distance
zoom
1:1
Buffer 3(GD013194.N04(F)), Rotated 0°, XY axes [nm], Z axis [nm]

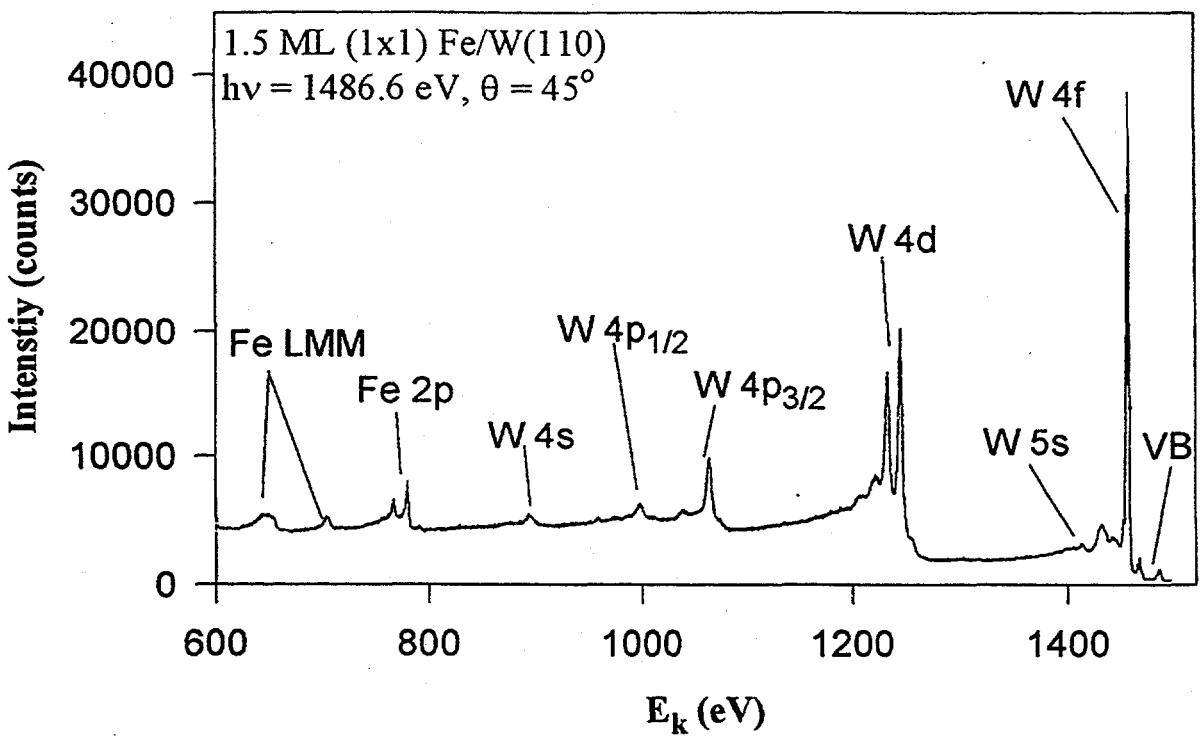

Fig. 5.24 Photoelectron overview spectrum taken from a 1.5 ML (1x1) Fe film grown on W(110) and annealed to 700 K for 5 min. The spectrum was taken eight hours after the film was prepared using Al Kα excitation (1486.6 eV photons) and an emission angle θ of 90° with respect to the surface.

Fig. 5.25 Photoelectron spectra from a 100 ML Gd(0001) film grown on W(110): (a) Overall spectrum taken with $h\nu = 700$ eV, $\theta = 90°$ and (b) Valence band spectrum taken with $h\nu = 38$ eV, $\theta = 90°$.

a)

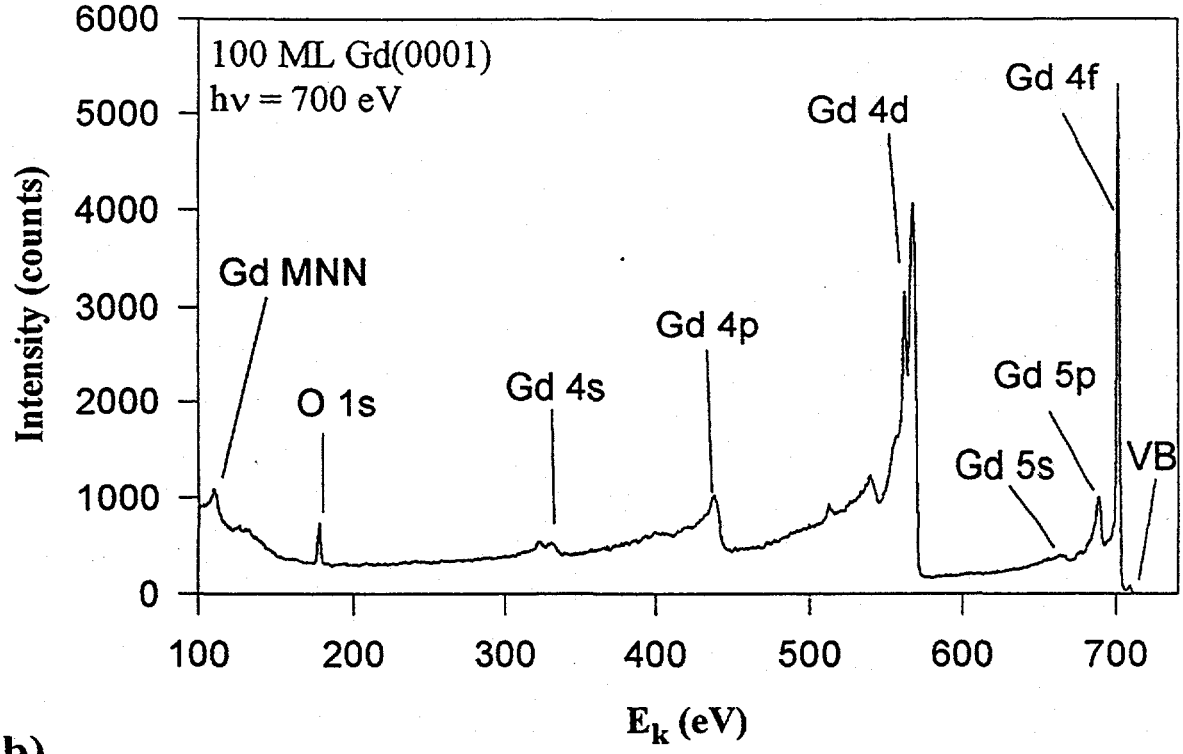
100 ML Gd(0001)
hν = 700 eV
Gd MNN
O 1s
Gd 4s
Gd 4p
Gd 4d
Gd 4f
Gd 5p
Gd 5s
VB
Intensity (counts)
E_k (eV)

b)

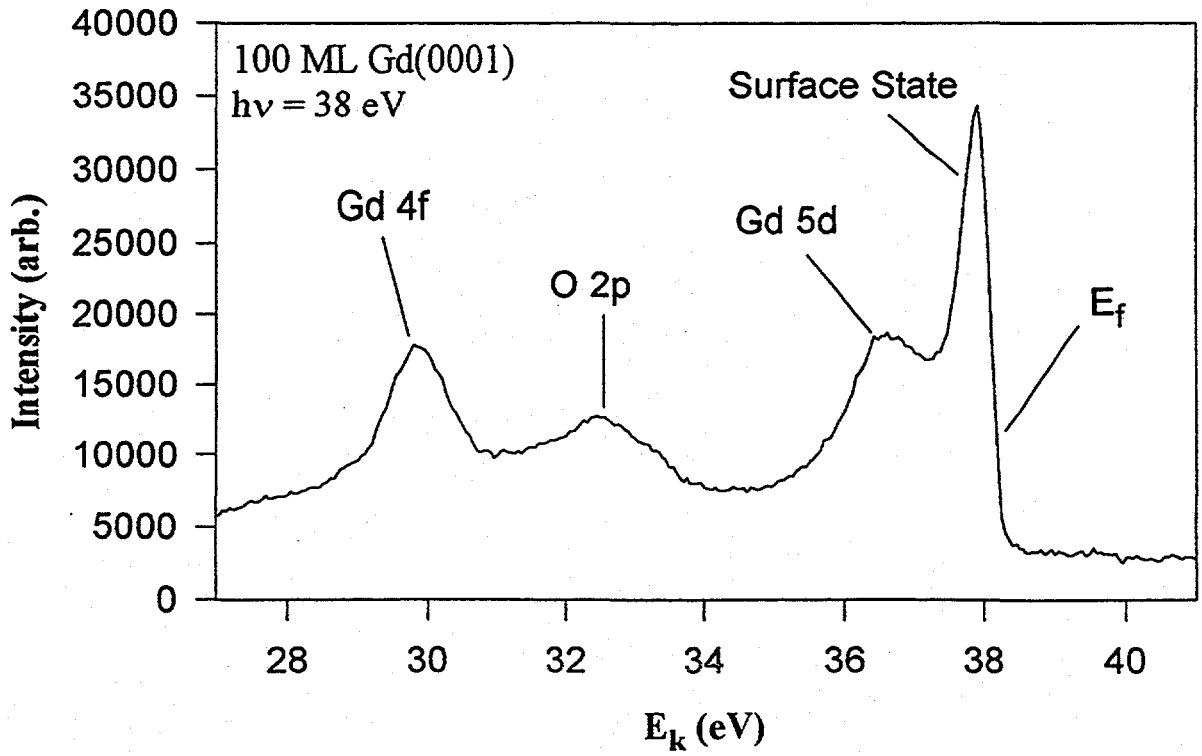
100 ML Gd(0001)
hν = 38 eV
Surface State
Gd 4f
Gd 5d
O 2p
E_f
Intensity (arb.)
E_k (eV)

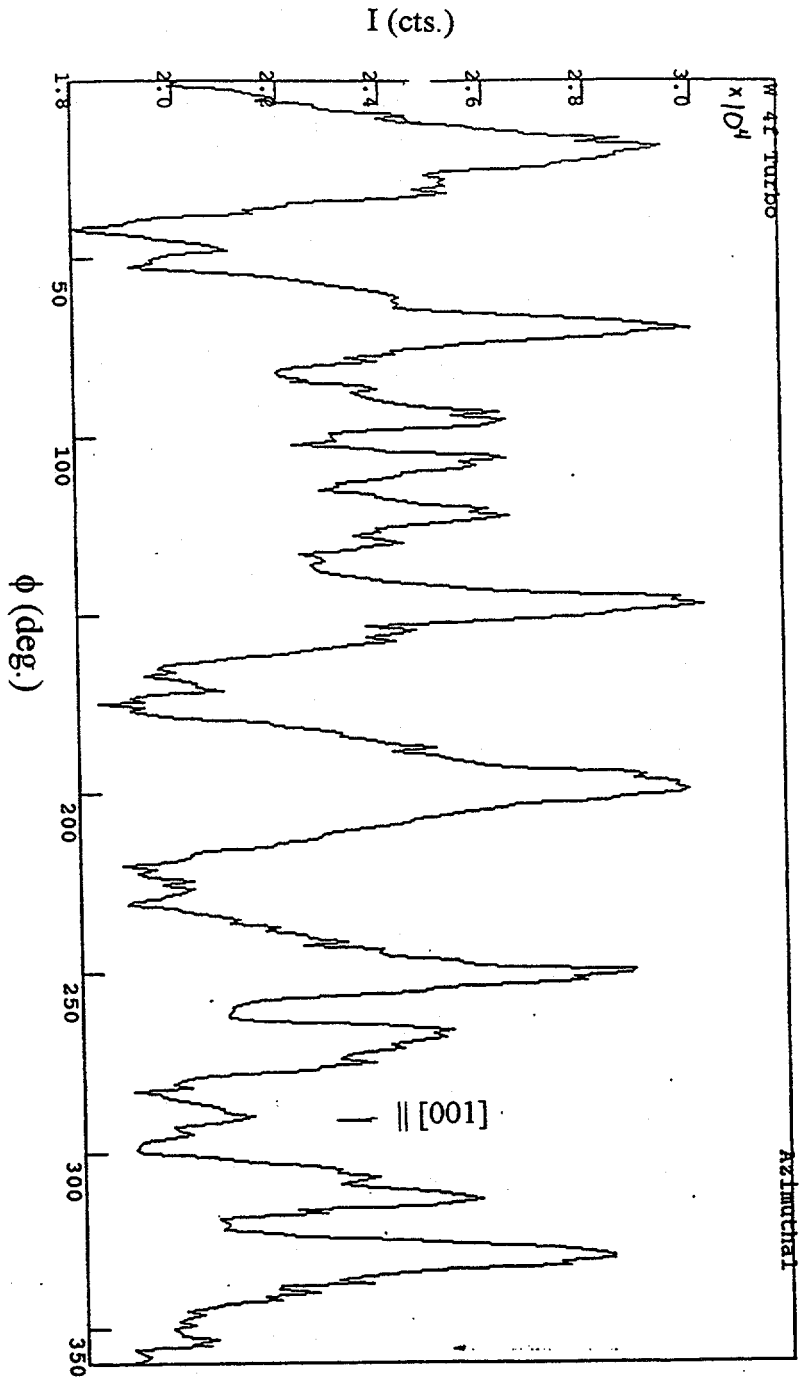

Fig. 5.26 A full 360° azimuthal PD scan of the W 4f peak taken from a clean W(110) surface at a polar angle $\theta = 45°$ using Al Kα x-ray excitation ($h\upsilon = 1486.6$ eV).

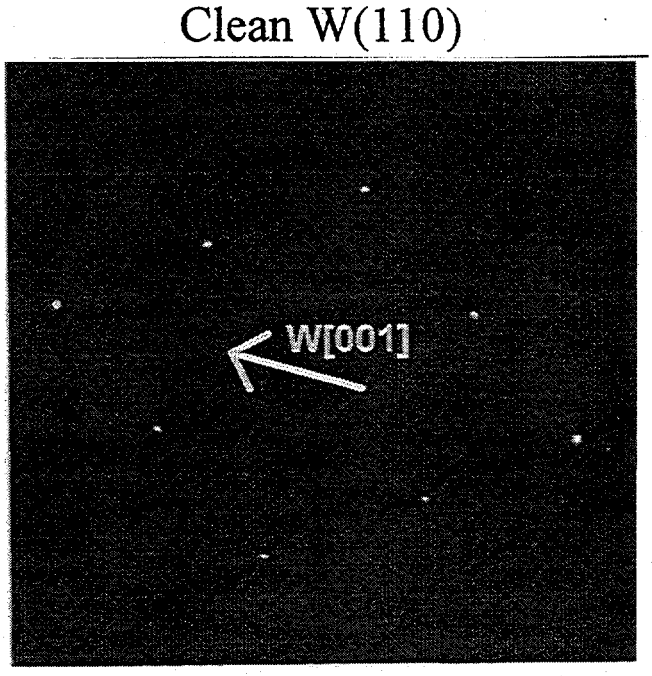

Fig. 5.27 A LEED pattern taken from a clean W(110) surface with a beam energy of 108 eV.

Chapter 6.

Concluding Remarks

In the effort to understand more fully the magnetic properties of thin films and surfaces, it is important to examine the interplay of elements such as surface/film morphology and growth, interfacial and surface atomic structure, short range and surface magnetic ordering, and the overall magnetic response of the film or surface. In this dissertation, the experimental techniques of scanning tunneling microscopy (STM), low energy electron diffraction (LEED), photoelectron diffraction (PD), spin-polarized photoelectron diffraction (SPPD) excited by high-brightness synchrotron radiation, and magneto-optic Kerr effect (MOKE) have been combined and used in conjunction with a full multiple scattering theory of PD to provide a unique opportunity for examining these varied elements for thin films and surfaces composed of the simple ferromagnets Fe and Gd grown on W(110). This work involved the development of unique new instrumentation, particularly at the Advanced Light Source in Berkeley. The significant conclusions from these studies are discussed in the following paragraphs, together with some promising areas for future investigation.

STM measurements on as-grown and annealed Gd films deposited on W(110) have supplied a much more detailed view of the growth modes and scaling properties of these thin films. Furthermore, examining the morphology of such films allowed a quantitative structural explanation for previously-measured magnetic properties and, in combination with LEED, revealed a new two-dimensional structure for the first monolayer. As deposited at room temperature, Gd does not grow in the Frank-Van der Merwe (smooth layer-by-layer) mode, but rather as multilayers of different thicknesses. Upon analyzing the film roughness as a function of coverage and lateral length scale, one observes that the growing Gd surface follows scaling laws for a self-affine surface. This behavior is characterized by the two scaling exponents α and β. The values determined for these

exponents indicate that growth may be mediated by surface diffusion in conjunction with step flow and/or island nucleation. The morphology of these Gd films in the 1 nm - 1 μm length scale has important implications for magnetic behavior. Annealing such as-deposited films at elevated temperatures is found to drastically alter the morphology of these films, as seen by both STM and LEED. Annealing films thicker than 7 ML at 530 K produces smooth, monatomically stepped surfaces. For coverages in the range of $1 \leq \theta \leq 7$ ML, 530 K annealing produces films containing large 3D islands with quasi-hexagonal symmetry and relatively uniform size resting on a base monolayer; this is thus an example of Stranski-Krastanov growth. Annealing to 710 K is observed to create even larger islands with a critical coverage for smooth films increasing to ~20 ML. Careful measurement of the island dimensions for an 11 ML film enables the prediction of a 97% reduction in peak intensity for ac magnetic susceptibility, and of a Curie temperature of approximately 284 K; these results are in excellent agreement with the prior experimental studies of these two properties. Finally, the first monolayer of Gd is observed to form a (7x14) superstructure with pseudo-(7x7) symmetry as well that is consistent with a minimally-distorted hexagonal two-dimensional Gd(0001) film. Evidence for this superstructure is seen in both our LEED and STM data. The superstructure arises due to the incommensurate epitaxial Gd 1st monolayer resting on top of the W(110) surface with a coincidence lattice match for Gd:W of 6:7 and 5:7 along W [001] and $[\bar{1}10]$, respectively.

In order to examine the atomic structure at the interfaces of Fe and Gd films grown on W(110), the W $4f_{7/2}$ core-level shifts have been utilized to perform interface-specific PD on these two systems. Fe grown on W(110) has been found to grow pseudomorphically in a (1x1) structure, as observed by LEED. In contrast, Gd is found to grow quite differently in an epitaxial, yet non-pseudomorphic overlayer as discussed in the prior paragraph. The full 2π PD data obtained for the (1x1) Fe/W(110) interface, coupled with full multiple scattering calculations, has allowed us to determine both the geometry at the

interface (bridge site), as well as the interlayer spacings Z_{12} (between the Fe and 1st W layer) and Z_{23} (between the 1st and 2nd W layers). This is the first such interface-specific PD structure determination for a metal-metal system. Because of the multiplicity of W-Gd bonding sites, the PD from the (7x14) Gd/W(110) interface was shown to be quite similar to that of the clean W(110) surface, and thus very different from the (1x1) Fe case. The large -390 meV interface core level shift (ICLS) for the Gd covered surface suggests greater core-hole screening by this overlayer as compared to emission from the clean (-320 meV ICLS) and Fe-covered (-235 meV ICLS) surfaces. Although we have here studied only the simplest case of interfaces under a single monolayer, it should nonetheless be possible to use such interface-specific PD for studying more deeply buried metal-metal interfaces, with the only requirements being that the system studied has a narrow enough core level, that it exhibits a large enough ICLS to be resolved, and that the combination of interface depth, (tunable) photoelectron energy, and photon flux are such that a reasonable count rate is obtainable from an emitting species at the interface. Such experiments thus represent a promising new direction for study at third-generation synchrotron radiation sources.

In order to examine the surface magnetic ordering of the rare-earth ferromagnet Gd, spin polarized photoelectron diffraction measurements were carried out on Gd(0001) utilizing both the 4s and 5s photoelectron multiplets. This system is unique in that it has in a few prior studies been shown to display a higher Curie temperature for the surface (T_{cs} $\cong$ 350 K) as compared to the bulk (T_{cb} = 293 K). These SPPD measurements further confirm this, and reveal the presence of ferromagnetic-to-paramagnetic transitions occurring at the bulk Curie temperature of 293 K and at a surface Curie temperature of ~350-375 K. Our value for the surface Curie temperature is thus in excellent agreement with the prior data, although perhaps 10-20 K higher than prior values. The maximum change in the 5s spin asymmetry with temperature is measured to be nearly 5% for both normal emission and emission at an angle θ of 54° with respect to the surface, with ϕ

parallel to the "$\bar{b}$" axis in plane ($\phi = 180°$). When ϕ is rotated by 90° from the last-mentioned position (i.e. $\theta = 54°$, $\phi = 90°$, lying in an axis symmetry equivalent to "a") no distinct breaks in the asymmetry are observed, illustrating the strong angular dependence of this effect. SPPD performed with more bulk sensitive conditions on the 4s level reveals a 2.6 to 3.3% effect at normal emission, with a more pronounced change in the asymmetry occurring near T_{cb}. The 4s data also show distinct dips near both the bulk and surface Curie temperatures. Both the 5s and 4s SPPD asymmetries are observed to reach a constant value or a slow monotonic variation for temperatures $T > 375$ K, indicating that short range magnetic order ceases beyond this point. Full multiple scattering calculations based upon the Rehr-Albers approximation predict the SPPD effects qualitatively as a function of emission angle between the fully ordered ferromagnetic and disordered paramagnetic states. At least three ferromagnetically aligned atomic layers are required in the calculations to produce significant SPPD asymmetries, indicating that such transitions arise from the near surface layer and not a single "magnetically-live" layer. Furthermore, the ^7S to ^9S peak ratio of the 4s multiplet is observed to greatly exceed the ratio of 7/9 obtained from a simple atomic model, giving additional support for the importance of correlation effects in the case of 4s emission. However, these effects appear to act on the 4s intensity ratio in the opposite direction to those discussed previously for the analogous 3s intensity ratio in Mn. Finally, the ^7S to ^9S peak separation in the 5s spectra is observed to vary systematically with temperature, showing a minimum with a 60 meV drop and two small dips as the temperature is increased through the bulk and surface Curie temperatures. Such effects on multiplet relative intensity and separation may be related to changes in the exchange splitting due to the valence electrons, to correlation induced effects creating regions with different temperature dependence within a CI manifold, and/or to spin- and temperature- dependent screening effects. The temperature-dependent multiplet splitting might also be useful as a new probe of bulk and surface magnetic transitions.

As is the case with most studies of a nature similar to those contained in this dissertation, a number of questions or directions of further study are produced in addition to the answers or results discussed in prior chapters. A few directions that additional study should take will now be mentioned. Annealing of thin Gd films was found to produce islands of nearly uniform size and separation. This suggests that such methods could be used to generate arrays of nanometer-scale ferromagnetic particles for study, as well as perhaps technological application. E.g., isolated ferromagnetic particles in a non-magnetic medium have previously been shown to display giant magneto-resistance and RKKY type interactions. For smooth Gd films, the bulk Curie temperature has been shown to decrease for film thicknesses below 30 ML. What will be the behavior of the surface magnetic transition as Gd films become thinner? How thick is the layer over which the elevated Curie temperature exists? How strongly is the surface coupling governed or affected by the bulk behavior? Furthermore, how will this change as one forms Gd islands by annealing to elevated temperature and what will the dependence be on the average island dimensions? Finally, for studying interface structures, what will be the effect of growing thicker Fe and Gd films on W(110)? Will PD still be feasible for these thicker films? Such questions go beyond the scope of a single dissertation and represent exciting areas for future study.

APPENDIX A.

Gd 4s & 5s Curve Fitting for SPPD

Properly determining the temperature dependence of the ^7S to ^9S peak asymmetries requires careful and consistent fitting of the resultant photoelectron spectra. To perform these fittings, the average peak shape parameters were determined for both the 5s and 4s Gd multiplets over all of the spectra acquired for these experiments. The individual fitting was done using the Scienta ESCA-200 fitting routines provided in the driving software for the ES-200 spectrometer. Each spectrum was fit using a Shirley background and two asymmetric Voigt functions (one for the ^7S and another for the ^9S). In the case of the Gd 4s multiplet, low levels of nitrogen contamination on the surface (~0.03 ML) produced a small peak at higher binding energy. Figure A.1 shows the Gd 5s and 4s multiplets fit using the aforementioned package for a 100 ML Gd film held at 500 K. The parameters used for the fitting were fixed using the average values:

PEAK	A(^7S)	A(^9S)	FW(^7S)	FW(^9S)	M(^7S)	M(^9S)	R(^7S/^9S)
Gd 5s	0.26	0.17	3.47 eV	2.56 eV	0.40	0.04	0.80
Gd 4s	0.33	0.21	7.74 eV	6.82 eV	0.00	0.40	1.06
N 1s	0.21		2.0 eV		0.00		

where A is the peak asymmetry, FW is the peak full width at half maximum, M is the mix, and R is the ratio of the ^7S to ^9S peak intensity.

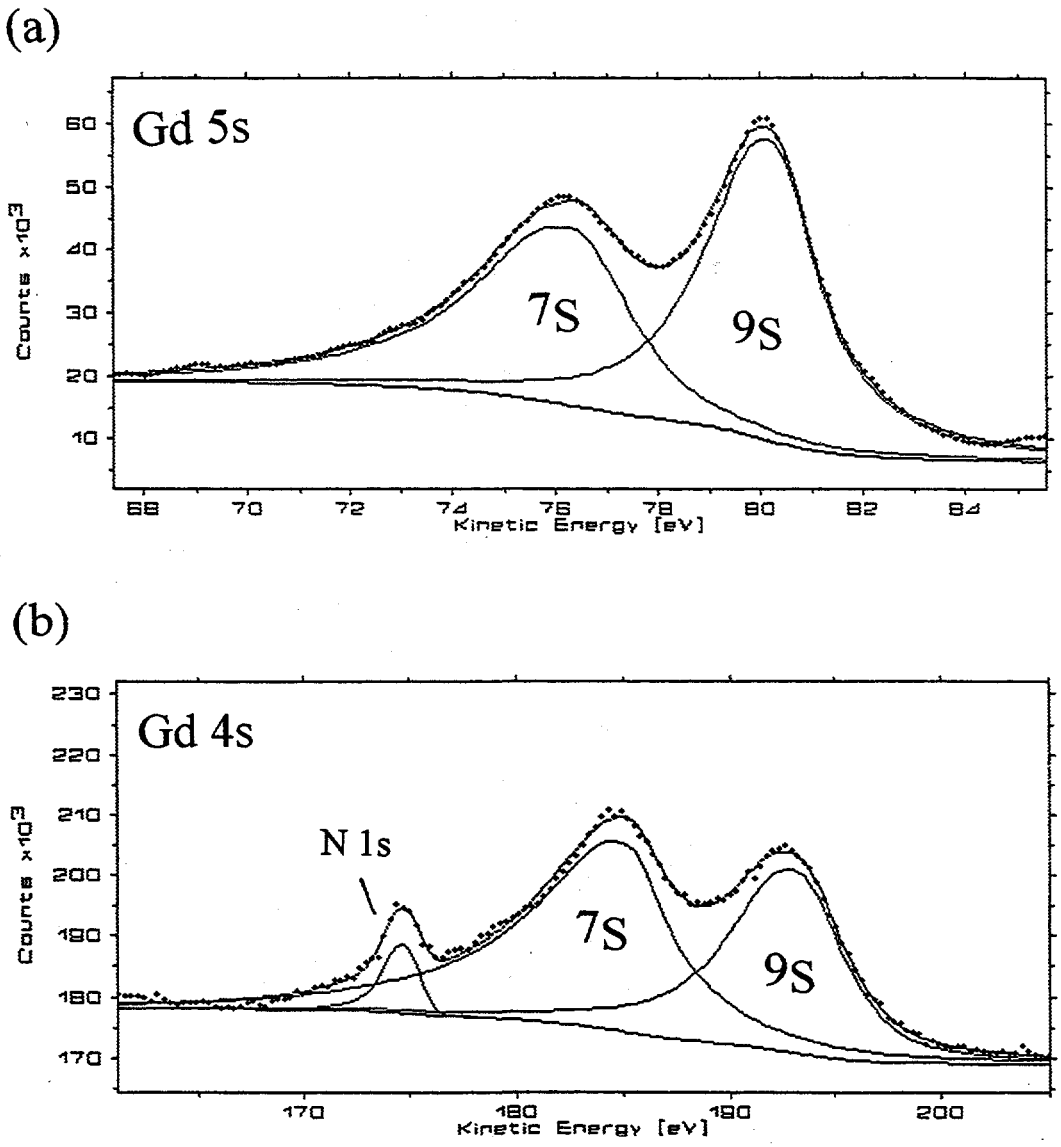

Fig. A.1 Photoelectron spectra from 100 ML Gd (0001) films held at 500 K: (a) the Gd 5s multiplet ($h\nu$ = 120 eV, normal emission) and (b) the Gd 4s multiplet ($h\nu$ = 565 eV, normal emission), have shown 10 hours after deposition with a small N 1s peak due to contaminatinon ($\leq$ 0.03 ML N).